



HAL
open science

Control of fire smokes in road tunnels equipped with mechanical ventilation systems

Fateh Chaabat

► **To cite this version:**

Fateh Chaabat. Control of fire smokes in road tunnels equipped with mechanical ventilation systems. Other. Université de Lyon, 2020. English. NNT : 2020LYSEC006 . tel-02896587

HAL Id: tel-02896587

<https://theses.hal.science/tel-02896587>

Submitted on 10 Jul 2020

HAL is a multi-disciplinary open access archive for the deposit and dissemination of scientific research documents, whether they are published or not. The documents may come from teaching and research institutions in France or abroad, or from public or private research centers.

L'archive ouverte pluridisciplinaire **HAL**, est destinée au dépôt et à la diffusion de documents scientifiques de niveau recherche, publiés ou non, émanant des établissements d'enseignement et de recherche français ou étrangers, des laboratoires publics ou privés.



ÉCOLE
CENTRALE LYON

N° d'ordre NNT : 2020LYSEC06

THESE DE DOCTORAT DE L'UNIVERSITE DE LYON
opérée au sein de l'Ecole Centrale de Lyon

Ecole Doctorale N° 162
Mécanique, Energétique, Génie civil, Acoustique

Spécialité de doctorat :
Mécanique des fluides et énergétique

Soutenue publiquement le 11 février 2020, par :
CHAABAT Fateh

**Control of fire smokes in road tunnels equipped
with mechanical ventilation systems**

Devant le jury composé de :

JAY Jacques	Professeur	INSA de Lyon	Président / Rapporteur
BOULET Pascal	Professeur	Université de Lorraine	Rapporteur
BERAUD Elisa	Dir. des études Tech.	EIFFAGE	Examinatrice
MOS Antoine	Responsable adjoint	CETU	Examineur
SALIZZONI Pietro	Professeur	Ecole centrale de Lyon	Directeur
CREYSSELS Mathieu	M. de conférence	Ecole centrale de Lyon	Co-directeur

,

I would like to dedicate this thesis to my loving parents, my brothers, my sisters and all my friends.

DECLARATION

I hereby declare that except where specific references are made to the work of others, the contents of this dissertation are original and have not been submitted in part or in whole for consideration for any other degree or qualification in this, or any other University. This dissertation is the result of my own work that is supported by the Région Auvergne Rhône-Alpes and carried out in partnership with the Centre d'Etude des Tunnels (CETU).

CHAABAT Fateh

ACKNOWLEDGEMENTS

This thesis was carried out at the Laboratoire de Mécanique des Fluides et d'Acoustique of the Ecole Centrale de Lyon. First of all, I would like to thank the laboratory's director BLANC-BÉNON Philippe and the director of the Ecole Centrale de Lyon DEBOUCK Franck, who gave me access to the laboratory and research facilities. Financial support by the Région Auvergne Rhône-Alpes is gratefully acknowledged. Without their funding, this project would not have been done.

I would like to express my sincere gratitude to my supervisor SALIZZONI Pietro for the continuous support of my PhD study and related research, for his motivation, patience, and immense knowledge. His guidance helped me in all the time of research and writing of this thesis. I could not have imagined having a better supervisor and mentor for my PhD research.

Besides my supervisor, I would like to thank my co-supervisor CREYSSELS Mathieu to have opened the door of the research to me after supervising my master's internship, for his insightful comments and encouragement, but also for his support during my PhD thesis.

The work was conducted in partnership with the Centre d'Etude des Tunnels of Bron. I would particularly like to thank MOS Antoine, who helped us define the thesis work plan based on its technical experience and knowledge on road tunnel fires.

I should like to express my warm thanks to the members of my dissertation committee: BOULET Pascal, JAY Jacques, BERAUD Elisa and MOS Antoine.

Many thanks to the thesis monitoring committee members LEVEQUE Emmanuel and VINCENS Eric who evaluated the progress of my research during the three years of my PhD study.

This work would not have been possible without the presence of the colleagues and friends, MEJEAN Patrick and MARRO Massimo who helped me immensely with acquisition programs, JIANG Lei and WINGRAVE Joy who supported me during several measurement campaigns, but also POUILLOUX Laurent who helped me with his precious knowledge on numerical computations. I extend sincere thanks to all the technical staff of the Laboratoire de Mécanique des Fluides et d'Acoustique, particularly, CORREIA Horacio,

TELALI Ahmed and POIREL Bruno for their availability to help me design the transverse ventilation system, as well as for their enthusiasm and their good mood. I want to acknowledge GROSJEAN Nathalie for all her guidance and clarity on the PIV, her good humour, her availability and above all her patience. I also extend greetings to all the administrative staff.

My sincere thanks also goes to the group AIR – Atmosphere: SOULHAC Lionel, CHARVOLIN Perrine, LAMAISON Guillevic and NGUYEN Chi-Vuong for the great times and memories we shared together. I would also like to express my deep gratitude to my office-PhD mates and all the closest friends in this adventure: VIDALI Cristina, FELLINI Sofia, KUBWIMANA Thierry, COUDON Thomas, SLIMANI Mehdi, MEJIA-ESTRADA Jheyson, LEBBAL Smail, BO Matteo, OTALORA Marcia, IACOBELLO Giovanni, GRANDONI Livia, TOSCANO Domenico, ORSI Michel and CINGI Pietro. I would like to thank GOSTIAUX Louis, MAFFIOLI Andrea and all the other members of the LMFA laboratory team for the discussions, the support and the friendly atmosphere that I have felt every day within the group.

I would like to thank my mother, my father, my brothers and my sisters for the unconditional love and support throughout writing this thesis. I apologize for not being with them in delicate moments during these years spent abroad.

Finally, I wish to show my gratitude to everyone who has contributed directly or indirectly to the effective conduct of my doctoral dissertation.

It has been a pleasure working with you and I am sending you my best wishes for the future.

Résumé

Lors d'un incendie en tunnel, la perte de visibilité due à la densité optique des fumées et leurs problèmes de toxicité sont considérés comme les risques principaux auxquels les usagers sont exposés. Pour cela, le contrôle de la fumée est souvent la partie la plus importante de la planification d'urgence. Les systèmes de ventilation sont l'une des principales mesures de protection à adopter pour empêcher la fumée de se répandre. Cependant, la propagation de la fumée est un phénomène très complexe et il est donc parfois difficile à contrôler. Cette complexité exige de meilleurs outils de sécurité pour améliorer l'efficacité des systèmes de ventilation et assurer ainsi la sécurité des personnes en cas d'incendie, ce qui constitue l'objectif principal de nos travaux de recherche.

Dans cette thèse, l'étude des incendies dans les tunnels routiers équipés de systèmes de désenfumage longitudinaux et transversaux a été réalisée expérimentalement et numériquement. Les expériences ont été menées dans une maquette froide aérodynamique située au LMFA dont le foyer est modélisé par le rejet d'un mélange d'air et d'hélium dans de l'air frais. En utilisant le code de calcul FDS (Fire Dynamics Simulator), des expériences ont été reproduites numériquement avec la méthode de simulation des grandes échelles LES (Large Eddy Simulation). Il est à noter qu'avec ce type de simulation d'incendie, les pertes de chaleur par rayonnement et par conduction à travers les parois du tunnel ne sont pas prises en compte, mais le modèle peut néanmoins fournir des informations sur la phénoménologie et les champs de données pouvant être comparés à des incendies réels.

Dans le cas de la ventilation longitudinale, les paramètres d'intérêt sont la vitesse critique et la longueur de la nappe de retour. La vitesse critique est définie comme la vitesse de ventilation minimale à partir de laquelle toutes les fumées sont repoussées en aval du feu, dans le même sens que le flux de ventilation. La longueur de la nappe de retour correspond à la distance parcourue par la fumée en amont de la source, dans le sens contraire du flux de ventilation, lorsque la vitesse de ventilation est inférieure à la vitesse critique. Dans le cas de la ventilation transversale, la longueur de la nappe de retour, la vitesse de confinement et la stratification de la fumée sont les paramètres d'intérêt. Dans ce cas, la longueur de la nappe de retour est la distance parcourue par la fumée en dehors de la zone d'extraction, définie comme la distance entre deux trappes adjacentes situées de part et d'autre de la source. La vitesse de confinement est la vitesse de ventilation minimale requise pour limiter toutes les fumées dans la zone d'extraction. La stratification de la fumée est un phénomène fondamental dans les systèmes de ventilation semi-transversaux et transversaux, qui se produit en raison des différences de densité entre les gaz légers (chargés de fumée) et l'air ambiant.

La stabilité des conditions de cette stratification est un élément essentiel pour garantir la visibilité aux usagers lors de l'évacuation.

Dans la première partie de la thèse, des mesures de champ de vitesse ont été effectuées à l'aide de la technique de vélocimétrie par images de particules PIV (Particle Image Velocimetry) pour étudier la dynamique des rejets flottants dans des tunnels à ventilation longitudinale. L'objectif est d'évaluer, dans les conditions critiques de ventilation, les effets non Boussinesq (liés aux grandes différences de densité entre le rejet flottant et l'air ambiant) sur la dynamique des rejets "forcés" et "paresseux", dominés respectivement par le flux de quantité de mouvement et le flux de flottabilité. Pour chaque type, deux rejets sont considérés, un rejet Boussinesq et un rejet non-Boussinesq. Les résultats ont montré que les amplitudes des contraintes de cisaillement et des fluctuations (dimensionnées par la vitesse d'injection W_i) sont plus élevées dans les panaches que dans les jets. Ceci implique que la flottabilité a pour effet d'améliorer le processus d'entraînement turbulent et donc d'augmenter le mélange turbulent entre le fluide du panache flottant et le fluide ambiant. Cette augmentation de d'entraînement amène le panache à être moins "sensible" (comparé aux cas des jets forcés) aux conditions imposées à la source, ce qui peut conduire à une indépendance entre la vitesse critique sans dimension $U_{0,cr}/W_i$ et le rapport de densité ρ_i/ρ_0 . Il convient de noter que pour le reste de l'étude, seuls les panaches paresseux sont considérés, puisque ils sont représentatifs des rejets flottants induits par la présence d'un incendie.

L'effet de barrières solides (connues sous le nom "d'écrans de cantonnement" et placées au plafond du tunnel) sur la propagation des fumées d'incendie dans des tunnels à ventilation longitudinale est ensuite étudié. Deux types d'obstacles ont été examinés: des "petites barrières", conçues pour être fixées le long du plafond du tunnel, et des "grandes barrières", conçues pour être mobiles et déployées uniquement en cas d'incendie. Les expériences ont été réalisées avec et sans les effets de blocage des véhicules. Ces véhicules sont modélisés par des blocs cubiques de différentes tailles et placés en amont de la source. Les résultats ont montré que les barrières peuvent contrôler efficacement la propagation de la fumée, même à basses vitesses de ventilation. Le taux de réduction de la vitesse critique dépend du taux de blocage créé par les obstacles (barrières, blocs ou les deux) situés juste en amont de la source. Cependant, l'ajout de barrières induit une augmentation des pertes de charge et potentiellement une augmentation de la capacité des ventilateurs à installer. Ces pertes ont été donc évaluées et les résultats ont montré que les grandes barrières sont plus efficaces que les petites barrières car elles empêchent la formation de la nappe de retour à des vitesses de ventilation très faibles et induisent moins de pertes de charge dans les tunnels encombrés.

Ensuite, à l'aide d'un système de ventilation transversale, les conditions de confine-

ment des fumées entre deux trappes d'extraction situées de part et d'autre de la source sont étudiées. Les effets de la forme et de la position des trappes (y compris le cas particulier des trappes de pleine largeur) sur les performances du système de ventilation transversale ont été évalués. Les résultats ont montré que plus la largeur de la trappe est importante et plus la trappe est placée près du centre du tunnel, plus le système de ventilation est efficace pour confiner la fumée dans la zone d'extraction et assurer la stabilité de la stratification des fumées. L'effet des barrières solides placées au plafond du tunnel (sur les bords des trappes les plus loin de la source) a été également évalué. Il a été constaté que les grandes barrières peuvent améliorer l'efficacité des trappes qui ne couvrent pas toute la largeur du tunnel, en réduisant la vitesse de confinement et en améliorant la stratification des fumées dans le tunnel.

Enfin, des simulations numériques d'incendies dans un tunnel avec ventilation longitudinale et transversale sont réalisées à l'aide du logiciel FDS et l'approche LES. Plusieurs simulations expérimentales sont reproduites numériquement pour compléter l'interprétation des résultats expérimentaux. Un bon accord est généralement atteint entre les résultats expérimentaux et les prédictions numériques. Néanmoins, un certain désaccord a été observé pour les panaches paresseux non-Boussinesq qui mériteront des études ultérieures. Les effets des barrières solides ainsi que ceux de la forme et de la position des trappes d'extraction sur le contrôle des fumées nocives sont bien reproduits numériquement. Les prédictions des vitesses critiques et de confinement sont similaires à celles obtenues expérimentalement, mais les longueurs de nappe de retour sont différentes dans la grande majorité des cas.

Mots-clés: Tunnel, feux, Panache flottant, Ventilation longitudinale, Vélométrie par images de particules, Vitesse critique, Nappe de retour, Barrières, Obstacles, Ventilation transversale, Trappes d'extraction, Vitesse de confinement, Stratification des fumées, FDS, LES.

Abstract

In this thesis, fires in road tunnels with longitudinal and transverse ventilation systems are investigated numerically and experimentally. The fire smoke is simulated as a buoyant plume obtained by injecting a mixture of air and helium into ambient air. With this simplified representation, the radiation and the heat losses at the walls are not taken into account, but the model can nevertheless provide relevant information on phenomenology and data fields that can be compared to real fires. The study aims to meet various objectives, in particular increasing the efficiency of the mechanical ventilation systems and improving the safety of tunnels users in the event of fires.

In longitudinal ventilation, the parameters of interest are the critical ventilation velocity and the backlayer length. The critical ventilation velocity is the minimum ventilation velocity required to ensure that all the smoke remains downstream of the source, in the same direction as the ventilation flow. The backlayer length is the distance that the smoke travels upstream of the source, against the direction of ventilation flow, when the ventilation velocity is below the critical velocity. In transverse ventilation, the backlayer length and confinement velocity as well as the smoke stratification are the parameters of interest. In this case, the backlayer length is the distance the smoke extends away from the source outside the extraction zone, which is defined as the distance between two adjacent vents either side of the source of emission. The confinement velocity is the minimum induced longitudinal velocity required to restrict all the smoke within the extraction zone. Smoke stratification is a fundamental phenomenon in semi-transverse and transverse ventilation systems, which occurs due to differences in density between the light gases and the ambient air. The stability of the stratification conditions is indispensable to ensure the safety of the tunnel users.

The study includes four distinct parts. First, experiments are conducted to measure, using Particle Image Velocimetry (PIV) system, the velocity fields induced by turbulent buoyant plumes released within a longitudinally ventilated tunnel. The aim is to study, in the critical ventilation conditions, the non-Boussinesq effects (i.e. effects related to large density differences between the buoyant plume and the ambient air) on the dynamics of the momentum-driven releases and buoyancy-driven releases. For each type, two cases are considered a case with a Boussinesq release and a case with a non-Boussinesq release. The results show that the magnitude of both shear stresses and fluctuations (scaled by the injection velocity W_i) are much higher in buoyancy-dominated releases than in jets. This means that the buoyancy acts to enhance turbulent entrainment process and therefore to

increase the turbulent mixing between the buoyant plume fluid and the ambient fluid. This increase in entrainment makes the plume less "sensitive" (compared to the cases of forced jets) to the conditions defined at the source, which can lead to independence between the dimensionless critical velocity $U_{0,cr}/W_i$ and the density ratio ρ_i/ρ_0 . Note however that only the buoyancy-dominated releases are considered for the rest of the study, since they are representative of the buoyant releases induced by the presence of a fire.

The effect of solid barriers, placed at the tunnel ceiling, on the propagation of smoke in fire events within longitudinally ventilated tunnels is then studied. Two types of barrier are considered: "small barriers" designed to be fixed in place and "large barriers" designed to be mobile in real tunnels. Experiments are carried out with and without vehicular blockage, modelled by blocks of different sizes and placed upstream of the source. It is found that the presence of barriers and/or blocks prevents the smoke back-layering flow and reduces the critical velocity. The reduction rate of the latter depends on the blocking rate created by the obstacles (barriers, blocks or both) located just upstream of the source. Subsequently, the effect of blockages on pressure losses inside the tunnel is investigated. It is shown that the large barriers are more effective than small ones because they prevent the smoke back-layering at very low critical velocities and they induce less pressure losses in congested tunnels.

Then, using a transverse ventilation system, the conditions of confinement of the smoke flow between two exhaust vents located on either side of a buoyant source are investigated. The effect of the shape and the position (with respect to the tunnel axis) of the dampers, including the specific case of full-width dampers, on the performance of the transverse ventilation system is evaluated. The extent of the backflow length beyond the extraction dampers, the confinement velocity and the stability of the smoke stratification are studied. Results show that the greater the proportion of the tunnel width the vent covers and the closer to the centre of the tunnel the vent is placed, the more efficient the ventilation system at confining the smoke to the extraction zone and ensuring the stability of the smoke stratification. The effect of solid barriers placed at the tunnel ceiling is also evaluated with transverse ventilation and it's found that large barriers can improve the efficiency of vents that do not cover the full width of the tunnel, by reducing the confinement velocity and enhancing the stability of the smoke stratification.

Finally, numerical simulations of fires in a tunnel with longitudinal and transverse ventilation are carried out using Fire Dynamics Simulator (FDS) software and Large Eddy Simulation (LES) approach. Several physical simulations are numerically reproduced to complete the interpretation of the experimental results. A good agreement is usually reached between the experimental and the numerical results. Nevertheless, some disagreement re-

garding the effects of the density ratio (ρ_i/ρ_0) on the dimensionless critical velocity ($U_{0,cr}/W_i$) is observed for non-Boussinesq lazy plumes, which will certainly require additional studies. The effects of solid barriers as well as the effects of the shape and position of the exhaust vents on smoke control are well reproduced numerically. In general, the critical velocities and confinement velocities are similar to those obtained experimentally, but the lengths of the smoke back-layer are different in a great majority of the cases. This difference may be due to the limitations of the numerical code in characterising the behaviour of the boundary layer flow close to the walls.

Keywords: Tunnel, Fire, Buoyant plume, Longitudinal ventilation, Particle image velocimetry, Critical velocity, Backlayer, Barriers, Blocks, Transverse ventilation, Exhaust vents, Confinement velocity, Smoke stratification, FDS, LES.

CONTENTS

Contents	xii
List of Figures	xvi
List of Tables	xxvi
1 General Introduction	1
1.1 Fires in road tunnels	1
1.2 Tunnel fire hazards	2
1.3 Smoke behaviour and Ventilation strategies	3
1.3.1 Smoke behaviour	3
1.3.2 Ventilation strategies	4
1.3.2.1 Natural ventilation	4
1.3.2.2 Longitudinal ventilation	5
1.3.2.3 Transverse ventilation	6
1.4 Fire tunnel simulation approaches	7
1.4.1 Full-scale tests	7
1.4.2 Small-scale tests	7
1.4.3 Numerical simulations	8
1.5 Objectives, methods and plan of study	9
1.5.1 Objectives of study	9
1.5.2 Methods and plan of study	9
2 Influence Of The Non-Boussinesq Effects On The Dynamics Of Buoyant Plumes	11
2.1 Introduction	12
2.2 Problem setting and dimensional analysis	13
2.3 Experiments & PIV measurements	15
2.3.1 Critical velocity measurements	15
2.3.2 Velocity field measurements	17

2.4	Results and discussions	19
2.4.1	Forced plumes	20
2.4.1.1	Average velocity	20
2.4.1.2	Velocity fluctuations	26
2.4.2	Lazy plumes	31
2.4.2.1	Average velocity	31
2.4.2.2	Velocity fluctuations	37
2.5	Conclusions	44
3	The Effects Of Solid Barriers And Blocks On The Propagation Of Smoke Within Longitudinally Ventilated Tunnels	46
3.1	Introduction	47
3.2	Experimental set-up	49
3.3	Effect on backlayering and critical velocity	55
3.3.1	Tunnel without blocks	56
3.3.1.1	Smoke back-layering flow length	56
3.3.1.2	Critical longitudinal ventilation velocities	58
3.3.2	Tunnel with blocks	60
3.3.2.1	Effect of blocks in tunnel with no barriers	61
3.3.2.2	Effects of blocks in tunnel with barriers	61
3.4	Effect on the pressure losses along the tunnel	64
3.4.1	Effects of barriers	65
3.4.2	Effects of vehicular blockage	66
3.4.2.1	Tunnel with blocks but no barriers (i.e. circles in black)	66
3.4.2.2	Tunnel with blocks and barriers (i.e. stars in red)	66
3.5	Conclusions	68
4	Smoke Control In Tunnel With A Transverse Ventilation System: An Experimental Study	70
4.1	Introduction	71
4.2	Experimental set-up and measurement techniques	74
4.2.1	The reduced scale model	74
4.2.2	Flow control parameter and similarity	77
4.2.3	Calibration of rotameters and oxygen sensors	79
4.2.4	Experimental protocol	81
4.3	Results and discussions	83
4.3.1	Smoke backflow length	83

4.3.2	Confinement velocity	86
4.3.3	Effect of extraction rate on smoke stratification	88
4.3.3.1	Rectangular-shaped dampers (RSD)	88
4.3.3.2	Square-shaped dampers positioned in the centre (SSD-PC)	89
4.3.3.3	Square-shaped dampers positioned in the side (SSD-PS) .	90
4.3.4	Effect of solid barriers on the propagation and behaviour of smoke .	91
4.4	Conclusions	94
5	Numerical Simulations Of Fires In Road Tunnels: A Complementary Study	96
5.1	Introduction	97
5.2	Numerical simulations	98
5.3	Results	100
5.3.1	Behaviour of densimetric plumes in a longitudinally ventilated tunnel	100
5.3.1.1	Determination of the critical velocity	101
5.3.1.2	Study of average and fluctuating flow components	102
5.3.1.2.1	Forced plumes	104
5.3.1.2.1.1	Average velocity	104
5.3.1.2.1.2	Velocity fluctuations	108
5.3.1.2.2	Lazy plumes	113
5.3.1.2.2.1	Average velocity	113
5.3.1.2.2.2	Velocity fluctuations	117
5.3.2	Effect of solid barriers on the propagation of fire smoke within a longitudinally ventilated tunnel	122
5.3.2.1	Numerical simulations for studying the effects of barrier .	122
5.3.2.2	Results and discussion	123
5.3.2.2.1	Small barriers	123
5.3.2.2.2	Large barriers	126
5.3.3	Effects of the shape and position of vents on the confinement of fire smoke in a tunnel with a transverse ventilation system	129
5.3.3.1	Numerical simulations for studying the effects of the shape and position of dampers	129
5.3.3.2	Results and discussion	130
5.3.3.3	Effects of the solid barriers on the propagation of smoke .	134
5.4	Conclusions	136
	General Conclusions	138

A Particle Image Velocimetry Technique: Acquisition, Post-processing And Quality Of PIV Data	140
A.1 Equipment and Apparatus	140
A.2 Camera calibration	141
A.3 Recording and Processing of PIV Data	143
A.3.1 Preliminary Tests of PIV	143
A.3.2 PIV Data Acquisition	144
A.3.3 PIV Data Processing	145
A.4 Quality of PIV measurements	148
A.4.1 Systematic errors	148
A.4.2 Statistical errors - steady flow	150
 B Modelling a physical problem	 155
B.1 General form of the equations	155
B.2 System of equations at a low Mach number	156
B.2.1 Equation of state	156
B.2.2 Equation of enthalpy	158
B.2.3 Poisson’s equation	159
B.3 Turbulence modeling	159
B.3.1 Reynolds-Averaged Navier–Stokes method (RANS method)	160
B.3.2 Large eddy simulation method (LES method)	161
B.4 Fire Dynamics Simulator	164
B.4.1 General presentation of FDS	164
B.4.2 Different physical models	164
B.4.2.1 Subgrid models	164
B.4.2.1.1 Constant coefficient Smagorinsky model	164
B.4.2.1.2 Dynamic Smagorinsky model	165
B.4.2.1.3 Deardorff’s model	165
B.4.2.1.4 Vreman’s model	165
B.4.2.2 Combustion and Radiation models	166
B.4.2.2.1 Combustion model	166
B.4.2.2.2 Radiation model	167
B.4.3 Solution Procedure	167
B.4.3.1 Predictor	167
B.4.3.2 Corrector	169
 References	 171

LIST OF FIGURES

1.1	Behaviour of fire smoke in a tunnel without considering slope and airflow.	3
1.2	Behavior of smoke in a sloping tunnel with natural ventilation [9].	5
1.3	Fire-induced smoke longitudinal control [17].	5
1.4	Fire-induced smoke transverse control [17].	6
2.1	Experimental set-up for critical velocity measurements in the tunnel with a longitudinal smoke control system.	15
2.2	Experimental setup for PIV measurements in the tunnel with a longitudinal smoke control system.	19
2.3	Non-dimensional average velocity fields of the vertical component \bar{u}_z/W_i	20
2.4	Profiles of the non-dimensional vertical velocity (black curves) and their average across the source diameter (blue curves) at $z/H = 0.05$	21
2.5	Profiles of the non-dimensional vertical velocity at $z/H = 0.08$, $z/H = 0.40$ and $z/H = 0.70$ versus the non-dimensional longitudinal distance x/H	22
2.6	Non-dimensional average velocity fields of the longitudinal component \bar{u}_x/W_i	23
2.7	Profiles of the non-dimensional longitudinal velocity (black curves) and their average over the tunnel height (blue curves) at $x/H = 0.60$	24
2.8	Profiles of the non-dimensional longitudinal velocity at $z/H = 0.05$, $z/H = 0.50$ and $z/H = 0.99$ versus the non-dimensional longitudinal distance x/H	25
2.9	Non-dimensional standard deviation of the vertical velocity component σ_z/W_i	26
2.10	Profiles of the non-dimensional standard deviation at $z/H = 0.10$, $z/H = 0.50$ and $z/H = 0.80$ versus the non-dimensional longitudinal distance x/H	27
2.11	Non-dimensional standard deviation of the longitudinal velocity component σ_x/W_i	28
2.12	Profiles of the non-dimensional standard deviation at $z/H = 0.10$, $z/H = 0.50$ and $z/H = 0.80$ versus the non-dimensional longitudinal distance x/H	29

2.13	Fields of non-dimensional Reynolds shear stress σ_{xz}/W_i^2	30
2.14	Profiles of the dimensionless Reynolds shear stress at $z/H = 0.10$, $z/H = 0.30$ and $z/H = 0.50$ versus the non-dimensional longitudinal distance x/H	31
2.15	Non-dimensional average velocity fields of the vertical component \bar{u}_z/W_i	32
2.16	Profiles of the non-dimensional vertical velocity (black curves) and their average across the source diameter (blue curves) at $z/H = 0.04$	33
2.17	Profiles of the non-dimensional vertical velocity at $z/H = 0.07$, $z/H = 0.20$ and $z/H = 0.70$ versus the non-dimensional longitudinal distance x/H	34
2.18	Non-dimensional average velocity fields of the longitudinal component \bar{u}_x/W_i	35
2.19	Profiles of the non-dimensional longitudinal velocity (black lines) and their average over the tunnel height (blue lines) at $x/H = 0.40$	35
2.20	Profiles of the non-dimensional longitudinal velocity at $z/H = 0.05$, $z/H = 0.50$ and $z/H = 0.99$ versus the non-dimensional longitudinal distance x/H	37
2.21	Non-dimensional standard deviation of the vertical velocity component σ_z/W_i	38
2.22	Profiles of the non-dimensional standard deviation at $z/H = 0.30$, $z/H = 0.60$ and $z/H = 0.95$ versus the non-dimensional longitudinal distance x/H	39
2.23	Non-dimensional standard deviation of the longitudinal velocity component σ_x/W_i	40
2.24	Profiles of the non-dimensional standard deviation at $z/H = 0.25$, $z/H = 0.50$ and $z/H = 0.98$ versus the non-dimensional longitudinal distance x/H	41
2.25	Fields of non-dimensional Reynolds shear stress σ_{xz}/W_i^2	42
2.26	Profiles of the dimensionless correlations between vertical and longitudinal velocity fluctuations at $z/H = 0.15$, $z/H = 0.35$ and $z/H = 0.55$ versus the non-dimensional longitudinal distance x/H	43
3.1	Schematic of the experimental setup with barriers fixed at the tunnel ceiling. h is the height of barrier, d is the distance between the source and the large barrier and S is the distance between each two adjacent small barriers.	51
3.2	Critical ventilation condition with $\Gamma_i = 2$. a) Tunnel without barriers ($U_{0,cr} = 0.256$ m/s). b) Tunnel with a largest barrier of height $H/3$ placed just upstream of the source ($U_{0,cr} = 0.143$ m/s).	52
3.3	The block locations in the experiment. a) Block1: 0.05 m^3 . b) Block2: 0.08 m^3 . c) Block3: 0.12 m^3 . We keep the same configuration of blocks in the case of a tunnel with barriers fixed to the ceiling.	53

3.4	Schematic representations of obstacles placed in tunnel of rectangular cross-section. Obstacle is represented by a block in figure (a) and by a barrier in figure (b). $A_1, U_{0,1}, A_2, U_{0,2}$ are the relative flow velocities and tunnel cross-sectional area (in grey).	54
3.5	Smoke dimensionless back-layering length, L/H , measured in the tunnel with and without small barriers against the ratio of longitudinal ventilation velocity to the critical velocity $U_0/U_{0,cr}$; $U_{0,cr}$ is the critical velocity in the tunnel without barriers.	57
3.6	Smoke dimensionless back-layering length, L/H , measured in the tunnel with and without large barriers against the ratio of longitudinal ventilation velocity to the critical velocity $U_0/U_{0,cr}$. a) The barrier is placed just upstream of the source. b) The barrier is placed at a distance H upstream of the source.	58
3.7	a) Dependence of the critical velocity $U_{0,cr}$ on the buoyancy flow buoyancy flux B_i . b) Dependence of non-dimensional critical velocity $U_{0,cr}/W_i$ on the plume Richardson number Γ_i . All data are fitted with a power-law of the form $aX^{1/3}$. The estimated error rate of the experimental data is 5%. R-squared is the coefficient of determination for regression curves. The results for the small barriers presented here concern those with the configuration $S = H$	59
3.8	The velocity ratio R_c , given by the critical velocity in the tunnel with barriers to the critical velocity in the empty tunnel, against the plume Richardson number Γ_i	60
3.9	The velocity ratio R_c , given by the critical velocity in the tunnel with obstacles to the critical velocity in the empty tunnel, against the number of pairs of blocks N_{PB} . $D_i = 0.1$ m, $\Gamma_i = 2$ and $\rho_i/\rho_0 = 0.7$	62
3.10	Reduction of the critical velocities $(1 - R_c)$ against the tunnel blockage ratios ϕ of obstacles (barrier, block, or both) located just upstream of the source.	63
3.11	Dimensionless pressure coefficient C_f , against the dimensionless barrier height, h/H	65
3.12	Head loss coefficient C_f , evaluated in the presence of the blocks in the tunnel for both cases with and without barriers against the number of pairs of blocks, N_{PB}	67
4.1	Experimental setup with transverse smoke control system. a) A picture of the setup. b) A schematic of the setup.	75

4.2	Schematic top view of the different exhaust vents with their location on the tunnel ceiling. a) Exhaust vent with transverse rectangular shape (RSD). b) Exhaust vent with square shape placed in the centre of the tunnel ceiling (SSD-PC). c) Exhaust vent with square shape placed on the sides of the tunnel ceiling (SSD-PS).	76
4.3	Diagram of the experimental setup with large barriers ($h = H/3$) fixed to the tunnel ceiling just upstream of the dampers (in this case, the exhaust vents are represented by square-shaped dampers placed in the centre of the tunnel ceiling, the same is applied for other types of dampers and for the barrier of height $h = H/4$).	77
4.4	Experimental set-up for calibration of rotameters and oxygen sensors. . . .	80
4.5	The dependence between the measured flow rate q_r and the prescribed flow rate q_i for $0.5 \leq \rho_i/\rho_0 \leq 1$. " β " is the linear correlation factor between q_r and q_i . a) Rotameter with a range: 6.4-64 m ³ /h. b) Rotameter with a range: 16-160 m ³ /h.	80
4.6	Variation of the oxygen concentration measured by the two sensors (expressed in Volt) against the density of the mixture. a) The voltage V_i versus the density ρ_i . b) The dimensionless voltage V_i/V_0 versus the dimensionless density ρ_i/ρ_0	81
4.7	Schematic view of all input and output flows in a tunnel with two extraction points.	82
4.8	Smoke visualisation in the tunnel with a two-point transverse extraction system (rectangular dampers, $\Gamma_i = 8$). a) Non-confinement ventilation conditions: smoke back-layer appears downstream of the dampers. b) Confinement ventilation conditions: smoke backflow is completely suppressed. . . .	83
4.9	a) Dimensionless back-layering length L/H against the extraction Froude number Fr_e . b) Dimensionless back-layering length L/H against the longitudinal Froude number Fr_0 , for different shapes and locations of the exhaust vents.	85
4.10	a) The confinement velocity $U_{0,c}$ and the associated extraction confinement velocity $U_{e,c}$ against the buoyancy flux B_i and the associated heat release rate Q_c . b) The confinement Froude number $Fr_{0,c}$ and the associated extraction confinement Froude number $Fr_{e,c}$ against the plume Richardson number Γ_i , for different shapes and locations of the exhaust vents.	87
4.11	Visualisation of the different stratification regimes of the buoyant smoke flow in the tunnel equipped with rectangular shaped dampers (RSD).	89

4.12	Visualisation of the different stratification regimes of the buoyant smoke flow in the tunnel equipped with square-shaped dampers located in the centre (SSD-PC).	90
4.13	Visualisation of the different stratification regimes of the buoyant smoke flow in the tunnel equipped with square-shaped dampers located on the side of the tunnel ceiling (SSD-PS).	90
4.14	The velocity ratio R_c , given by the confinement velocity in the tunnel with barriers to the confinement velocity in the empty tunnel, against the plume Richardson number Γ_i , for different shapes and locations of the exhaust vents and with both barriers of height $H/4$ and $H/3$	92
4.15	Visualisation of the smoke flow in the tunnel equipped with square shaped dampers placed on one of the sides of the tunnel ceiling (confinement conditions with $\Gamma_i = 40$). a) Tunnel without barriers ($Fr_{0,c} = 1.10$). b) Tunnel with a large barrier $H/4$ ($Fr_{0,c} = 0.75$). c) Tunnel with a largest barrier of height $H/3$ ($Fr_{0,c} = 0.50$).	93
5.1	Boundary conditions for numerical simulations of tunnel fires using a mixture of air/helium. a) Longitudinal ventilation. b) Transverse ventilation. . .	99
5.2	Results of a fire simulation under critical ventilation conditions. a) Fluid density profile obtained along the tunnel ceiling. b) Mean density field in the region within which the source is located.	100
5.3	Instantaneous velocity fields of the vertical component taken from case3. a) With grid sizes of 1 mm (appearance of numerical instabilities). b) With grid sizes of 2 mm (no numerical instabilities).	102
5.4	Numerical results on the average velocity fields of the vertical component (case1). a) With grid sizes of 5 mm. b) With grid sizes of 1 mm.	103
5.5	Non-dimensional average velocity fields of the vertical component \bar{u}_z/W_i for case1 ($\Gamma_i = 0.0075$ and $\rho_i/\rho_0 = 0.8$). a) An experimental result. b) A numerical result.	104
5.6	Experimental and numerical profiles of the non-dimensional longitudinal velocity component plotted at $x/H = 0.3$ (a) and $x/H = 0.1$ (b).	105
5.7	Profiles of the non-dimensional vertical velocity at $z/H = 0.10$, $z/H = 0.40$ and $z/H = 0.70$ against the non-dimensional longitudinal distance x/H (experimental profiles vs numerical profiles, case1: $\Gamma_i = 0.0075$ and $\rho_i/\rho_0 = 0.8$).	106

5.8	Non-dimensional average velocity fields of the longitudinal component \bar{u}_x/W_i for case1 ($\Gamma_i = 0.0075$ and $\rho_i/\rho_0 = 0.8$). a) An experimental result. b) A numerical result.	107
5.9	Profiles of the non-dimensional longitudinal velocity at $z/H = 0.04$, $z/H = 0.50$ and $z/H = 0.99$ against the non-dimensional longitudinal distance x/H (experimental profiles vs numerical profiles, case1: $\Gamma_i = 0.0075$ and $\rho_i/\rho_0 = 0.8$).	108
5.10	Non-dimensional standard deviation of the vertical velocity component σ_z/W_i for case1 ($\Gamma_i = 0.0075$ and $\rho_i/\rho_0 = 0.8$). a) An experimental result. b) A numerical result.	109
5.11	Standard deviation profiles of the vertical velocity component plotted at $z/H = 0.30$, $z/H = 0.50$ and $z/H = 0.80$ against the non-dimensional longitudinal distance x/H (experimental profiles vs numerical profiles, case1: $\Gamma_i = 0.0075$ and $\rho_i/\rho_0 = 0.8$).	110
5.12	Non-dimensional standard deviation of the longitudinal velocity component σ_x/W_i for case1 ($\Gamma_i = 0.0075$ and $\rho_i/\rho_0 = 0.8$). a) An experimental result. b) A numerical result.	110
5.13	Standard deviation profiles of the longitudinal velocity component plotted at $z/H = 0.30$, $z/H = 0.50$ and $z/H = 0.80$ against the non-dimensional longitudinal distance x/H (experimental profiles vs numerical profiles, case1: $\Gamma_i = 0.0075$ and $\rho_i/\rho_0 = 0.8$).	111
5.14	Non-dimensional Reynolds shear stress σ_{xz}/W_i^2 for case1 ($\Gamma_i = 0.0075$ and $\rho_i/\rho_0 = 0.8$). a) An experimental result. b) A numerical result.	112
5.15	Profiles of the non-dimensional Reynolds shear stress at $z/H = 0.25$, $z/H = 0.40$ and $z/H = 0.55$ against the non-dimensional longitudinal distance x/H (experimental profiles vs numerical profiles, case1: $\Gamma_i = 0.0075$ and $\rho_i/\rho_0 = 0.8$).	113
5.16	Non-dimensional average velocity fields of the vertical component \bar{u}_z/W_i for case3 ($\Gamma_i = 1.45$ and $\rho_i/\rho_0 = 0.8$). a) An experimental result. b) A numerical result.	114
5.17	Profiles of the non-dimensional vertical velocity at $z/H = 0.10$, $z/H = 0.40$ and $z/H = 0.70$ against the non-dimensional longitudinal distance x/H (experimental profiles vs numerical profiles, case3: $\Gamma_i = 1.45$ and $\rho_i/\rho_0 = 0.8$).	115
5.18	Non-dimensional average velocity fields of the longitudinal component \bar{u}_x/W_i for case3 ($\Gamma_i = 1.45$ and $\rho_i/\rho_0 = 0.8$). a) An experimental result. b) A numerical result.	116

5.19	Experimental and numerical profiles of the non-dimensional longitudinal velocity component plotted at: a) $x/H = 0.30$, b) $x/H = 0.15$	116
5.20	Profiles of the non-dimensional vertical velocity at $z/H = 0.05$, $z/H = 0.50$ and $z/H = 0.99$ against the non-dimensional longitudinal distance x/H (experimental profiles vs numerical profiles, case3: $\Gamma_i = 1.45$ and $\rho_i/\rho_0 = 0.8$).	117
5.21	Non-dimensional standard deviation of the vertical velocity component σ_z/W_i for case3 ($\Gamma_i = 1.45$ and $\rho_i/\rho_0 = 0.8$). a) An experimental result. b) A numerical result.	118
5.22	Standard deviation profiles of the vertical velocity component plotted at $z/H = 0.20$, $z/H = 0.40$ and $z/H = 0.60$ against the non-dimensional longitudinal distance x/H (experimental profiles vs numerical profiles, case3: $\Gamma_i = 1.45$ and $\rho_i/\rho_0 = 0.8$).	119
5.23	Non-dimensional standard deviation of the longitudinal velocity component σ_x/W_i for case3 ($\Gamma_i = 1.45$ and $\rho_i/\rho_0 = 0.8$). a) An experimental result. b) A numerical result.	119
5.24	Standard deviation profiles of the longitudinal velocity component plotted at $z/H = 0.20$, $z/H = 0.40$ and $z/H = 0.60$ against the non-dimensional longitudinal distance x/H (experimental profiles vs numerical profiles, case3: $\Gamma_i = 1.45$ and $\rho_i/\rho_0 = 0.8$).	120
5.25	Non-dimensional Reynolds shear stress σ_{xz}/W_i^2 for case3 ($\Gamma_i = 1.45$ and $\rho_i/\rho_0 = 0.8$). a) An experimental result. b) A numerical result.	121
5.26	Profiles of the non-dimensional Reynolds shear stress at $z/H = 0.20$, $z/H = 0.40$ and $z/H = 0.60$ against the non-dimensional longitudinal distance x/H (experimental profiles vs numerical profiles, case3: $\Gamma_i = 1.45$ and $\rho_i/\rho_0 = 0.8$).	121
5.27	Smoke dimensionless back-layering length, L/H , against the ratio of longitudinal ventilation velocity to the critical velocity $U_0/U_{0,cr}$; $U_{0,cr}$ is the critical velocity measured experimentally in the tunnel without barriers. a) Tunnel without barriers vs. tunnel with small barriers ($h = H/10$ and $S = H$). b) Tunnel without barriers vs. tunnel with small barriers ($h = H/10$ and $S = 2H$).	124

5.28 Simulations of smoke back-layering flow for $\Gamma_i = 2$, $\rho_i/\rho_0 = 0.7$, $D_i/H = 0.56$ and $U_0/U_{0,cr} = 0.83$. a) Tunnel without small barriers: appearance of a smoke back-layering flow, $L/H \approx 4$. b) Tunnel with small barriers ($S = H$): the barrier located upstream of the source at a distance equal to the tunnel height prevents the passage of smoke, $L/H = 1$. c) Tunnel with small barriers ($S = 2H$): the barrier located just upstream of the source prevents the passage of smoke, $L/H = 0$ 125

5.29 Simulations of smoke back-layering flow for $\Gamma_i = 2$, $\rho_i/\rho_0 = 0.7$, $D_i/H = 0.56$ and $U_0/U_{0,cr} = 0.77$. a) Tunnel without small barriers: appearance of a smoke back-layering flow, $L/H \approx 6.5$. b) Tunnel with small barriers ($S = H$): the barrier located upstream of the source at a distance equal to twice the tunnel height prevents the passage of smoke, $L/H = 2$. c) Tunnel with small barriers ($S = 2H$): the barrier located upstream of the source at a distance equal to twice the tunnel height prevents the passage of smoke, $L/H = 2$ 126

5.30 Smoke dimensionless back-layering length, L/H , against the ratio of longitudinal ventilation velocity to the critical velocity $U_0/U_{0,cr}$. a) Empty tunnel vs. tunnel with large barrier of height $H/4$ placed just upstream of the source. b) Empty tunnel vs. tunnel with large barrier of height $H/4$ placed at a distance H upstream of the source. 127

5.31 Smoke dimensionless back-layering length, L/H , against the ratio of longitudinal ventilation velocity to the critical velocity $U_0/U_{0,cr}$. a) Empty tunnel vs. tunnel with largest barrier of height $H/3$ placed just upstream of the source. b) Empty tunnel vs. tunnel with largest barrier of height $H/3$ placed at a distance H upstream of the source. 128

5.32 Simulation of smoke back-layering flow for $\Gamma_i = 2$, $\rho_i/\rho_0 = 0.7$, $D_i/H = 0.56$ and $U_0/U_{0,cr} = 0.67$. a) Tunnel without the barrier: appearance of the smoke back-layering flow, $L/H \approx 14.5$. b) Tunnel with a large barrier $H/4$ placed just upstream of the source: no smoke back-layering flow upstream of the source. 128

5.33 Simulation of smoke back-layering flow for $\Gamma_i = 2$, $\rho_i/\rho_0 = 0.7$, $D_i/H = 0.56$ and $U_0/U_{0,cr} = 0.56$. a) Tunnel without the barrier: appearance of the smoke back-layering flow, $L/H \approx 24$. b) Tunnel with a largest barrier $H/3$ placed just upstream of the source: no smoke back-layering flow upstream of the source. 129

5.34	Numerical and experimental results on dimensionless back-layering length L/H versus the extraction Froude number Fr_e . a) Rectangular vents. b) Square centre vents. c) Square side vents.	132
5.35	Behaviour of smoke in the confinement conditions. a) Rectangular vents ($Fr_{e,c} = 1.76$). b) Square centre vents ($Fr_{e,c} = 4.81$). c) Square side vents ($Fr_{e,c} = 5.76$).	132
5.36	Time-averaged density ratio scenes near the tunnel ceiling for square vents placed on one side (top view). a) $Fr_e = 3.94$. b) $Fr_e = 4.85$. c) $Fr_e = 9.10$	133
5.37	Numerical results in the steady state for a Froude number $Fr_e = 9.10$. a) Side view of the instantaneous density field. b) Side view on the behaviour of the smoke.	134
5.38	Effects of solid barriers on the spread of smoke for square side vents. a) Barrier with height $h = H/4$ ($Fr_{e,c} = 3.94$ and $Rc = 0.68$). b) Barrier with height $h = H/3$ ($Fr_{e,c} = 2.42$ and $Rc = 0.47$).	135
5.39	Effects of solid barriers on the spread of smoke for square centre vents. a) Barrier with height $h = H/4$ ($Fr_{e,c} = 2.84$ and $Rc = 0.59$). b) Barrier with height $h = H/3$ ($Fr_{e,c} = 1.78$ and $Rc = 0.37$).	135
A.1	Location of the calibration plate and the size of area of interest.	142
A.2	Overall scheme of the PIV experimental device with double-frame recording method.	144
A.3	Evaluation of PIV recordings using cross-correlation.	146
A.4	Example of velocity vector map of instantaneous flow field (sample number 1013, case1).	147
A.5	Estimation of the peak locking coefficient of a vector field (sample number 70, case1). a) Histogram of velocity components, $u = (u_x, u_z)$. b) Histogram of particle displacement modulo 1. c) Histogram of particle displacement modulo 0.5 (i.e. histogram of particle displacement modulo 1 folded on itself with respect to 0.5).	149
A.6	a) Peak locking coefficient of each instantaneous vector field (case1). b) PDF of the peak locking coefficients.	150
A.7	Location of the chosen points in the plane of an instantaneous velocity field (instantaneous field of vertical velocity taken from the first case).	151

A.8 Typical statistical convergence of the components of mean velocity and their associated uncertainty at three points P1 ($x = 0$ mm, $z = 15$ mm), P2 ($x = 0$ mm, $z = 90$ mm) and P3 ($x = 0$ mm, $z = 165$ mm) against the number of samples for the first case. a) Evolution of the mean value of \bar{u}_x . b) Convergence of the associated uncertainty $\varepsilon_{st,x}$. c) Evolution of the mean value of \bar{u}_z . d) Convergence of the associated uncertainty $\varepsilon_{st,z}$ 152

LIST OF TABLES

1.1	Dimensioning fires retained by technical instruction [9].	2
2.1	Experimental conditions of the tests conducted.	16
2.2	Summary of the experimental results on the critical velocity associated with each equivalent HRR in a small and full scale tunnel, as well as the corresponding dimensionless values of critical velocity and HRR.	17
3.1	Blockage rates induced by blocks and barriers.	55
3.2	Velocity reduction rates induced by both the pair of blocks and the barrier located on the same cross-section just upstream of the source.	62
5.1	Numerical results on the critical velocity and their comparison with the experimental results.	102
A.1	Quality parameters and errors for PIV measurement.	154

LISTE DES SYMBOLES

Roman Symbols

\bar{D}	Hydraulic diameter of the tunnel (m)
\bar{u}_x	Time-averaged longitudinal velocity (m/s)
\bar{u}_z	Time-averaged vertical velocity (m/s)
Δp	Pressure difference (Pascal)
Δt	Time delay between the successive pulses (μs)
A_d	Cross-sectional area of an extractor vent (m ²)
B_i	Buoyancy flux (m ⁴ /s ³)
C_D	Constant of Deardorff model (-)
C_f	Dimensionless pressure coefficient (-)
C_p	Specific heat at constant pressure (J/kg K)
d	Distance between a large barrier and the source (m)
D^*	Characteristic fire diameter (m)
D_i	Diameter of the source (m)
e_{cm}	Combining relative error (-)
e_{st}	Relative statistical error (-)
$Fr_{0,c}$	Longitudinal Confinement Froude number (-)
Fr_0	Longitudinal Froude number (-)

$Fr_{e,c}$	Extraction Confinement Froude number (-)
Fr_e	Extraction Froude number (-)
g	Gravity acceleration (m/s ²)
H	Height of the tunnel (m)
h	Height of the barrier (m)
k_{sgs}	Sub-grid scale kinetic energy (m ² /s ²)
L	Smoke back-layering flow length (m)
l	Characteristic length (m)
L_{1-2}	Distance between the two pressure measurement points P1 and P2 (m)
n	Number of samples (-)
N_{PB}	Number of pairs of blocks (-)
P_d	Position of the dampers (-)
q	Volume flow (m ³ /s)
Q_c	Heat release rate of the fire (kW)
Q_c^*	Dimensionless heat release rate
Rc	Confinement velocity ratio in a transverse system (-)
Rc	Critical velocity ratio in a longitudinal system (-)
Ri	Tunnel Richardson number (-)
S	Spacing between each two adjacent small barriers (m)
S_d	Shape of the dampers (-)
sc	Image scale (mm/pixel)
T	Temperature (K)
$U_{0,cr}$	Critical velocity (m/s)
$U_{0,c}$	Confinement velocity (m/s)

U_0	Induced longitudinal ventilation velocity in a transverse system (m/s)
U_0	Ventilation velocity in a longitudinal system (m/s)
$U_{e,c}$	Extraction confinement velocity (m/s)
U_e	Extraction velocity (m/s)
u_x	Instantaneous longitudinal velocity (m/s)
u_z	Instantaneous vertical velocity (m/s)
W	Width of the tunnel (m)
W_i	Velocity of the light flow at the source (m/s)
X	Volume fraction (-)
L_s	Left side of the tunnel (-)
Re	Reynolds number (-)
R_s	Right side of the tunnel (-)
V	Sensor output voltage (volt)

Greek Symbols

α	Plume entrainment coefficient (-)
Δ	Filter width (m)
Γ	Plume Richardson number (-)
μ_t	Turbulent viscosity (Kg/ms)
ρ	Density (Kg/m ³)
σ_{xz}	Reynolds shear stress (m ² /s ²)
σ_x	Standard deviation of the longitudinal velocity (m/s)
σ_z	Standard deviation of the vertical velocity (m/s)
θ	Scale reduction ratio (-)
ε_{st}	Statistical error (m/s)

ϵ_{sys} Systematic error (m/s)

φ Tunnel blockage ratio (-)

Subscripts

0 Property of the ambient condition

e Property of the flow at the exhaust vents

f Refer to the full-scale tunnel

he Helium Properties

i Property of plume at the source

r Property of the flow in the rotameter

s Refer to the small-scale tunnel

Acronyms / Abbreviations

ACH Air Changes per Hour

CCD Charge Coupled Device

CFD Computational Fluid Dynamics

CFL Courant-Friedrichs-Lewy constraint

CMOS Complementary Metal-Oxide Semiconductor

FDS Fire Dynamics Simulator

HGVs Heavy Goods Vehicles

HRR Heat Release Rate

LES Large Eddy Simulation

MPI Message Passing Interface

Nd:YAG Neodymium-doped Yttrium Aluminum Garnet

NIST National Institute of Standards and Technology

PIV Particle Image Velocimetry

RSD	Rectangular-Shaped Damper
SSD-PC	Square-Shaped Damper Placed in the Centre of the tunnel ceiling
SSD-PS	Square-Shaped Damper Placed on the Side of the tunnel ceiling
VN	Von Neumann constraint

GENERAL INTRODUCTION

1.1 Fires in road tunnels

Today, the problem of road tunnel fires is one of the authorities' major concerns in terms of risks, because of the consequences of such accidents on the safety of tunnel users, infrastructure and economic activities. In recent years, several fatal fires have occurred in Europe's road tunnels, with tragic and catastrophic consequences that remain etched in our memories. 39 dead and 30 injured in March 1999 following a truck fire in the road tunnel of Mont Blanc between France and Italy [1–3]. Two months after this accident, in May 1999, 12 people were killed and 40 injured in the Tauern Tunnel near Salzburg, Austria, after an accident between a truck and a car, setting off a chain of explosions [1, 3, 4]. In October 2001, a collision between two trucks caused a fire inside St Gotthard road tunnel in Switzerland, killing eleven and injuring many more, and occasioning extensive material damage [3]. The disastrous consequences of these fires have forced researchers and engineers to conduct extensive analysis and research of real accidents to develop more sophisticated techniques in order to obtain good safety for tunnel users. In Europe, according to Nævestad and Meyer [5], about two vehicle fires occur per 100 million vehicle-km in road tunnels, and about 30% of these fires come from the heavy trucks, although they account for only 15% of the total traffic volume. The most common causes of these fires include the collisions, electrical failure, overheating of brakes, tyres or engines [6]. Collisions involving heavy vehicles are overrepresented among the serious fires that resulted a lot of injuries and fatalities [7]. The fires caused by these types of vehicles are much more powerful than those produced by small vehicles. Their flames are large and they can spread to vehicles located near the scene of the disaster.

The heat release rate (HRR) generated by the fire varies considerably depending on the number, type and load of the vehicles involved. The evolution of the HRR and the circula-

1.2 Tunnel fire hazards

tion of hot smoke are also influenced by the geometry of the tunnels. The regulation [8, 9] defines so-called "dimensioning fires" (see Table 1.1) by linking the HRR to the height of the tunnels, the type of vehicles involved and their cargo (i.e. transport of hazardous substances (THS) or no). These fires were chosen because they cover the vast majority of fires produced in road tunnels and are therefore not the worst fires that can occur. In particular, the firepower of heavy goods vehicles (HGVs) prohibited for the transport of hazardous substances is fixed at 30 MW. Whereas, in the case of HGVs loaded with combustible materials not classified as hazardous substances, their fires may, in exceptional circumstances, reach powers of the order of 100 MW or more. In addition, there is no experimental data available for dangerous goods vehicles (DGVs), although similar or more severe fires than HGVs fires can be expected [10, 11]. The fires of such vehicles can be catastrophic in the tunnel with a high traffic density, especially in the presence of a longitudinal flow, which contributes to the spread of flames and to the increase of the fire growth rate [12, 13]. In such instances, the HRR can reach values between 300 MW and 700 MW according to Ingason [14].

Table 1.1: Dimensioning fires retained by technical instruction [9].

The tunnel height (H)	The vehicle type	The heat release rate
$H < 2$ m	2 or 3 of light-duty vehicles	8 MW
$2 \text{ m} < H < 3.5$ m	A van	15 MW
$H > 3.5$ m (without THS)	A heavy goods vehicle (HGV)	30 MW
$H > 3.5$ m (with THS)	A dangerous goods vehicle (DGV)	200 MW

1.2 Tunnel fire hazards

During a tunnel fire, the main risk that the tunnel users encounter is the loss of visibility due to the high smoke density. This slows down their movement and makes it difficult to locate emergency exits. Within a few minutes, the breathing becomes an increasing struggle and the visibility is further impaired, which can be disorientating for anyone trying to escape. The users are then blocked in the confined space and inhale toxic fumes that can cause asphyxiation leading to loss of consciousness followed by death [15]. It should be noted that the end products of the fuel combustion are mainly CO₂, H₂O, CO and HCN, which are asphyxiant gases and toxic products in high doses [16]. Other hazardous products can be formed depending on the burning of materials (plastics, wood, tyres, etc.) and the types of gases and goods carried by lorries. Another fire hazard in the confined spaces concerns the flames and the high temperatures generated from the combustion. These pose a direct threat to tunnel users located near the fire, restrict rescue service intervention, damage tunnel

1.3 Smoke behaviour and Ventilation strategies

equipment and structure, and lead to collapse and expensive renovation [6]. Typically, in case of a fire, 2/3 of the total heat release rate is transferred by convection and 1/3 by radiation [6]. The effect of the radiation decreases rapidly with the distance from the source and the spread of toxic smoke remains the main threat for tunnel users, even for those who are far from fire. Therefore, controlling this smoke becomes a priority to ensure the safety of tunnel users and to increase the access firefighters have to fight the fire.

1.3 Smoke behaviour and Ventilation strategies

1.3.1 Smoke behaviour

During a fire in the tunnel, the temperature difference between the hot gases produced by a fire and the ambient air induces driving forces causing an upward movement of the smoke towards the ceiling. This results in a turbulent thermal plume rising above the fire source (Fig. 1.1a).

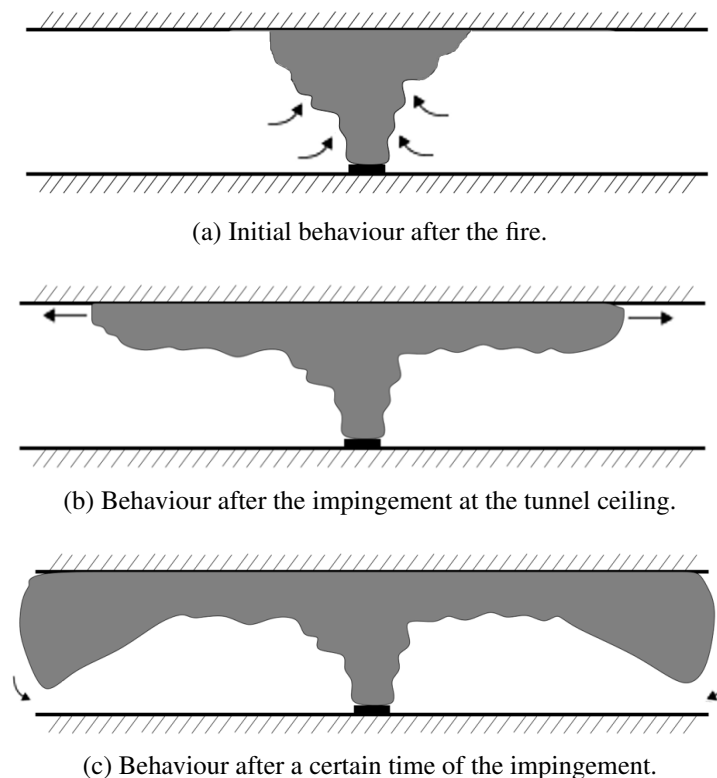


Figure 1.1: Behaviour of fire smoke in a tunnel without considering slope and airflow.

1.3 Smoke behaviour and Ventilation strategies

As the plume rises to the ceiling, it widens due to the entrainment of the ambient air at its edges. Several effects control the motion of the plume within the tunnel, including buoyancy (density differences), momentum (inertia) and diffusion. Once the plume impinges the ceiling, considering a tunnel without slope or air flow, the hot smoke spreads symmetrically on both sides of the fire source and maintains its stratification along the tunnel (Fig. 1.1b). The velocity of smoke propagation depends on the heat release rate; the higher the HRR, the higher the propagation velocity. As the smoke spreads morley away from the source, the smoke layer mixes with ambient air and can return to the source under the effect of the opposite natural flow (Fig. 1.1c). For this purpose the presence of ventilation systems for smoke control is essential.

1.3.2 Ventilation strategies

Ventilation in tunnels is critical for a variety of reasons. In normal operational conditions, the ventilation ensures a good air quality by removing pollutants and exhaust emission of automobile engines. In case of a fire, the ventilation controls the smoke propagation and maintains the air temperatures within acceptable limits. There are mainly three strategies of tunnel ventilations: natural, longitudinal and transverse. The short tunnels are naturally ventilated but long tunnels require mechanical ventilation. Longitudinal ventilation is appropriate for unidirectional traffic as it is designed to force all the smoke out one side of the tunnel but for bidirectional traffic or in any tunnel where congestion is likely, transverse ventilation is necessary. In transverse ventilation, smoke is extracted through vents in the ceiling of the tunnel.

1.3.2.1 Natural ventilation

This ventilation strategy does not involve any mechanical system to ensure ventilation in the tunnel. The airflow is created either by the pressure difference between the two ends of the tunnel, or by the natural slope of the tunnel that helps the smoke to move towards the highest end because of the stack effect (Fig. 1.2). This strategy is allowed only in special cases such as urban road tunnels less than 300 metres long, non-urban road tunnels less than 500 metres long, or non-urban tunnels less than 1000 metres which are light traffic tunnels. These lengths are fixed for tunnel heights greater than 3.5 metres [9].

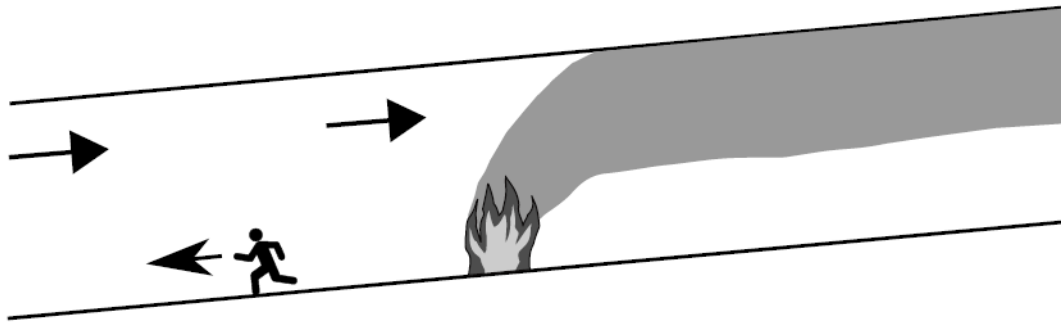


Figure 1.2: Behavior of smoke in a sloping tunnel with natural ventilation [9].

1.3.2.2 Longitudinal ventilation

This ventilation system is suitable for one-directional long tunnels with low levels of traffic congestion. As shown in Fig. 1.3, the strategy is designed to produce a longitudinal flow along the tunnel to push all smoke downstream of the fire source while creating a smoke-free path upstream. The longitudinal flow is provided using jet fans located on the ceiling or on the sidewalls of the tunnel. The evacuation is supposed to take place upstream of the fire, while downstream users are expected to leave the tunnel by driving their vehicles. As well, the firefighters can safely reach the fire from the smoke-free side of the tunnel.

In order for this strategy to be effective, it is imperative to avoid the so-called "backlayering phenomenon" by imposing a velocity exceeding a threshold value, known as critical velocity $U_{0,cr}$. The critical velocity is therefore defined as the minimum ventilation velocity that prevents smoke from flowing upstream of the source. The backlayer length (L) is the length of smoke flowing upstream of the source against the direction of ventilation when the ventilation velocity is less than its critical value. Both the parameters are considered in the present study.



Figure 1.3: Fire-induced smoke longitudinal control [17].

1.3 Smoke behaviour and Ventilation strategies

It should be noted, however, that the longitudinal system presents some drawbacks. Firstly, the ventilation velocity must be approximately constant throughout the tunnel, which requires a lot of fans and therefore high energy consumption. Secondly, adding ventilation could fuel the fire, light it for longer and transmit it to other vehicles nearby. Thirdly, some tunnels require a strong thrust to achieve the critical velocity, especially downhill tunnels where the adverse "chimney effect" is strong.

1.3.2.3 Transverse ventilation

Transverse ventilation is a way of permitting the safe egress of users in case of a fire in road tunnels, even with severe congestion or bidirectional traffic. It consists in extracting the fire smoke through dampers, which are generally located on the ceiling (Fig. 1.4), whilst controlling the longitudinal air flow in the tunnel. With this system, the tunnel users can be evacuated and firefighters can intervene in both tunnel directions. Two objectives are generally pursued: the preservation of the natural stratification and the confinement of the smoke within a limited section of the tunnel, in which the extraction takes place.

The literature on the dependance of ventilation control parameters in transverse systems is much scarcer than its counterparts in longitudinal systems. The main parameter is the confinement velocity, defined as the minimum induced longitudinal velocity required to prevent the smoke from propagating beyond the extraction dampers (and the associated extraction flow rate). In this study, the influence of parameters such as the shape and position of the extraction dampers on the efficiency of the transverse ventilation system is studied.

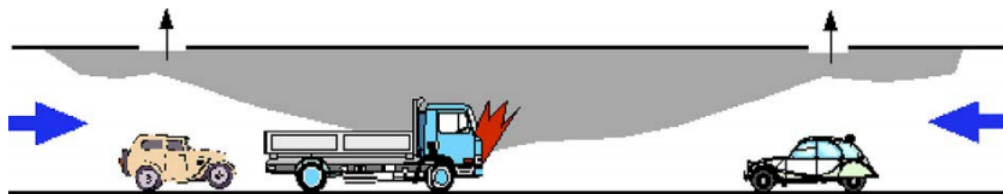


Figure 1.4: Fire-induced smoke transverse control [17].

A transverse ventilation system is an appropriate way for fighting fires and controlling the spread of smoke since it is suitable for both one-way tunnels and two-way tunnels. The system must be powerful enough to create longitudinal flows from both sides of the tunnel to confine the smoke between the vents located on either side of the fire. However, the generation of high extraction flow rates can in some cases disturb the stability of the smoke stratification and put tunnels users at risk, which is a major drawback of this type of system.

1.4 Fire tunnel simulation approaches

A better knowledge of fire phenomena in tunnels is needed to develop procedures and tools to effectively ensure the safety of users. Various national and international organisations are conducting research to this end. The investigation methods are divided into three groups: full-scale tests, small-scale tests, and numerical simulations.

1.4.1 Full-scale tests

Large-scale tests are conducted in real tunnels, such as abandoned tunnels, tunnels undergoing renovation, or tunnels before being put into service. These tests provide valuable information to dimension mechanical ventilation systems and form a strong basis for fire safety strategies. However, their preparation is expensive and some of the necessary measures are not attainable (e.g. \$40 million for the Memorial Tunnel campaign [18]). During these tests, fires are generally reproduced by the burning of fuel or wooden pallets. Larger fires (fires involving car/trailer loads or petrol pool fires with a load up to 100 MW) are also reproduced, as in the EUREKA-Project EU499 performed in northern Norway in 1992 [19], the Memorial Tunnel Fire Ventilation Test Program conducted in West Virginia in 1995 [18] or also the Runhamar Test Program achieved in Norway in 2003 [20].

1.4.2 Small-scale tests

Compared to full-scale tests, the small-scale tests have several advantages: *i*) the cost of experiments is lower and *ii*) the experimental conditions are fully controlled. The small-scale tunnel models can be divided into two groups: thermal models and densimetric models.

In thermal models, the fire source can be modelled, for example, by propane fires [21, 22], n-heptane pool fires [23] or methanol pool fires [24]. With this type of installation, the firepower is often unstable over time and it is difficult to estimate accurately the convective heat release rate (this can be controlled using gas burners, which provide stable firepower over time but are relatively low).

In densimetric models, the fire source is modelled by injecting a light gas into the ambient air. The smoke is therefore simulated using density differences rather than temperature differences. The light gas can be presented, for example, by a mixture of air and helium [17, 25–27] or by a mixture of nitrogen and helium [28]. As shown by Jiang et al. [27], the densimetric plumes can reliably reproduce the smoke behaviour produced by a fire for all cases where the size of the flames is less than half the height of the tunnel. Indeed, this method provides a simple way to study flow dynamics while allowing accurate control of

the density and the flow rate at the source. Note that, in this modelling approach, the flow dynamics will not be affected by all the phenomena related to heat losses at tunnel walls.

In the fire safety engineering community, the physical scaling technique known as ‘Froude scaling’ is widely used to obtain the corresponding parameters in large-scale cases of those obtained in small scale experiments. The Froude number is defined as the ratio between the inertial forces and the buoyancy forces. The similarity rules adopted for tunnel fire experiments impose a strict conservation of the Froude number while keeping the Reynolds number sufficiently high to ensure a turbulent flow inside the tunnel. Based on the Froude modelling, the velocities between model and full scale are fixed in the ratio of the square root of the geometrical scale θ , and the scaling of the heat release rates and mass flow rates is fixed in the ratio $\theta^{5/2}$ [29]. While the density differences and the temperature fields are preserved between small-scale and large-scale tests.

1.4.3 Numerical simulations

Computational Fluid Dynamics (CFD) is widely used in tunnel fire simulations. The main advantage of numerical simulations is that they provide access to quantitative values and variables that are difficult to measure with experimental devices and allow a wider range of scenarios to be simulated and more parameters to be investigated. However, their main drawback is that they require powerful computers and often take a high computational time.

CFD codes numerically solve the Navier-Stokes equations in a discretized domain by computing all variables of the fluid flows in time and space. The equations governing fluid motion can be solved accurately without any turbulence model using the Direct Numerical Simulation (DNS) method. However, this method requires enormous computational costs and is therefore not suitable for tunnel fire simulations. For such reason, modelling approaches have been developed and adopted in a wide range of engineering applications, including tunnel fire applications. These are divided into two groups: Large Eddy Simulations (LES) and Reynolds-Averaged Navier-Stokes (RANS). LES directly solve unsteady motion of large scale eddies, while modelling the effects of small scales. RANS models instead provide time-averaged solutions of the velocity field by introducing a system of closure equations to model the turbulent transfer of heat and momentum.

1.5 Objectives, methods and plan of study

1.5.1 Objectives of study

In this research, fires in road tunnels with longitudinal and transverse ventilation systems are investigated numerically and experimentally. The main objective is to study the smoke propagation during a tunnel fire and to evaluate certain means and parameters of smoke control in order to increase the efficiency of the ventilation systems and improve the safety for tunnel users. For this purpose, one of the possible solutions is proposed in this study and concerns the installation of solid barriers at the tunnel ceiling. The idea is to place ceiling barriers, which can be fixed or mobile depending on their height, to control the spread of smoke even at low ventilation velocities. These barriers are currently not implemented in tunnels, but they could help satisfy the ventilation objectives and could be useful mainly to:

- Reduce the construction cost by reducing the amount of required space for ventilation equipment in the tunnel, or simply by reducing the critical velocity, hence the number of necessary fans.
- Control the smoke in tunnels where the ventilation velocity is low or the stack effect is high.
- Ensure the confinement of fire smoke while maintaining the stratification of the smoke layer in the transverse ventilation.

Other aims are also envisaged, in particular the investigation of the effects of the large density differences (referred to as "non-Boussinesq effects") on the fluid dynamics, which remains an open question that has not been fully elucidated in the ventilation of confined spaces.

1.5.2 Methods and plan of study

In this study, small-scale experiments on the tunnel scale model (1/25 scaling factor) of the LMFA laboratory were carried out using a helium-air plume to simulate the fire, a method which has been consolidated through the study of the critical velocity and back-layering phenomenon [25–27]. The interpretation of the experimental results was completed by numerical simulations conducted using the Fire Dynamics Simulator (FDS) software and the LES approach. This study is divided into four chapters and in each chapter the results are presented in the form of a research paper. Note, however, that this way of structuring the manuscript involves some repetition of basic concepts and experimental apparatus. Chapter

1.5 Objectives, methods and plan of study

2 is dedicated to study, using Particle Image Velocimetry (PIV) system, the non-Boussinesq effects on the dynamics of the turbulent plumes released within a longitudinally ventilated tunnel. Chapter 3 focuses on the effects of the solid barriers on the propagation of fire smoke in a longitudinally ventilated tunnel, with and without vehicular blockage. In Chapter 4, we study the influence of the shape and position of the extraction dampers, including the specific case of full-width dampers, on the efficiency of the transverse ventilation system. In Chapter 5, we conduct numerical simulations by reproducing some physical tests mainly to complete the interpretation of the experimental results. Finally, we present conclusions and some perspectives at the end of the report.

INFLUENCE OF THE NON-BOUSSINESQ EFFECTS ON THE DYNAMICS OF BUOYANT PLUMES

Experiments are conducted to measure, using Particle Image Velocimetry (PIV) system, the velocity fields induced by light (a mixture of air and helium) turbulent plumes released within a longitudinally ventilated tunnel. Two types of plumes are considered, forced plumes (i.e. momentum-driven releases) and lazy plumes (i.e. buoyancy-driven releases). For each type, two cases are produced by varying the values of the density ratio ρ_i/ρ_0 and setting the plume Richardson number Γ_i and the ratio between the source diameter and the tunnel height D_i/H . The ventilation flow is set to the so called "critical condition", i.e. implying a longitudinal ventilation velocity that do not allow the light gas release to move upstream the source, against the ventlation flow. The objective is to study, in the critical ventilation conditions, the non-Boussinesq effects (i.e. the effect due to large density differences between the light gas and the ambient fluid) on the dynamics of the forced and lazy plumes. For this purpose, 2000 instantaneous velocity fields per experiment were acquired from which the statistics of the mean and fluctuating flow components are derived. For each type of plume, analyses and comparisons between the test results are performed. The analysis of time-averaged velocity fields shows that the magnitude of the fluctuations are much higher in buoyancy-dominated releases than in jets (i.e. momentum-dominated plumes). As well, the amplitude of the Reynolds shear stress is significant with buoyancy-driven releases. These results suggest that the buoyancy acts to enhance turbulent entrainment process and therefore to increase the turbulent mixing between the buoyant plume fluid and the ambient fluid.

Keywords: Longitudinal ventilation, Forced plume, Lazy plume, Particle image velocimetry, Turbulent flow, Entrainment.

2.1 Introduction

An open question that has not been fully elucidated in the ventilation of confined spaces in the presence of fires and buoyant releases is related to the effects of the large density differences on the fluid dynamics. These effects are often linked to non-dimensional parameters that can be the ratio between the density of the plume (ρ_i) and that of the ambient air (ρ_0), or alternatively the Atwood number, and refer to as non-Boussinesq effects [25, 30]. Concerning the road tunnel ventilation, recent works by Jiang et al. [31] have shown that the dependence of the critical velocity $U_{0,cr}$ on the source conditions clearly exhibits a different behaviour depending on the relative strength of the momentum and buoyancy flux imposed at the source, related to its diameter D_i , its density ρ_i and the velocity of the release W_i . Notably, Jiang et al. [31] have identified two regimes, one for high forced releases ($\Gamma_i < 1$) [32] and the other for lazy releases ($\Gamma_i > 1$) [33], Γ_i is the plume Richardson number which is defined as the ratio between buoyancy forces and inertial forces at the source. In the former regime, the non-dimensional critical velocity $U_{0,cr}/W_i$ clearly exhibits a dependence on the density ratio ρ_i/ρ_0 . Whereas, in the case of buoyancy-dominated releases, non-Boussinesq effects could not be detected, even when imposing large density differences at the source (pure helium plume in air). In their work, Jiang et al. [31] limited their study to measurements of bulk flow quantities which could be evaluated experimentally by mean of flow visualisations. The different roles of the density ratio in momentum-dominated releases and buoyancy-dominated releases could not therefore be observed in local flow variables.

In order to provide further insight on these flows, we have therefore performed new experiments on velocity field measurements using the Particle Image Velocimetry (PIV) system. The goal of these experiments is twofold: first to provide an experimental description of these flows in order to identify the similarity and differences in flow dynamics depending on the source conditions and, second to provide a reference data-set to test the performance of the numerical models.

Particle image velocimetry is an optical method of flow visualisation used to obtain instantaneous velocity measurements and related properties in fluids, by means of motion of the seeding particles. PIV was introduced in the late 1980's. A few years later, it became popular in the applications of fluid mechanics and turbomachinery. Today, it is developed to become one of the most powerful high-speed imaging systems in the world of research and development, as well as in many industrial sectors. This technique can be used for example: i) in wind tunnel experiments to test the aerodynamics of different objects and structures (such as cars, trains, planes and buildings, etc.); ii) in flow velocity measurements (research in hydrodynamics, turbomachinery, flow in pipes and channels, etc.); iii) in environmental

2.2 Problem setting and dimensional analysis

research (combustion research, wave and plume dynamics, fluvial hydrology, etc.); iv) in biomedical research with a view to increasing biological or medical knowledge, on experimental research in fluid turbulence and flow behaviour. PIV has also been used to study the behaviour of fire plumes in ventilated tunnels. Oka et al. [34] carried out a series of fire tests in a small-scale tunnel and used the PIV system to measure the values of the coefficients included in their developed correlation to estimate the velocity and temperature attenuation of a ceiling-jet along a horizontal tunnel axis. Klein et al. [35] conducted small-scale experiments of fires modelled by injection of light gases (air/helium mixture) and used the PIV method to determine the resulting flow fields and corresponding velocity and vorticity distributions in the longitudinally ventilated tunnel. Lozano et al. [36] used the PIV system to study the different dynamic structures of fluids present within a propagating fire in a wind tunnel. Kim et al. [37] carried out quantitative measurements of PIV in a small-scale tunnel model to investigate the influence of the longitudinal ventilation on fire smoke dispersion phenomena. Rie et al. [38] studied the characteristics of smoke movement using PIV to assess the effectiveness of the smoke vent system in providing a tenable environment for the evacuation of passengers in case of a fire in an underground train tunnel.

Fire simulation experiments are carried out in a small-scale tunnel by injecting a mixture of air and helium into ambient air. Two types of plumes are considered, momentum-driven forced plumes and buoyancy-dominated plumes. For each type of plume, two cases are performed to study the non-boussinesq effects on plume dynamics by fixing the other two control parameters at the source (i.e. the plume Richardson number Γ_i and the ratio between the source diameter and the tunnel height D_i/H). The critical velocities are first evaluated then, under these conditions, the PIV system is introduced to obtain instantaneous velocity measurements at each field of view of each case tested. The statistics of mean velocity and standard deviation components are thereafter derived from all instantaneous velocity fields. The results of different cases are then discussed and compared with each other for each type of plume.

2.2 Problem setting and dimensional analysis

Jiang et al. [27] studied the difference between a buoyant plume and a fire plume in the longitudinally ventilated tunnel, by combining experiments and numerical simulations. Their results show that the buoyant plumes of air and helium mixture can be used to simulate the combustion of a vehicle for all cases where the height of the flame is less than half the height of the tunnel. In accordance with this result, the fire simulation in this study is performed by injection of light gas (the mixing of air and helium) into the ambient air.

2.2 Problem setting and dimensional analysis

The source of a fire is associated to its convective heat release rate defined by $Q_c = \rho_i C_p q_i (T_i - T_0)$ whereas the buoyant plume is quantified by its buoyancy flux defined by $B_i = g q_i \frac{\rho_0 - \rho_i}{\rho_0}$, where ρ_0 is the density of the smoke at the source, C_p is the specific heat capacity, q_i is the flow rate at the source, T_i is the temperature of the smoke at the source, T_0 is the ambient air temperature, g is the gravitational acceleration and ρ_0 is the density of the ambient air.

Assuming smoke acts as a perfect gas, for a low Mach number, the term of the pressure variations can be neglected, and the ideal gas law can be reduced to: $\rho_0 T_0 = \rho_i T_i$ that can be rewritten as $T_0(\rho_0 - \rho_i) = \rho_i(T_i - T_0)$. Replacing the term $\rho_i(T_i - T_0)$ by $T_0(\rho_0 - \rho_i)$ in the equation of the heat release rate (HRR), we obtain the following relationship that can associate the HRR with the buoyancy flux:

$$Q_c = B_i \frac{\rho_0 C_p T_0}{g} \quad (2.1)$$

For a horizontal and infinitely long tunnel of width W and height H with assumption of negligible diffusive effects, the non-dimensional critical velocity $U_{0,cr}/W_i$ can be expressed as a function of three dimensionless parameters [25]:

$$\frac{U_{0,cr}}{W_i} = f\left(\Gamma_i, \frac{\rho_i}{\rho_0}, \frac{D_i}{H}\right) \quad (2.2)$$

where D_i is the diameter of the source, W_i is the injection velocity and $\Gamma_i = \frac{5g(\rho_0 - \rho_i)D_i}{16\alpha\rho_0 W_i^2}$ is the plume Richardson number and $\alpha = 0.127$ is a reference value for the top-hat entrainment coefficient [39]. The value of Γ_i determines the typology of the buoyant release as one of three types: momentum-driven forced plumes when $\Gamma_i < 1$ [32], pure plumes when $\Gamma_i = 1$ (i.e. dynamic balance between momentum and buoyancy) and buoyancy-driven lazy plumes when $\Gamma_i > 1$ [33].

Jiang et al. [31] performed a series of experiments in a reduced-scale tunnel to investigate the effect of each dimensionless parameter given in Eq. 2.2 on the dimensionless critical velocity $U_{0,cr}/W_i$. Their results show that there is a dependence between $U_{0,cr}/W_i$ and the three dimensionless groups for forced releases ($\Gamma_i < 1$), whereas for lazy plumes ($\Gamma_i > 1$), the plume Richardson number is the only parameter that affects the dimensionless critical velocity. However, in order to obtain more details on the dynamics of the buoyant plumes, we consider in the present study four different cases (two for each type of plume). For each type of plume, we perform the experiments by fixing the Richardson number Γ_i and the dimensionless source diameter D_i/H and taking two different values of the density ratio ρ_i/ρ_0 .

2.3 Experiments & PIV measurements

2.3.1 Critical velocity measurements

The experiments are conducted on a 1/25 tunnel scale model of 8.4 m of length, a schematic view of the installation is presented in Fig. 2.1. The cross section is rectangular with a width of 0.36 m and a height of 0.18 m. The fire is modelled by a light fluid of a mixture of air and helium. Both gases are controlled by flow meters and mixed in a long pipe to ensure a homogeneous flow. The air/helium mixture is then seeded with nebulized oil to allow visualisation of the smoke by means of a light sheet which is emitted from a lens installed at the tunnel inlet. The mixture is then released from a circular source located at ground level in the centre of the tunnel. The side wall is made of glass which permit visualisation of the smoke flow. Longitudinal airflow is induced by an extraction fan set at the tunnel outlet. The ventilation velocity in the tunnel (averaged over the cross section) is measured by means of a Pitot tube placed at the tunnel inlet.

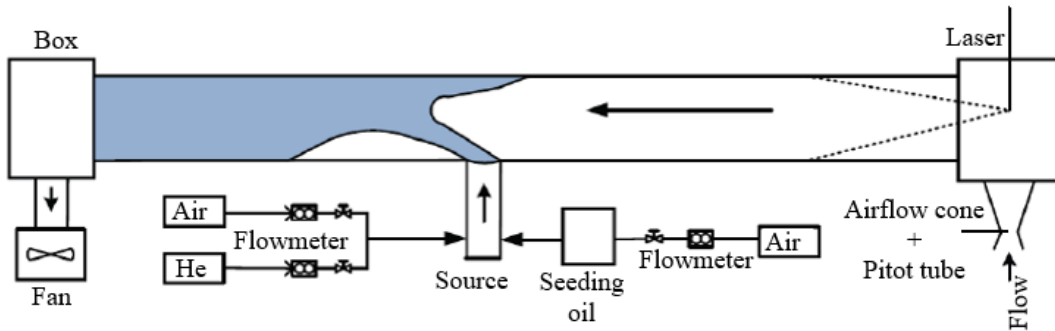


Figure 2.1: Experimental set-up for critical velocity measurements in the tunnel with a longitudinal smoke control system.

Table 2.1 presents a summary of all the experimental conditions simulated. Four tests were considered, two with forced releases (i.e. the buoyant plume is momentum-driven, $\Gamma_i < 1$) and two with lazy releases (i.e. the buoyant plume is buoyancy-driven, $\Gamma_i > 1$). Forced plumes are characterised by a plume Richardson number $\Gamma_i = 0.0075$ and dimensionless source diameter $D_i/H = 0.14$. For lazy plumes we have instead $\Gamma_i = 1.45$ and $D_i/H = 0.28$. For each type of plume, two values of density ratio are considered to evaluate dynamical effects referred to as non-Boussinesq: $\rho_i/\rho_0 = 0.8$ and $\rho_i/\rho_0 = 0.2$ for momentum-driven releases, $\rho_i/\rho_0 = 0.8$ and $\rho_i/\rho_0 = 0.3$ for buoyancy-driven releases. For

2.3 Experiments & PIV measurements

each test, the corresponding injection velocity W_i and buoyancy flux B_i are calculated and represented in Table 2.1.

Table 2.1: Experimental conditions of the tests conducted.

Case	Γ_i	D_i/H	ρ_i/ρ_0	W_i (m/s)	B_i (m^4/s^3)
1	0.0075	0.14	0.8	4.00	0.0038
2	0.0075	0.14	0.2	7.98	0.0305
3	1.45	0.28	0.8	0.41	0.0016
4	1.45	0.28	0.3	0.77	0.0104

Critical ventilation conditions are achieved by adjusting the power of the extraction fan until the front of the smoke back-layering is set at the source position (all smoke is pushed downstream of the source). The results obtained on the critical velocity $U_{0,cr}$ are shown in Table 2.2 with their corresponding dimensionless critical velocity $U_{0,cr}/W_i$. Using Eq. 2.1, the heat release rate Q_c corresponding to each buoyancy flux given in Table 2.1 is calculated and presented in Table 2.2 with their corresponding dimensionless heat release rate Q_c^* defined by Wu and Bakar [22] as $Q_c^* = Q_c / (\rho_0 C_p T_0 g^{1/2} H^{5/2})$. The corresponding heat release rate and critical velocity in the real tunnel are calculated by applying the scale relationships [29]: $(Q_c)_s / (Q_c)_f = (\theta)^{5/2}$ and $(U_{0,cr})_s / (U_{0,cr})_f = (\theta)^{1/2}$, where $\theta = l_s/l_f$ is the scale reduction ratio (equal to 1/25 in our tunnel model), l is the characteristic length, "s" and "f" refer to small-scale and full-scale.

The results clearly show that the effect of the density ratio on the non-dimensional critical velocity appears only in the case of forced plumes (i.e. case1 and case2 where $\Gamma_i = 0.0075$), whereas for lazy plumes, $U_{0,cr}/W_i$ is constant and equal to 0.36 m/s in both cases 3 and 4. This is in fact consistent with the previous results of Jiang et al. [31] and confirms their conclusion that the non-Boussinesq dynamic effects are significant only in the case of moment-driven releases, although they become negligible with buoyancy-driven releases. Moreover, they also showed that the dependence between the non-dimensional critical velocity and density ratio for low Richardson numbers ($\Gamma_i \ll 1$) is of the form $U_{0,cr}/W_i \propto (\rho_i/\rho_0)^{1/2}$ that is in accordance with our result obtained with $\Gamma_i = 0.0075$, i.e. $\frac{U_{0,cr}/W_i(case1)}{U_{0,cr}/W_i(case2)} = 195 \approx \sqrt{\frac{\rho_i/\rho_0(case1)}{\rho_i/\rho_0(case2)}} = 2$, which means a reduction in the dimensionless velocity $U_{0,cr}/W_i$ as the flow achieves non-Boussinesq conditions.

Table 2.2: Summary of the experimental results on the critical velocity associated with each equivalent HRR in a small and full scale tunnel, as well as the corresponding dimensionless values of critical velocity and HRR.

Case	Small scale tunnel		Full scale tunnel		Dimensionless values	
	$U_{0,cr}$ (m/s)	Q_c (KW)	$U_{0,cr}$ (m/s)	Q_c (MW)	$U_{0,cr}/W_i$ (-)	Q_c^* (-)
1	0.60	0.14	3.00	0.44	0.150	0.009
2	0.62	1.12	3.10	3.49	0.077	0.072
3	0.15	0.06	0.75	0.18	0.365	0.004
4	0.28	0.38	1.40	1.19	0.364	0.025

2.3.2 Velocity field measurements

Particle Image Velocimetry (PIV) is a non-intrusive optical measurement technique used to obtain instantaneous velocity fields on a plane, in order, notably, to understand the behaviour and structure of turbulent flows (a detailed description is provided in Appendix A). This technique is used in this study to obtain details on the dynamics of the different plumes studied above. The experimental configuration with the PIV system is shown in Fig. 2.2. The system mainly includes the following elements and components: Laser, Camera, Seeding particles, Synchronisation and acquisition tools.

The continuous light source, used previously for flow visualisations, is replaced by the Nd:YAG laser (Nd:YAG is the abbreviation for Neodymium-doped Yttrium Aluminum Garnet). This laser consists of a coupled dual-cavity and operates in pulsed mode. The successive pulses have durations of 5 nanoseconds and separated by only a few microseconds. The laser uses a frequency doubler to achieve high-intensity pulses by converting infrared light of a fundamental wavelength of 1064 nm to a visible green light of 532 nm. The laser energy is 2x150 mJ and its acquisition frequency is limited to 8 Hz. A semi-cylindrical lens through which the laser beam passes is placed at a height of about two meters above the tunnel model and is adjusted so that the sheet is focused on the area of interest (Fig. 2.2). The laser sheet produced is about 1 mm thick and illuminates the area studied through a glass panel on a two-dimensional divergent plane. The plane of the light sheet is precisely adjusted during the calibration of the camera (see A.2).

The Imager sCMOS camera is used to acquire instantaneous measurements of the fluid velocity fields. sCMOS image sensors offer a large field of view simultaneously in one image with very fast frame rates and extremely low noise [40]. The camera sensor comprises an array of 2560 x 2160 pixels and each pixel has a size of about 6.5 μm square, resulting in a sensor size of 16.6 x 14 mm². This significant number of pixels (approximately 5.5 million) allows to compute a large number of velocity vectors. The camera is capable of taking

2.3 Experiments & PIV measurements

multiple frames at high speeds, spaced a few microseconds apart, with exposure times of a few nanoseconds (which depends on the pulse duration of the laser). It is positioned perpendicular to the laser plane at some distance from the area of interest (Fig. 2.2). It is calibrated before being used to record instantaneous velocity fields. Both the camera and the laser are remotely controlled via LaVision DaVis software (8.4) installed in a computer that meets all required specifications. The system includes a Programmable Timer Unit (PTU) that can send the required trigger signals and provide connection and synchronisation between the camera and the laser.

To visualise the flow and obtain the displacement fields, both the plume fluid and ambient air are seeded. The flow constituting the densimetric plume (mixture of air and helium) is seeded with nebulised oil (section 2.3.1). The ambient air in the tunnel is seeded using a theatre smoke generator placed at the entrance of the tunnel (Fig. 2.2). This device can operate continuously with the ability to adjust the amount of fog flow during operation in order to fill the enclosure uniformly. The fog produced is very close to the natural fog, its particles (spherical particles of polyethylene glycol of size 1 μm) have practically no movement of their own; they follow the air currents and make them visible in the presence of light sources. Since the flow velocity is obtained by measuring the particle image displacements, some precautions are needed regarding the concentration of the tracer particles and the diameter of the particle images. Indeed, a number of particles of 8 to 10 per interrogation area and a size of particle images of 2 to 3 pixels in diameter are desirable for calculating the cross-correlation function while minimising the bias errors [41] (see A.1 and A.4.1).

After performing the calibration of the camera and conducting some primary tests in order to optimise the pulse separation time (Δt) between the successive light pulses and to check the correct operating of the PIV system (see A.3.1), the recording of the images of the tracer particles is carried out. PIV recordings are performed in double-frame mode, i.e. two separate frames are recorded between each two illumination pulses and stored on one "double-frame". For each case, 2000 samples are acquired over a period of approximately 5 minutes (per experiment). Acquisition, PIV correlation and image processing are carried out by DaVis[®] commercial software (see A.3.2 and A.3.3 for more details). A study of the quality of PIV measurements shows very low levels of total uncertainty (systematic and statistical errors, refer to A.4), which leads to the conclusion that these measures can be considered completely reliable. For each case, the statistics of the mean and fluctuating flow components are calculated from 2000 instantaneous velocity fields obtained by PIV correlation and the results obtained are presented below.

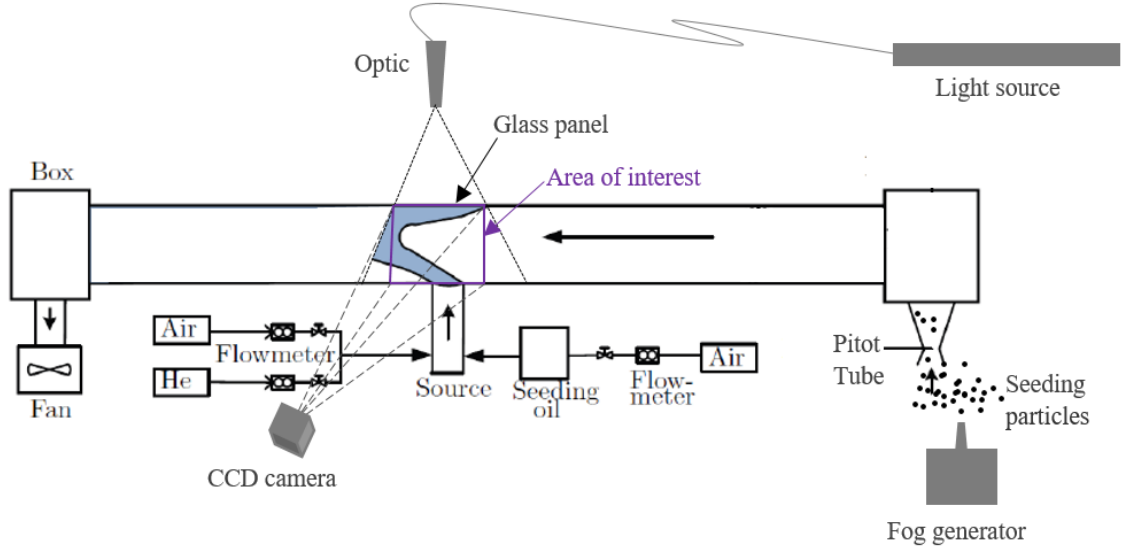


Figure 2.2: Experimental setup for PIV measurements in the tunnel with a longitudinal smoke control system.

2.4 Results and discussions

This section presents the results obtained by PIV measurements on the mean and standard deviation statistics. For each interrogation area, the average velocity \bar{u}_i and the standard deviation σ_i are calculated from the instantaneous velocity u_i as follows:

$$\bar{u}_i = \frac{1}{n} \sum u_i \quad (2.3)$$

$$\sigma_i = \sqrt{\frac{1}{n} \sum (u_i - \bar{u}_i)^2} \quad (2.4)$$

where $n = 2000$ is the number of samples and $i = x, z$. The Reynolds shear stress σ_{xz} is calculated by the following formula:

$$\sigma_{xz} = \frac{1}{n} \sum (u_x - \bar{u}_x) (u_z - \bar{u}_z) \quad (2.5)$$

For each case, the average velocity and standard deviation data are scaled by the corresponding injection velocity W_i provided in Table 2.1, and the values on both axes (x -axis and z -axis) are scaled by the tunnel height H .

The results are presented below first for forced plumes, then for lazy plumes. For each type of plume, the results between the two testes are compared and the discussions on non-Boussinesq effects are conducted.

2.4.1 Forced plumes

The results obtained for momentum-driven releases (i.e. case1 and case2) are shown here. The results analysis is first carried out on the mean velocity, then on the velocity fluctuations.

2.4.1.1 Average velocity

The statistical analysis of the average velocity fields allows us to show the overall behaviour of smoke plumes in the longitudinally ventilated tunnel. Fig. 2.3 shows the non-dimensional average velocity fields of the vertical component (\bar{u}_z/W_i) for case1 (Fig. 2.3a) and case2 (Fig. 2.3b). For each velocity field, the structure of the flow appears clearly in the form of a plume that develops perpendicular to the tunnel floor surface and moves towards the ceiling. For both cases, the plume appears slightly inclined in the same direction as the ventilation flow (at the upper half of the tunnel) and impinges the tunnel ceiling in the region between $0.15H$ and $0.3H$ downstream of the source. Just upstream of the source, a flow recirculation zone can be seen close to the tunnel ceiling in both fields. This is the result of the interaction between the smoke back-layering (formed after impingement) and the longitudinal flow of ventilation.

However, the variation of the non-dimensional vertical velocity \bar{u}_z/W_i of the flow with the height z/H is different from one case to another. In the vicinity of the source (at the bottom of the image), the red colour indicates a very high non-dimensional vertical velocity which is greater than 1. Here, $\bar{u}_z > W_i$ because the injection velocity is averaged over the cross-sectional area of the source while \bar{u}_z is the time-averaged velocity of the flow measured at each point. Indeed, the accuracy of the velocity values provided by PIV was verified by

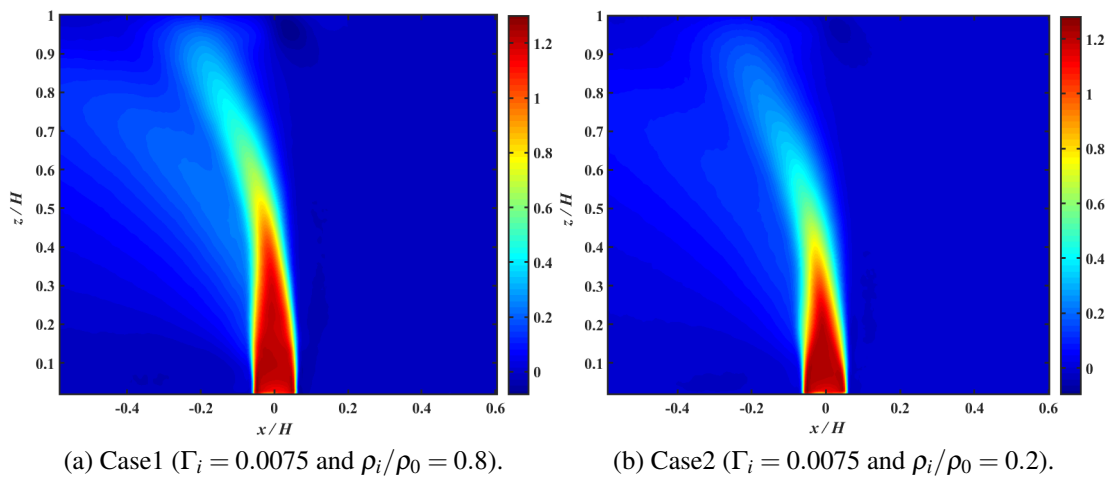


Figure 2.3: Non-dimensional average velocity fields of the vertical component \bar{u}_z/W_i .

taking the profiles of \bar{u}_z/W_i near the source and applying a trapezoidal numerical integration to calculate, from these profiles, the average velocity value across the source diameter, i.e. $\overline{\bar{u}_z/W_i}$. An example where the profile of the non-dimensional vertical velocity is taken close to the source at $z/H = 0.05$ is shown in Fig. 2.4 (black curves). For both cases, the average of the non-dimensional vertical velocity across the diameter of the source is calculated and presented in the same figure by the blue line. The results show that $\overline{\bar{u}_z/W_i}$ is close to one, which means that the estimated injection velocity with the PIV measurement is close to that calculated from the volume flow of the mixture. Returning to Fig. 2.3, the results

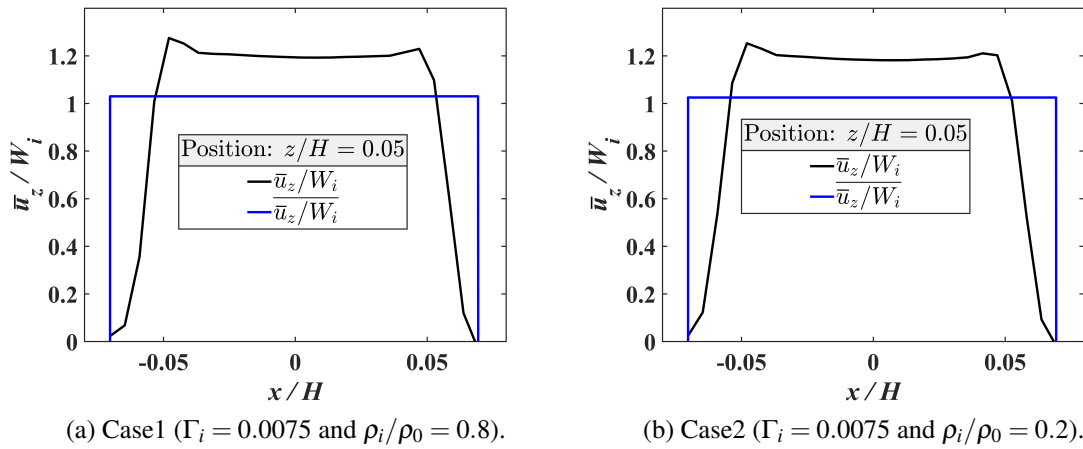


Figure 2.4: Profiles of the non-dimensional vertical velocity (black curves) and their average across the source diameter (blue curves) at $z/H = 0.05$.

show that in the centre of the tunnel, the colour then changes from red to green as the plume moves away from the source. This occurs when z/H is approximately equal to 0.5 in case1 and to 0.4 in case2. Then, once z/H is greater than 0.75 in case1 and 0.6 in case2, \bar{u}_z/W_i decreases rapidly with the height until its value becomes zero in the blue area near the tunnel ceiling. In addition, it should be noted that in both cases, the non-dimensional vertical velocity is almost zero in the right tunnel area (upstream of the source). But in the left area (downstream of the source), $\bar{u}_z/W_i = 0$ only in the lower part and under the ceiling of the tunnel while in the centre, it is different from zero (but remains low) due to the dispersion of the smoke in the direction of the longitudinal ventilation.

Fig. 2.5 shows the evolution of the non-dimensional vertical velocity at $z/H = 0.08$, $z/H = 0.40$ and $z/H = 0.70$ according to the non-dimensional longitudinal distance x/H . Near the source (i.e. $z/H = 0.08$), the trends marked by the two curves are the same. The two curves are roughly symmetric with respect to the vertical axis (defined by $x/H = 0$) and the maximum value of the non-dimensional vertical velocity is reached at the centre of

the plume where $\bar{u}_z/W_i = 1.2$. By moving from this position to the position $z/H = 0.40$, the curves become asymmetric relative to the vertical axis and \bar{u}_z/W_i decreases to reach its new maximum values of 1.04 with the first case and 0.77 with the second case. This is accompanied by an enlargement of the plume on the left side of the source ($x/H < 0$). In the upper part of the tunnel ($z/H = 0.70$), the curves continue to tilt towards the left side of the vertical axis and \bar{u}_z/W_i decreases to reach 0.48 in case1 and 0.3 in case2 as maximum values.

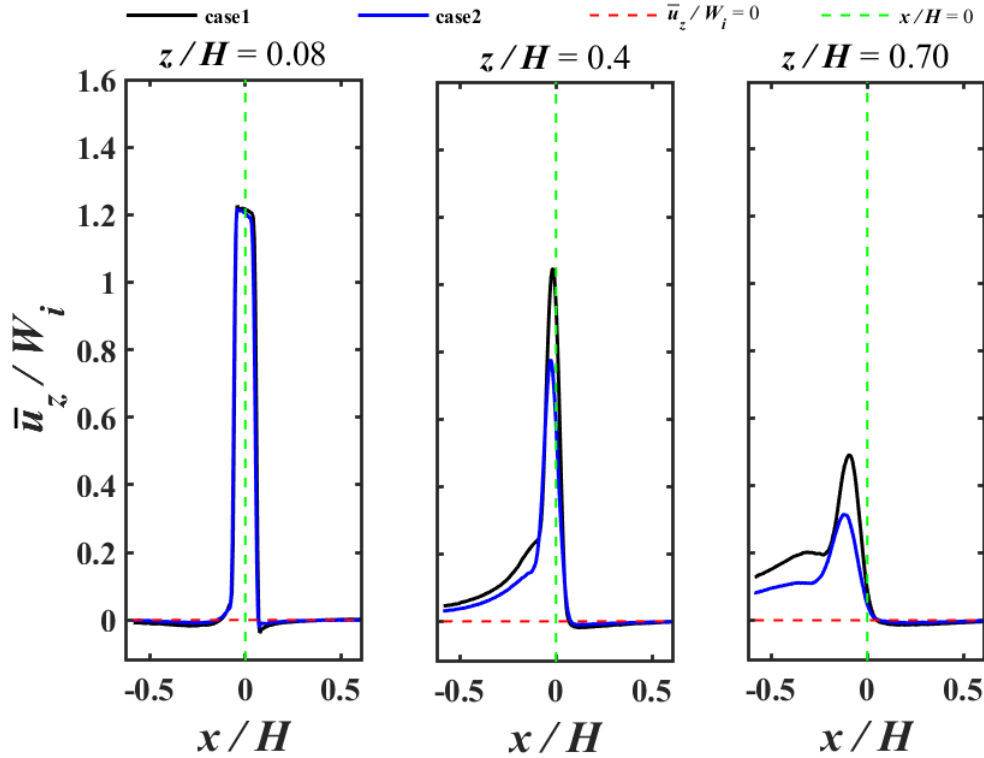


Figure 2.5: Profiles of the non-dimensional vertical velocity at $z/H = 0.08$, $z/H = 0.40$ and $z/H = 0.70$ versus the non-dimensional longitudinal distance x/H .

According to the above results (Fig. 2.3 and Fig. 2.5), the behaviour of momentum-driven forced plumes is marked by three different regions. The first is characterised by a good symmetry of the plume and a high vertical velocity which remains almost constant in the centre of the plume. This region extends from the source to a certain height above the source that depends on the density ratio at the source; the higher the density ratio, the higher the height of the region (this height is approximately equal to $z = 0.45H$ for $\rho_i/\rho_0 = 0.8$ and $z = 0.35H$ for $\rho_i/\rho_0 = 0.2$). The second is marked by the beginning of an asymmetry of the plume relative to the centre of the source and by a significant decrease in its vertical velocity. This region appears in the centre of the tunnel and it is strongly affected by the longitudinal

ventilation flow. The third appears in the upper part of the tunnel and extends to the ceiling. In this region, the smoke constituting the plume is completely dispersed under the effect of ventilation and its vertical velocity decreases rapidly to zero at the impingement point on the ceiling.

Fig. 2.6 shows the non-dimensional average velocity fields of the longitudinal component (\bar{u}_x/W_i) obtained with case1 (Fig. 2.6a) and case2 (Fig. 2.6b). The negative values of the velocity indicate that the flow is in the same direction as the ventilation, i.e. from the right to the left of the tunnel. While the positive values indicate that the smoke flow moves forward against the ventilation. In both fields, it can be seen that the colour of the area

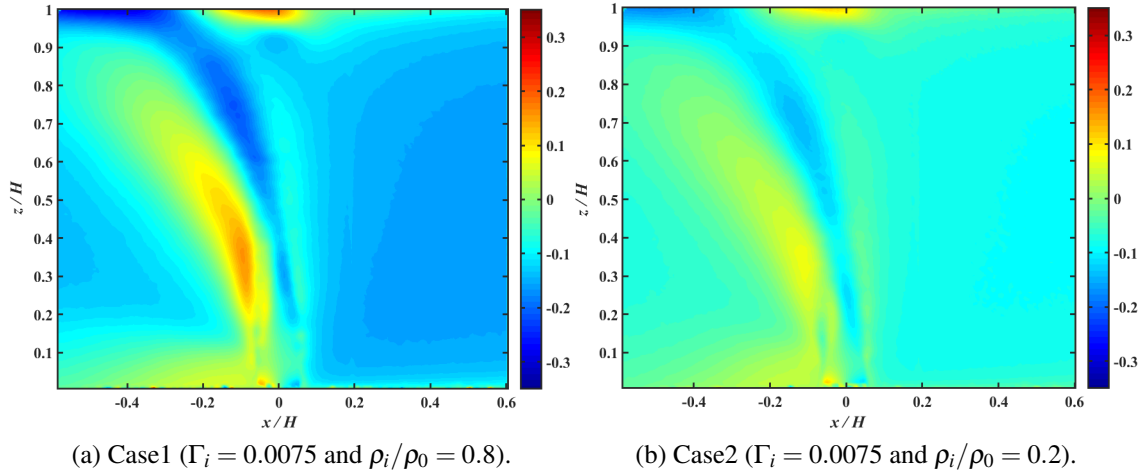


Figure 2.6: Non-dimensional average velocity fields of the longitudinal component \bar{u}_x/W_i .

upstream of the source is different from one case to another. In this area, for each point, the absolute value of \bar{u}_x/W_i measured in the first case is greater than that measured in the second case. This means that the density ratio has an effect on the non-dimensional longitudinal velocity and therefore on the non-dimensional critical velocity. As already done in Fig. 2.4, for each case, a velocity profile of the longitudinal flow is taken upstream of the source at $x/H = 0.60$ (where the ventilation flow is not affected by the buoyant plume) to calculate the average of \bar{u}_x/W_i over the height of the tunnel, i.e. $\overline{\bar{u}_x/W_i}$. The profiles, plotted in Fig. 2.7 (black lines), are very similar to those in a fully developed channel flow. For both cases, the average velocity over the height of the tunnel ($\overline{\bar{u}_x/W_i}$) is calculated and presented in the same figure by the blue line. Its absolute value is equal to 0.149 m/s for case1 and to 0.082 for case2, which are very close to those measured by means of the flowmeter placed at the tunnel entrance (see Table 2.2). In analysing the horizontal section of the flow (Fig. 2.6),

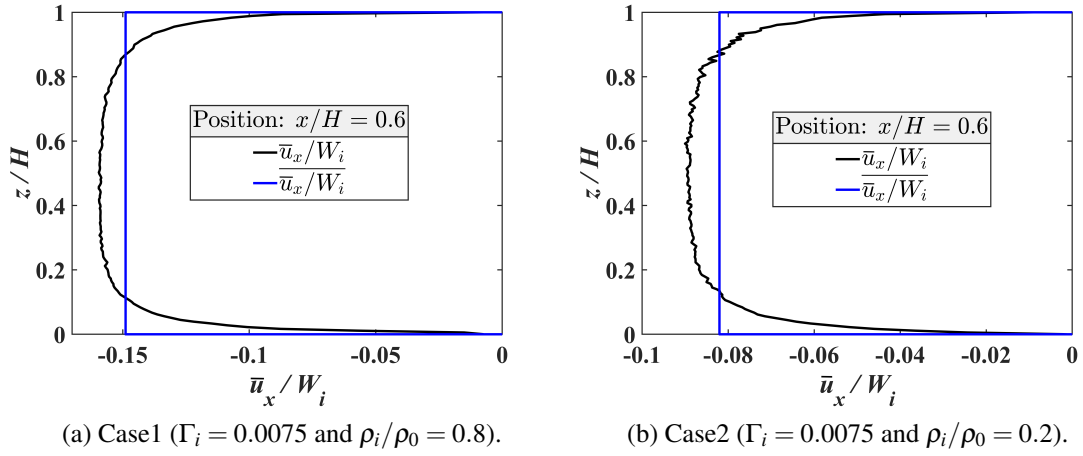


Figure 2.7: Profiles of the non-dimensional longitudinal velocity (black curves) and their average over the tunnel height (blue curves) at $x/H = 0.60$.

we can clearly identify two regions: in the part on the right side of the source, the smoke flows in the same direction as the ventilation flow, its longitudinal velocity is negative and reaches the maximum absolute value in the upper part of the tunnel. While in the part on the left side of the source, the smoke flows in the opposite direction of the ventilation flow, its longitudinal velocity is positive in the lower half of the tunnel and reaches its maximum value near the centre of the tunnel at z/H between 0.2 and 0.5. Close to the tunnel ceiling, we can see also a flow that moves forward against the ventilation. This represents the smoke backlayer which forms after impingement of the release at the tunnel ceiling, whose front is set at the up-wind border of the source by imposing a critical ventilation velocity.

For further clarity, we plotted profiles of the non-dimensional longitudinal velocity against the non-dimensional longitudinal distance x/H at three different positions: $z/H = 0.05$, $z/H = 0.50$ and $z/H = 0.99$. For both cases, these profiles are presented in Fig. 2.8. Near the buoyant source (i.e. $z/H = 0.05$), the longitudinal velocity profiles of both cases within the buoyant plume are superposed (area surrounded by a magenta circle) and each profile is almost antisymmetric relative to the origin of the x/H and z/H axes. In this region, the absolute value of the longitudinal velocity is less than one-tenth of the injection velocity. Outside this region, the absolute velocity is greater upstream of the source than downstream. This means that the smoke flow is mainly directed towards the top of the tunnel and the longitudinal ventilation flow is deflected on both sides of the plume during its impact with it. In addition, the velocity remains positive over a certain distance downstream of the source. This can be explained by the existence of backflow towards the source due to jet entrainment during plume rise. In the centre of the tunnel (i.e. $z/H = 0.50$), for each

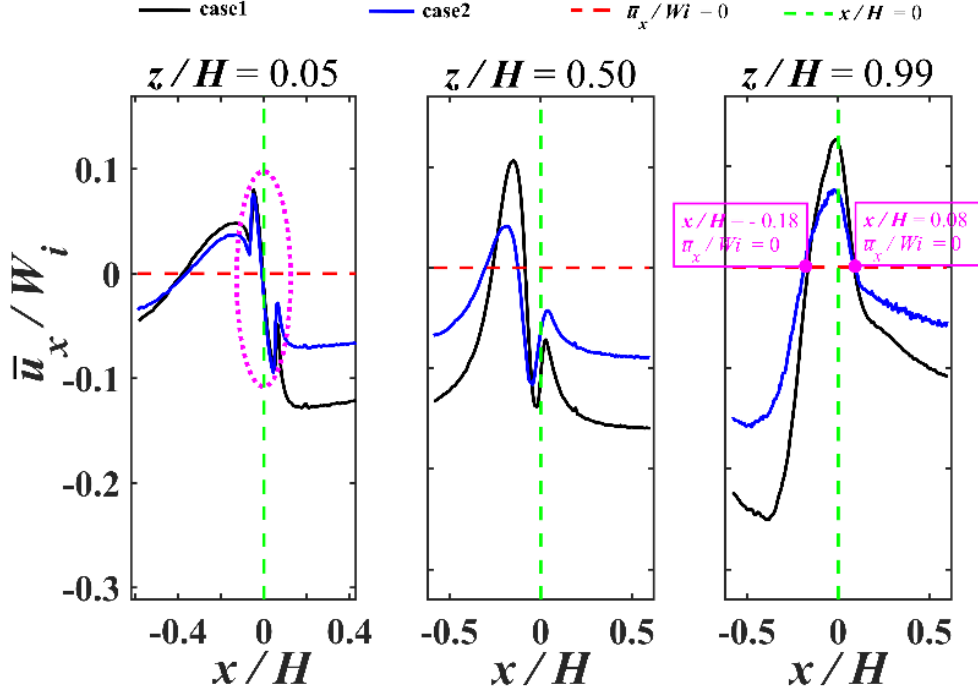


Figure 2.8: Profiles of the non-dimensional longitudinal velocity at $z/H = 0.05$, $z/H = 0.50$ and $z/H = 0.99$ versus the non-dimensional longitudinal distance x/H .

case, the maximum absolute velocity within the plume is reached on its right part (-0.14 and -0.12 in the right part, against 0.11 and 0.04 in the left part of the plume for case1 and case2, respectively). This is the result of the ventilation flow that forces the buoyant plume to move downstream of the source. For each case, the absolute velocity measured further downstream and upstream of the source is close to each other. Indeed, this can be observed in Fig. 2.6. approximately in the range $0.2 < z/H < 0.60$ for the first case (Fig. 2.6a) and in the range $0.2 < z/H < 0.50$ for the second case (Fig. 2.6b). Close to the tunnel ceiling (i.e. $z/H = 0.99$), for each case, the velocity profile changes sign upstream of the source at $x/H = 0.08$. This behaviour marks the presence of the smoke backlayer produced after the impingement of light-gas release at the ceiling. The front of this backlayer is located at a distance approximately equal to the radius of the source (i.e. $D_i/2H = 0.07$, see Table 2.1). The second point in which the flow velocity profile changes the sign downstream of the source indicates the position of the impingement point. This occurs at $x/H = -0.18$ for both cases. Downstream this point, the absolute longitudinal velocity of the flow increases rapidly to reach its maximum of -0.25 at $x/H = -0.40$ with the first case and -0.16 at $x/H =$

-0.48 with the second case.

2.4.1.2 Velocity fluctuations

The statistical analysis of the velocity fluctuations provides valuable information on the behaviour of the studied flow, in particular on the level of instability and turbulence. In this section, we present the results obtained as regards the standard deviation of the two components of the velocity and the Reynolds shear stress of both cases 1 and 2. For each case, the fields and profiles of the dimensionless magnitude of these quantities are presented and the results of the two cases are compared to evaluate the effects of the density ratio ρ_i/ρ_0 .

Fig. 2.9 shows the non-dimensional standard deviation of the vertical velocity component (σ_z/W_i) for case1 (Fig. 2.9a) and case2 (Fig. 2.9b). In both cases, the vertical velocity fluctuations develop throughout the plume, except in the core of the buoyant jet where the gas-flow conditions seem to remain laminar. The fluctuations are significant on both sides of the plume, but more pronounced on the right side than on the left side and in the z direction rather than in the x direction. This is because the releases emitted from the circular sources entrain the surrounding ambient air, resulting in a high shear between the two gases (air and smoke) and a strong mixing as the buoyant plumes rise [31, 42]. This then leads to the identification of strong fluctuations due to the turbulence on all plume boundaries. The effect of the density ratio on the velocity fluctuations is remarkable for the two fields shown in Fig. 2.9. Both the height of the core of the release where the flow remains laminar and the

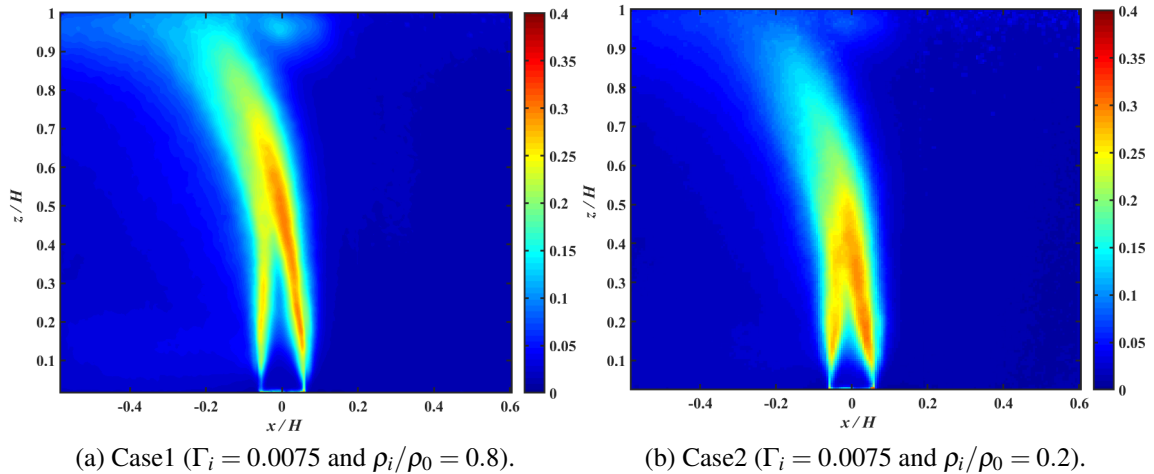


Figure 2.9: Non-dimensional standard deviation of the vertical velocity component σ_z/W_i .

extension of the fluctuations towards the ceiling are greater in the first case (Fig. 2.9a) than

in the second case (Fig. 2.9b). While the layer of the region where the velocity fluctuations are significant is thicker in the lower half of the tunnel with case2 than with case1.

To analyse the evolution of these fluctuations as well as their order of magnitude, three profiles are taken at three different positions $z/H = 0.10$, $z/H = 0.50$ and $z/H = 0.80$ (see Fig. 2.10). In the lower part of the tunnel (i.e. $z/H = 0.10$), far upstream and downstream of the source, the velocity fluctuations do not exceed 4% of the injection velocity. But in the interfaces between the light-gas and the ambient air, for each case, two distinct peaks appear on each side of the plume. The amplitude of these peaks is significant in case2 rather than in case1 and on the right side rather than on the left side of the plume. It reaches, from right to left, 0.27 and 0.24 with case2, 0.22 and 0.21 with case1. The intensity of the velocity fluctuations decreases rapidly between the two peaks until reaching its minimum value at the centre of the plume (0.07 with case2 and 0.03 with case1). As the buoyant plume rises

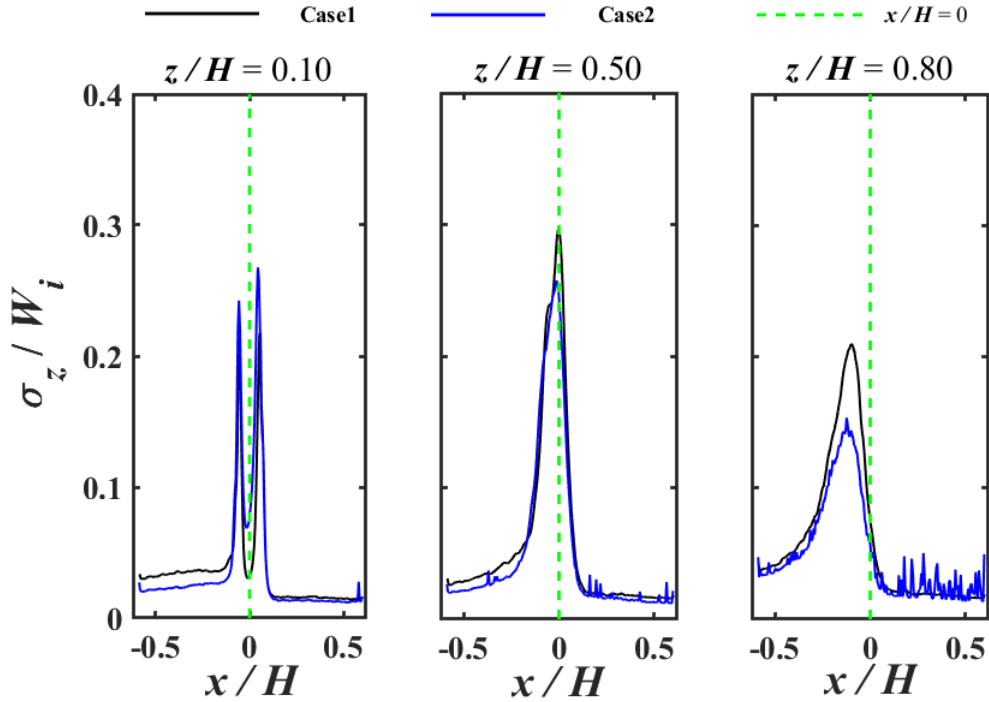


Figure 2.10: Profiles of the non-dimensional standard deviation at $z/H = 0.10$, $z/H = 0.50$ and $z/H = 0.80$ versus the non-dimensional longitudinal distance x/H .

and mixes with the ambient air, the two peaks join up to form a single large peak. According to Fig. 2.9, this occurs at approximately $z/H = 0.32$ with the first case and at $z/H = 0.16$ with the second case. In the centre of the tunnel (i.e. $z/H = 0.50$), the vertical velocity fluctuations become significant at the centre of the plume, with a maximum intensity of 0.3 in case1 and 0.26 in case2. These values are effectively high, which means that the flow is very turbulent. These fluctuations remain significant until $z/H = 0.70$ in the first case (Fig.

2.9a), but they start to decrease from this position (i.e. $z/H = 0.50$) in the second case (Fig. 2.9b). At $z/H = 0.80$, the peak of the fluctuation for both cases is displaced downstream of the central axis of the source. At this position, the maximum values of σ_z/W_i are equal to 0.21 and 0.15 for case1 and case2. Close to the tunnel ceiling, the fluctuations become less than 15% and 10% of the injection velocity with case1 and case2 (Fig. 2.9).

Fig. 2.11 shows the results of PIV measurements on the non-dimensional standard deviation of the longitudinal velocity component (σ_x/W_i) for case1 (Fig. 2.11a) and case2 (Fig. 2.11b). Similar to what has been previously pointed out concerning the vertical velocity fluctuations, momentum-driven release also causes strong longitudinal fluctuations along the buoyant plume, except in its core at the bottom of the tunnel. In general, in the lower half of the tunnel, for case1, the vertical fluctuations are slightly less significant than the longitudinal fluctuations (see Fig. 2.9a and Fig. 2.11a). While in case2, the vertical fluctuations appear a little more significant than the longitudinal velocity fluctuations (see Fig. 2.9b and Fig. 2.11b). This shows that the fluid flow is strongly anisotropic. In addition, in both cases, the upward structure of the longitudinal fluctuations (Fig. 2.11) seems to be more inclined downstream of the source than that of the vertical fluctuations (Fig. 2.9). Fig. 2.11 shows also that the effect of the density ratio on the amplitude of the longitudinal fluctuations is more pronounced; the higher the density ratio, the greater the amplitude of the longitudinal fluctuations.

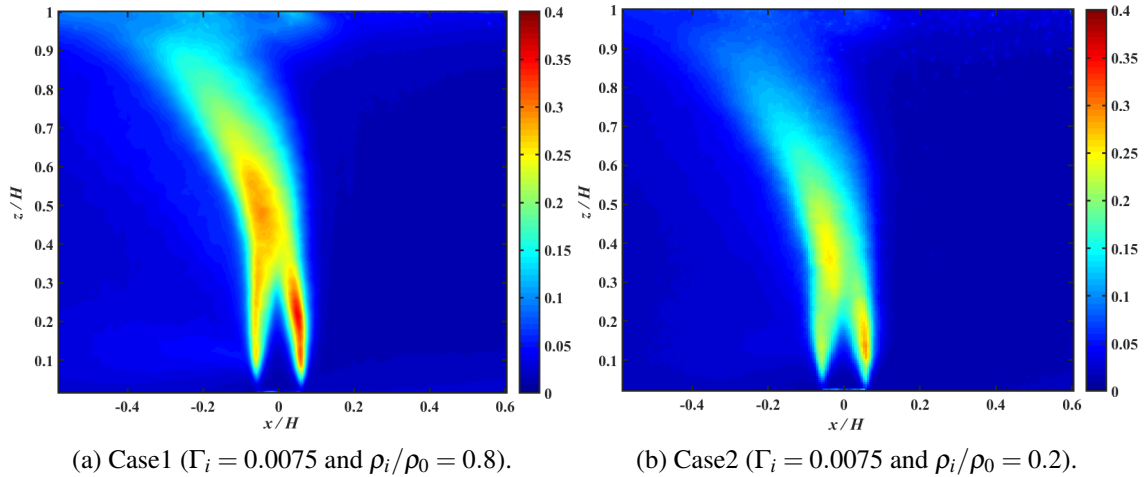


Figure 2.11: Non-dimensional standard deviation of the longitudinal velocity component σ_x/W_i .

Fig. 2.12 shows the evolution of σ_x/W_i against x/H at $z/H = 0.10$, $z/H = 0.50$ and

$z/H = 0.80$. Similar to the previous analysis performed with vertical fluctuations, near the source (i.e. $z/H = 0.10$), the magnitude of the longitudinal fluctuations is significant in the interfaces between the plume and the ambient air. From right to left, σ_x reaches 31% and 25% of the injection velocity with case1, 27% and 22% with case2. Fig. 2.11 shows that the maximum values of longitudinal fluctuations are reached in case1. These are located upstream of the central axis of the source in the region spanning from $z/H = 0.20$ to $z/H = 0.30$ (zone in deep red colour in Fig. 2.11a, where $\max(\sigma_x) = 0.35W_i = 1.4$ m/s). In the centre of the tunnel (i.e. $z/H = 0.50$), the peaks of the fluctuations in case1 and case2 are located at $x/H = -0.05$ and $x/H = -0.08$ and their values are 0.29 and 0.22, respectively. At $z/H = 0.80$, these peaks move further upstream of the source to take their new positions at $x/H = -0.18$ in case1 and $x/H = -0.21$ in case2 and their magnitudes decrease to about 0.19 for case1 and 0.12 for case2. In Fig. 2.12, it can also be noted that the area with large longitudinal velocity fluctuations extends in the direction of the ventilation as the plume rises towards the ceiling of the tunnel. At each position z/H , the peak width provides information on the size of the area where the mixing between the ventilation air flow and the buoyant fluid is significant.

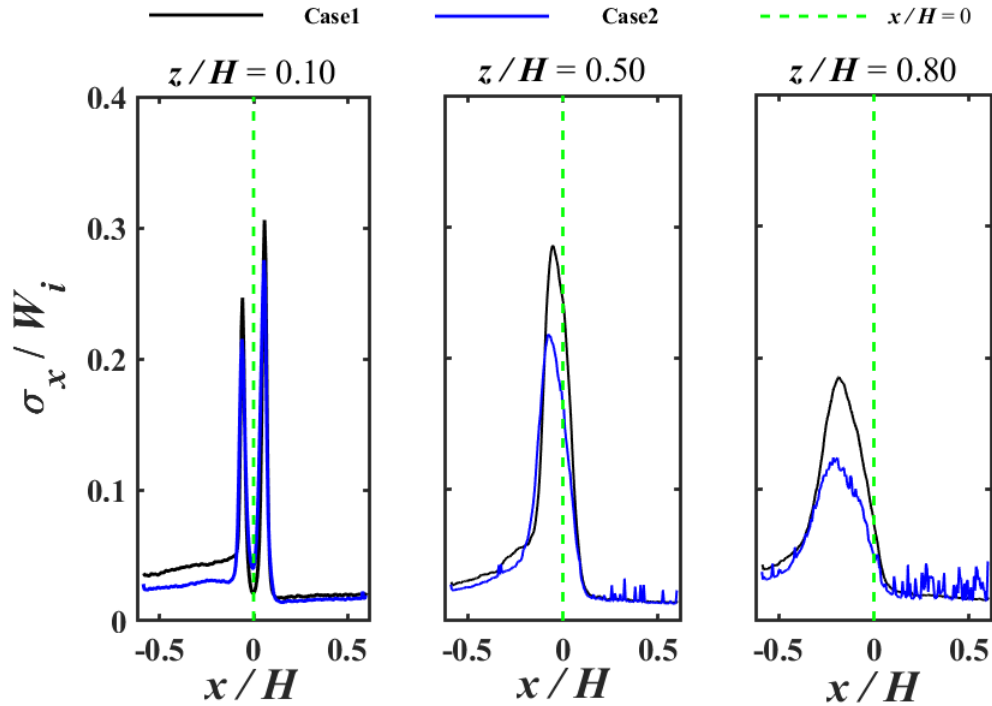


Figure 2.12: Profiles of the non-dimensional standard deviation at $z/H = 0.10$, $z/H = 0.50$ and $z/H = 0.80$ versus the non-dimensional longitudinal distance x/H .

2.4 Results and discussions

The dimensionless Reynolds shear stress σ_{xz}/W_i^2 , for case1 and case2, is shown in the fields presented in Fig. 2.13. As expected, the results indicate a high Reynolds stress at the interfaces between the buoyant plume and the ambient air, over the entire area which ranges from approximately $z/H = 0.05$ to $z/H = 0.60$ in case1 and from $z/H = 0.05$ to $z/H = 0.50$ in case2. The values of σ_{xz} are positive on the right-hand boundary of the plume and negative on the left-hand boundary. Fig. 2.14 shows the evolution of σ_{xz}/W_i^2 against

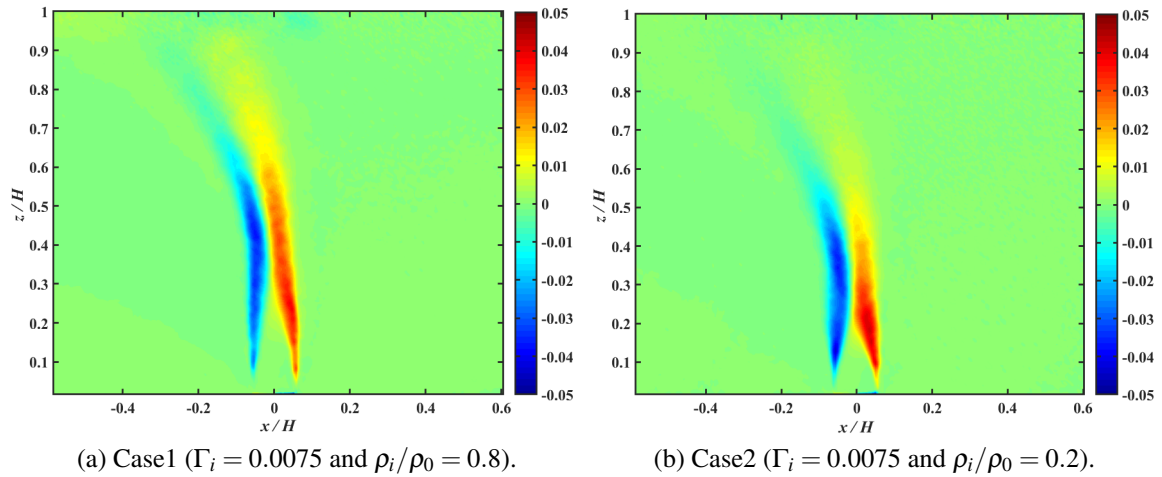


Figure 2.13: Fields of non-dimensional Reynolds shear stress σ_{xz}/W_i^2 .

x/H at $z/H = 0.10$, $z/H = 0.30$ and $z/H = 0.50$. It is interesting to note that although the magnitude of σ_{xz}/W_i^2 is different from case to another, the general trend of the correlations is similar. With the exception of the plume boundaries (Fig. 2.14), the longitudinal and vertical velocity fluctuations are uncorrelated, there would be no turbulent momentum transport in these regions. At $z/H = 0.10$, the absolute values of the correlation peaks are higher in the second case than in the first case. From right to left, they reach 0.039 and 0.031 with case2 and 0.023 and 0.026 with case1. This means that the intensity of the turbulent generated near the source with low-density gas releases is more important than that generated with high-density releases. At $z/H = 0.30$, in the left part of the plume, the absolute value of σ_{xz}/W_i^2 is 0.034 in both cases, while in the right part it is 0.033 with case1 and 0.027 with case2. This means that the intensity of the disturbance, relative to the previous position (i.e. $z/H = 0.10$), increased in case1 and decreased in case2. Nevertheless, it can be noted that the peak width (i.e. the thickness of the turbulent flow layer) has increased. In the centre of the tunnel (i.e. $z/H = 0.50$), in both cases, the absolute value of the fluctuations decreases but more significantly in case2. It reaches, from right to left, 0.026 and 0.030 with case1 and 0.012 and 0.019 with case2. Beyond this position (i.e. $z/H = 0.50$) for case2 and the position $z/H = 0.60$, the intensity of the correlations decreases rapidly until reaching zero

near the ceiling (Fig. 2.13).

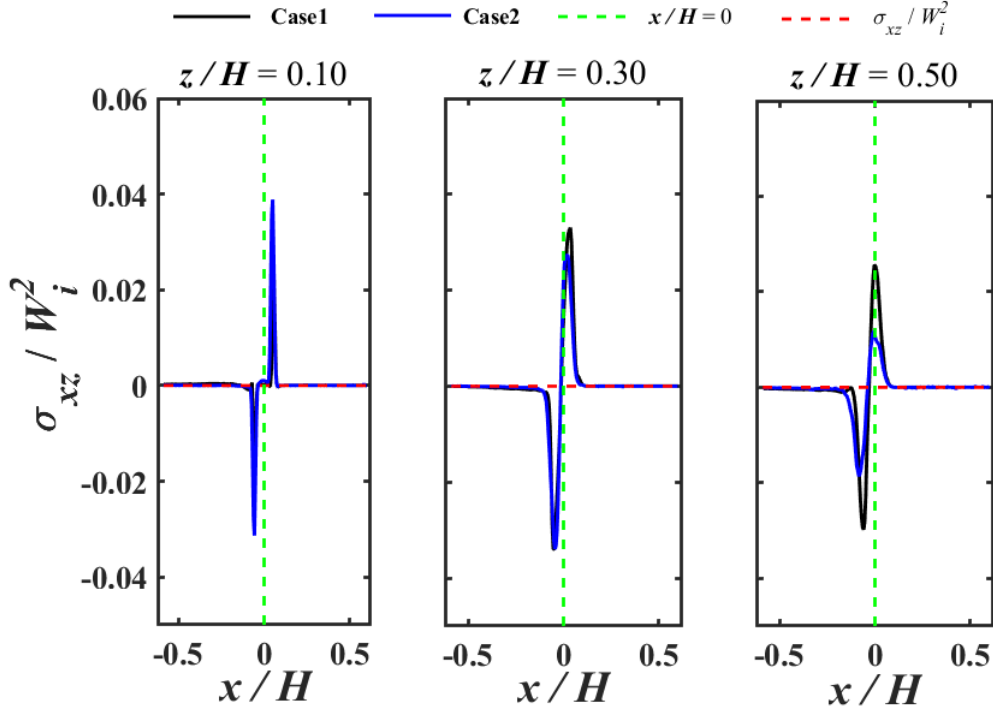


Figure 2.14: Profiles of the dimensionless Reynolds shear stress at $z/H = 0.10$, $z/H = 0.30$ and $z/H = 0.50$ versus the non-dimensional longitudinal distance x/H .

2.4.2 Lazy plumes

The results for the mean and fluctuating flow components obtained with buoyancy-driven releases (i.e. case3 and case4) are presented below. As for the forced releases (section 2.4.1), the analysis begins by examining the statistical average of the flow velocity followed by the study of the velocity fluctuations.

2.4.2.1 Average velocity

Fig. 2.15 shows the non-dimensional average velocity fields of the vertical component (\bar{u}_z/W_i) for case3 (Fig. 2.15a) and case4 (Fig. 2.15b). It can be seen that, compared to forced plumes, vertical velocity fields of lazy plumes are largely deflected in the direction of longitudinal ventilation. This deviation begins to appear directly above the source and becomes more important as the plumes rise towards the ceiling, especially in the case4, where the density of the emitted fluid is lower. Consequently, the light-gas releases impinge the ceiling of the tunnel in the regions situated far downstream of the source. It can also be seen that downstream of the source, a section of the plume is separated from the main plume and

forms a second independent plume that moves in the same direction as the ventilation flow. This occurs immediately above the source with case3 and at a height $z/H = 0.15$ with case4. In general, the structure of each of the fields presented in Fig. 2.15 can be described in three main zones already observed in case of forced plumes. The first zone (red zone), which extends from the source up to a certain height, is characterised by high vertical velocities. The size of this zone is very different from one case to another, it is high with case3 where $\rho_i/\rho_0 = 0.8$ and small with case4 where $\rho_i/\rho_0 = 0.3$. This difference indicates the importance of the density of the buoyant fluid releases on their dynamics and their behaviour, more the release is light more the dimensionless vertical velocity decreases rapidly. The second zone (green zone) is characterised by a slow decrease in vertical velocity and a high inclination of the plume. As shown in Fig. 2.15, this zone extends laterally over a considerable distance downstream from the source, more particularly in case4. The third zone (green to blue) is marked by a sharp decrease in vertical velocity due to the longitudinal ventilation flow which forces the smoke flow to be directed and dispersed in the longitudinal direction.

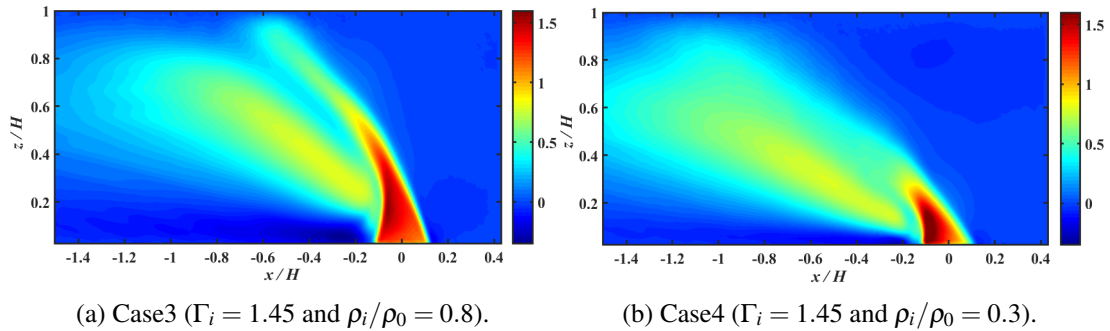


Figure 2.15: Non-dimensional average velocity fields of the vertical component \bar{u}_z/W_i .

Fig. 2.16 shows the non-dimensional vertical velocity profiles (black lines) plotted near the source at $z/H = 0.04$ for case3 (Fig. 2.16a) and case4 (Fig. 2.16b). At this position, the profiles are not axisymmetric and the maximum vertical velocity is equal to 1.35 of the injection velocity in the case3 and to 1.76 in the case4. For each case, the average value of the dimensionless vertical velocity across the diameter of the source is calculated and plotted with blue lines in the same figure. The results show that these average velocities are almost identical to those directly measured by the flowmeter.

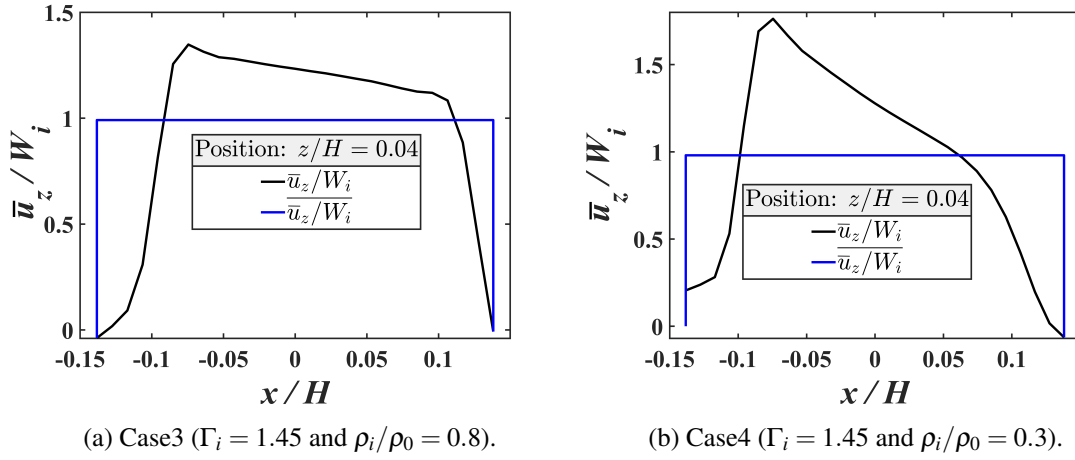


Figure 2.16: Profiles of the non-dimensional vertical velocity (black curves) and their average across the source diameter (blue curves) at $z/H = 0.04$.

Fig. 2.17 shows the profiles of the non-dimensional vertical velocity taken at the position at $z/H = 0.07$, $z/H = 0.20$ and $z/H = 0.70$ against the dimensionless longitudinal distance for case3 and case4. Compared to the results obtained with forced plumes, the vertical velocity profiles obtained at $z/H = 0.07$ for lazy plumes are very tight near the source and they are different from one case to another. The profiles are completely asymmetrical with regard to the central vertical axis and their maximum is reached on the left-hand part of the source, it is equal to 1.42 in case3 and to 1.80 in case4. In some regions upstream and downstream of the source, the vertical velocity changes from a positive value to a negative value. This can be interpreted by the existence of the flow recirculation zones caused by the entrainment of ambient air within the plume. These recirculation zones are more important in case4, where the vertical velocity reaches a maximum absolute value of 0.28 of the injection velocity. At $z/H = 0.20$, for both cases, the curves have more or less the same general trend: the vertical velocity increases to reach the first peak in the main plume and then decreases with height, then increases again to reach a second peak in the secondary plume. The position of these peaks varies from one case to another, they are further away from the centre of the source in case4 (i.e. the plume moves further downstream of the source when its density is low). The magnitude of the first and second peaks is 1.55 and 0.71 with case3, 1.33 and 0.77 with case4. In the upper part of the tunnel (i.e. $z/H = 0.70$), the position of the peaks continues to move further downstream and their amplitude remains significant. At this position, only one peak appears in the velocity profile corresponding to case4. This is because, at a certain height above the ground level, the two plumes (main and secondary) seem to be merged again to form a single plume (see Fig. 2.15b), a feature that we do not observe in case3 (see

Fig. 2.15a).

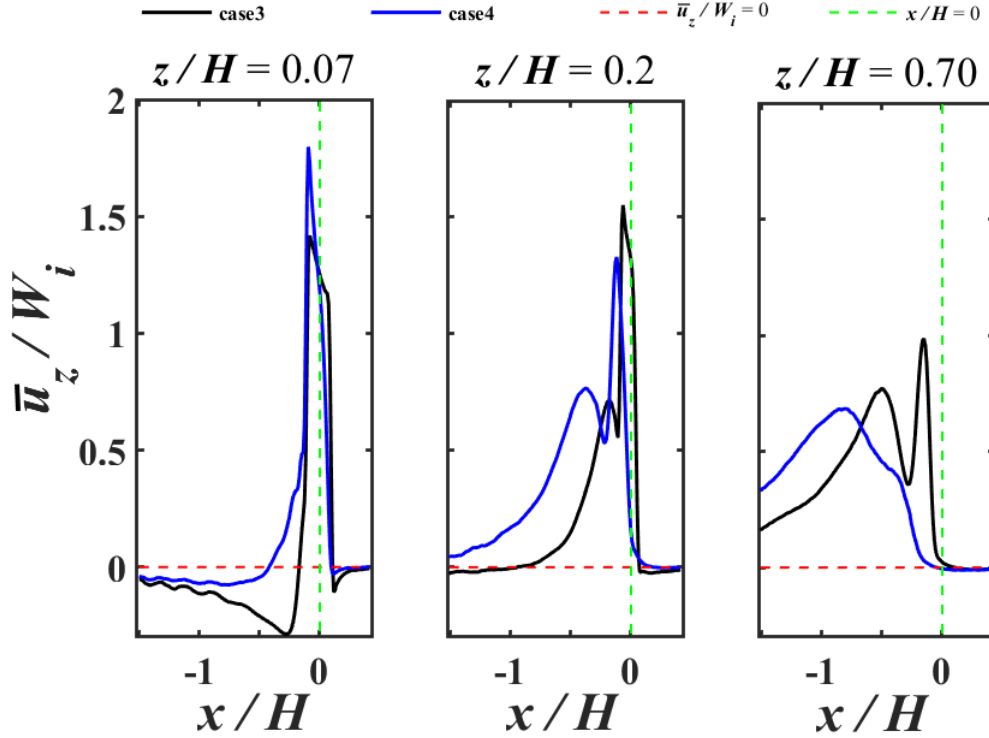


Figure 2.17: Profiles of the non-dimensional vertical velocity at $z/H = 0.07$, $z/H = 0.20$ and $z/H = 0.70$ versus the non-dimensional longitudinal distance x/H .

Fig. 2.18 shows the dimensionless average velocity fields of the longitudinal component for case3 (Fig. 2.18a) and case4 (Fig. 2.18b). In this figure, we can see that the colour of the fields upstream of the source is in general similar in both cases. Therefore, at each position x/H upstream of the source, the vertical profiles of the non-dimensional average longitudinal velocity of the two cases may be approximately similar. An example on the evolution of these profiles against the dimensionless vertical distance is presented in Fig. 2.19. The profiles are taken at $x/H = 0.40$, their average over the tunnel height is calculated and presented in the same figure (blue lines). The profiles are not perfectly axisymmetric with respect to the central axis of the tunnel. Nevertheless, their absolute average value over the height of the tunnel is approximately the same with both cases. It is equal to 0.39 in case3 and to 0.38 in case4, which are close to those obtained by means of the flowmeter (Table 2.2). Fig. 2.18 shows that the maximum values of the negative velocities are reached in the right-hand part of the plume (blue areas), in particular at the centre of the tunnel

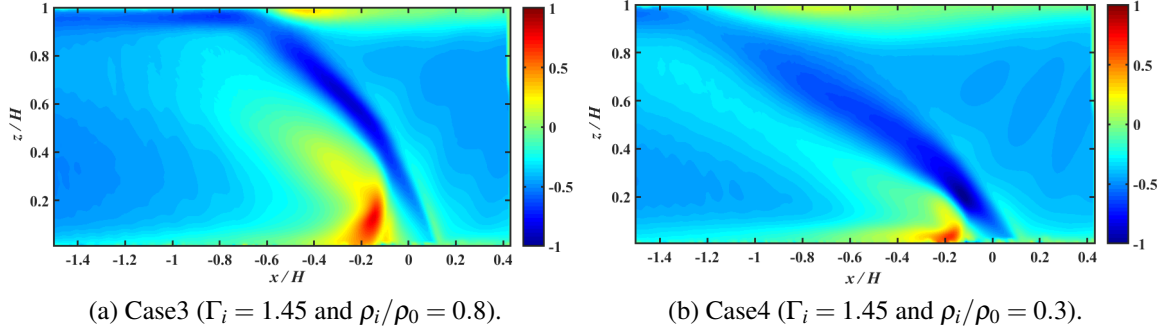


Figure 2.18: Non-dimensional average velocity fields of the longitudinal component \bar{u}_x/W_i .

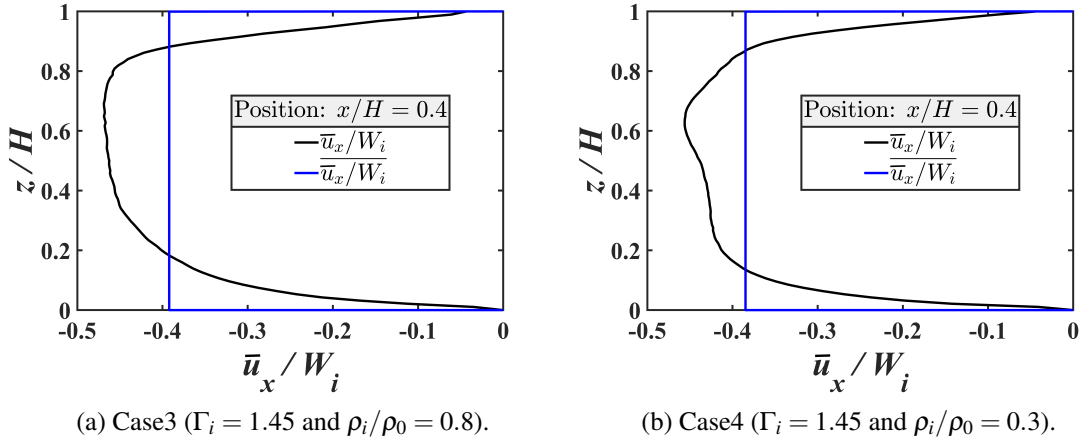


Figure 2.19: Profiles of the non-dimensional longitudinal velocity (black lines) and their average over the tunnel height (blue lines) at $x/H = 0.40$.

with case3 and at the bottom with case4. This means that the dynamics of the buoyancy-dominated releases is strongly affected by the longitudinal ventilation flow. Their center of mass moves more and more downstream of the source as they rise to the ceiling and mix with the ambient fluid. With low-density releases, these effects occur immediately as soon as the plume rises from the source (see Fig. 2.18b). While the maximum values of the positive velocities are reached downstream of the source approximately in the range $-0.25 < x/H < -0.15$ for both cases (red areas at the bottom of the tunnel). As already shown in Fig. 2.15, these regions show the recirculation zones resulting from the entrainment of ambient air within the buoyant plume (extensive for case3). Near the tunnel ceiling, the areas with positive longitudinal velocity represent the smoke flow formed after impingement of the releases on the ceiling and directed against the ventilation flow. It can be also noted that,

for both cases, the longitudinal ventilation velocity further upstream and downstream of the source is approximately the same, except in the regions close to the ceiling. This means that at a certain distance downstream from the source, the mixture of ambient air and smoke flow becomes homogeneous and flows at the same velocity as that of the ventilation flow upstream of the source.

Fig. 2.20 shows the profiles of the dimensionless longitudinal velocity plotted at the position $z/H = 0.05$, $z/H = 0.50$ and $z/H = 0.99$ against the dimensionless longitudinal distance for case3 and case4. Near ground level (i.e. $z/H = 0.05$), for each case, the velocity profiles show two peaks, a peak with a negative value of the velocity and a peak with a positive value. The peaks with negative values (pointing downwards in Fig. 2.20) appear on the right-hand half of the plume, their absolute amplitude is 0.33 in case3 and 0.49 in case4. The positive peaks appear instead within the flow recirculation zones and their magnitude is 0.57 in both cases. In the centre of the tunnel (i.e. $z/H = 0.50$), both velocity profiles are below the axis defined by $\bar{u}_x/W_i = 0$ (dotted red line in Fig. 2.20). This means that all the smoke is pushed downstream of the source in the same direction as the ventilation flow. However, the absolute longitudinal velocity of the "smoke" propagation constituting the secondary plume is small in case3 (i.e. region close to $x/H = -0.50$). This means that, compared to the case4, this part of the plume is slightly affected by the ventilation flow and, therefore, the smoke constituting this part of the plume tends to move in the opposite direction of the ventilation. Close to the tunnel ceiling (i.e. $z/H = 0.99$), for each case, the velocity profiles change the sign in two positions. The left-hand positions indicate the impingement points of the buoyant releases on the ceiling, located at $x/H = -1.0$ in case4 and at $x/H = -0.56$ in case3. From each point, a backlayer of buoyant fluid is formed and moved, under the effect of a pressure gradient, forward against the ventilation. The position of its extremity is determined once the longitudinal momentum flux (and the pressure force) of the buoyant flow balance the momentum flux imposed by the ventilation flow at the ceiling. This occurs at $x/H = -0.07$ and marks the critical conditions for both cases (i.e. the length of backlayer upstream of the source is zero). The distance between left-hand and right-hand positions gives the length of the backflow. In comparison to forced plumes (where this length is identical in both cases, see Fig. 2.8), with lazy plumes, it differs from one case to another, it is high with case4. The difference between the two types of plumes is that the highly forced releases impinge the tunnel ceiling at the same location, just upstream of the source, whatever their density, which means that the momentum-driven releases are jet-like impinging releases. While for lazy plumes, their impingement region is located far downstream of the source and varies with their density, the lower the density, the more the impingement point moves downstream of the source, which means therefore that the

buoyancy-driven releases are plume-like releases.

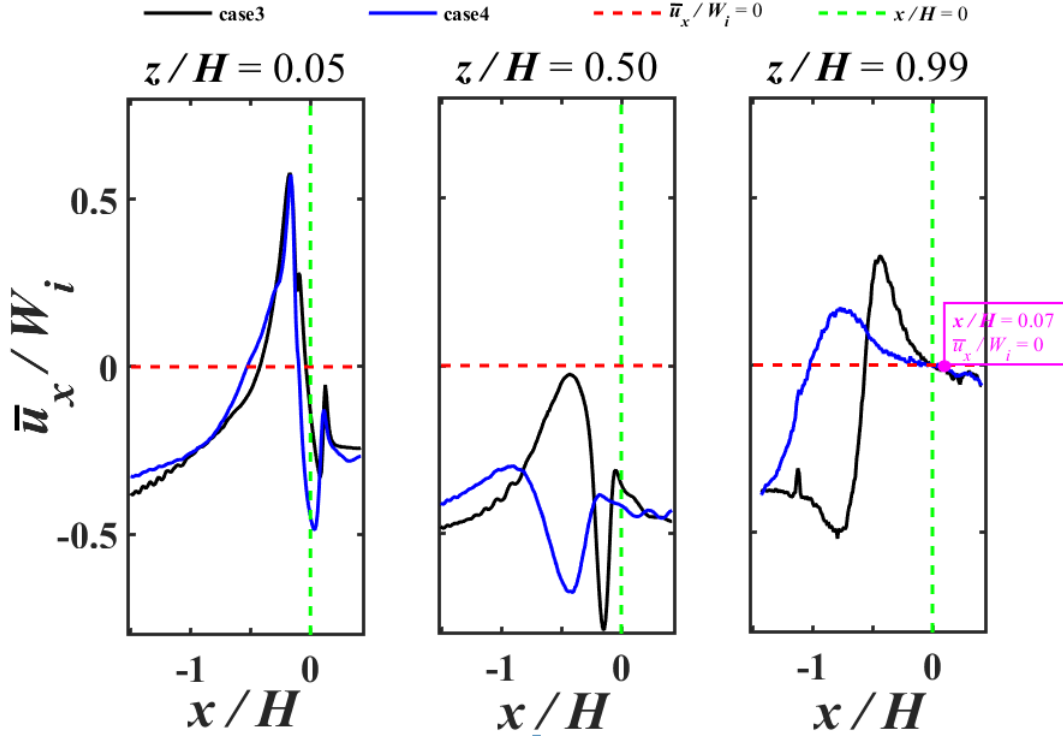


Figure 2.20: Profiles of the non-dimensional longitudinal velocity at $z/H = 0.05$, $z/H = 0.50$ and $z/H = 0.99$ versus the non-dimensional longitudinal distance x/H .

2.4.2.2 Velocity fluctuations

Fig. 2.21 shows the non-dimensional standard deviation of the vertical velocity component (σ_z/W_i) for case3 (Fig. 2.21a) and case4 (Fig. 2.21b). The results show that in the lower part of the tunnel, the vertical fluctuations only develop on the plume boundary, while the smoke flow constituting their core (zone extending from ground level to approximately $z/H = 0.33$ in case3 and to $z/H = 0.10$ in case4) seems to remain laminar. Above these areas, the mixing between the buoyant flow and the ambient flow is significant, resulting in a markedly stronger presence of vertical fluctuations, particularly in the subregion shown in red in Fig. 2.21b. These fluctuations appear only within the main plume, they are negligible in the secondary plume. This is because the longitudinal flow slows down considerably due to its interaction with the buoyant fluid constituting the main plume, resulting in a weak interaction with the second plume. It can also be noted that the thickness of the fluctuation zone is large with low-density releases (i.e. case4). In the upper part of the

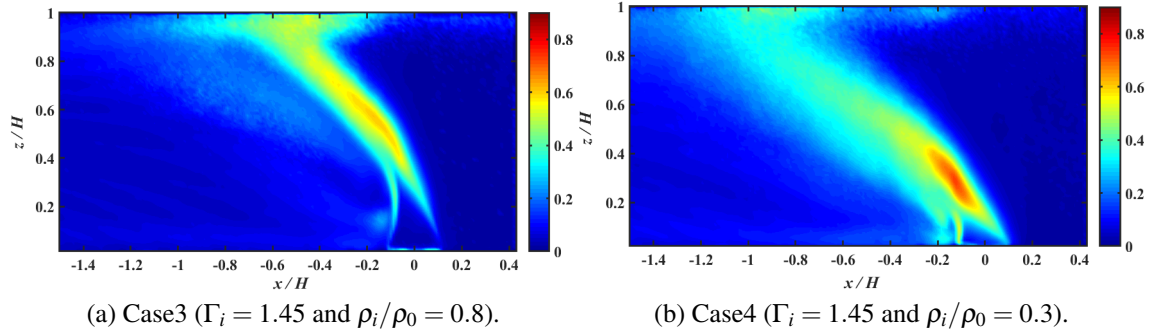


Figure 2.21: Non-dimensional standard deviation of the vertical velocity component σ_z/W_i .

tunnel, the vertical fluctuations remain significant, especially in the case3. The thickness of the fluctuation zones gradually increases to become wider at the ceiling, where the impact between the backflow and the longitudinal ventilation flow seems to be strong. In general, dimensionless vertical fluctuations are greater with lazy plumes than with forced plumes (see Fig. 2.9 and Fig. 2.21). To determine the order of magnitude of these fluctuations, as well as their evolution against the dimensionless longitudinal distance in the case of lazy plumes, some profiles are taken from the two fields of Fig. 2.21 and plotted in Fig. 2.22. In the lower part of the tunnel (i.e. $z/H = 0.30$), we can see the presence of two peaks for case3 (one on each side of the centre of the plume) and a single peak for case4. The magnitude of these peaks is higher in case4, where it reaches a value of 0.71 against 0.42 and 0.39 in case3. This implies that, at this position just above the source, the turbulence is already very significant in the case of a low-density release. For a high-density release, this region appears to be roughly similar to that of forced plume, with the exception of a marked slope of the fluctuation field pattern of the lazy plume. In the centre of the tunnel (i.e. $z/H = 0.60$), the vertical fluctuations become high in case3 and low in case4. Their maximum values reach respectively 59% and 43% of the injection velocity, at the positions 0.2 and 0.5 downstream of the centre of the source. Near the tunnel ceiling (i.e. $z/H = 0.95$), for each case, the maximum value of the fluctuations remains almost identical to that in the centre of the tunnel, but its position moves further downstream of the source. In both cases, the thickness of the areas with large fluctuations is greater at the ceiling of the tunnel, as can be seen clearly in Fig. 2.21. In summary, in the case of buoyancy-driven releases, the variation in vertical velocity component fluctuations depends on the conditions of the source. For low-density releases, the intensity of the fluctuations is higher in the lower part of the tunnel. Its maximum deviates rapidly from the central axis of the source as the rising column rises towards the ceiling. Whereas, for high-density releases, the large fluctuations occur in the upper part of the tunnel and their peaks are less strongly deflected

in the direction of the flow ventilation, compared to those in the forced releases (case1 and case2).

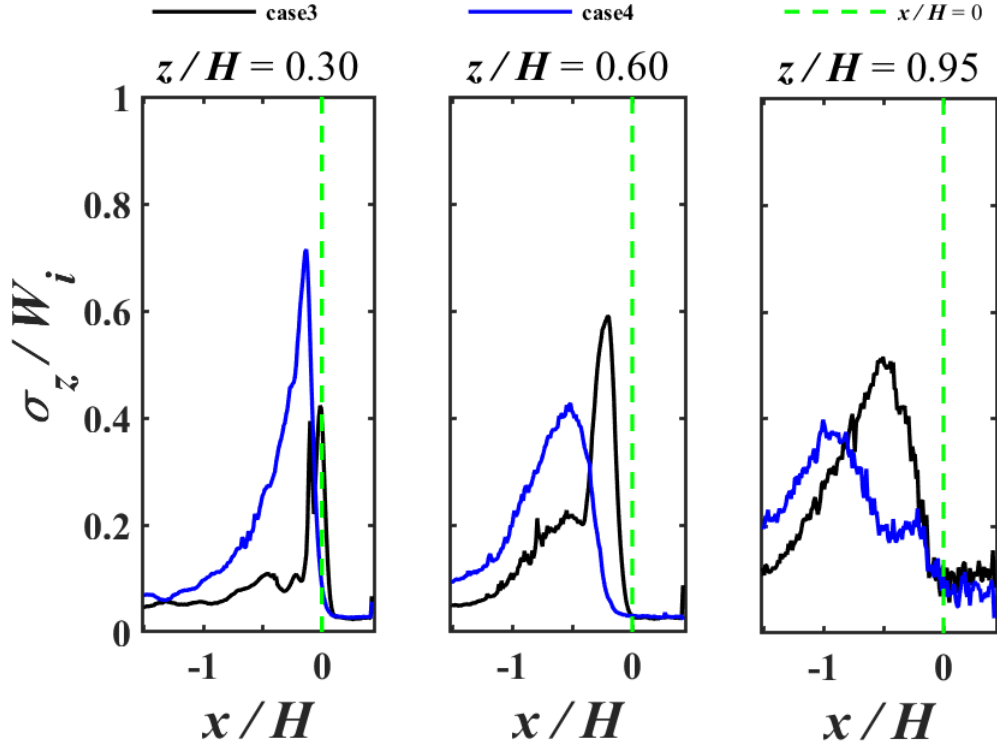


Figure 2.22: Profiles of the non-dimensional standard deviation at $z/H = 0.30$, $z/H = 0.60$ and $z/H = 0.95$ versus the non-dimensional longitudinal distance x/H .

Fig. 2.23 shows the fields of the non-dimensional standard deviation of the longitudinal velocity component (σ_x/W_i) for case3 (Fig. 2.23a) and case4 (Fig. 2.23b). Fig. 2.23a shows that the longitudinal fluctuations in the lower part of the tunnel (i.e. $z/H < 0.38$) are small, except in the plume boundary. Above this position, the turbulence intensity appears to be significant within the buoyant plume. This remains almost constant in the first part (i.e. region between approximately $z/H = 0.38$ and $z/H = 0.62$) and then gradually decreases with increasing vertical distance from the source until z/H is close to 1. At this position (i.e. tunnel ceiling), both the amplitude of the velocity fluctuations and the thickness of the turbulence zone reach their maximum. However, in the other field (corresponding to a low-density release), Fig. 2.23b shows that the longitudinal velocity fluctuations are higher in the lower part of the tunnel (i.e. the region between $z/H = 0.15$ and $z/H = 0.30$), especially on the left-hand side of the plume. This corresponds to the interaction zone between the recirculation flow and the buoyant plume rising from the source, with instabilities developing

on the left side of the plume perimeter. In this part of the tunnel, the thickness of the high turbulence zone is greater than that of the previous case. Above this zone (i.e. $z/H > 0.30$), the turbulence intensity is less pronounced and decreases rapidly with height until z/H is close to 0.95. At this position, the velocity fluctuations become relatively high and extend over a considerable longitudinal distance near the tunnel ceiling.

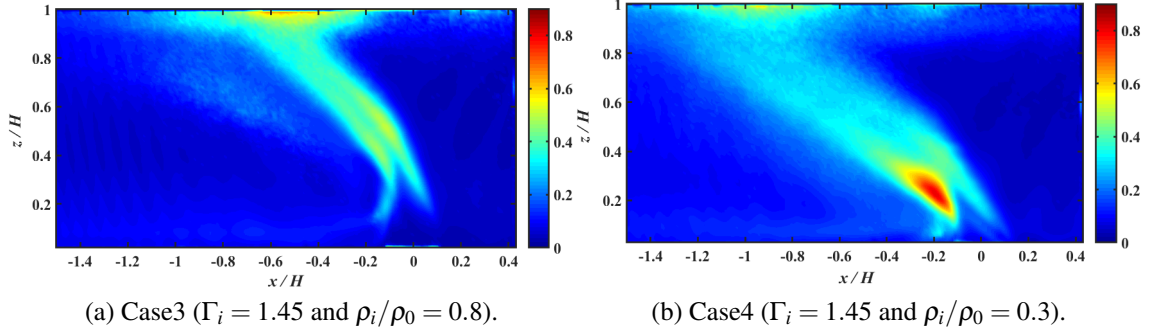


Figure 2.23: Non-dimensional standard deviation of the longitudinal velocity component σ_x/W_i .

Fig. 2.24 shows non-dimensionalised profiles of the standard deviation σ_x/W_i against the longitudinal distance x/H for both cases (case3 and case4). At $z/H = 0.25$, the maximum turbulence intensity is 0.76 in case4 and 0.3 in case3 (value reached at each of the two peaks). The difference between these two magnitudes is large, once again indicating the high interaction between the ambient air flow and the buoyant flow of the low-density releases in the lower part of the tunnel. On the left side of these peaks, the velocity fluctuations decrease rapidly in case3 to reach an almost stable value of 0.08. While in case4, the profile decreases rapidly from $\sigma_x/W_i = 0.76$ to $\sigma_x/W_i = 0.25$ in the range $-0.38 < x/H < -0.22$ and progressively in the range $-1.0 < x/H < -0.38$ to reaches its final value of about 0.1. This result implies, again, the presence of mixing between the smoke constituting the secondary plume and the ambient air. In the centre of the tunnel (i.e. $z/H = 0.50$), the profiles are similar in form to those of the vertical velocity fluctuations, the maximum amplitude of the longitudinal velocity fluctuations is obtained with case3 at a position closer to the central axis of the source than that in case4. The value of the maximum dimensionless fluctuations reaches 0.5 at $x/H = -0.11$ in case3 and 0.34 at $x/H = -0.57$ in case4. Near the tunnel ceiling (i.e. $z/H = 0.98$), for each case, the maximum of the non-dimensional vertical fluctuations is slightly increased in magnitude compared to that obtained in the centre of the tunnel: it reaches 0.58 in case3 and 0.5 in case4. This is the effect of the excess of momentum flux of the buoyant backflow at the tunnel ceiling, generating an increased interaction with the momentum flux imposed by the ventilation flow, and therefore large fluctuations in longitudinal

velocity. It is important to note that the maximum fluctuations of both velocity components are very significant in the plumes (i.e. buoyancy-driven releases) compared to the jets (i.e. momentum-driven releases).

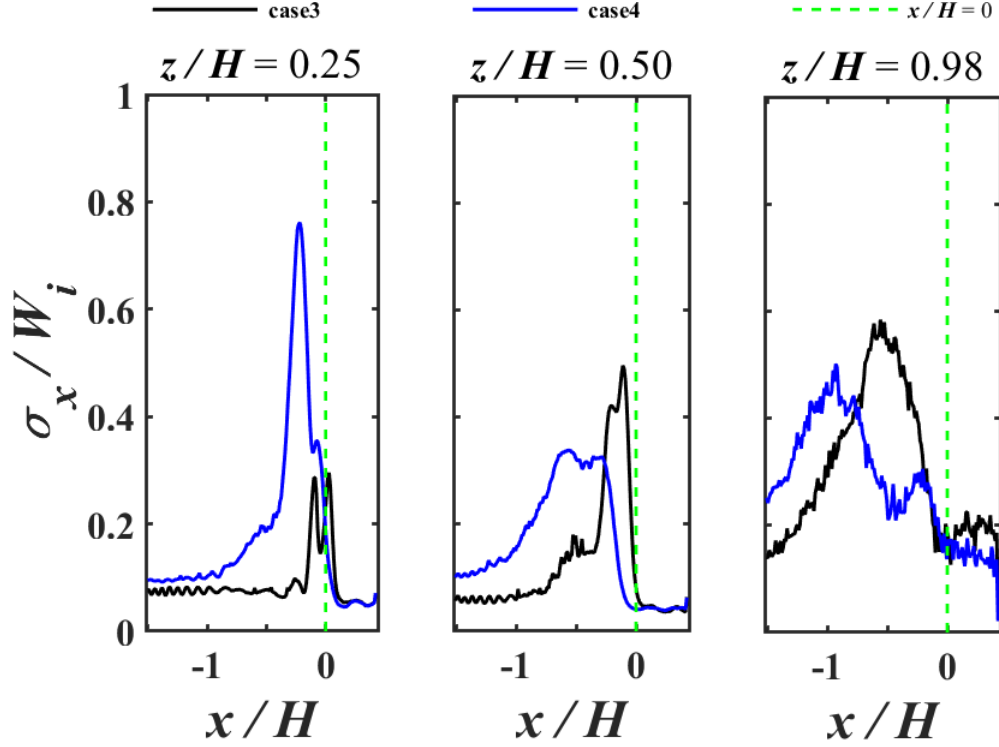


Figure 2.24: Profiles of the non-dimensional standard deviation at $z/H = 0.25$, $z/H = 0.50$ and $z/H = 0.98$ versus the non-dimensional longitudinal distance x/H .

Fig. 2.25 shows the results of the dimensionless Reynolds shear stress (σ_{xz}/W_i^2) for case3 (Fig. 2.25a) and case4 (Fig. 2.25b). Fig. 2.25a shows that, in the lower part of the tunnel ($z/H = 0.20$), the Reynolds shear stress is very low. From $z/H = 0.20$ to about $z/H = 0.35$, the shear layer develops at the edges of the main plume and the magnitude of the shear stress seems to be slightly higher on the left boundary of the plume. This may be due to a high shear between the recirculation flow and the buoyant flow, thereby causing an increase in entrainment of ambient fluid into the plume. From approximately $z/H = 0.35$ to $z/H = 0.65$, the correlations between the fluctuations of the two velocity components increase in amplitude on the right edge of the plume and the shear layers continue to expand on the perimeter of the main plume, then penetrate into its core. In this region, the turbulent shear stresses are high, which implies that the cross-stream transport of momentum, and therefore entrainment, is considerable. Above $z/H = 0.65$, σ_{xz}/W_i^2 decreases rapidly with

the height until reaching low values at the tunnel ceiling. The same overall behaviour can be observed in case4 (Fig. 2.25b) but in different regions from those observed for case3. About $z/H = 0.05$ above the source, the fluctuations of the velocity components appear to be well correlated, in particular on the left-side plume boundary (the lighter blue area extending to $z/H = 0.22$). These can also be due to entrainment of the recirculation flow into the buoyant plume rising from the source. The red area shows that the shear layers appear in the main plume and in the interface between the main plume and the secondary plume. Concerning the main plume (red zone in the right-hand side of the blue zone), the shear layers first develop at the edges of the plume and the amplitude of the turbulent shear stress increases progressively with increasing distance from the source. At approximately $z/H = 0.25$, the shear layers completely penetrate into the plume core due to the increased entrainment and turbulent mixing between the buoyant flow and the ambient air, resulting in an increase in the spreading rate and eventually destroying the buoyant plume. In the second plume (red zone in the left-hand side of the blue zone), the magnitude of the correlations between the fluctuations of the two velocity components is maximal from about $z/H = 0.10$ to $z/H = 0.30$, which indicates the presence of high shear stresses between the surfaces in direct contact of the two plumes. Above $z/H = 0.55$, the shear level becomes almost low throughout the field.

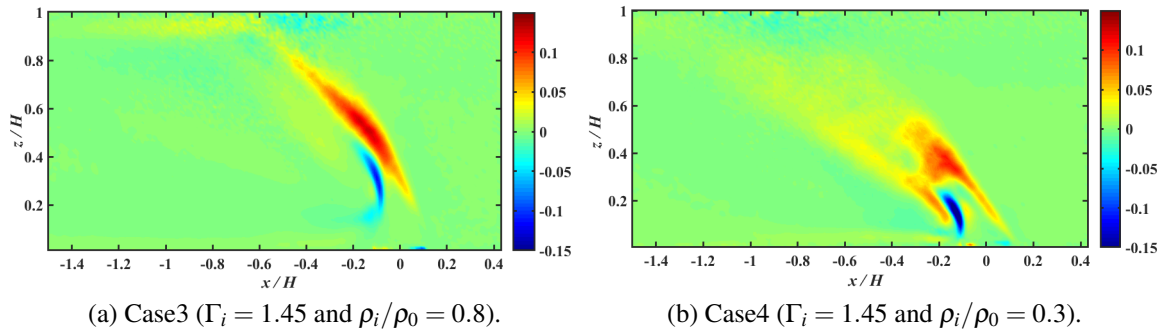


Figure 2.25: Fields of non-dimensional Reynolds shear stress σ_{xz}/W_i^2 .

Fig. 2.26 shows the profiles of the dimensionless Reynolds shear stress, σ_{xz}/W_i^2 , measured at three different heights, z/H , against the scaled longitudinal distance x/H . At $z/H = 0.15$, the profiles show three positive peaks and one negative peak in case4. From right to left, the first peak is at the right edge of the plume, the second and third at the left edge of the plume, while the last positive peak is at the interface between the main plume and the secondary plume. The magnitude of these peaks is high, particularly at the left edge of the plume where the absolute value of the negative peak is equal to 0.19. At $z/H = 0.35$, the profiles show two peaks in case3, one on each side of the plume boundary and two peaks

in case4, one in the core of the main plume and the other at the interface between the main plume and the secondary plume. In case3, the absolute value of the peaks is higher at the left side of the plume compared to the right side (0.1 versus 0.07). In case4, the maximum value of σ_{xz}/W_i^2 is reached in the core of the plume where it is equal to 0.1 against 0.03 at the interface between the plumes. At $z/H = 0.55$, the magnitude of the shear stress decreases in case4 and increases in case3, its maximum value is 0.03 in case4 and 0.12 in case3 and is reached in the core of each main plume.

In summary, for a low-density release, Reynolds shear stresses and turbulence intensities are significant immediately above the source, in particular at the left edge of the plume. As the plume rises from the source, the ambient fluid is entrained into its core, resulting in an increase in the turbulent mixing process. This occurs in the lower half of the tunnel and extends up to the centre of the tunnel, from which the shear stress rapidly becomes negligible. In the case of a high-density release, the shear stress increases with the height in the lower half of the tunnel. It reaches its maximum in the centre of the tunnel where the ambient flow is entrained into the core of the plume. In the upper half, the shear stress first remains significant then decreases rapidly to reach low values near the ceiling.

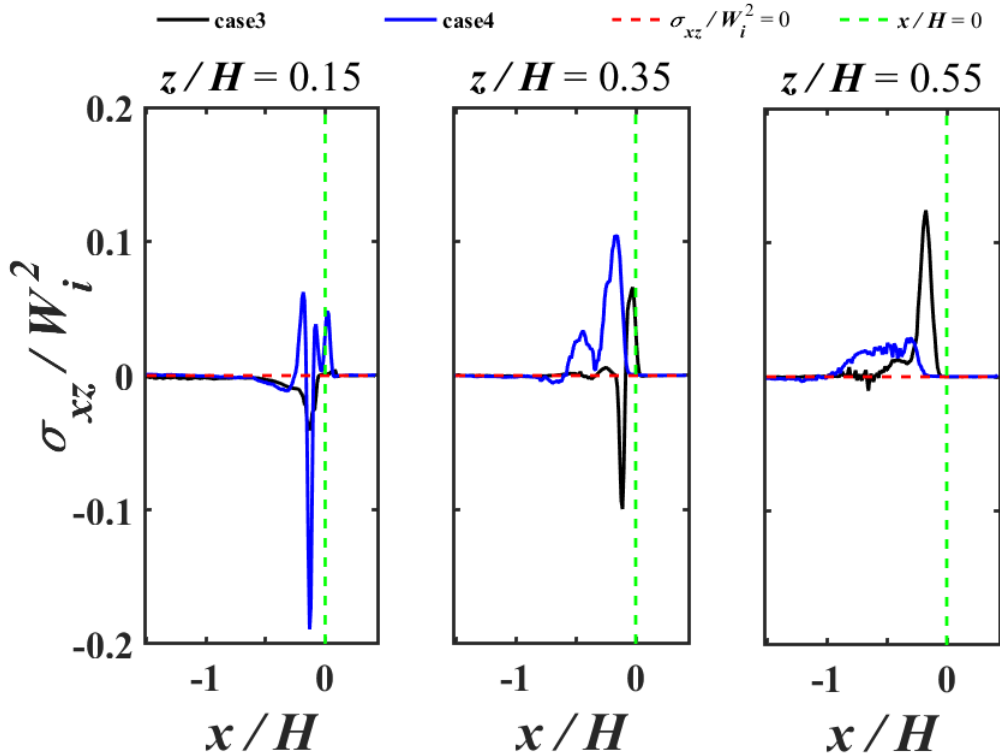


Figure 2.26: Profiles of the dimensionless correlations between vertical and longitudinal velocity fluctuations at $z/H = 0.15$, $z/H = 0.35$ and $z/H = 0.55$ versus the non-dimensional longitudinal distance x/H .

The results show that the magnitude of σ_{xz}/W_i^2 obtained with lazy plumes are greater than those obtained with forced plumes. This implies that, for a lazy plume, buoyancy acts to enhance entrainment and turbulence in the shear layer and therefore the mixing of ambient flow into the plume.

2.5 Conclusions

In this study, an experimental investigation on the behaviour of continuous buoyant releases in a reduced scale tunnel, using particle image velocimetry (PIV), was carried out. The aim was to study, in the critical ventilation conditions, the non-Boussinesq effects on the dynamics of the forced and lazy plumes. For this purpose, four different tests were conducted (two tests for each type of plume) by varying the values of the density ratio ρ_i/ρ_0 and setting the other two control parameters at the source (i.e. the plume Richardson number Γ_i and the ratio between the source diameter and the tunnel height D_i/H). For each test, 2000 instantaneous velocity fields were acquired from which the statistics of the mean and fluctuating flow components were computed. For each plume, discussions and comparisons between the test results are performed.

The velocity field of the vertical component showed that the shape of the upward forced plumes is slightly affected by the longitudinal ventilation flow. Their centre of mass is first located at the central axis of the source throughout the lower half of the tunnel, then gradually moved downstream as the rising column raised to the ceiling. On the other hand, the lazy plumes are more affected by the longitudinal flow. Their shape is deflected immediately above the source in the same direction as the ventilation flow, especially in the case of a low-density release. This results in a sort of secondary plume, detached from the main plume, which widens as it moves away from the separation zone.

The longitudinal velocity field showed that the two forced plumes impinge the tunnel ceiling almost at the same point, located at approximately $H/5$ downstream from the centre of the source. The position of the impingement point for the lazy plume is instead located further downstream of the source and depends on the density ratio: the lower the density ratio, the more the impingement point is displaced further downstream. As previously reported by Jiang et al. [31], the results showed that the dimensionless critical velocity depends on the density ratio only in the case of forced momentum-dominated releases.

In order to explain this dependence and to reveal further interesting features of the plumes, we analysed the second moments of the turbulent velocity fields. The results showed that the magnitude of the non-dimensionalised standard deviation of both velocity components and, therefore, the level of the turbulent intensity is higher in lazy plumes than

in forced plumes. For each type of plume, the turbulent intensities first appear in the plume boundary then into its core, and extend to the tunnel ceiling with lazy releases. Their evolution against the height varies with the type of plume and the density ratio. In addition, the results showed that the amplitude of the Reynolds shear stress is significant with buoyancy-dominated releases. For forced plumes, the shear layers only develop at the edges of the plume. For lazy plumes, the shear layers first appear on the plume boundary and then penetrate into its core. These findings suggest that the buoyancy produces the vorticity which acts to enhance entrainment and turbulence in the shear layer and therefore the turbulent mixing process by which the ambient flow penetrates into the plume. Consequently, the dilution rate of the light-gas release in ambient air increases as the lazy plume rises toward the ceiling. Upon reaching the ceiling, the plume loses information on its source conditions, in particular its density [43], which results in independence between the dimensionless critical velocity and the density ratio. This is not the case with the jet-like releases because of the low turbulent entrainment of ambient fluid compared to the plumes.

CHAPTER 3

THE EFFECTS OF SOLID BARRIERS AND BLOCKS ON THE PROPAGATION OF SMOKE WITHIN LONGITUDINALLY VENTILATED TUNNELS

A series of experiments were conducted to investigate the effect of solid barriers, placed at the tunnel ceiling, on the behaviour of smoke in fire events within longitudinally ventilated tunnels, namely on the smoke back-layering lengths and on the critical velocity. For this purpose, we considered two types of barrier: "small barriers" designed to be fixed in place and "large barriers" designed to be mobile in real tunnels. The study was carried out in a small scale tunnel, by simulating fire smokes with a light gas mixture of air and helium. Experiments were performed with and without blocks within the tunnel, representing vehicles. Results show that the presence of barriers and/or blocks prevents the smoke back-layering flow, therefore reducing the critical velocity. The reduction rate of the latter depends on the blocking rate created by the obstacles (barriers, blocks or both) located just upstream of the source. Further experiments were conducted to investigate the effects of blockages on pressure losses inside the tunnel. The results reveal a proportionality between head losses and height of barriers, and between pressure drops and size of the blocks. When both blocks and barriers are present, the pressure losses induced by the small barriers are very high compared to those induced by the large barriers, especially in the tunnel with large blocks. These findings suggest that large barriers are more effective than small ones because they prevent the smoke back-layering at very low critical velocities and they induce less pressure losses in congested tunnels.

Keywords: Tunnel ventilation, Solid barriers, Blocks, Buoyant plume, Back-layering, Critical velocity, Pressure losses.

3.1 Introduction

After the recent violent fires in road tunnels, such as the tragic fire that occurred in the Mont-Blanc tunnel between France and Italy (1999, 39 dead), road tunnel safety has become a national and international issue. In France, since 1999, legislation and regulations concerning the construction and operation of road tunnels have therefore been revised with a view to improving safety. Recently, many studies have been conducted on tunnel fires, either in large-scale tunnel tests or in small-scale thermal and densimetric models. Most of these studies concerned the control of smoke flow in the tunnel fires [21, 22, 44–48], the evaluation of the critical velocity and smoke back-layering flow length [49–56], the determination of the power or the heat release rate (HRR) of the fire inside road tunnels [57–62] and the aerodynamics of buoyant releases within a longitudinally ventilated tunnel [25, 32, 33, 47, 63].

In the instance of a fire in a tunnel, smoke control is often the most important part of emergency planning. Ventilation systems are one of the main protective measures to be adopted to prevent the spread of smoke upstream of the fire. They allow tunnel users to ensure their own safety in reaching the refuges and provide better access to fight the fire. If the ventilation velocity is low, the smoke produced by the fire may move upstream of the fire. This phenomenon is called ‘back-layering’ and appears when the ventilation velocity is lower than the “critical velocity” [64], which is defined as the minimum ventilation velocity able to ensure all the combustion products remain downstream of the fire source in the tunnel.

Other than the heat release rate, many parameters are involved in the determination of the critical velocity, including heat transfer processes [26, 27], the tunnel geometry [22, 48, 52], the positions of the fans and the size of the fire [51, 55]. Despite the evident complexity of the physical system, the values of the critical velocities, against the HRR, can be controlled using different strategies. One approach is that of using fixed solid barriers at the tunnel ceiling, which can prevent the spread of fire and smoke upstream of the source, even for low ventilation velocities. In other words, by combining this strategy with the longitudinal ventilation, the local longitudinal velocity increases in the tunnel cross-section area where the barrier is installed. Therefore, a slower ventilation flow, compared to that in a empty tunnel, would be sufficient to prevent smoke from spreading upstream of the fire. This strategy could be then effective in improving the safety of people and firefighters upstream of the fire, since a large proportion of the smoke should be blocked near the ceiling.

Öttl et al. [65] tested a new system in the 5400 m long Katschberg tunnel (Austria), which consists of a new developed synthetic material in the form of curtains. Their ex-

periments revealed that the new system is effective in controlling the smoke propagation at low longitudinal air velocity. A systematic investigation on the use of flexible devices for controlling smoke and fire propagation in road tunnels was carried out by Bettelini and Rigert [66, 67]. Their numerical results show that flexible smoke curtains in longitudinally ventilated road tunnels allows the critical velocity to be reduced. They concluded that this application offers important benefits in terms of controlling smoke. The effect of fixed smoke barriers on the evacuation environment in road tunnel fires with natural ventilation was investigated by Seike et al. [68] using CFD simulation. Their results show that smoke barriers help stop the propagation of the smoke and improve safety in tunnel fires.

In the perspective of evaluating the role of the blocking effect induced by barriers at the tunnel ceiling, it is also important to consider the blocking effect induced by the presence of vehicles within the tunnel. In fact, the size and density of these vehicles affect the longitudinal ventilation flow and therefore the dependence of the critical velocity on the heat release rates (HRR). To date, several authors have studied the effects of vehicle blockages on smoke propagation upstream of fire and on critical velocities in longitudinally ventilated tunnels. An initial study on the effects of vehicular blockages on critical velocities was performed by Oka and Atkinson [21] who placed propane gas burners above solid blocks of broken vehicles in reduced scale experiments. They concluded that solid blockages near the fire result in a reduction of the critical velocity. Lee and Tsai [69] conducted small-scale experiments and numerical simulations considering three vehicles types in different arrays, positioned upstream of the fires. Fires were located first on the tunnel centre line and then downstream of vehicle obstructions. They found that the critical velocity decreased due to vehicular obstruction when the ventilation flow reached fires directly, with a reduction ratio approximately equal to the vehicle blockage ratio. On the contrary, they showed that the critical velocity increased when the vehicle obstructions did not allow the ventilation flow to directly reach the fires. These general tendencies were then further confirmed by Tang et al. [70], Rojas Alva et al. [71] and Jiang [43]. Tang et al. [70], who conducted experiments by placing a block upstream of a porous burner source on the centreline of the tunnel and varying the relative distance between the block and fire source. Rojas Alva et al. [71] conducted an experimental study, in a small-scale tunnel model in which the buoyant plume is modelled with an air/helium mixture, using three sizes of vehicular obstacles and considering different arrays and various positions of the fire source along the tunnel width. Jiang [43] simulated the fire source by means of a densimetric plume and considered different configurations, so that the buoyant source was placed downstream either directly behind the vehicles or behind the spacing between the vehicles. He further showed that the critical velocity is affected only by the block located close to the fire source, while the effect of

the other blocks located further upstream is negligible. Besides that, Gannouni and Maad [72] performed numerical simulations of fires in a longitudinal ventilation tunnel to study the effect of the blockage on the critical velocity and the backflow length by varying the distance between the bottom of the obstacle and the tunnel floor. Their results shows that the reduction in the critical velocity is slightly higher with increasing distance between the bottom of the obstacle and the tunnel floor. Based small-scale experimental results, Zhang et al. [73] proposed a physical model to predict the length of the smoke back-layering under the blockage effect of metro train in subway tunnel.

The aim of this work is to analyse experimentally the effects of solid barriers placed at the tunnel ceiling on the propagation of smoke in the instance of a fire within longitudinally ventilated tunnels. In the experiments, the hot smokes are simulated by releases of light fluid, which have been shown [27] to induce ventilation conditions that are similar to those induced by the presence of a fire (provided that its flames do not exceed the tunnel half height).

We consider two types of barriers: small fixed barriers with a height equal to $H/10$ (H is the tunnel height) and larger but mobile barriers with a height equal to $H/4$ and $H/3$. Unlike fixed ones, mobile barriers are deployed only in the event of fire and placed upstream of the source in longitudinal ventilation.

This work is split into two parts. In the first part, we evaluate the effects of barriers on the spread of smoke upstream of the fire source in the tunnel. In the second part, we examine the effects of these barriers on pressure drops. In both parts, we carry out the study, first in an empty tunnel (without vehicles), then in a tunnel with vehicles placed upstream of the source. Vehicles are modelled by blocks of three different sizes; small, medium and large blocks which could represent approximately small cars, lorries and Heavy Goods Vehicles in real tunnels, respectively. Conclusions are drawn regarding the effectiveness of the barriers to control the propagation of smoke by evaluating the results of both parts.

3.2 Experimental set-up

The experiments have been performed with a densimetric reduced scale model of a tunnel (see Fig. 3.1), in which the fire-induced smoke is represented by a continuous release of a light fluid, a mixture of air and helium. The tunnel model, whose scale can be considered in the range between $1/25$ and $1/30$ of a real scale tunnel, is the LMFA (Laboratoire de Mécanique des Fluides et d'Acoustique) laboratory, consists of a 8.4 m long channel with a rectangular cross-section of 0.36 m wide and 0.18 m high. The rear wall is made of 19 mm thick chipboard panels and the side wall is made of toughened glass which allows

3.2 Experimental set-up

visualisation of the flow coming from the source. The floor and ceiling are made of 19 mm panels Medium Density Fiberboard (MDF). To induce a longitudinal air flow, the tunnel is equipped with an extraction fan at its end, which can generate a varied airflow between 20 and 355 m³/h. A potentiometer is wired to this fan to control its speed. The ventilation velocity inside the tunnel is measured by means of a Pitot tube placed within an airflow cone at the tunnel inlet, which has been calibrated before being placed in the tunnel. The buoyant source is modelled by a densimetric plume [27], mixture of air and helium. The flow rates of air and helium are controlled independently and measured by two flow metres. The light plume is released from a circular source with a diameter of $D_i = 0.1$ m. The top surface of the source is set flush with the floor on the axis of the tunnel, and placed at a distance of 4.55 m from the tunnel inlet. The mixture of air and helium is seeded with oil particles before being injected in the plenum. These particles or tracers diffuse the intense light of the laser sheet emitted by a lens placed at the inlet box of the tunnel. This technique reveals a two-dimensional slice of the flow in the area of interest inside the tunnel. The air flow that is used for seeding is controlled by a flow meter. This is taken into account and added to the mixing flow of air and helium to determine the conditions at the source, i.e. density and velocity. Compared to the mixture of air-helium flow, the air flow used for seeding is very low, which implies that the mass of oil added to seed does not affect the density of the mixture.

The plume density at the source (ρ_i) is:

$$\rho_i = X_0\rho_0 + X_{he}\rho_{he} \quad (3.1)$$

where ρ_0 is the density of air, ρ_{he} is the density of helium and X_0 , X_{he} , are the volume fractions of air and helium, respectively given by:

$$X_0 = \frac{q_0}{q_i} = \frac{\rho_i - \rho_{he}}{\rho_0 - \rho_{he}}, \quad X_{he} = \frac{q_{he}}{q_i} = \frac{\rho_0 - \rho_i}{\rho_0 - \rho_{he}} \quad (3.2)$$

where $q_i = q_0 + q_{he}$ the volume flow defined by the sum of the two volume flows of air (q_0) and helium (q_{he}).

We have produced a variety of light fluid releases, with different buoyancy flux values $B_i = gq_i \frac{\rho_0 - \rho_i}{\rho_0}$ (g is the gravitational acceleration) in the range $0.0139 < B_i(\text{m}^4/\text{s}^3) < 0.062$. These releases are characterised by a varying plume Richardson number larger than unity. The latter is defined as:

$$\Gamma_i = \frac{5}{16\alpha} \frac{(\rho_0 - \rho_i)g}{\rho_0} \frac{D_i}{W_i^2} \quad (3.3)$$

3.2 Experimental set-up

where $W_i = \frac{4q_i}{\pi D_i^2}$ is the velocity at the source and $\alpha = 0.127$ is a reference entrainment coefficient [32]. The value of the plume Richardson number allows for a classification of different plume typology [32, 33]. A plume with $\Gamma_i < 1$ is referred to a "forced" plume, whose dynamics are momentum dominated, whereas a plume with $\Gamma_i > 1$, whose dynamics are dominated by the role of buoyancy, is said to be "lazy". The condition $\Gamma_i = 1$ corresponds instead to a "pure" plume, in which buoyancy and momentum effects are in balance. As shown by Jiang et al. [27] the back flow of light fluid at the ceiling induced by a lazy plume accurately reproduces the behaviour of hot smokes produced by a fire with flames whose length does not exceed the tunnel half height. The experimental tests were therefore carried out for lazy plumes, where $\Gamma_i = 2, 4, 6, 8$ and 10 . The density ratio was fixed and equal to $\rho_i/\rho_0 = 0.7$. As shown by Salizzoni et al. [26], its variations do not affect the dynamics of buoyancy generated releases.

An initial investigation concerns the influence of the longitudinal ventilation velocities on the buoyant fluid propagation inside the tunnel without barriers. The measurements

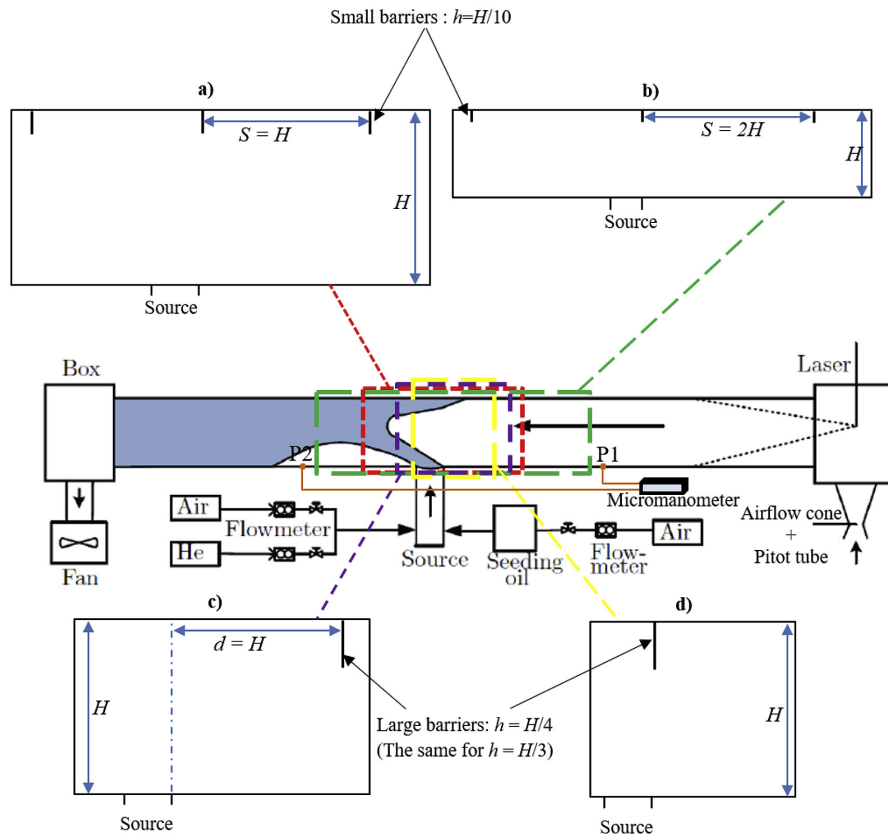


Figure 3.1: Schematic of the experimental setup with barriers fixed at the tunnel ceiling. h is the height of barrier, d is the distance between the source and the large barrier and S is the distance between each two adjacent small barriers.

consist of determining the length of back-layering flow inside the tunnel, by means of flow visualisation, against the longitudinal airflow. For each value of the plume Richardson number, the critical velocities are reached by increasing the ventilation velocities until the back-layering flow disappears.

To investigate the effect of barriers, two types of barriers were tested, small and large barriers. The barriers are solid and their width is equal to the tunnel width. The small barriers have a height equal to $1/10$ the tunnel height. They are fixed at the tunnel ceiling over a distance that ranges from 2.4 to 5.4 meters (i.e. 2.15 m upstream of the source and 0.75 m in downstream of the source). The barriers are placed so that one of these is fixed just upstream of the source. Two configurations are tested, in the first, all the barriers are placed so that $S = H$ (Fig. 3.1a) and in the second $S = 2H$ (Fig. 3.1b), where S is the distance between each two adjacent barriers. For the large barriers only one barrier will be fixed to the tunnel ceiling, we choose two heights $H/4$ and $H/3$. For each case, the barrier is initially placed just upstream of the source (Fig. 3.1d) and then placed at a distance equal to the tunnel height upstream of the source, i.e. $d = H$ (Fig. 3.1c).

The flow was illuminated by a laser sheet emitted by a lens installed at the tunnel inlet. In the laser sheet technique, the buoyant mixture is seeded with nebulised oil particles. A thin sheet of light is then introduced in the same direction of flow, illuminating the seed particles. The image of the flow thus illuminated is then recorded using a camera. By adjusting the fan power, we can determine the critical velocities and the back-layering lengths of each tested longitudinal ventilation velocity. Typical critical ventilation conditions for a tunnel

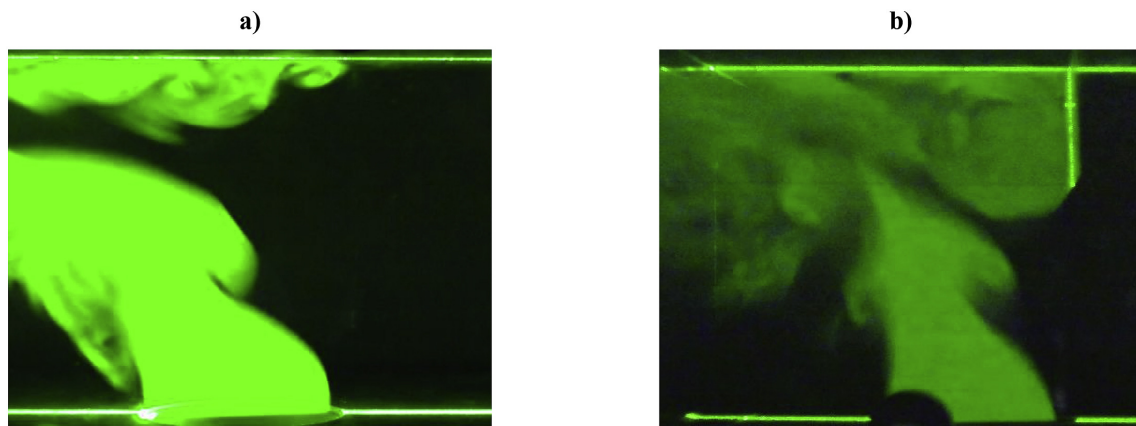


Figure 3.2: Critical ventilation condition with $\Gamma_i = 2$. a) Tunnel without barriers ($U_{0,cr} = 0.256$ m/s). b) Tunnel with a largest barrier of height $H/3$ placed just upstream of the source ($U_{0,cr} = 0.143$ m/s).

with the largest barrier ($H/3$) and tunnel without barriers are shown in Fig. 3.2b and Fig.

3.2 Experimental set-up

3.2a, respectively. Both flow visualisations are taken with the same source conditions, but at different critical conditions. The critical velocity, $U_{0,cr}$, measured in the case without barrier is equal to 0.25 m/s, while that measured in the tunnel with barrier is equal to 0.14 m/s. This means that the large barrier ($H/3$) can prevent the smoke back-layer at a reduced critical ventilation velocity. In this case: $U_{0,cr \text{ with barrier}} \approx 0.56 U_{0,cr \text{ without barrier}}$, which means that the reduction of the critical velocity is about 44%.

Note that the interaction between the longitudinal flow and the smoke plume exhibits fluctuations implying uncertainties in the visual estimates of smoke back-layering length. These uncertainties are estimated to equal approximately 10% of the value of measured back-layer length.

In order to simulate the effect of vehicles on the smoke propagation, we examined three kinds of cubic blocks: cubes with dimensions 0.05 m (block1), 0.08 m (block2) and 0.12 m (block3). Blocks 1, 2 and 3 may represent approximately small vehicles, lorries and Heavy Goods Vehicles (HGVs), respectively, in the real tunnels. Fig. 3.3 shows a schematic

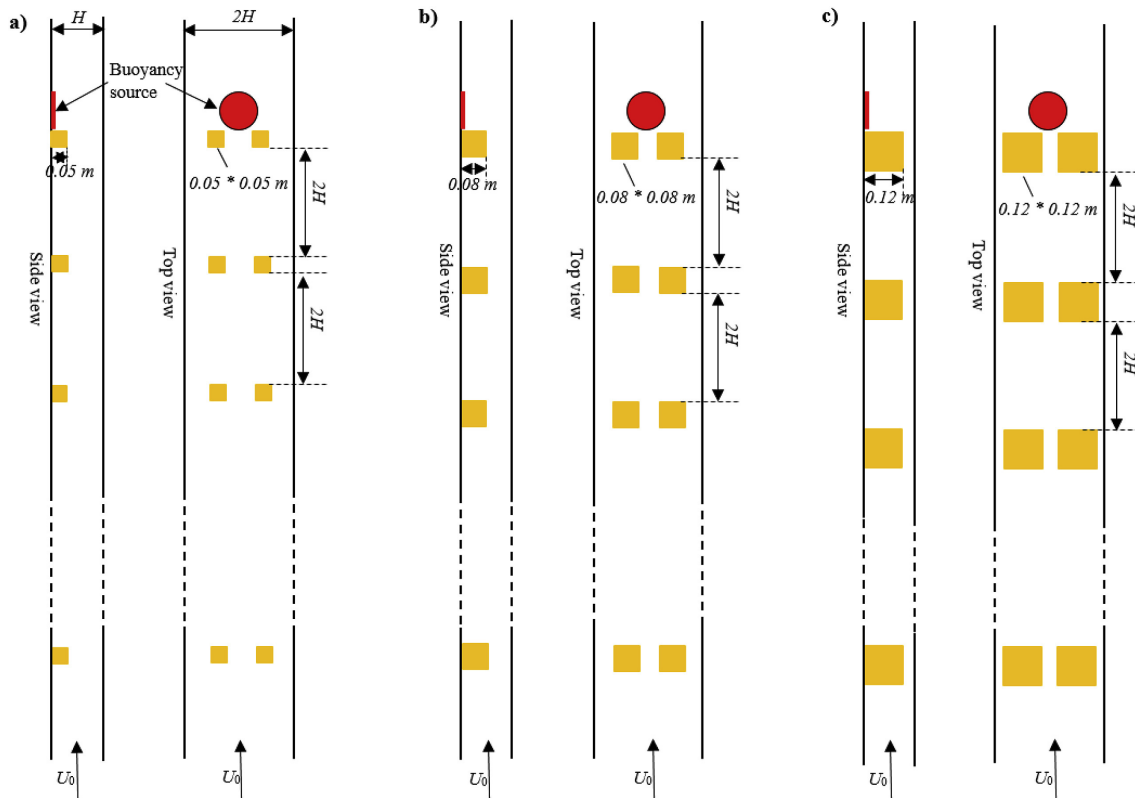


Figure 3.3: The block locations in the experiment. a) Block1: 0.05 m^3 . b) Block2: 0.08 m^3 . c) Block3: 0.12 m^3 . We keep the same configuration of blocks in the case of a tunnel with barriers fixed to the ceiling.

diagram of the top view and the side view in the tunnel cross-section of block locations in the experiment. For each set of blocks, we consider only one configuration in which two rows of blocks were placed at the sides upstream of the source. The aim is to represent the case of unidirectional tunnels which might be used for two-lane traffic.

In order to evaluate the effect of traffic congestion in the tunnels, we do the experiments with a variable number of pairs of blocks ranging from one to six for large blocks, from one to seven for medium blocks and from one to eight for small blocks. In these experiments, the Richardson number at the source was set to 2 and the density ratio was set to 0.7.

In order to assess the impact of the distance between the source and the position of the blocks, we first placed all the blocks in such a way that the last pair is positioned just upstream of the source, then for each successive test the pair of blocks closest to the source is removed. The distance between each pair of blocks remains constant along the two lanes and is equal to $2H$.

We performed experiments with and without barriers, with the configurations sketched in Fig. 3.1. However, for large barriers only the case where the barrier is placed just upstream of the source is presented as we only want to study their effects on the critical velocities in the presence of vehicular blockage. The barriers also represent a blockage entailing a reduction of the tunnel cross-section (see Fig. 3.4b).

In what follows both the effect of barriers and blocks will be considered as a function of their blockage ratio, defined as the ratio between the cross section occupied by the obstacle and the cross section of the tunnel. This ratio can be linked to an equivalent increase ratio of the local critical velocity. To enlighten this we define $U_{0,1}$, A_1 , the flow velocities and tunnel cross sectional areas at position (1), i.e. away from the block and $U_{0,2}$, A_2 , the flow velocities and tunnel cross sectional areas at position (2), where the block is placed (see Fig. 3.4a). The tunnel blockage rate is given by $\varphi = (A_1 - A_2) / A_1$. Since the volume flow

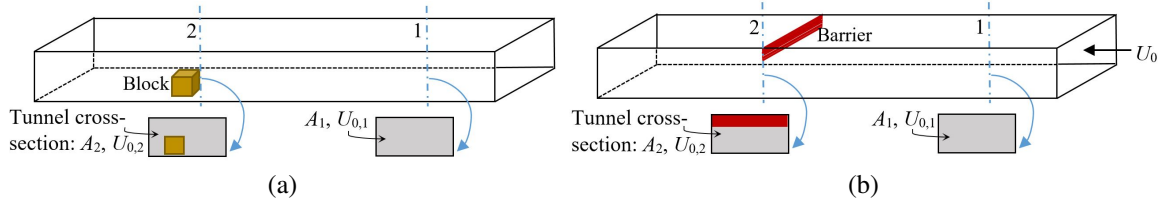


Figure 3.4: Schematic representations of obstacles placed in tunnel of rectangular cross-section. Obstacle is represented by a block in figure (a) and by a barrier in figure (b). A_1 , $U_{0,1}$, A_2 , $U_{0,2}$ are the relative flow velocities and tunnel cross-sectional area (in grey).

conservation implies that: $U_{0,1}A_1 = U_{0,2}A_2$, we can evaluate an equivalent ratio between the

3.3 Effect on backlayering and critical velocity

local critical velocity $U_{0,2}$ and that in the empty tunnel $U_{0,1}$ as:

$$\frac{U_{0,1}}{U_{0,2}} = \frac{A_2}{A_1} \quad (3.4)$$

In Table 3.1, we summarise the obstacle-induced blocking rates of all the possible combinations of blocks and barriers placed on the same cross-section.

Table 3.1: Blockage rates induced by blocks and barriers.

	Without barriers	Barrier with height $H/10$	Barrier with height $H/4$	Barrier with height $H/3$
Without blocks	00%	10%	25%	33%
Pair of block1	08%	18%	33%	41%
Pair of block2	20%	30%	45%	53%
Pair of block3	44%	54%	69%	77%

Note that the blocking rates induced by the presence, on the same cross section, of larger blocks (block3) and large barriers ($H/4$ or $H/3$), i.e. 69% and 77%, respectively, are significantly higher compared to all others. Therefore, we placed the last pair of block3 slightly behind the large barrier at a distance of about one centimetre. The aim is to both slightly reduce the blockage ratio and potentially avoid contact between the barrier and the blocks.

3.3 Effect on backlayering and critical velocity

Our aim is to clarify the effect of solid barriers placed at the tunnel ceiling on the propagation of smoke upstream of the source in a longitudinally ventilated tunnel. In particular, two aspects are studied:

- Effects of barriers on the extension of smoke back-layer according to source conditions and ventilation flows.
- Effects of barriers on the critical velocity according to the source conditions.

The study of these parameters is first done in the tunnel without blocks. The objective is to compare the results obtained in the two tunnel configurations with and without barriers and to determine the reduction of the critical velocity due to each type of barrier. The study is then extended to include the effects of blocks to assess the influence of vehicular traffic on critical ventilation velocities in the tunnel with and without barriers.

3.3.1 Tunnel without blocks

Experimental results of the effects of barriers on smoke propagation inside the tunnel with and without barriers are presented hereafter. First, we evaluate the effects of barriers on the smoke back-layering lengths. Then, we conduct more experiments to study their effects on critical ventilation velocities.

3.3.1.1 Smoke back-layering flow length

Several experimental measurements were performed to evaluate the smoke back-layering flow length against the ventilation velocity. The experiments are carried out, both in the tunnel without barriers and in the tunnel with different barriers, under the same source conditions (i.e. $\Gamma_i = 2$, $\rho_i/\rho_0 = 0.7$).

Fig. 3.5 and Fig. 3.6 show a plot of the dimensionless back-layering flow length, L/H , against the velocity ratio $U_0/U_{0,cr}$. $U_{0,cr}$ refers to the critical velocity measured in the empty tunnel (tunnel without barriers). The ratio $U_0/U_{0,cr}$ is the parameter that reveals the effects of the barriers on the smoke propagation. Fig. 3.5 compares the results obtained in the empty tunnel and in the tunnel with small barriers of both configurations $S = H$ and $S = 2H$. The results show that the critical velocity reduction ratio by the effect of the barriers (i.e. the minimum ratio that corresponds to a back-layer length = 0) is improved for the instant when $S = 2H$. In this case, the barrier located just upstream of the source prevents the smoke back-layering flow for any velocity $U_0 > 0.83U_{0,cr}$. Meanwhile in the case when $S = H$, the first barrier placed just upstream of the source prevents the return of smoke for any velocity ratio $U_0/U_{0,cr} > 0.91$. Therefore, a different reduction ratio between the two configurations explains the importance attached to the distance S fixed between each two adjacent barriers. In the case where $S = H$, the reduction of the critical velocity is low because the first barrier located downstream of the source creates an obstruction for the smoke which forces it to go upstream. This obstruction has less influence when the distance S is large. In such a case, the barrier is located far from the impingement region of the buoyant releases and the smoke flows downstream of the source without being blocked. Consequently, a lower ventilation velocity, compared to that when $S = H$, is needed to prevent smoke from flowing upstream of the source. However, for velocity less than the threshold value specified above (i.e. $U_0 < 0.83U_{0,cr}$ when $S = 2H$ and $U_0 < 0.91U_{0,cr}$ when $S = H$), the smoke back layer can be seen even with barriers in place, although the back layer length is reduced compared to the case with no barriers. This is expected because the barriers placed further upstream of the source prevent the back-layering flow at low ventilation velocities.

3.3 Effect on backlayering and critical velocity

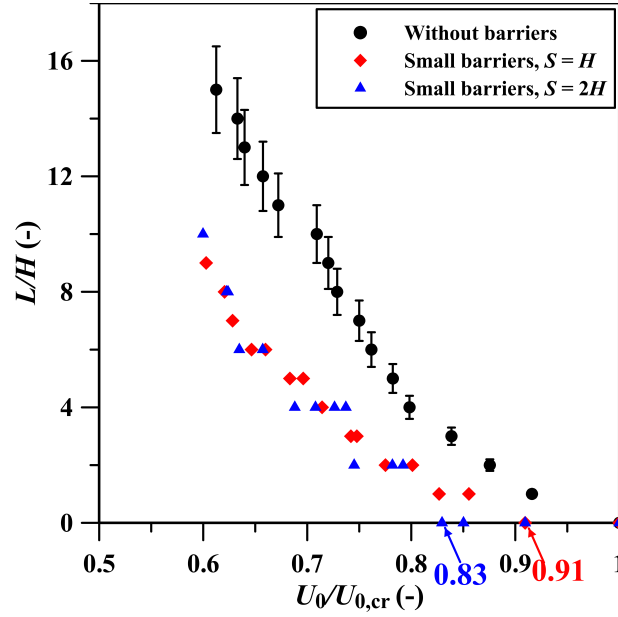


Figure 3.5: Smoke dimensionless back-layering length, L/H , measured in the tunnel with and without small barriers against the ratio of longitudinal ventilation velocity to the critical velocity $U_0/U_{0,cr}$; $U_{0,cr}$ is the critical velocity in the tunnel without barriers.

Results for the tunnel with a large barrier ($H/4$ and $H/3$) are shown in Fig. 3.6 and compared to those obtained in the empty tunnel. Fig. 3.6a shows the result for the case when the large barrier is placed just upstream of the source and Fig. 3.6b shows the result when the barrier is fixed at a distance H upstream of the source. In both cases, the results show that the large barrier prevents the smoke from flowing upstream of the source for any ventilation velocity greater than or equal to $0.67U_{0,cr}$ for barrier height $H/4$ and $0.56U_{0,cr}$ for barrier height $H/3$. This means that the distance between the barrier and the source position does not affect the reduction ratio, i.e. the effectiveness of the barrier is not dependent on its distance from the source. This is important because, in practice, it is impossible to predict where a fire will occur inside the tunnel and, therefore, each barrier should be able to cover a large area whatever its location in the tunnel. However, for any velocity U_0 less than $0.67U_{0,cr}$ for $h = H/4$ and $0.56U_{0,cr}$ for $h = H/3$, the barrier can not stop the propagation of the smoke upstream of the source, but it does nevertheless play a significant role in minimising the back layer length. As shown in Fig. 3.6a and Fig. 3.6b, the back-layer length in the tunnel with a large barrier remains lower than that in the tunnel without the barrier. Finally, by comparing all the previous results, we can conclude that the effectiveness of barriers increases with increasing height.

3.3 Effect on backlayering and critical velocity

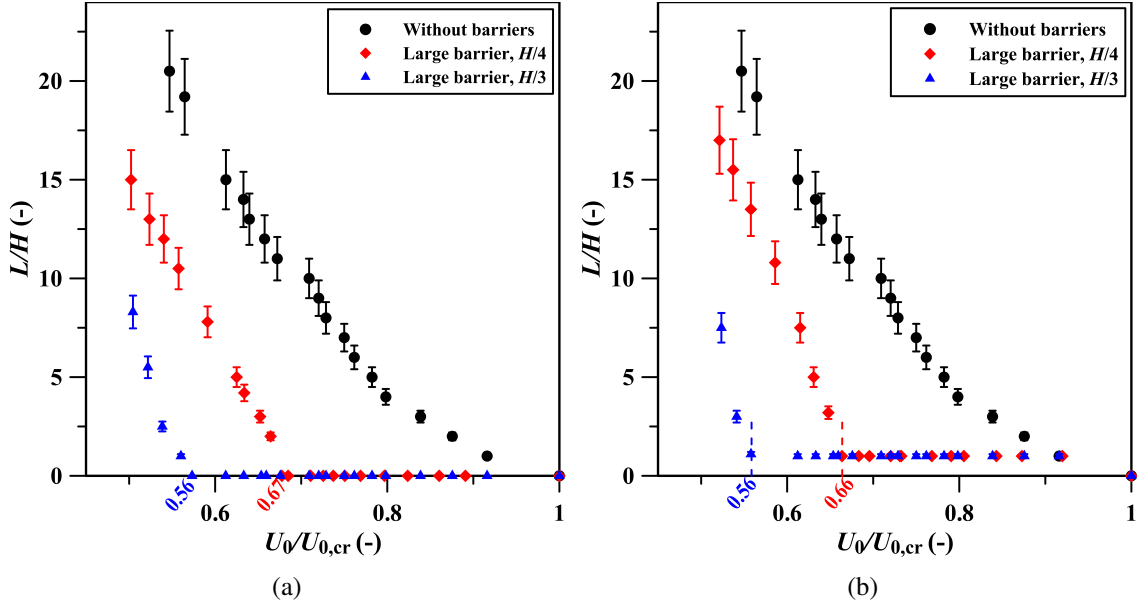


Figure 3.6: Smoke dimensionless back-layering length, L/H , measured in the tunnel with and without large barriers against the ratio of longitudinal ventilation velocity to the critical velocity $U_0/U_{0,cr}$. a) The barrier is placed just upstream of the source. b) The barrier is placed at a distance H upstream of the source.

3.3.1.2 Critical longitudinal ventilation velocities

More experiments were conducted to study the effect of barriers on the critical velocity $U_{0,cr}$. The critical velocity in the empty tunnel and in the tunnel with barriers is defined as:

- The minimum longitudinal velocity needed to prevent the back-layering flow upstream of the buoyant source in the tunnel with no barriers.
- The minimum longitudinal velocity for which the barrier placed just upstream of the source prevents the back-layer flow in the tunnel with barriers.

Fig. 3.7a and Fig. 3.7b show the dependence of the critical ventilation velocity $U_{0,cr}$ on the buoyancy flux B_i and the dependence of the dimensionless critical velocity $U_{0,cr}/W_i$ on the plume Richardson number Γ_i , respectively. As expected, for all cases, $U_{0,cr}$ increases with the increasing of the buoyancy flux B_i and dimensionless critical velocity $U_{0,cr}/W_i$ increases with the plume Richardson number Γ_i . As shown by Le Clanche et al. [25], these dependences can be conveniently fitted by power laws in the form $U_{0,cr} = aB_i^{1/3}$ and $U_{0,cr}/W_i = b\Gamma_i^{1/3}$. Note however that the 1/3 power laws are expected to fit data for releases with $\Gamma_i \gg 1$ and that therefore we would not expect these to hold for releases with Γ_i of order one [31]. This explains why values with lower Γ_i (corresponding to releases with highest

3.3 Effect on backlayering and critical velocity

B_i) do not fit well the regression curve. The constants "a" and "b", obtained by a best-fit to the experimental data, both decrease when the size of the barriers increases (passing from an empty tunnel to a tunnel with the largest barrier, this constant is reduced by forty five percent). Note that the values of the constants $a = 0.96$ and $b = 0.36$ obtained in the empty tunnel (tunnel without barriers) are very similar to those determined by Le Clanche [25] in similar experiments in another experimental set-up.

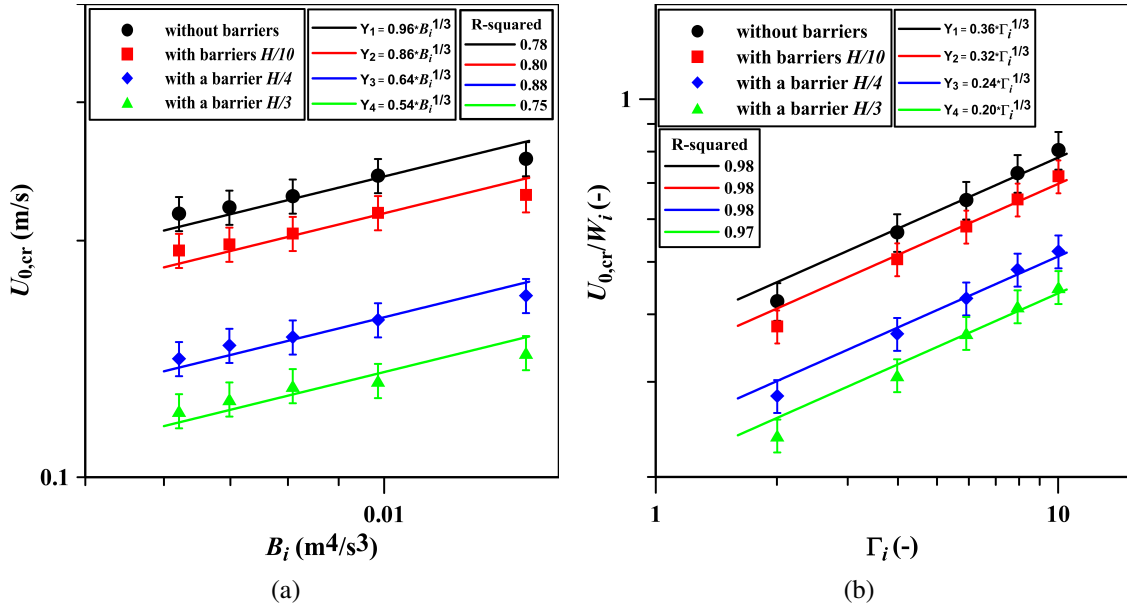


Figure 3.7: a) Dependence of the critical velocity $U_{0,cr}$ on the buoyancy flux B_i . b) Dependence of non-dimensional critical velocity $U_{0,cr}/W_i$ on the plume Richardson number Γ_i . All data are fitted with a power-law of the form $aX^{1/3}$. The estimated error rate of the experimental data is 5%. R-squared is the coefficient of determination for regression curves. The results for the small barriers presented here concern those with the configuration $S = H$.

In order to evaluate the effect of the barriers on the critical velocities, we have calculated the ratio between the critical velocities of a tunnel with barriers and those of a tunnel without barriers:

$$R_c = \frac{U_{0,cr \text{ with barrier}}}{U_{0,cr \text{ without barrier}}} \quad (3.5)$$

The results, presented in Fig. 3.8, shows that the critical velocity ratio is almost independent of the plume Richardson number, i.e. this ratio is independent of the dynamical conditions at the buoyancy source. However, the ratio does depend on the barrier height, it decreases when the barrier height is large and vice versa. Fig. 3.8 shows that the barriers

3.3 Effect on backlayering and critical velocity

with heights, $H/10$, $H/4$ and $H/3$ reduce 10%, 34% and 44% of critical velocities measured in the empty tunnel, respectively. In addition, the reduction ratio (i.e. $1 - R_c$) for $U_{0,cr}$ is approximately equal the tunnel blockage ratio ϕ induced by the different barriers (presented in Table 3.1: 10% for the barrier height $H/10$, 25% for the barrier height $H/4$ and 33% for the barrier height $H/3$). This is simply a consequence of the Venturi effect induced by the presence of barriers, i.e. an acceleration of the flow due to a reduction of the tunnel section, according to basic mass-conservation principle.

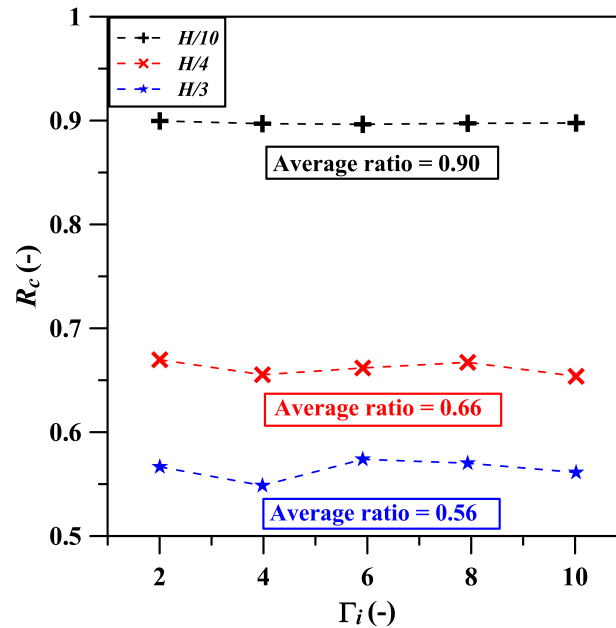


Figure 3.8: The velocity ratio R_c , given by the critical velocity in the tunnel with barriers to the critical velocity in the empty tunnel, against the plume Richardson number Γ_i .

3.3.2 Tunnel with blocks

The experimental data regarding the effects of obstacle blocking on critical velocities in case of fire in a longitudinally ventilated tunnel are plotted in Fig. 3.9, showing the results of all the possible combinations between the barriers and the blocks in a tabular form (presenting the three blocks in three rows and the four barrier configurations in four columns). The data are plotted as the critical velocity ratio, R_c , (given by Eq. 3.5) against the number of pairs of blocks, N_{PB} (because there are two rows of blocks). In Fig. 3.9 the black, blue and red symbols show the results obtained in the tunnel with blocks, with barriers and with set of blocks and barriers, respectively. The effects of barriers on critical velocities in empty tunnel have already been analysed in section 3.3.1.2 and presented here for comparison purposes. Now, we shall particularly focus on the effects of blocks in tunnels with and without barriers

(i.e. the two series in black and red).

3.3.2.1 Effect of blocks in tunnel with no barriers

Fig. 3.9 shows that the influence of the blocks on the critical velocity varies according to the size of the blocks and the blockage-source distance, in agreement with what was observed by Jiang [43]. For small blocks (i.e. Block1), the results show that only the pair of blocks located just upstream of the source can slightly modify the value of the critical velocity, while the effect of the other blocks placed further upstream is negligible. The reduction in critical velocity due to the pair of small blocks located close to the source is equal to about 5%. This value is approximately equal to half of the blocking rate induced by the blocks. Regarding Block2 and Block3, the data show that when the distance between the blockage and the source decreases, the velocity ratio first decreases progressively, then suddenly drops once the source-blocks distance is zero. As a result, the critical velocity reductions associated with placing a pair of block2 and block3 directly behind the source are about 16% and 39% respectively. These values are close to the blocking rates induced by the same blocks (see Table 3.1). On the other hand, we can see that the reduction of the critical velocity due to the blocks situated further upstream of the source does not exceed 9% for both block2 and block3.

3.3.2.2 Effects of blocks in tunnel with barriers

The comparison between the results obtained in the case of a tunnel with barriers and those obtained in the case of a tunnel with blocks and barriers allows us to make two conclusions concerning the effects of source-blocks distance on the ventilation critical velocity. The first conclusion can be made from the case where the blocks are placed further upstream of the source. In this instance Fig. 3.9 shows a clear correlation between the blue and red curves in almost all tunnel configurations, excluding a few points with a lower value of R_c for when both blocks and barriers are present opposed to just barriers. This means that the blocks placed further upstream of the source have no effect on the critical velocity and the reduction observed in the series in red is only induced by the presence of the barriers. The second conclusion can be drawn from the case where the last pair of blocks is positioned close to the source. In this instance, we clearly see a drop in the values of the velocity ratio R_c appearing on all the curves of Fig. 3.9. This indicates that the critical velocity is only influenced by the blocks located just upstream of the source. Furthermore, it is clear from this figure that the decrease of R_c depends on both the size of the barriers and the size of the blocks; the reduction is high with large barriers or with large blocks and exceedingly high with the combination of both large barriers and large blocks.

3.3 Effect on backlayering and critical velocity

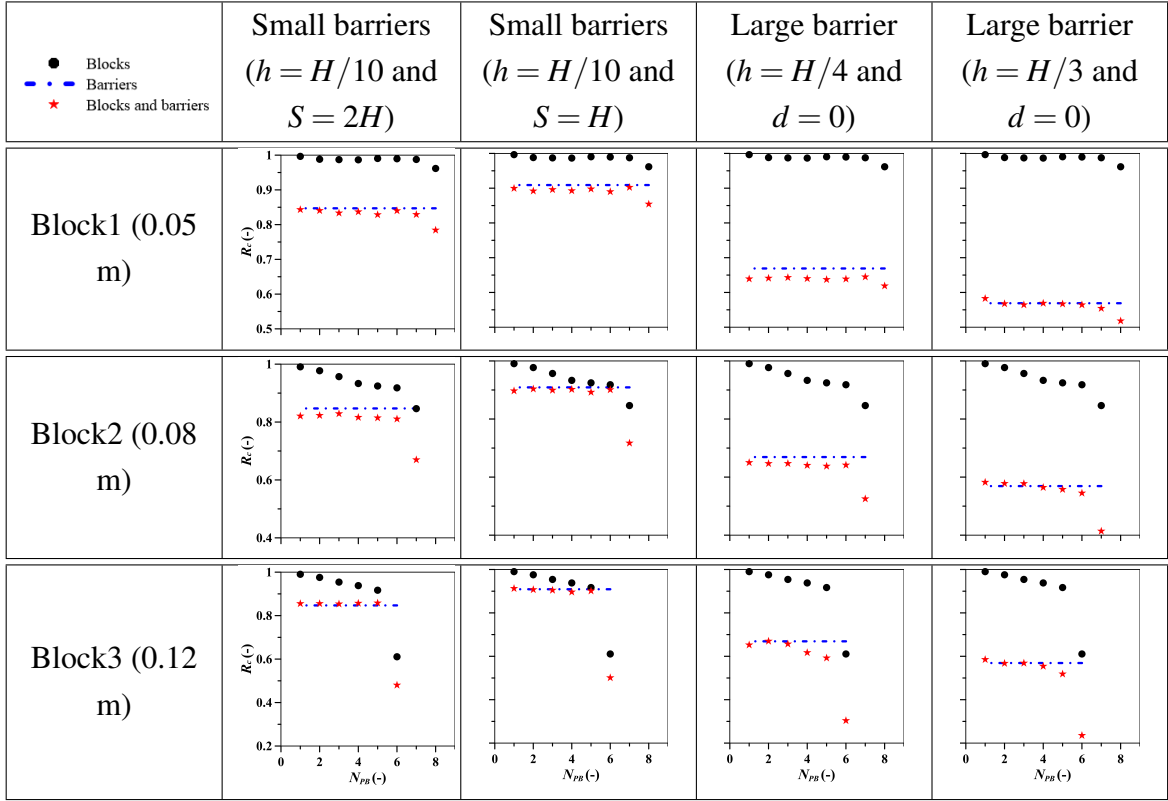


Figure 3.9: The velocity ratio R_c , given by the critical velocity in the tunnel with obstacles to the critical velocity in the empty tunnel, against the number of pairs of blocks N_{PB} . $D_i = 0.1$ m, $\Gamma_i = 2$ and $\rho_i/\rho_0 = 0.7$.

Table 3.2 summarises the rates of velocity reduction due to the location on the same cross section of a pair of blocks and a barrier upstream near the source.

Table 3.2: Velocity reduction rates induced by both the pair of blocks and the barrier located on the same cross-section just upstream of the source.

	Small barriers ($h = H/10$ and $S = 2H$)	Small barriers ($h = H/10$ and $S = H$)	Large barrier ($h = H/4$ and $d = 0$)	Large barrier ($h = H/3$ and $d = 0$)
Pair of block1	22%	15%	38%	48%
Pair of block2	33%	28%	48%	59%
Pair of block3	52%	50%	70%	77%

The data for the reduction of the critical velocities ($1 - R_c$) due to blockage caused by barriers, blocks or both are collected and plotted in Fig. 3.10 according to the corresponding tunnel blockage ratios ϕ . Only results with obstacles located just upstream of the source are

3.3 Effect on backlayering and critical velocity

presented in this figure. By fitting the data with a linear regression, results suggest that the critical velocity reduction rate is proportional to the blockage ratio, i.e. $1 - R_c = \varphi$. Using Eq. 3.5, this relationship can be written in the form:

$$\frac{U_{0,cr \text{ with blockage}}}{U_{0,cr \text{ without blockage}}} = 1 - \varphi \quad (3.6)$$

which is equivalent to Eq. 3.4. derived from the conservation principle of the volume flow. This means that when an obstacle is located near the source (provided it does not directly affect the longitudinal airflow that reaches the smoke plume), a lower ventilation flow is sufficient to force all the smoke downstream of the source, since the local ventilation velocity increases in proportion to the reduction of the tunnel cross section. Therefore, the reduction ratio of the critical velocity will be almost equal to the tunnel blockage ratio.

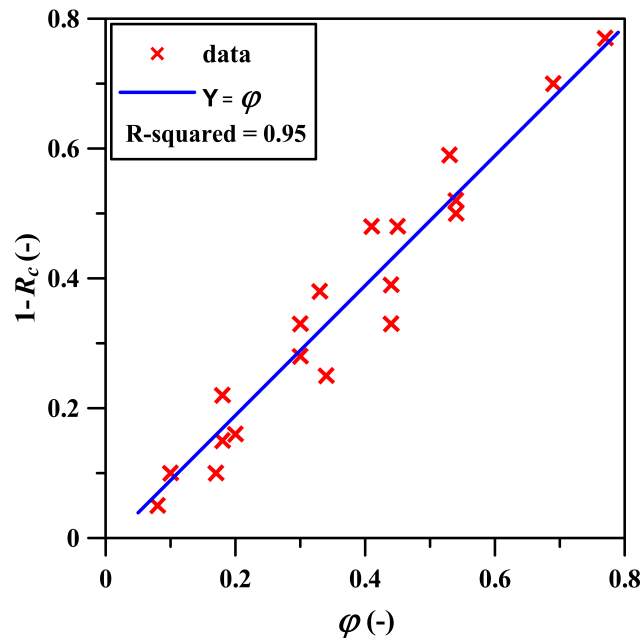


Figure 3.10: Reduction of the critical velocities ($1 - R_c$) against the tunnel blockage ratios φ of obstacles (barrier, block, or both) located just upstream of the source.

However, when the distance between the blocks and the source is equal to or greater than twice the height of the tunnel, the reduction in the critical velocity is too low (Fig. 3.9). Therefore, to obtain a complete critical ventilation model considering the blockage and the source-blockage distance, additional tests are required (these should be performed by reducing the increasing distance between the source and the blocks).

3.4 Effect on the pressure losses along the tunnel

In the case of a tunnel without any blocks, we have seen that the barriers prevent the smoke back-layer up to a certain so-called critical velocity ratio, which depends mainly on the barrier height. On the other hand, in the presence of blocks inside the tunnel, the critical velocity was greatly affected by the size of blocks which are placed close to the source. However, the design and dimensioning of the ventilation systems installed in the tunnels are determined by the sum of the pressure losses created in the ventilation networks. Adding barriers or blocks in the tunnel induces an increase in pressure drops and potentially an increase in the capacity of machines to be installed. It is therefore essential to evaluate these additional pressure losses generated by the obstacles. For that purpose, an experimental study was carried out to first examine the effects of barriers on the pressure drop in a tunnel without any blocks, then the effects of vehicular blockage in the tunnel with and without barriers. The experiments on pressure losses were performed in the reduced-scale tunnel shown in Fig. 3.1, without releasing any buoyant fluid.

To study the effects of the barriers, we consider almost the same configurations presented previously and illustrated in Fig. 3.1. We focus on the effect of the number of small barriers fixed to the tunnel ceiling and the effect of barrier heights. To analyse the effects of the vehicular blockages on the pressure drops, we perform the same experiments as those presented previously (see Fig. 3.3). By considering the same blocks placed on the tunnel floor in the same configuration as that shown in Fig. 3.3 (except here the source of buoyancy is not considered). In that we focus mainly on the effect of the number of blocks placed in the tunnel and the effect of the block sizes.

The pressure difference was measured between two points, one upstream and the other downstream of the obstacle positioning area. The obstacle positioning area extends from 2.4 m to 5.4 m and the two points P1 and P2 are located at ground level of the tunnel (Fig. 3.1) at 2.1 m and 5.7 m from the inlet, separated by the distance $L_{1-2} = 3.6$ m. The measurements were performed using a highly-accurate measuring device (FCO510 Micromanometer [74]). The instrument contains a highly sensitive ultra-low-range differential pressure transducer with a resolution of up to 0.001 pascals. It is capable of making pressure difference measurements in the range of 2-20 mmH₂O with a measurement accuracy of $\pm 0.25\%$ of reading between 10% of lowest range and full scale. The micromanometer retrieves the pressure difference every 0.3 seconds and sends the values to the computer where they are averaged over 5 min using the software LabVIEW. This mean value corresponds to the mean pressure difference Δp .

As pressure differences are caused by the dynamic pressure, it is convenient to introduce

3.4 Effect on the pressure losses along the tunnel

a dimensionless pressure coefficient C_f defined as:

$$C_f = \frac{\Delta p/L_{1-2}}{\frac{1}{2}\rho_0 U_0^2/\bar{D}} \quad (3.7)$$

where \bar{D} is the hydraulic diameter of the tunnel defined as $\frac{2HW}{(H+W)}$, W is the width of the tunnel, H is the height of the tunnel, ρ_0 is the density of ambient air and U_0 is the longitudinal ventilation velocity.

3.4.1 Effects of barriers

To investigate the effects of the barriers on pressure losses, we consider the three barriers having heights $H/10$, $H/4$ and $H/3$. In case of the small fixed barriers, i.e. $H/10$, we consider two different configurations, with a spacing between the barriers of $S = H$ and $S = 2H$. For the large barriers i.e. $H/4$ and $H/3$, a single barrier is fixed to the tunnel ceiling. Fig. 3.11 shows the results concerning the dependence of dimensionless pressure coefficient, C_f , against the ratio h/H at a high Reynolds number ($Re > 17000$). The additional pressure loss

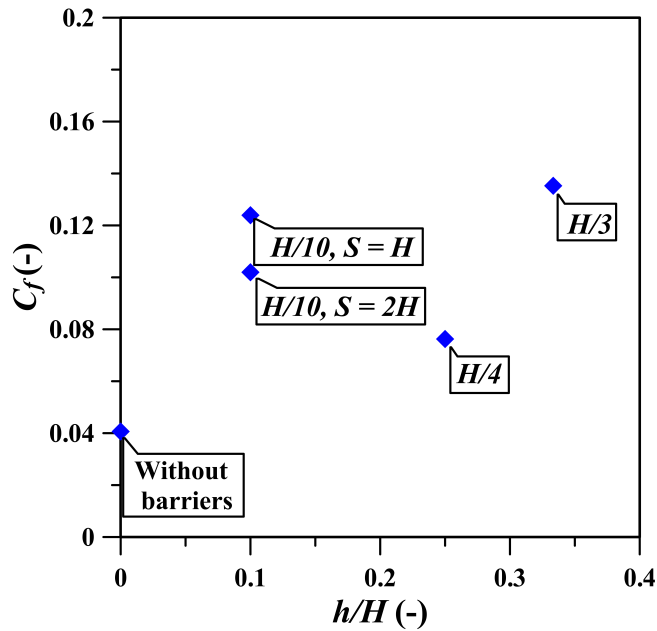


Figure 3.11: Dimensionless pressure coefficient C_f , against the dimensionless barrier height, h/H .

produced in the tunnel as a result of the barriers is compared to that induced in the empty tunnel. The results show that:

- The coefficient of pressure loss increases with the increase in the number of obstacles:

3.4 Effect on the pressure losses along the tunnel

for small barriers, the pressure losses induced by the barriers in the configuration with a spacing $S = H$ is greater than those induced in the case with $S = 2H$.

- The pressure losses increase with increasing the barrier height: for large barriers, the pressure loss induced by the largest barrier $H/3$ is higher than that induced by the barrier of the height $H/4$.
- The pressure losses created by the largest barrier $H/3$ are slightly greater than those created by nineteen small barriers, i.e. the number of barriers with the configuration $S = H$.

3.4.2 Effects of vehicular blockage

Fig. 3.12 shows the results for the pressure drops due to the presence of the blocks in the tunnel for both cases with and without barriers against the number of pairs of blocks N_{PB} . Taking the results in the tunnel without blocks as a reference case (i.e. curves in blue), we can classify two cases:

3.4.2.1 Tunnel with blocks but no barriers (i.e. circles in black)

It can be observed that: i) the pressure losses increase with the size of the blocks. As shown in the graphs, the pressure losses induced by all the small blocks placed in the tunnel (i.e. Block1) remain lower than those created by the barriers. Whereas those generated by one pair of large blocks (i.e. Block3) are already greater than those created by the barriers. ii) The pressure losses increase with the number of cubes placed in the tunnel, in particular in the tunnel with large blocks where the growth is very pronounced. Based on these findings, it can be deduced that two parameters are connected with pressure losses: the blocking rate (i.e. ratio between blocking area and tunnel cross section) and the number of vehicles. Indeed, the higher the blocking rate and/or the number of vehicles, the greater the pressure losses.

3.4.2.2 Tunnel with blocks and barriers (i.e. stars in red)

Fig. 3.12 clearly shows that the addition of barriers in a tunnel with vehicular blockages results in a significant increase in pressure loss. However, for small blocks (Block1), the highest values of dimensionless pressure coefficients are recorded in the two tunnel configurations "tunnel with small barriers $S = H$ " and "the tunnel with the largest barrier, $H/3$ ". Meanwhile, these dimensionless pressure coefficients are relatively small in the case of a tunnel with a large barrier, $H/4$. On the other hand, in the tunnel with large blocks

3.4 Effect on the pressure losses along the tunnel

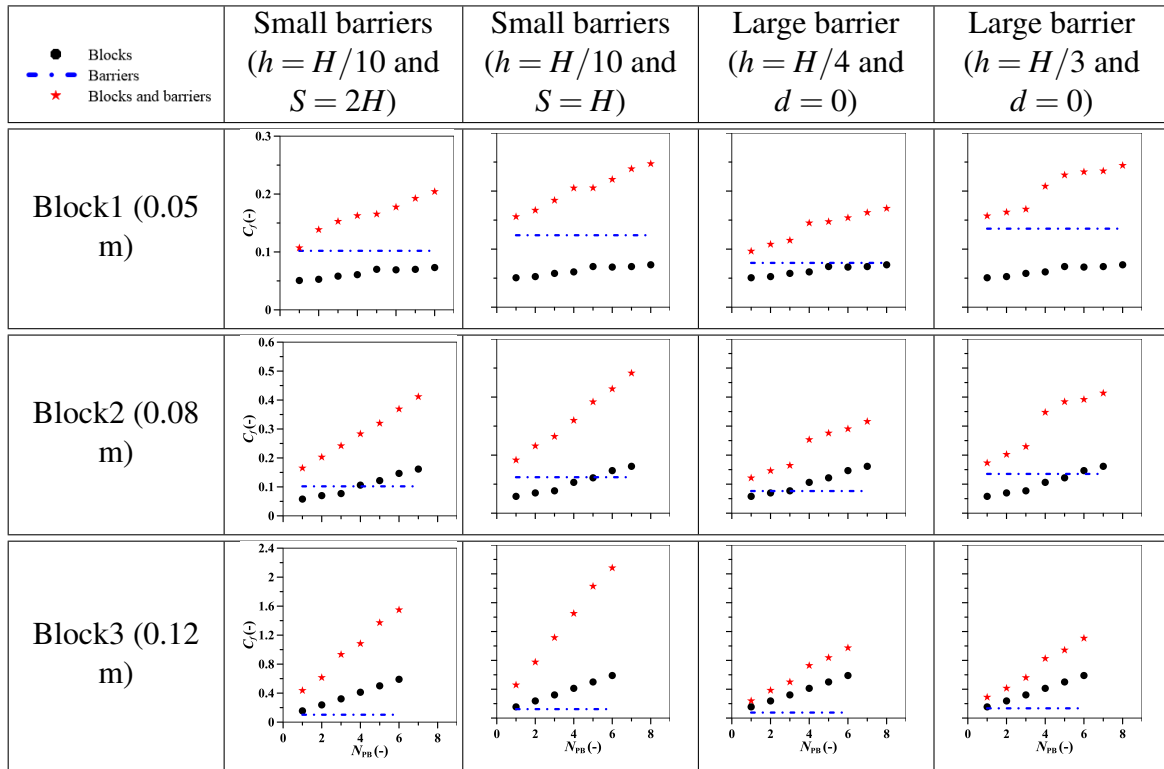


Figure 3.12: Head loss coefficient C_f , evaluated in the presence of the blocks in the tunnel for both cases with and without barriers against the number of pairs of blocks, N_{PB} .

(Block2 and Block3), the pressure losses induced by small barriers are much higher than those induced by each of the large barriers, especially in the case with the largest blocks (i.e. Block3). This is because the installation of several small barriers at the tunnel ceiling causes many changes and reductions within the tunnel cross sections and even more so in the case of a traffic jam, which consequently produces more singular pressure losses.

Comparing the two configurations of small barriers, we see that in the case where $S = 2H$, the pressure loss is less and therefore preferable for minimising the energy consumption of the ventilation system, on the one hand, and on the other more effective in reducing the critical velocity, according to the previous results reached in the first part of this study. Furthermore, Fig. 3.9 and Fig. 3.12 show that large barriers are more efficient and more reliable than small ones because they prevent the smoke backflow at greatly reduced critical velocities and they generate less loss pressure in the tunnels even in the situations with vehicular blockages.

3.5 Conclusions

Small-scale experiments were conducted in a reduced-scale tunnel to investigate the effects of solid barriers and blocks on the behaviour of smoke in fire events within longitudinally ventilated tunnels. Two types of barriers fixed to the tunnel ceiling were examined, small barriers with a height equal to $H/10$ and large barriers with heights equal to $H/4$ and $H/3$. The vehicles in the tunnel are modelled by blocks of different sizes placed upstream of the buoyancy source. The smoke backflow lengths, the critical velocities and the pressure losses were evaluated. The main conclusions are:

- The barriers prevent the back-layer flow from moving upstream of the source at low ventilation velocities (or at least they reduce its length).
- The effectiveness of the barrier in preventing the smoke back-layering depends on its height, the greater the height of the barrier, the more effective it is.
- The critical velocity is highly affected by the blocks located close to the source, while the effect of other blocks placed further upstream of the source becomes negligible as the distance between the blocks and the source increases.
- The reduction ratio of the critical velocity is very close to the reduction in cross-section of the tunnel induced by the obstacles located close to the source (blocks, barriers or both), i.e. $1 - Rc = \varphi$.
- The effect of the barriers on the pressure loss is negligible compared to that induced by HGVs.
- The simultaneous presence of blocks and barriers in the tunnel leads to a large increase in pressure losses. This increase is much greater with small barriers than with large barriers, especially when they are coupled with large blocks.
- The large mobile barriers are much better than the small fixed barriers because they prevent the formation of the back-layer flow at a much smaller ventilation velocity without generating excessive pressure losses.

In conclusion, ceiling barriers could help in improving safety in longitudinally ventilated road tunnels. This solution may be particularly helpful, for example, in existing tunnels where the available space does not allow many jet fans to be installed, or in tunnels with low traffic to reduce the renovation cost, as well as in some tunnels that require a strong thrust to achieve the critical velocity, especially downhill tunnels where the adverse "chimney

effect" is strong in case of fire. Therefore, by reducing the critical velocity, barriers could help satisfy the ventilation objectives. However, positioning barriers inside the tunnel might be challenging and the installation of mobile barriers requires an entire automated control system, as they are designed to be deployed only in case of a fire, once detected. Finally, it is worth noting that the barrier heights investigated in this paper are not necessarily optimal, and can be adjusted on a case-to-case basis. Further studies could focus on the study of the behaviour and control of smoke in the transverse ventilation tunnel, as well as the impact of solid barriers on the performance of the extraction system.

SMOKE CONTROL IN TUNNEL WITH A TRANSVERSE VENTILATION SYSTEM: AN EXPERIMENTAL STUDY

We carried out a series of experiments in a small-scale tunnel to study the confinement of smoke flow between two exhaust vents located on either side of a buoyant source placed at ground level within a ventilated tunnel. The objective of our study is to quantify the influence of the shape and the position (with respect to the tunnel axis) of the dampers, including the specific case of full-width dampers, on the performance of the transverse ventilation system. To that purpose, we investigated the extent of the backflow length downstream of the dampers, the "confinement velocity" (suppressing the back-layering flow downwind of the vents) and the stability of the smoke stratification. The results show that the best performances are achieved when the width of the dampers is the same as the tunnel width: this minimises the extent of the back-layering flow (for given extraction flow rates) and ensures the stability of the smoke stratification. The worst conditions are observed with square-shaped dampers located on the side of the ceiling, this configuration disturbs the stratification of the smoke layer before the confinement conditions are reached. Subsequently, we evaluated the effect of solid barriers -placed on the tunnel ceiling downstream of same three dampers typologies- on the propagation of the smoke. The results show that these barriers improve significantly the efficiency of system with square-shaped dampers located on the side of the ceiling: they reduce the confinement velocity and enhance the stability of the smoke stratification.

Keywords: Road tunnel safety, Smoke control, Transverse ventilation, Buoyant plume, Back-layering, Confinement velocity, Solid barriers.

4.1 Introduction

The consequences of an event such as a fire or an accident in confined spaces such as a tunnel can be tragic. In these structures, due to the components and materials of the vehicle (plastics, tires, etc.) as well as all hazardous substances transported (fuel, wood, textile, plastic, etc.), fires can produce a large amount of toxic smoke. This smoke causes a loss of visibility that can prevent the evacuation of users who end up inhaling harmful gases and toxic substances. The smoke is indeed the major source of death in tunnel fires. Therefore, the installation of safety systems is imperative to ensure good safety conditions for tunnel users and emergency services in case of fire. Ventilation is one of the most important systems for fighting fires and controlling the dispersion of toxic smokes in these spaces. Based on traffic mode (i.e. one-directional or bi-directional) and flow regime (i.e. congested or uncongested) in the tunnels, two types of mechanical ventilation can be defined: longitudinal and transverse ventilation systems.

Longitudinal ventilation is required for road tunnels with unidirectional low traffic and is designed to produce a longitudinal flow in the same direction as vehicle traffic (Fig. 1.3). With this strategy smoke and combustion products are pushed downstream of the fire source location to ensure the safe evacuation of people located upstream of the fire and to facilitate the intervention of rescue forces. Transverse ventilation systems are instead suitable for long bidirectional tunnels or congested unidirectional traffic tunnels (Fig. 1.4). These are cases in which longitudinal ventilation is not suitable because, in these cases, pushing the smoke in one direction can endanger the tunnel users. With transverse ventilation, the smoke is extracted through dampers, which are generally located on the ceiling, whilst controlling the longitudinal air flow in the tunnel. Two objectives are generally pursued: the preservation of the natural stratification and the confinement of the smoke within a limited section of the tunnel, in which the extraction takes place.

While the smoke control in longitudinal ventilation has been the subject of extensive research [21, 22, 64, 75], the literature is much scarcer regarding transverse ventilation. In this latter strategy, a main flow control parameter is referred to as ‘the confinement velocity’, defined as the minimum adverse velocity required to prevent the smoke from propagating beyond the extraction dampers, and the associated extraction flow rate at the ceiling vents. Vauquelin and Mégret [76] conducted fire experiments in a small-scale tunnel equipped with two mechanical exhaust ducts located one on either side of a fire source to study the influence of their location and their shape on the exhaust system efficiency for different fire heat release rates (HRR). They concluded that a duct with the transverse rectangular shape located at the tunnel ceiling is more efficient than the other ducts tested, whatever their shape

and location. Vauquelin and Telle [77] performed another experimental study with a single vent activated downstream of the source (and assuming that smoke flow would be symmetrical with respect to the fire location). They evaluated the stratified smoke layer length downstream of the vent and the confinement velocity, for several values of HRR. Vauquelin [17] then performed other experiments with the same experimental set-up, but with a two vents system, to estimate the extraction flow rate required for a given HRR. Wang et al. [78] carried out a series of full-scale burning experiments in tunnel with roof openings to study the effect of natural smoke exhaust on the behaviour of smoke propagation, velocity and temperature fields under the ceiling, height of smoke layer and backflow distance. Due to the high costs and the difficulties inherent when conducting such fire experiments in a real tunnel, they extended this study by performing numerical simulations to include other fire scenarios with various vertical shaft arrangements on tunnel roof [79]. Ingason and Li [80] conducted a series of small scale fire experiments to investigate the efficiency of a single extraction system and a two-point extraction system. They concluded that the induced longitudinal velocity required to confine all smoke is low in the case with two-point extraction system. Fan et al. [81] conducted experimental simulations of fires in a tunnel equipped with a vertical shaft to quantify the effect of plug-holing on the smoke exhaust efficiency under natural ventilation. Their results showed that a high mixing process between the hot smoke layer and the cold air layer occurs because of the stack effect inside the shaft. Li et al. [82] used the Fire Dynamics Simulator (FDS) software to study the plug-holing phenomenon that occurs under the mechanical smoke exhaust in a tunnel when fresh air is drawn directly into the smoke extraction system from the bottom layer. This phenomenon is undesirable and should be avoided as it greatly reduces the efficiency of smoke extraction in tunnel fires [17, 83–87]. In recent years, further experimental [88–91] and numerical [92–94] studies investigated the performance and efficiency of extraction systems on smoke control in the case of a fire focusing on the vent size and fire source location [92], the tunnel slope [90] and the location and shape of the exhaust vents [76].

The ventilation of road tunnels can be also controlled by combining both ventilation systems, transverse and longitudinal, an approach that has been recently considered in the tunnel ventilation literature. Lee et al. [95] conducted fire tests in a small-scale tunnel to evaluate the performance of the smoke extraction duct under natural and longitudinal ventilation flow conditions. Their results showed that the efficiency of the smoke extraction through the dampers is better with natural ventilation than with longitudinal ventilation, because of the preservation of the smoke stratification in the tunnel. Chen et al. [96] carried out experiments in a reduced-scale tunnel to study the effect of the distance between ceiling extraction and heat source on thermal buoyant smoke back-layering length in a tunnel

with combination of longitudinal ventilation and ceiling extraction opening at the downstream side only. They found that the smoke back-layering length increases with increasing distance between the ceiling extraction opening and the heat source. Yao et al. [97] considered the case with a vertical shaft upstream of the fire source to investigate the length of the smoke back-layering flow in longitudinally ventilated tunnel fires. Their experimental results showed that the vertical shaft can considerably reduce the smoke back-layering flow length (compared to the tunnel without a vertical shaft). In the same small-scale tunnel previously used by Chen et al. [96] and with the same ventilation system, Tang et al. [98] carried out a series of experiments to investigate the behaviour of the buoyant smoke flow stratification. They found that the combination of both ventilation systems had a strong influence on the smoke stratification and the flow configuration could be classified into different regimes.

In this study, we present the results obtained in the experimental analysis of smoke control using transverse ventilation in a scale model tunnel. The fire smoke in the tunnel is modelled by the continuous release of a light gas (mixture of air and helium), a method which has been consolidated through the study of the critical velocity and back-layering phenomenon [26, 99]. The smoke is extracted through two mechanical exhaust vents located on the ceiling of the tunnel, one on each side of the source and equidistant from the buoyancy source. As already mentioned, the confinement velocity is defined as the minimum induced longitudinal velocity required to prevent the smoke from flowing downstream of the vent. When the induced longitudinal velocity is lower than the confinement velocity, a smoke back-layering flow appears downstream of the exhaust vent. The back-layering length is measured between the downstream edge of the exhaust vents and the extremity of the smoke backlayer. We test two different shapes of the extraction dampers, a square shape and a transverse rectangular shape (Fig. 4.2). The two dampers have the same cross-sectional area and the rectangular damper extends across almost the whole width of the tunnel (Fig. 4.2a). The square-shaped exhaust vent is placed on the ceiling in two different locations: firstly in the centre of the ceiling (Fig. 4.2b) and the secondly on one of the ceiling edges (Fig. 4.2c), over a width about one-third the tunnel width. Our work focuses on the measurement of smoke back-layering lengths, the determination of confinement velocities and the potential provision of qualitative information on stratification according to the source conditions and the extraction flow rates. The aim is to compare the results obtained with the different exhaust vents in order to evaluate the influence of the previously defined parameters (i.e. shape and location of the extraction dampers) on the performance of the smoke extraction system. Once this analysis has been carried out, we test the effect of the solid screens on the smoke confinement by fixing barriers to the tunnel ceiling, one downstream of each damper.

4.2 Experimental set-up and measurement techniques

In a full scale tunnel, these barriers are designed to be mobile and would be deployed in the event of fires only. The influence of these barriers on the propagation of buoyant smoke in the tunnel with a longitudinal ventilation has already been studied (Chapter 3). The results showed that the large barriers prevent the smoke back-layer downstream of the source even at low ventilation velocities. The goal here is to examine their effects on the confinement velocity as well as on the stratification of the buoyant smoke layer in order to determine if they can improve the efficiency of the smoke extraction system.

4.2 Experimental set-up and measurement techniques

4.2.1 The reduced scale model

Fire simulation experiments are carried out in a 1/25 reduced-scale model tunnel developed at the Laboratoire de Mécanique des Fluides et Acoustique (LMFA) at the Ecole Centrale de Lyon (Fig. 4.1a). A schematic view of the experimental setup is presented in Fig. 4.1b. The model tunnel is a channel with a rectangular cross-section. It is 8.4 m long, 0.36 m wide and 0.18 m high. Fire-induced smoke is simulated by a release of a light gas, a mixture of air and helium, into ambient air. The air and helium flow rates are controlled and measured using two flow meters. Both gases are well mixed in a long pipe and seeded with nebulised oil before being injected in the plenum. The air flow used to seed the oil particles, controlled by a flowmeter, is low so as not to influence the density of the mixture [31]. The mixture is then injected through a circular source of diameter $D_i = 0.1$ m placed at the centre of the tunnel at ground level. The side wall of the tunnel is made of transparent toughened glass, enabling visualisation of the buoyant fluid (seeded with particles) on a two-dimensional longitudinal plane illuminated by a laser beam emitted from a lens located at the inlet box of the tunnel.

The tunnel is equipped with two dampers placed on the ceiling, one on each side and set the same distance from the source (i.e. $5H$, H is the height of the tunnel). Each of them is connected to a mechanical exhaust fan. Both fans are remotely controlled and their rotation speed is easily adjusted by means of a potentiometer wired to each of them. Each fan produces an extraction airflow in the range 5 - 150 m³/h. Assuming that the tunnel is infinite with a periodic location of the dampers (every $10H$), if we take as reference the volume of the area between each two exhaust vents (i.e. $10H \times H \times 2H \approx 0.117$ m³), the extract rate produced by each fan in terms of "Air Changes per Hour (ACH)" ranges from about 43 to 1286 ACH.

4.2 Experimental set-up and measurement techniques

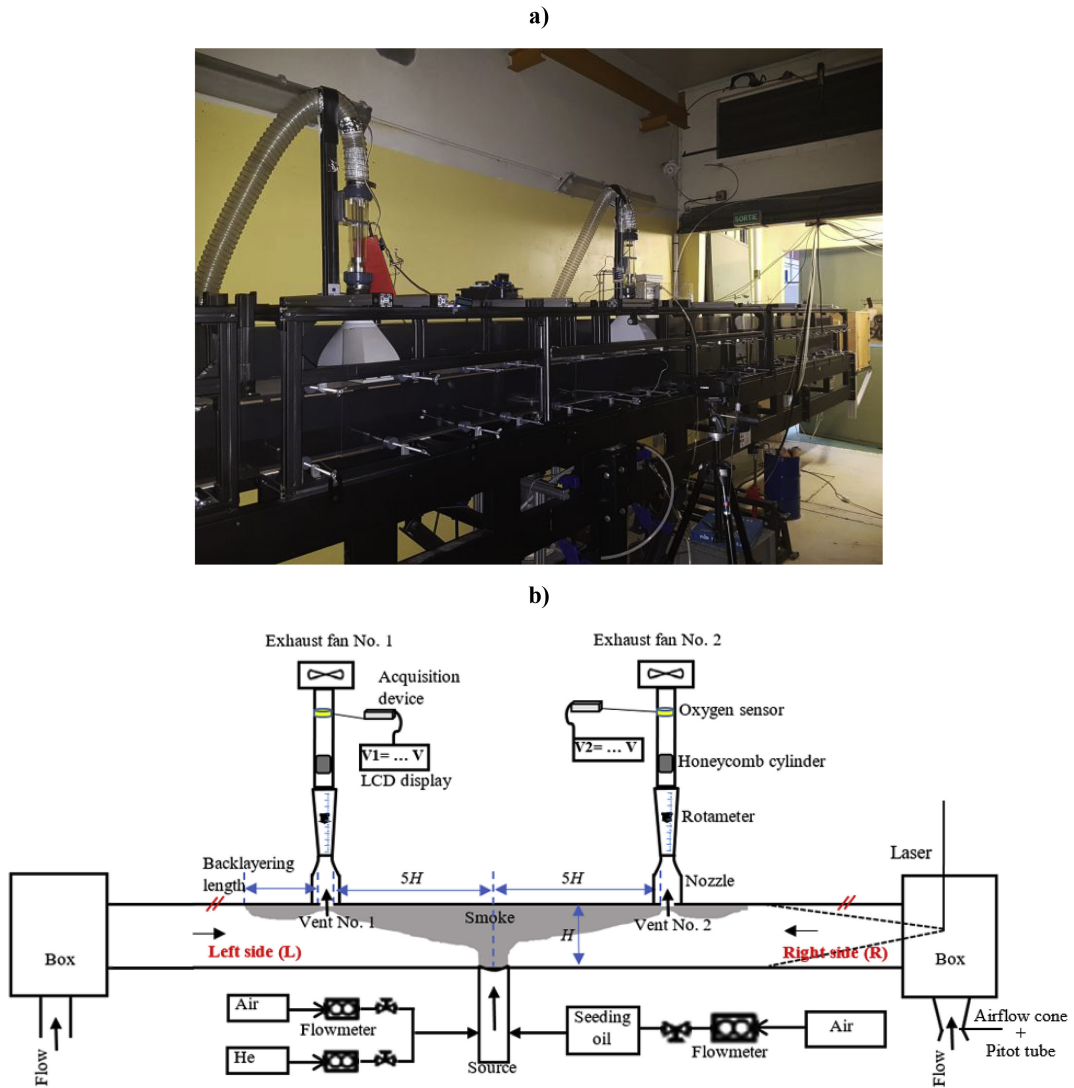


Figure 4.1: Experimental setup with transverse smoke control system. a) A picture of the setup. b) A schematic of the setup.

Two different forms of dampers were used to carry out these experiments, a square shape "SSD" (Fig. 4.2b and Fig. 4.2c) and a transverse rectangular shape "RSD" (Fig. 4.2a) with an identical surface area of approximately 0.011 m^2 . Their dimensions are $0.104 \text{ m} \times 0.104 \text{ m}$ and $0.32 \text{ m} \times 0.034 \text{ m}$, respectively. Two different positions of the square-shaped dampers were tested, the first position in the centre, referred to as "SSD-PC" (Fig. 4.2b), and the second on one of the sides of the tunnel ceiling, referred to as "SSD-PS" (Fig. 4.2c).

The dampers are designed to be easily installed in the tunnel ceiling with fixed connections (8 screws). On each side, a rotameter (section 4.2.3) with a range $6.4 - 64 \text{ m}^3/\text{h}$ (and from 16 to $160 \text{ m}^3/\text{h}$ for high flow rates) is used to measure the extraction flow rates through the exhaust duct. The nozzle placed between the damper and the rotameter particularly

4.2 Experimental set-up and measurement techniques

helps to ensure a uniform flow velocity at the rotameter entrance in order to avoid fluctuations of the rotating float inside the rotameter. The position of the float on a linear scale indicates the flow rate passing through the rotameter. However, the density of the smoke flows is lower than that of the air and a correction of the flow rates measured according to their densities is therefore required. For this purpose, a calibrated oxygen sensor is placed above each rotameter to measure the concentration of air within the exhaust smoke flow. A honeycomb cylinder is placed before the oxygen sensor to protect it from oil particles that could degrade its measurements.

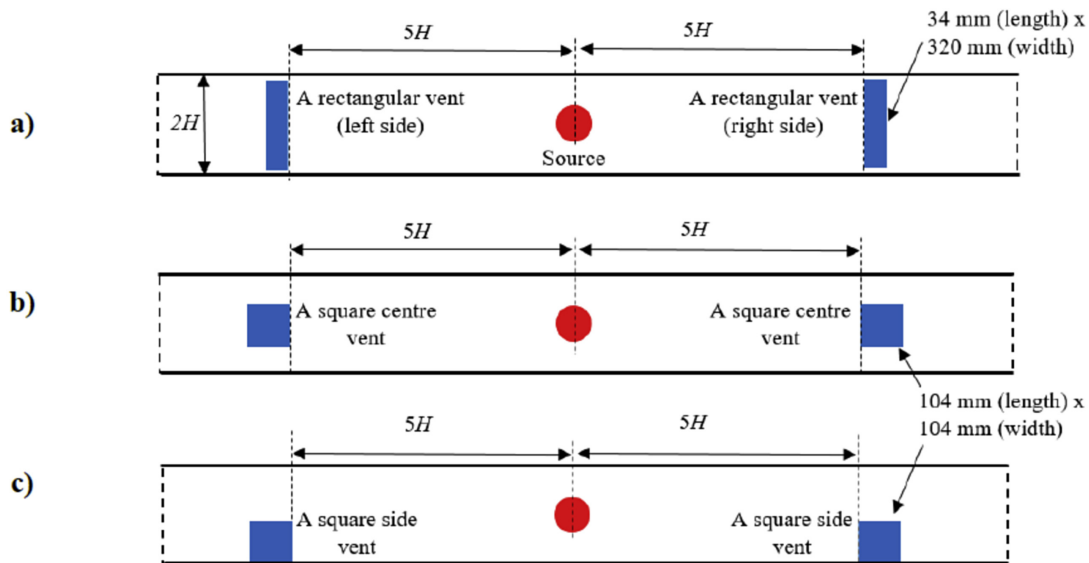


Figure 4.2: Schematic top view of the different exhaust vents with their location on the tunnel ceiling. a) Exhaust vent with transverse rectangular shape (RSD). b) Exhaust vent with square shape placed in the centre of the tunnel ceiling (SSD-PC). c) Exhaust vent with square shape placed on the sides of the tunnel ceiling (SSD-PS).

To study the effect of barriers on the propagation of the smoke, two large barriers used in our recent work (see Chapter 3) were considered. Their heights are $h = H/4$ and $h = H/3$ and their widths are equal to the width of the tunnel. The barriers are solid to withstand the smoke flow forces and the induced longitudinal airflow forces. For each case of dampers, two barriers are fixed to the ceiling of the tunnel, one on each side of the source. The barriers (which are transparent to allow the smoke to be visualised) are located just downstream of the dampers, as is shown in Fig. 4.3. The idea is to evaluate the additional benefits they can offer to improve the efficiency of transverse ventilation systems, by comparing the results obtained with and without barriers. Note that in real tunnels, these barriers are designed to be mobile and will only be deployed in the instance of a fire.

4.2 Experimental set-up and measurement techniques

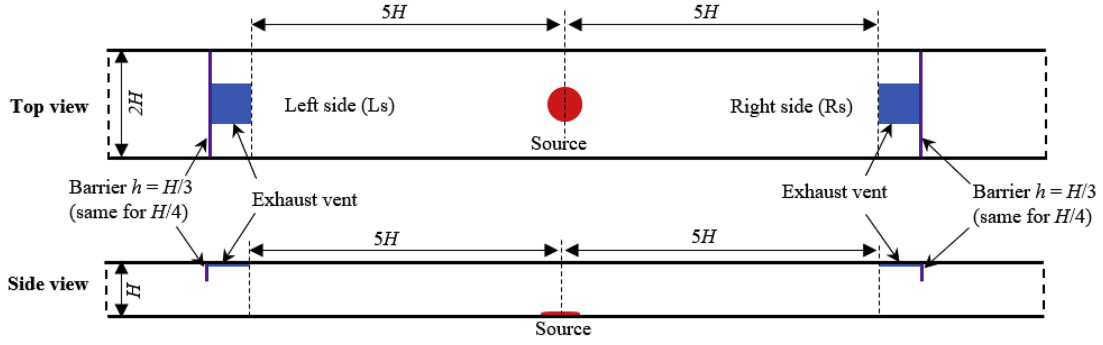


Figure 4.3: Diagram of the experimental setup with large barriers ($h = H/3$) fixed to the tunnel ceiling just upstream of the dampers (in this case, the exhaust vents are represented by square-shaped dampers placed in the centre of the tunnel ceiling, the same is applied for other types of dampers and for the barrier of height $h = H/4$).

4.2.2 Flow control parameter and similarity

As customary in small scale experiments, the fire source within the tunnel is modelled by means of the injection of light gas, a mixture of helium and air [27, 46]. As shown by Jiang et al. [27] in experiments with longitudinally ventilated tunnel, these densimetric plumes can be considered to reliably reproduce the smoke behaviour produced by a fire, provided that the size of the flames does not exceed the tunnel half-height. Of course, adopting this approach, we will fully neglect any dynamic and thermal effect induced by heat transfers from conduction at the tunnel walls or by radiation [17].

We consider a flow in an infinitely long tunnel equipped with a transverse ventilation system while fixing the geometrical parameters of the tunnel (the height H and the width W). We can assert that the extension " L " of the smoke back-layer could depend on the source parameters (i.e. the diameter of the source D_i , the velocity W_i and the density ρ_i of the buoyant gas release) and on the induced longitudinal velocity U_0 [25, 26], as well as on the geometrical parameters of the exhaust vents (i.e. the cross-sectional area A_d , the shape S_d and the position P_d). Adopting basic dimensional arguments [27, 46], assuming negligible diffusive effects, the dimensionless length of the back-layer can then expressed as:

$$\frac{L}{H} = f \left(\Gamma_i, \frac{\rho_i}{\rho_0}, \frac{D_i}{H}, \frac{U_0}{W_i}, \frac{A_d}{H^2}, S_d, P_d \right), \quad (4.1)$$

where ρ_0 is the ambient air density and $\Gamma_i = \frac{5}{4\alpha\pi} \frac{B_i}{D_i W_i^3}$ is the "plume Richardson number", with $\alpha = 0.12$ (a reference value for the "top-hat" entrainment coefficient [39] and

4.2 Experimental set-up and measurement techniques

where

$$B_i = gq_i \frac{\rho_0 - \rho_i}{\rho_0}, \quad (4.2)$$

is the buoyancy flux, with g the gravitational acceleration and q_i the total volume flow of the mixture at the source. Note that the buoyancy flux B_i can be directly linked to an equivalent heat release rate (Q_c) by the relation:

$$Q_c = B_i \frac{\rho_0 T_0 C_p}{g}, \quad (4.3)$$

where T_0 is the ambient air temperature and C_p is the specific heat capacity (assumed constant).

Since the confining velocity $U_{0,c}$ is defined as that inducing a null back-layering length, from Eq. 4.1, we can write

$$\frac{U_{0,c}}{W_i} = f \left(\Gamma_i, \frac{\rho_i}{\rho_0}, \frac{D_i}{H}, \frac{A_d}{H^2}, S_d, P_d \right) \quad (4.4)$$

Previous studies [26, 31] have shown that, considering highly buoyant releases, i.e. for $\Gamma_i > 1$, the relations (Eq. 4.1) and (Eq. 4.4) can be highly simplified. In these conditions the back layering length and the confinement velocity do not show any clear dependence on single source parameter, such as the diameter of the source D_i and the density ρ_i and exit velocity W_i of the buoyant gas release. These parameters affect the flow instead only as far as they induce variations in the source buoyancy flux B_i (Eq. 4.4). In these conditions Eq. 4.1 is therefore reduced to:

$$\frac{L}{H} = f \left(Fr_0, \frac{A_d}{H^2}, S_d, P_d \right), \quad (4.5)$$

with $Fr_0 = U_0 / (B_i/H)^{1/3}$ a Froude number, which expresses the ratio between the inertia forces induced by the ventilation flow and the buoyancy forces induced by the injection of the buoyant plume at the source. The relation (Eq. 4.5) is sometimes [26] presented as a function of "tunnel Richardson number" $Ri_0 = B_i / (HU_0^3) = Fr_0^{-3}$. In this study we will neglect the dependence of the damper opening area A_d (the area of the dampers A_d remains constant), in which case Eq. 4.5 is reduced to:

$$\frac{L}{H} = f(Fr_0, S_d, P_d), \quad (4.6)$$

4.2 Experimental set-up and measurement techniques

which implies that the confinement Froude number

$$Fr_{0,c} \propto U_{0,c} / (B_i/H)^{1/3} = \text{constant}, \quad (4.7)$$

is a function of the shapes and positions of the extractor vents, i.e. that

$$Fr_{0,c} = f(S_d, P_d) \quad (4.8)$$

The determination of the dependences expressed by Eq. 4.6 and Eq. 4.8 constitutes the object of our study.

Note that from Eq. 4.7 we have that the confinement velocity can be related to the buoyancy flux as $U_{0,c} \propto B_i^{1/3}$ (which means that the fire plume is only characterised by its buoyancy flux) and therefore to the heat release rate as $U_{0,c} \propto Q_c^{1/3}$.

4.2.3 Calibration of rotameters and oxygen sensors

The rotameter is a device used to measure the volumetric flow rate of fluid, it consists of a tapered tube with a rotating float inside that is pushed up by the drag force of the flow and pulled down by gravity. Since the drag force depends on the fluid density, for our purposes, the flowmeter scale requires a calibration to take into account the variation of the density of the gas, providing the relationship between the flow rate (indicated by the rotameter) for a reference air density and the actual flow rate, for any gas mixture. For this purpose, tests were carried out in another experimental set-up (Fig. 4.4), made up of: two flow meters to independently control air and helium flows; a long pipe to ensure a good mix of air and helium, a rotameter for flow measurements, two oxygen sensors to measure the concentration of oxygen in the gas mixture.

The tests were carried out for varying density ratios $\rho_i/\rho_0 = 0.5, 0.6, 0.7, 0.8, 0.9$ and 1 . For each of these values of the density ratio, the calibration of the rotameter is performed with mixing rates (q_i) ranging from 130 L/min to 700 L/min (i.e. 8 m³/h to 42 m³/h). The density of the gas mixture is estimated by measuring the oxygen concentration by means of electrochemical sensors placed downstream of the rotameter. This concentration is associated to a voltage value, it is acquired by an Arduino board (ARDUINO UNO - DIP REV3) and displayed on a digital screen (Grove - LCD RGB Backlight). Two rotameters with different measuring ranges of 6.4-64 m³/h and 16-160 m³/h were calibrated.

Fig. 4.5 shows the relationship between the flow rate provided by the rotameter (q_r) and the actual flow rate (q_i). Fig. 4.5a and Fig. 4.5b show the results of the rotameter with measuring ranges of 6.4 m³/h to 64 m³/h and 16 m³/h to 160 m³/h, respectively. A linear fit of the data is performed for each density ratio and a correlation is obtained in the

4.2 Experimental set-up and measurement techniques

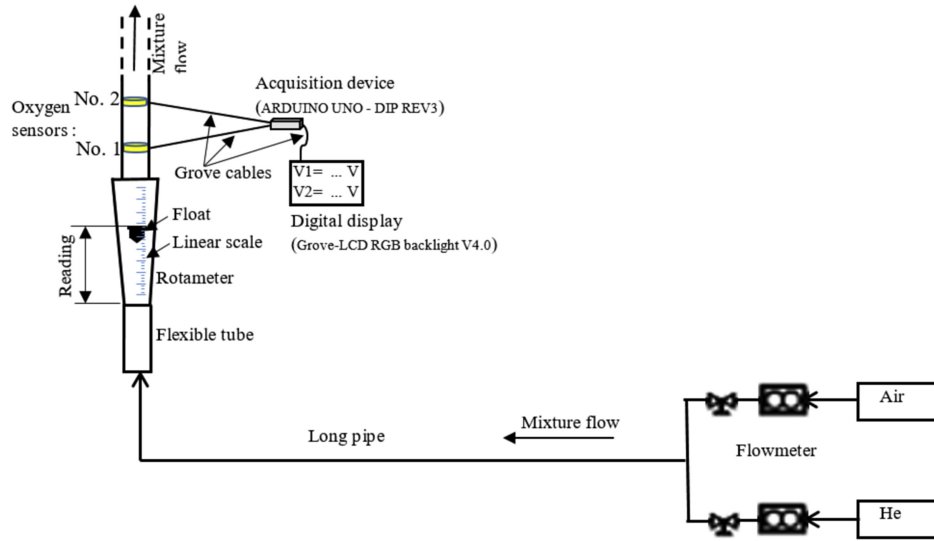


Figure 4.4: Experimental set-up for calibration of rotameters and oxygen sensors.

form: $q_r = \beta q_i$ where β is a constant, whose value depends only on the density of the gas mixture (it decreases with decreasing gas density). From these data we can plot the curve corresponding to any density ratio between 0.5 and 1 by a simple linear interpolation.

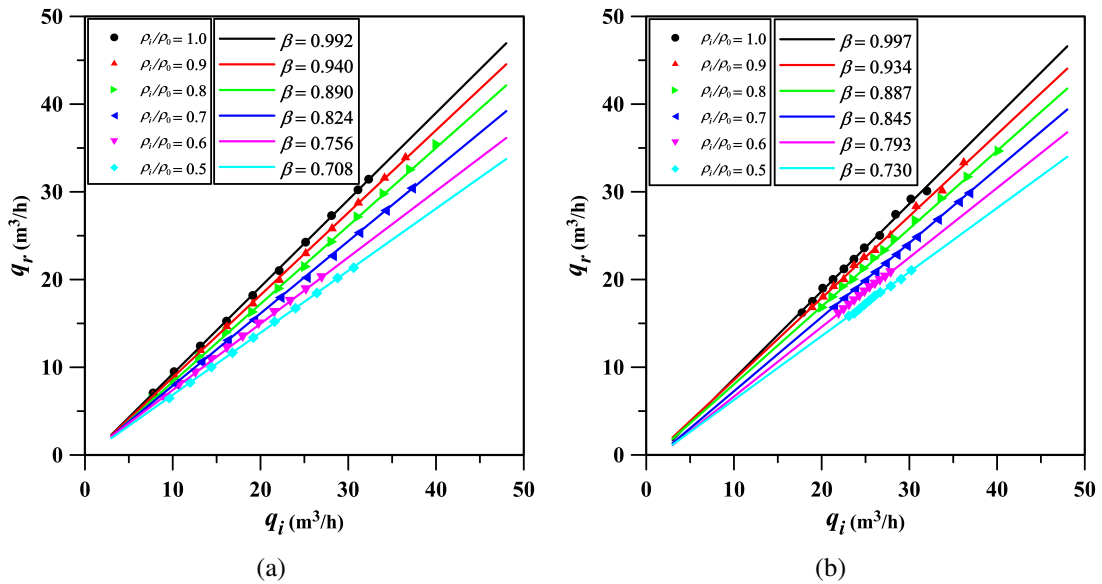


Figure 4.5: The dependence between the measured flow rate q_r and the prescribed flow rate q_i for $0.5 \leq \rho_i/\rho_0 \leq 1$. " β " is the linear correlation factor between q_r and q_i . a) Rotameter with a range: 6.4-64 m³/h. b) Rotameter with a range: 16-160 m³/h.

Fig. 4.6 shows the results on the oxygen concentration measured by both sensors de-

4.2 Experimental set-up and measurement techniques

pending to the density of the mixture. With the type of sensor used in these experiments, we know the percentage of oxygen in the gas mixture (or in the ambient air) through the given output voltage of each sensor. Fig. 4.6a shows that the output voltage V_i increases with the density ρ_i and changes from one sensor to another. Fig. 4.6b shows the dimensionless voltage V_i/V_0 (V_0 is the output voltage of each sensor measured in the ambient air) versus the dimensionless density ρ_i/ρ_0 . The two curves are similar, we can then conclude that both sensors have the same voltage response.

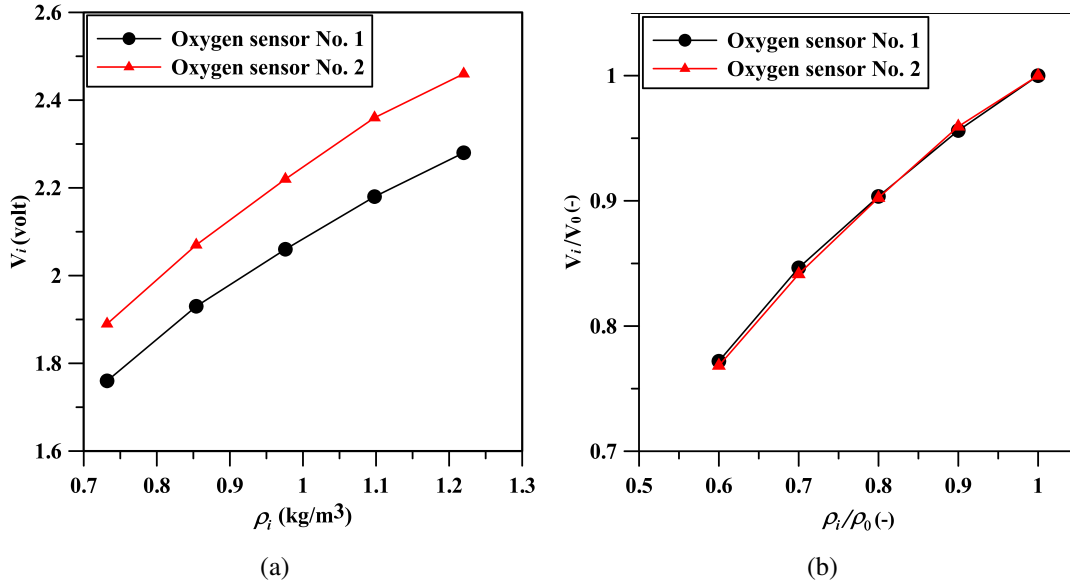


Figure 4.6: Variation of the oxygen concentration measured by the two sensors (expressed in Volt) against the density of the mixture. a) The voltage V_i versus the density ρ_i . b) The dimensionless voltage V_i/V_0 versus the dimensionless density ρ_i/ρ_0 .

From the two output voltage curves plotted in Fig. 4.6a, the density of the gas mixture in the two exhaust ducts can therefore be obtained. Knowing the density of the extraction smoke, the actual flow corresponding to that measured by each rotameter is obtained using the curves (or interpolation curves) plotted in Fig. 4.5.

4.2.4 Experimental protocol

Experiments were performed for a fixed density ratio $\rho_i/\rho_0 = 0.7$, a fixed source diameter $D_i/H = 0.56$, and a plume Richardson number in the range $1 \leq \Gamma_i \leq 40$. With these conditions, the average injection velocity (W_i) at the source varies from 0.13 m/s to 0.73 m/s, the buoyancy flux (B_i) is between $3 \cdot 10^{-3} \text{ m}^4/\text{s}^3$ and $2 \cdot 10^{-2} \text{ m}^4/\text{s}^3$ (and the corresponding heat release rate (Q_c) is between 0.11 KW and 0.71 KW in this reduced scale model).

4.2 Experimental set-up and measurement techniques

The average extraction velocities through the dampers (U_e) were calculated by dividing the extraction flow rate (once they are determined and corrected to the fluid density) by the cross-sectional area of the damper. As shown in Fig. 4.1b, the tunnel is equipped with a pitot tube at one end to estimate the ventilation flow rate. However, for most of the experiments, the ventilation flow rate was too low to be measured by this system. Therefore the longitudinal induced velocity U_0 and the relative air flow q_0 are estimated by a mass balance (assuming that the flow is perfectly symmetric with respect to the source position) as (see Fig. 4.7):

$$q_0 = \frac{\rho_e}{\rho_0} q_e - \frac{\rho_i}{\rho_0} q_i \quad (4.9)$$

where $q_0 = q_{01} = q_{02}$, $q_e = q_{e1} = q_{e2}$ and ρ_e is the density of the extraction smoke flow. Note that the symmetry of the flow has been verified, for a given range of airflow, by directly measuring the longitudinal velocities with a Pitot tube and comparing them to those calculated with Eq. 4.9.

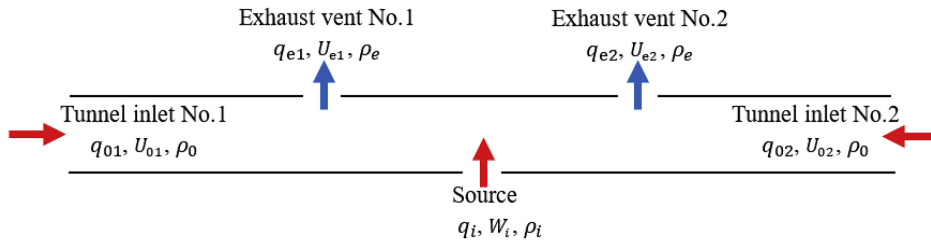


Figure 4.7: Schematic view of all input and output flows in a tunnel with two extraction points.

To ensure a symmetrical dispersion of the smoke flow in the tunnel with respect to the location of the source, the two exhaust fans must be controlled simultaneously and their power adjusted to impose the same flow on both sides. In this way, using flow visualisation and camera recordings, we can then measure the smoke back-layering lengths, determine the confinement velocities according to the source conditions, and report qualitative information about the stratification of the smoke layers in the tunnel with and without barriers. By regulating the power of the exhaust fans, we could set the front of the back-layering flow at the position of the extraction dampers, at the confinement conditions, characterised by a "confinement velocity" ($U_{0,c}$) within the tunnel, and to an associated extraction confinement velocity ($U_{e,c}$). Fig. 4.8 shows an example of smoke visualisation in the tunnel with rectangular exhaust vents for two different ventilation velocities. In case of a ventilation flow lower than the confinement condition (with $U_{e1} = 0.52$ m/s and $U_{e2} = 0.50$ m/s corresponding to $U_{01} = 0.069$ m/s and $U_{02} = 0.063$ m/s), a stratified smoke layer develops downstream

of the exhaust vents (Fig. 4.8a). The smoke layer is stable and symmetrical with respect to the position of the source, its length is equal to twice the tunnel height (i.e. $L/H = 2$).

By increasing the extraction flow rate of the two fans (Fig. 4.8b), the longitudinal velocity of the induced fresh air increases and the back-layering length downstream of the exhaust vents decreases progressively on both sides, until reaching confinement ventilation conditions (i.e. $L/H = 0$), here obtained for $U_{e1,c} = U_{e2,c} = 0.58$ m/s and $U_{01,c} = U_{02,c} = 0.08$ m/s.

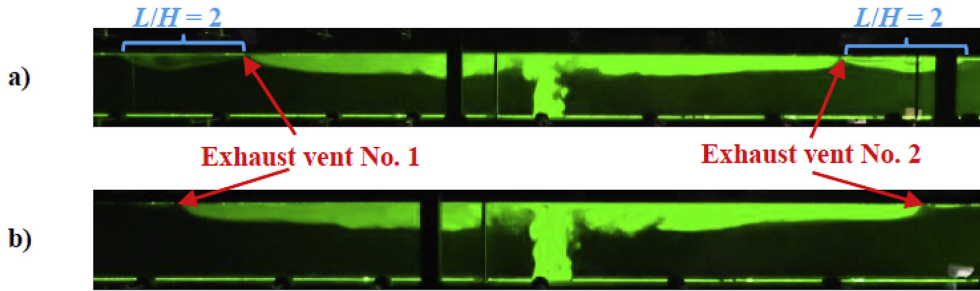


Figure 4.8: Smoke visualisation in the tunnel with a two-point transverse extraction system (rectangular dampers, $\Gamma_i = 8$). a) Non-confinement ventilation conditions: smoke back-layer appears downstream of the dampers. b) Confinement ventilation conditions: smoke backflow is completely suppressed.

4.3 Results and discussions

4.3.1 Smoke backflow length

Measurements of the smoke back-layer lengths downstream of the dampers were performed for given source conditions ($D_i/H = 0.56$, $\rho_i/\rho_0 = 0.7$ and $\Gamma_i = 8$). The flow rate of the two exhaust fans was first set to the minimum, then increased gradually. For each ventilation flow condition, the backlayer length downstream each of the two extraction vents and the corresponding extraction flow rates were recorded. Note that the uncertainty on the estimate of the flow rates with the rotameters is approximately ± 1 m³/h, while the uncertainty on the smoke length measurement is approximately $\pm H/2$. The results obtained for different shapes and locations of the exhaust vents are presented in Fig. 4.9. For all cases, the dimensionless backflow lengths L/H measured on both the left and right sides of the tunnel are plotted against the extraction Froude number $Fr_e = U_e / (B_i/H)^{1/3}$ in Fig. 4.9a and against the longitudinal Froude number $Fr_0 = U_0 / (B_i/H)^{1/3}$ in Fig. 4.9b. As expected (Eq. 4.9), the relationship between U_e and U_0 is linear (as well as between Fr_e and Fr_0), and each curve shown in Fig. 4.9a has the same trend as its corresponding curve in Fig. 4.9b. The results show that the backflow length decreases with the increase of the Froude number. For

each type of exhaust vent and for a fixed value of Froude number, the back-layering length on the right side (Rs) of the tunnel is greater than that measured on the left side (Ls). This is because the inlet flow at the two tunnel entrances are asymmetric, resulting in uneven distribution of head losses. However, for a reduced backlayering length (i.e. $L/H \leq 1$), the effect of these uneven head losses becomes negligible and the backflow becomes perfectly symmetrical (relative to the source location).

Two features can be distinguished from the comparison of the results obtained with dampers of square (SSD) and rectangular shapes (RSD): firstly, the length of the back-layer flow and secondly, on its correlation against the Froude number. With regard to the first point, for the same back-layering length, the Froude number is lower with the rectangular-shaped dampers than with the square-shaped dampers. This means that even though the cross-sectional area of the two shapes of dampers is the same, their efficiency in smoke extraction is different. Concerning the second point, the evolution of the backflow length against the extraction velocity is different for the two different shapes. For rectangular-shaped dampers, the back-layering length decreases very rapidly with increasing smoke extraction rate. As shown in Fig. 4.9, the dimensionless length (L/H) is reduced from 14 to 0 for an extraction Froude number (Fr_e) increasing from 1.10 to 1.72 (i.e. from 0.13 to 0.22 for Fr_0). In this particular case of full-width dampers, the smoke propagation downstream of the exhaust vents can be controlled with relatively low extraction rates, while preserving the stratification of the smoke layers (as illustrated in the example of Fig. 4.8b). For square-shaped dampers (SSD), the development of smoke back-layer exhibits different regimes, depending on the value of the Froude number. The first regime is characterised by a significant decrease in the back-layering length, as well as by the asymmetry of the smoke backflow with respect to the source location (i.e. Ls and Rs curves are not identical). This behaviour can be clearly observed in Fig. 4.9 for $L/H > 1$. The second regime is characterised by the case when $L/H < 1$: the backflow becomes perfectly symmetrical relative to the source location and its length is only slightly affected by changes in the extraction flow rate. In this regime, as observed during flow visualisation experiments, the smoke backlayer is suppressed for the extraction rate values that perturbs the stratification of the smoke layer, i.e. inducing a significant mixing between the ambient air layer and the smoke layer. Furthermore, for these high flow rates we observe the occurrence of a phenomenon called "plug-holing", i.e. the extraction of a large amount of fresh air flowing through the smoke layer. This phenomenon is clearly undesirable since it reduces the effectiveness of transverse ventilation systems. Fig. 4.9 also shows that the position of the square-shaped dampers plays a major role in the smoke back-layering lengths. Indeed, with the same ventilation conditions, the length of the backflow measured in each side of the tunnel is larger

with the vents located on the sides of the tunnel ceiling (SSD-PS) than with the vents in the centre (SSD-PC).

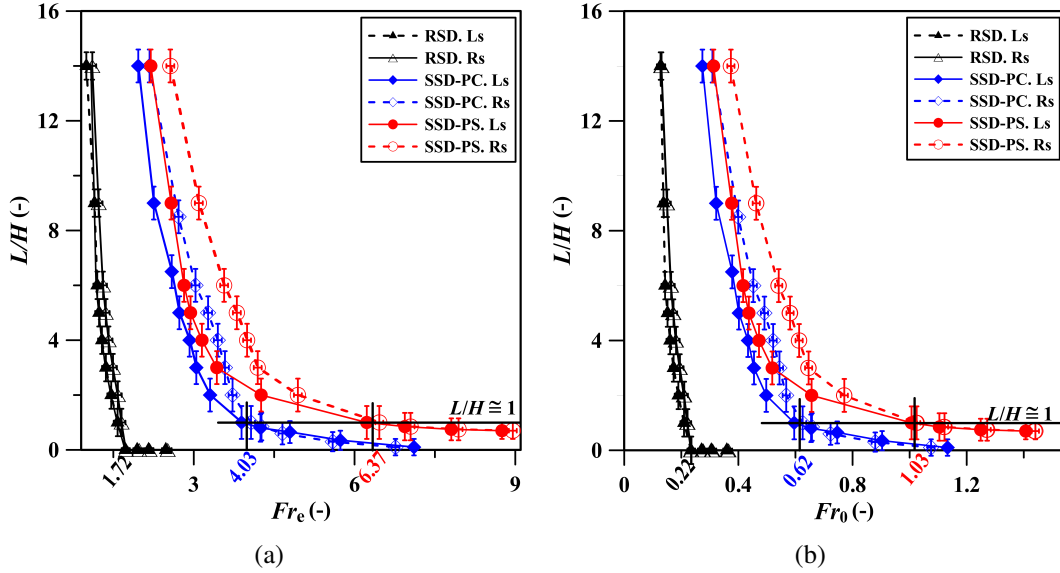


Figure 4.9: a) Dimensionless back-layering length L/H against the extraction Froude number Fr_e . b) Dimensionless back-layering length L/H against the longitudinal Froude number Fr_0 , for different shapes and locations of the exhaust vents.

The difference between the results obtained with the different dampers can be explained as follows: when the buoyant plume impinges the ceiling, the smoke layer extends in both longitudinal directions of the tunnel, it moves near the tunnel ceiling over its entire width. Once the smoke reaches the location of the vents, it is trapped by the full-width dampers, even at relatively low extraction rates. However, if the width of the dampers is much smaller than the width of the tunnel, only the smoke passing through the location of the exhaust vents is directly trapped, while the remaining smoke can flow downstream of the dampers through the remaining width of the tunnel (i.e. width not occupied by the dampers). To prevent this smoke from moving away from the vents, it is necessary to increase the induced longitudinal air flows on both sides of the tunnel. However, the extraction rates required with the vents located in the centre are significantly smaller than those needed with the vents placed on the sides.

Note that the non-dimensional density of the smoke measured by the sensors at the exhaust vents increases with the extraction flow rate for each of the three vent shapes investigated. The variation of ρ_e/ρ_0 was between 0.92 and 0.94 for the rectangular vents and

between 0.95 and 0.98 for the square centre vents and square side vents (where ρ_e is the density of the smoke measured at the exhaust vents). This implies that, under the same source conditions, the higher the extraction rate the greater the proportion of ambient air extracted. In other words, the higher the value of ACH the lower the concentration of smoke in the extracted air. This also explains why the density ratios measured with the square vents are higher than those measured with rectangular vents. This is because the airflow needed to reduce or prevent the smoke back-layering with square vents is greater to that required for rectangular vents.

4.3.2 Confinement velocity

In principle, the confinement condition is reached when the smoke backflow downstream the damper is suppressed, i.e. for $L/H = 0$. However, as can be observed in Fig. 4.9, this condition is difficult to reach for the cases with square shaped dampers (SSD). In these cases the confinement conditions are therefore defined differently, i.e. as those inducing an extent of the backflow which is equal to the tunnel height, i.e. for $L/H = 1$, which will then be assumed as the reference length corresponding to the confinement velocity (a similar criterion was adopted by Vauquelin and Telle [77]). We therefore consider that the confinement condition will be attained when $L/H = 0$ (i.e. total confinement) for the rectangular shaped dampers (RSD) and when $L/H = 1$ for the square shaped dampers (SSD).

The study was performed with the different vents, the velocity measurements are taken from both sides of the tunnel (Ls refers to left side and Rs to the right side). The results on the confinement velocity are represented in Fig. 4.10a as a function of buoyancy flux, with the corresponding best-fit curves. The associated extraction confinement velocities and heat release rates are shown on the right y-axis and at the top x-axis of the graph. Fig. 4.10a shows that for each shape (or position) of dampers, the results for the two sides (curves Ls and Rs) are very similar to each other. Moreover, as expected, $U_{0,c}$ (as well as $U_{e,c}$) increases with increasing buoyancy flux B_i and therefore with increasing HRR. In all cases considered, the general dependence between these quantities can be expressed in the form $U_{0,c} = aB_i^{1/3} = bQ_c^{1/3}$ (similar with $U_{e,c}$), where "a" and "b" are proportionality constants whose values depend on the shape and the location of the dampers (they are low with RSD) as well as on other parameters not considered in this study, such as the shape and the aspect ratio of the tunnel cross section [21, 22], the size of the source [25, 27] and the distance between the source and the extraction points.

The confinement Froude number $Fr_{0,c}$ (as well as $Fr_{e,c}$) is estimated and plotted in Fig. 4.10b against the plume Richardson number Γ_i . As shown in the figure, this number (i.e. $Fr_{0,c}$ or $Fr_{e,c}$) does not depend on the source conditions (Γ_i), it is only related to the

shape and position of the damper, which is in accordance with what is expected (Eq. 4.8). Its value is low with RSD ($Fr_{0,c}$ is around 0.22) and high with SSD-PS ($Fr_{0,c}$ is around 1.10). Note that this latter value exceeds that for a longitudinally ventilated tunnel [31] (which is of the order of unity). This proves that the square-shaped dampers placed on one side of the ceiling are not an effective means with which to control smoke propagation. Moving the dampers from the edge to the centre of the tunnel ceiling reduces the value of the confinement Froude number by approximately one-half and thus improves the efficiency of the ventilation systems.

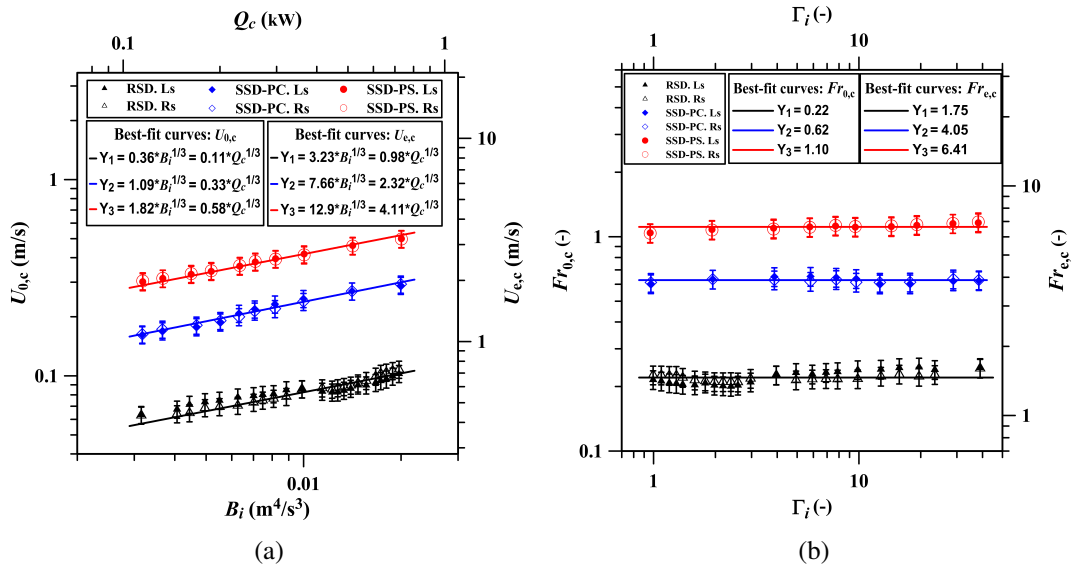


Figure 4.10: a) The confinement velocity $U_{0,c}$ and the associated extraction confinement velocity $U_{e,c}$ against the buoyancy flux B_i and the associated heat release rate Q_c . b) The confinement Froude number $Fr_{0,c}$ and the associated extraction confinement Froude number $Fr_{e,c}$ against the plume Richardson number Γ_i , for different shapes and locations of the exhaust vents.

It is worth noting that the results presented in Fig. 4.10 demonstrated that: i) the width of the damper is the relevant length scale for the smoke spread control in the tunnel with mechanical extraction systems, ii) the location of the damper relative to the centre of the tunnel plays a significant role in the confinement and extraction of smoke and iii) the confinement Froude number does not depend on the source conditions but only on the geometry of the exhaust vents.

It should be noted that, in confinement conditions, the density ratio (between the smoke and ambient air density) measured at the exhaust vents for each configuration increases with the plume Richardson number (i.e. with buoyancy flux and thus with the heat release rate).

For $1 \leq \Gamma_i \leq 40$ (i.e. $3 \cdot 10^{-3} \leq B_i \text{ (m}^4\text{s}^{-3}) \leq 2 \cdot 10^{-2}$), ρ_e/ρ_0 ranged from 0.91 to 0.97 with rectangular vents and from 0.96 to 0.99 with square vents. This can be explained by the fact that the higher the buoyancy flux (or the firepower), the higher the extraction rate, which causes a strong suction of the ambient air through the dampers. This means that the smoke concentrations in the extracted air decrease with increasing confinement values of ACH.

4.3.3 Effect of extraction rate on smoke stratification

Furthermore, we also focus on the stability of the smoke stratification within the tunnel. To that purpose, for each type of damper, the tests are performed with releases characterised by two values of Richardson number ($\Gamma_i = 8$ and $\Gamma_i = 40$) and a fixed density ratio 0.7. The procedure to investigate this effect is to increase (simultaneously) the flow rate of the two exhaust fans and at the same time observing the significant changes in the behaviour of the buoyant smoke flow. Images of these smoke behaviours are then recorded using a video camera and the flow regimes are expressed according to the Froude number Fr_0 . The camera used is the "Canon LEGRIA HF G40". This includes an HD CMOS PRO sensor that provides a high-quality image of 2.07 mega pixels (i.e. an array of 1920 x 1080 pixels) along with precise 20 x optical zoom. The camera can be used to record high bitrate AVCHD 1080p video with variable frame rates.

4.3.3.1 Rectangular-shaped dampers (RSD)

Fig. 4.11 shows the behaviour of the buoyant smoke flow for different stratification regimes with rectangular-shaped dampers (only the right side of the tunnel is shown). Fig. 4.11a shows the smoke in confinement conditions (for $Fr_{0,c} = 0.22$). In this flow configuration, we can see the existence of two distinct layers, an ambient air layer at the bottom and a smoke layer at the top, without any exchange of particles between the two layers. Thus, we consider that stratification is well preserved and refer this to as a "stable stratification" regime. The stratification remains relatively well-preserved until $Fr_0 = 0.60$, when a thin smoke appendix is formed below the exhaust vent (Fig. 4.11b). By further increasing the extraction rates, more ambient air is extracted through the exhaust vents and a larger amount of smoke is directed to the lower air layer (i.e. the plug-holing phenomenon). In this case, several vortices appear at the interface between the two layers, as well as in the lower air layer (Fig. 4.11c). Nevertheless, the visibility remains clear at the bottom of the tunnel. This configuration (i.e. when $0.6 \leq Fr_0 \leq 1.1$ approximately) marks the transition between a stable and unstable stratification regime. As the extraction rate increases further, the suction force increases, resulting in an increase in the induced longitudinal flow rate. The shear of generated instabilities induces the mixing between the upper and the lower fluid layers (see

Fig. 4.11d). In this case, the whole area between the both vents is completely filled with smoke giving rise to a flow regime that we refer to as "unstable".

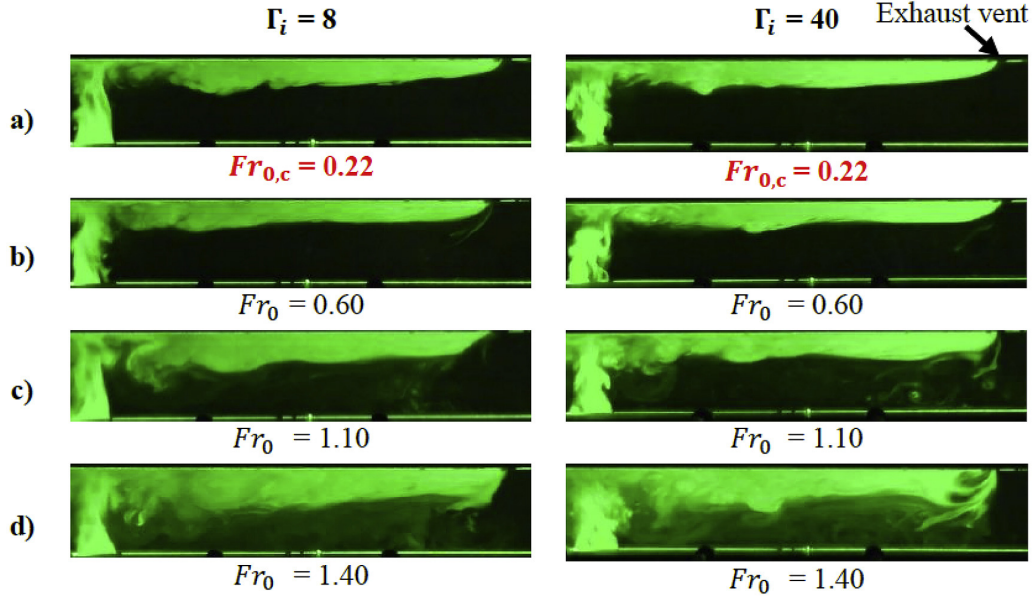


Figure 4.11: Visualisation of the different stratification regimes of the buoyant smoke flow in the tunnel equipped with rectangular shaped dampers (RSD).

4.3.3.2 Square-shaped dampers positioned in the centre (SSD-PC)

Fig. 4.12 shows the flow visualisations for square-shaped dampers placed in the centre (SSD-PC). As previously mentioned (section 4.3.2), the confinements conditions with the square-shaped vents are attained when the backflow downstream of the dampers becomes insensitive to the induced longitudinal air flow (i.e. for $L/H \approx 1$). The confinement Froude number is equal approximately to 0.60 (Fig. 4.12a). In this configuration, the stratification of the smoke layer is preserved. We can however notice the appearance of a small appendix (identical to that observed in Fig. 4.11b) at the bottom of the vents. This highlights the beginning of a transition between a stable stratification and an unstable stratification, which occurs for a Froude number identical to that estimated with rectangular-shaped dampers (i.e. $Fr_0 = 0.60$). By increasing the extraction flow rate, large smoke vortices are produced in the lower air layer (Fig. 4.12b), which we consider as representative of the unstable stratification regime. This happens for $Fr_0 = 0.80$, which is lower than that observed for the case of rectangular-shaped dampers (i.e. $Fr_0 = 1.10$). Fig. 4.12c and Fig. 4.12d show the configurations with a partial and complete de-stratification of the buoyant smoke layer. In these cases, the bottom of the tunnel is completely filled with smoke, therefore severely restricting the visibility.

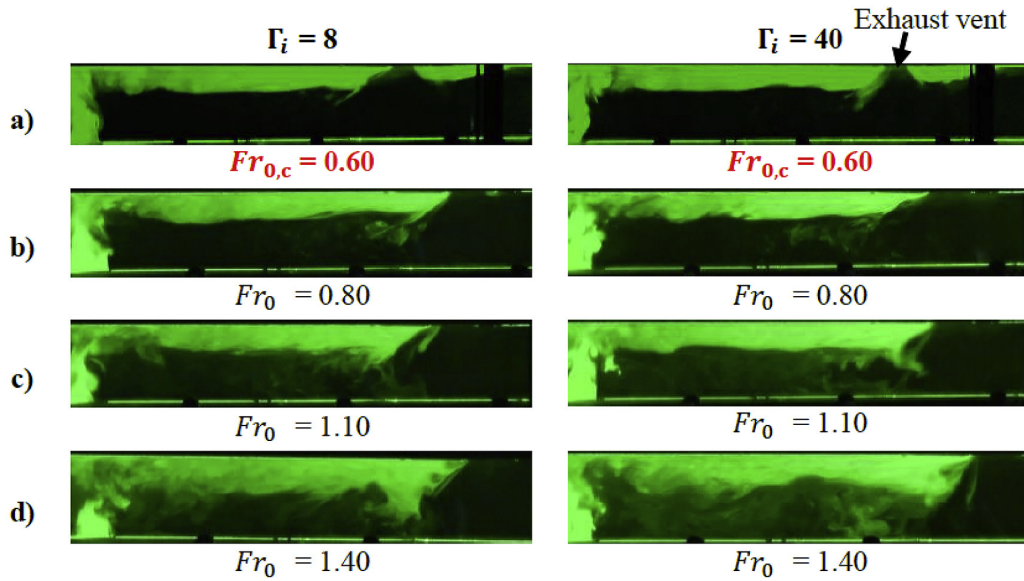


Figure 4.12: Visualisation of the different stratification regimes of the buoyant smoke flow in the tunnel equipped with square-shaped dampers located in the centre (SSD-PC).

4.3.3.3 Square-shaped dampers positioned in the side (SSD-PS)

Fig. 4.13 shows the flow visualisations for square shaped dampers placed on one side of the tunnel ceiling (SSD-PS). We observe that: i) the vortices at the interfacial regions (see Fig.

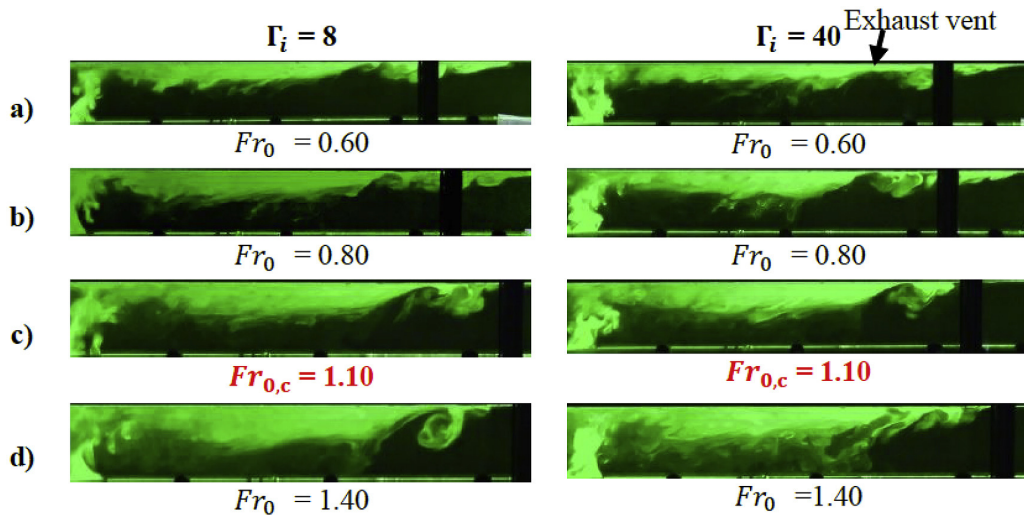


Figure 4.13: Visualisation of the different stratification regimes of the buoyant smoke flow in the tunnel equipped with square-shaped dampers located on the side of the tunnel ceiling (SSD-PS).

4.13a) are well developed and clearly visible, due to the strong shear; ii) the smoke layer is slightly thicker than that observed in the previous case where the position of the vents is

aligned on the same axis as the source location; iii) the stratification of the buoyant smoke layer is completely suppressed even before reaching the confinement conditions (see Fig. 4.13c), i.e. $Fr_{0,c} = 1.10$. In summary, the smoke stratification pattern can be classified into three regimes identical to those observed with square shaped dampers located in the centre: stable stratification for a $Fr_0 < 0.6$, stable-unstable transition for a $0.6 \leq Fr_0 \leq 0.8$ and unstable for a $Fr_0 > 0.8$.

Finally, it should be noted from Fig. 4.11, Fig. 4.12 and Fig. 4.13 that the smoke stratification behaviour for a constant Froude number is independent of the plume Richardson number (a similar smoke behaviour is observed with $\Gamma_i = 8$ and $\Gamma_i = 40$), however, it seems that this changes with the shape (or position) of the exhaust vents.

4.3.4 Effect of solid barriers on the propagation and behaviour of smoke

Our results show that the confinement conditions can be reached for flow rates that already induce a de-stratification of the smoke layer within the tunnel. It is therefore interesting to seek solutions to improve the efficiency of smoke extraction systems, i.e. the preservation of the stratification and the confinement of the smoke within a limited section of the tunnel, in which the extraction takes place. For this purpose, we consider here the effect of solid barriers downstream of the dampers on the reduction of the confinement velocity and on the stratification conditions.

The study was carried out in the same conditions as those established in the section 4.3.2. The results, shown in Fig. 4.14, are presented in terms of a dimensionless number Rc ; defined as the ratio between the confinement velocity in the tunnel with barriers and the confinement velocity in the tunnel with no barriers (for the same conditions). This ratio is written in the form $Rc = \frac{U_{0,c \text{ with barrier}}}{U_{0,c \text{ without barrier}}}$ and the quantity $(1 - Rc)$ characterises the reduction rate of the confinement velocity due to the presence of the barrier. It was verified that the confinement velocity reduction was the same for both sides of the tunnel. As shown in Fig. 4.14, the reduction of the confinement velocity is independent of the source conditions (i.e. in all cases the ratio Rc is independent of Γ_i). But it is very different according to the shape of the dampers.

With the rectangular-shaped dampers in place, the effect of the barriers on the reduction of the confinement velocities is very low (the reduction is less than 10% and is almost the same for both barriers $H/4$ and $H/3$). We have to conclude that the rectangular dampers are so effective in the smoke extraction, that the presence of the barriers has a very little effect on the smoke confinement. In tunnels equipped with such dampers, the use of barriers is therefore not necessary.

With the square-shaped dampers in place, the results show instead that the barriers can

significantly reduce the confinement velocities. This reduction increases with the height of the barriers and depends only slightly on the position of the dampers: it is slightly better with dampers placed in the centre of the tunnel ceiling where the reduction rates ($1 - R_c$) are 38% and 58% (with the barriers $H/4$ and $H/3$) against 32% and 55% with dampers placed on the side. This means that, in this case, the barriers can effectively control the spread of smoke downstream of the dampers even for relatively low extraction flow rates. They block the smoke that accumulates close to the dampers and is then easily extracted by the exhaust ducts. The smoke remains completely confined in the area between the two positions of the dampers, unlike the case with no barriers where a small layer of smoke appears downstream of the dampers, particularly with the dampers placed at the edge of the tunnel, even if the extraction rate is very high (as shown in Fig. 4.13).

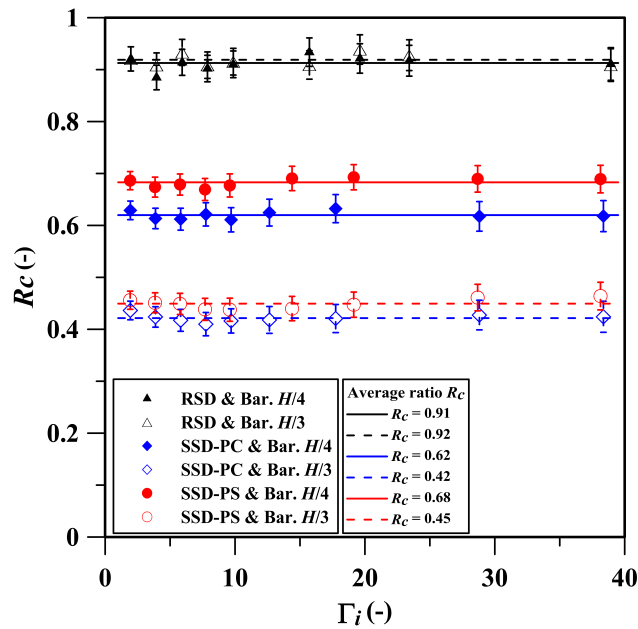


Figure 4.14: The velocity ratio R_c , given by the confinement velocity in the tunnel with barriers to the confinement velocity in the empty tunnel, against the plume Richardson number Γ_i , for different shapes and locations of the exhaust vents and with both barriers of height $H/4$ and $H/3$.

Fig. 4.15 shows a typical example of the visualisation of smoke behaviour in the tunnel with and without barriers equipped with square-shaped dampers placed on the side (i.e. case in which the confinement flow rates are higher and the level of stratification is worse). The three flow visualisations are obtained for same source conditions ($D_i/H = 0.56$, $\rho_i/\rho_0 = 0.7$ and $\Gamma_i = 40$) but for different ventilation flow. Fig. 4.15a shows the configuration with no barriers, which is the same as that presented previously in Fig. 4.13c, where we have seen

that the stratification of the gases is completely disturbed even before reaching the confinement conditions. The visualisation of the flow in the tunnel with a barrier of height $h = H/4$ is presented in Fig. 4.15b. In this case, the total confinement is reached for a $Fr_{0,c} = 0.75$ and the stratification condition of the smoke is better preserved compared to the case of a tunnel without barriers. Small vortices appear and disappear at the interface between the smoke layer and the underlying air flow, but the mixing between the two is small. The behaviour of the confinement smoke can therefore be considered to be in a transition between the stable and unstable stratification regime, which is however significantly different from the unstable regime observed in the case without barriers (Fig. 4.15a). The visualisation of the smoke flow in the tunnel with the largest barrier ($H/3$) is presented in Fig. 4.15c. In this case, the confinement Froude number is reduced by 55% of its reference value, i.e. in the tunnel without barriers. The stratification of the smoke layer is well preserved so that its behaviour can be identified as a "stable" regime. This means that the barrier $H/3$ allows a complete confinement of the smoke with a transition from an unstable stratification regime in the empty tunnel (Fig. 4.15a) to a fully stable regime in the tunnel with largest barriers (Fig. 4.15c). The presence of these barriers therefore results in an increased efficiency of the mechanical extraction systems and thus in an improvement of the safety conditions for the tunnel users.

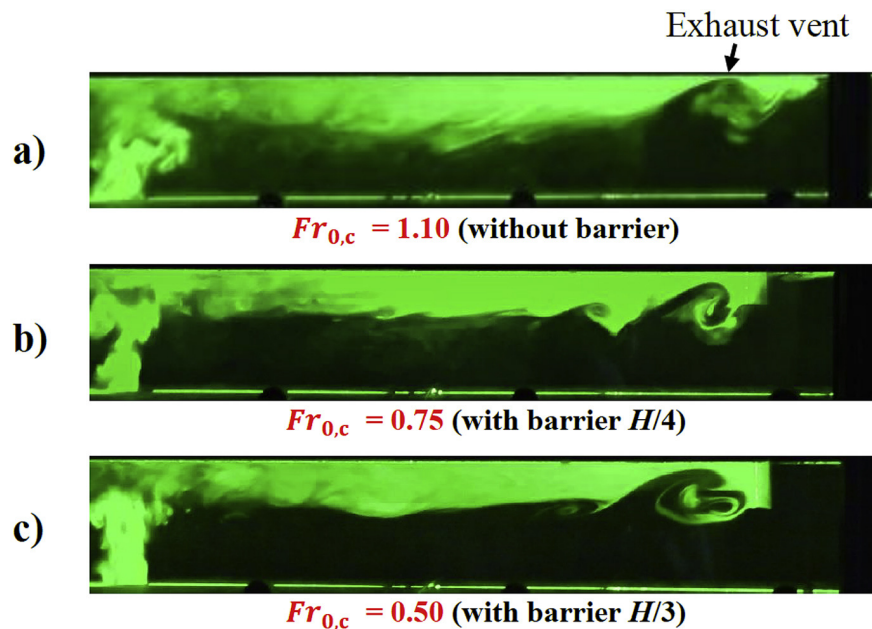


Figure 4.15: Visualisation of the smoke flow in the tunnel equipped with square shaped dampers placed on one of the sides of the tunnel ceiling (confinement conditions with $\Gamma_i = 40$). a) Tunnel without barriers ($Fr_{0,c} = 1.10$). b) Tunnel with a large barrier $H/4$ ($Fr_{0,c} = 0.75$). c) Tunnel with a largest barrier of height $H/3$ ($Fr_{0,c} = 0.50$).

4.4 Conclusions

In this study, we performed a series of experiments in a small-scale tunnel to study the propagation of buoyant smoke injected into a tunnel where the plume is confined between two exhaust vents located on each side of the source. Our analysis focuses on two main geometrical parameters: the shape of the dampers (square and rectangular with same surface area) and the position of the square-shaped dampers (in the centre and on the side of the tunnel ceiling). Our aim was to evaluate the influence of these parameters on i) the backflow length downstream of the dampers, ii) the confinement velocity and iii) the preservation of the stratification of the smoke flow. The main findings are:

- The back-layering length decreases more rapidly with rectangular shaped dampers. Its evolution, in the case of square-shaped dampers, begins with a rapid decline followed by a slight decrease when $L/H \approx 1$.
- In this study, where the area of the dampers relative to the height of the tunnel $\left(\frac{A_d}{H^2}\right)$ has been held constant, the Froude number defined as $Fr_{0,c} = U_{0,c}/(B_i/H)^{1/3}$ (or as $Fr_{0,c} = U_{0,c}/(Q_c/H)^{1/3}$ for a fire plume) is the only parameter that controls the flow. The confinement conditions are reached with a constant Froude number, this gives the relationship between $U_{0,c}$ and B_i/H (or Q_c/H) as follows: $U_{0,c} = Fr_{0,c}(B_i/H)^{1/3}$ (or $U_{0,c} = Fr_{0,c}(Q_c/H)^{1/3}$). The proportionality factor ($Fr_{0,c}$) depends on both the shape and the position of the dampers, its values are lowest with the rectangular dampers and are highest with the square dampers placed on the side of the tunnel ceiling.
- The stratification of the smoke layer is affected by the extraction rate. The higher the flow rate, the more unstable the smoke stratification. Depending on the Froude number, the flow configurations can be classified into three regimes: stable, transient and unstable.
- The confinement conditions are achieved in the stable regime with rectangular dampers, in the transition regime with square dampers placed in the centre and in unstable regime with square dampers placed on the side.

In conclusion, the shape and location of the dampers play an important role on the control of smoke in transverse ventilation tunnels. The results highlight two main features: first, the width of the damper is the relevant length scale; the larger it is, the better the smoke control and the second, the location of the vents on the tunnel ceiling is critical; the closer they are to the centre, the more effective they are.

Subsequently, we evaluated the effectiveness of solid barriers, placed at the tunnel ceiling downstream of the dampers, on improving the efficiency of the ventilation system. The results showed that they only have an influence when the width of the dampers are smaller than the width of the tunnel. In such a case, the confinement velocity is significantly reduced and the stratification level of the smoke layer is greatly enhanced, especially when the height of the barrier is large.

These results provide interesting indications for the optimisation of transverse ventilation systems. The reduction of the extraction flow rates is first and foremost an economical solution, since it allows for a reduction of the energy consumption. In addition, the definition of the optimal flow rate is also essential to ensure the safety of the tunnel users, by identifying the ventilation conditions preserving the stratification of the smoke layer confined between the two dampers. Installing mobile barriers can help with this, these barriers improve the performance of the smoke extraction system and therefore ensure a highest level of safety for users in the instance of a fire.

In this study, we focused on geometrical configurations of the dampers in which their distance from the buoyant source was fixed, and equal to $5H$. Further work will be then needed to study the effect of asymmetric dampers location (relative to the source position), of the variation of the distance between the source and the dampers, of the variation of the cross-sectional area of the extractor vents as well of the presence of traffic flows on the smoke propagation (see Chapter 3 for a similar study in the case of longitudinal ventilation) will be studied. Other research work will also have to investigate the role of heat losses induced by radiation and thermal conduction at tunnel walls (see Salizzoni et al. [26] for a similar study in the case of longitudinal ventilation).

NUMERICAL SIMULATIONS OF FIRES IN ROAD TUNNELS: A COMPLEMENTARY STUDY

Fires in road tunnels with longitudinal and transverse ventilation systems are investigated numerically using Fire Dynamics Simulator (FDS) software and adopting Large Eddy Simulation (LES) approach. The aim is to reproduce numerically experimental results presented previously in chapters 2, 3 and 4 in order to obtain further insight on the dynamics of the plume flows and to evaluate the capability of the numerical model to simulate the fires in road tunnels. First, the PIV experiments are reproduced numerically by considering both the forced plumes (with $\Gamma_i = 0.0075$) and the lazy plumes (with $\Gamma_i = 1.45$) and varying the values of the density ratio ρ_i/ρ_0 . Slight disagreements between the experimental and numerical results are observed for the non-Boussinesq lazy plumes, where the dimensionless critical velocity $U_{0,cr}/W_i$ exhibits a dependence on the density ratio ρ_i/ρ_0 that is not observed experimentally. The time-averaged fields of the two velocity components are well reproduced numerically, but the buoyant plumes are more inclined (in the same direction as the ventilation flow) in the numerical case, especially for forced releases. The dimensionless standard deviation of the two velocity components and the non-dimensional Reynolds shear stress are computed numerically, however their amplitude is relatively small in the numerical case. The effect of solid barriers on smoke propagation within a longitudinally ventilated tunnel is then investigated. The numerical data on the critical velocity reduction rates due to barriers of different sizes are in good agreement with the experimental data. However, the numerical data gives slightly greater lengths of the smoke back-layer. Finally, the effects of the shape and position of the dampers on the confinement of fire smoke in a tunnel equipped with a transverse ventilation system are evaluated. The comparison between the results of the physical experiments and numerical model shows that the confinement conditions are similar for the rectangular vents and slightly different for the square vents. For square side vents, the back-layer is larger for the numerical case at all extraction velocities, while for the

other two vents configurations, the difference between the numerical and experimental data is not significant. The effects of solid barriers on smoke control are then assessed only for square vents. The numerical findings are consistent with prior results of the experimental simulations.

Keywords: Fire dynamics simulator, Large eddy simulation, Road tunnel, Fire smoke, Back-layer, Critical velocity, Confinement Velocity.

5.1 Introduction

Computational Fluid Dynamics (CFD) is a very powerful tool for investigating a wide range of research and engineering problems in many fields of study and industries. CFD is able to simulate the free-stream flow of the fluid and its interaction with surfaces defined by boundary conditions, by numerically solving the equations governing the fluid. Numerical simulations allow access to all instantaneous information (velocity, pressure, temperature, density) at each point of the computational field.

In fire simulations, one of most commonly used software is known as "Fire Dynamics Simulator (FDS)" [100], developed by National Institute of Standards and Technology (NIST) [101]. So far, FDS has been used, for example, to analyse the smoke dispersion and fire propagation [102–105], to evaluate critical ventilation velocity (i.e. the minimum ventilation velocity required to prevent smoke from flowing upstream of the fire source) against the fire heat release rate [23, 54, 55, 72] and to estimate the temperature distribution of fire-induced smoke along mechanically ventilated tunnels [48, 106–108].

FDS numerically solves a low Mach number formulation of Navier-Stokes equations in a discretized domain by adopting a LES approach [109, 110]. Via low-pass filtering of the Navier–Stokes equations, the large eddies of the flow are explicitly resolved by LES while the smaller are modelled using Deardorff eddy viscosity model [111, 112]:

$$\mu_t = \rho C_D \Delta \sqrt{k_{sgs}}, \quad (5.1)$$

where μ_t is the turbulent viscosity, ρ is the density, C_D is the model constant and its value is set to 0.1 [113], Δ is the filter width which is taken as the maximum cell dimension, k_{sgs} is the sub-grid scale (sgs) kinetic energy (see B.4.2.1.3). Combustion and radiation are introduced into the governing equations via well-defined source terms in the energy transport equation (see B.4.2.2). More details on the governing equations and FDS software are provided in Appendix B.

In this study, numerical simulations of fires in a tunnel with longitudinal ventilation and transverse ventilation are carried out using FDS software. The objective is to reproduce

numerically some experimental tests presented in the previous chapters and to show some flow fields that we were not able to visualise during the experiments (e.g. the smoke behaviour at the tunnel ceiling in the case of a transverse ventilation). The study is divided into three parts and, in each part, the numerical results are analysed and compared with the experimental results. In the first part, the experimental test of PIV are reproduced and the mean velocity fields and the fluctuating velocity fields are obtained. In the second part, the effects of solid barriers (fixed to the tunnel ceiling) on smoke control are studied without taking into account the effects of vehicular blockage. In the third part, the effects of both the shape and the positions of the exhaust vents on the smoke propagation are investigated.

5.2 Numerical simulations

In all simulations, the fire smoke plume is modelled by an air/helium mixture, released from a square source with the same cross sectional area as in the experiment. The source is placed at the centre of the tunnel and its surface is set at floor level. The conditions defined at the source are the total volume flow of the air/helium mixture and the mass fraction of the helium (Fig. 5.1). For each simulation, these conditions are calculated from the corresponding experimental data. The wall is defined as a "concrete" of 3 mm thick and backed up to the ambient. The radiation and the heat losses at the tunnel walls are not taken into account. The tunnel walls are smooth and the near-wall velocity components are related with the wall shear stress components according to the wall model of Werner–Wengle [114]. In the longitudinal ventilation condition, the velocity is fixed at the tunnel inlet, while the tunnel outlet is set "open" to the external ambient environment (Fig. 5.1a). In the transverse ventilation condition, the extraction flow rates are fixed at the level of both exhaust vents while the two ends of the tunnel are set as "open" (Fig. 5.1b). The ambient temperature in the tunnel is set at 20° C across all simulations. The size of grids is chosen according to McGrattan et al. [100], estimating a characteristic fire diameter D^* defined as:

$$D^* = \left(\frac{Q_c}{\rho_0 C_p T_0 \sqrt{g}} \right)^{2/5}, \quad (5.2)$$

where Q_c is the heat release rate, ρ_0 is the ambient air density, T_0 is the ambient air temperature, C_p is the specific heat capacity and g the gravitational acceleration. McGrattan et al. [100] suggested that the measure of how well the flow field is resolved depends on the value of the non-dimensional ratio $\frac{D^*}{\delta x}$ and proved that a value in the range of 4 to 16 is acceptable to ensure reliable results; δx is the nominal size of a mesh cell. Both the

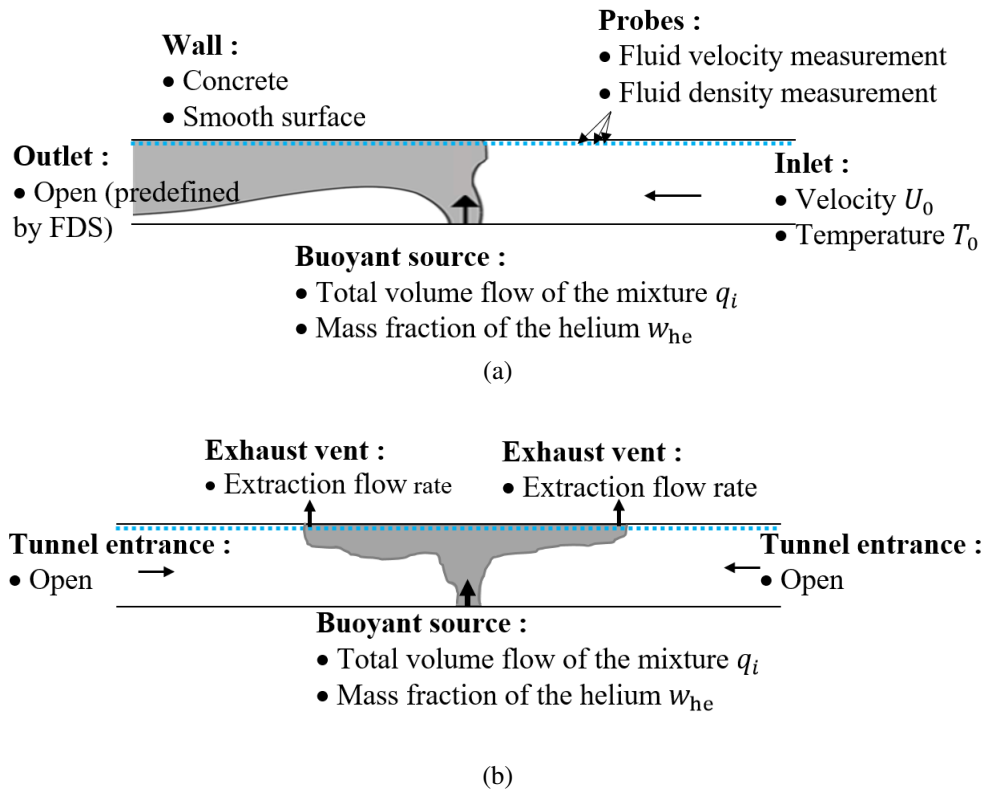


Figure 5.1: Boundary conditions for numerical simulations of tunnel fires using a mixture of air/helium. a) Longitudinal ventilation. b) Transverse ventilation.

Courant-Friedrichs-Lewy (CFL) constraint and the Von Neumann (VN) constraint are used to estimate the convergence calculation and maintain the stability of the numerical scheme (see B.4.3.1). In the default LES mode of operation, the time step is adjusted to ensure the CFL between 0.8 and 1 and the VN between 0.4 and 0.5. The simulation time is chosen so that the flow reaches a statistically stable state. In quasi-steady state, the backlayer lengths and the critical velocities in the tunnel can be determined either by measurements of the time-averaged longitudinal velocity, or the measurements of the time-averaged density (or temperature in the case of fires) of the flow (placing the probes just below the tunnel ceiling along the x -axis, see Fig. 5.1). Fig. 5.2 shows an example of evaluation of the critical velocity in the longitudinally ventilated tunnel by measuring the density of fluid flow along the length of the tunnel centre at the ceiling height every 0.01 m (i.e. probes placed along the x -axis at $y = 0.18$ m and $z = 0.17$ m).

Fig. 5.2a shows the evolution of the fluid density ρ against the distance x at the critical conditions (example taken from the simulated cases). As shown in Fig. 5.1a, the direction of the flow in the longitudinal ventilation is from right to left. Starting from the right and approaching the buoyant source, Fig. 5.2a shows that the density of the fluid in the

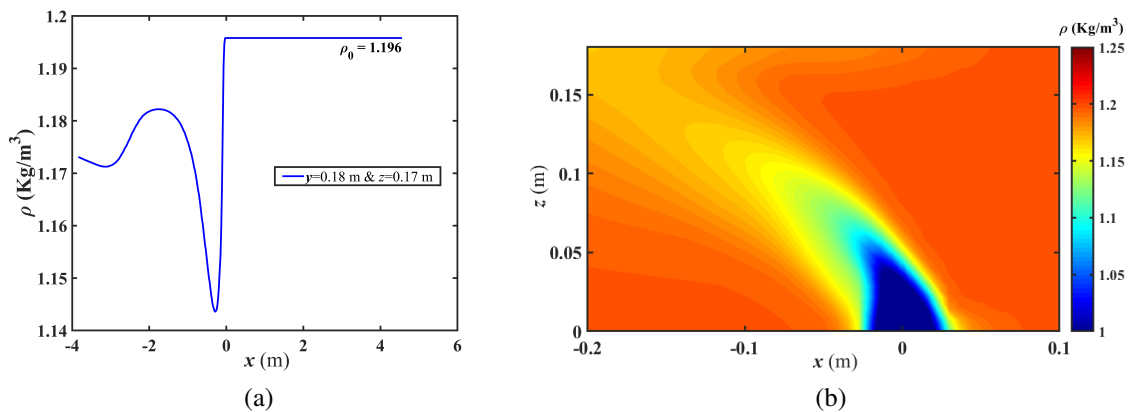


Figure 5.2: Results of a fire simulation under critical ventilation conditions. a) Fluid density profile obtained along the tunnel ceiling. b) Mean density field in the region within which the source is located.

tunnel ceiling remains constant and keeps the same value as that of the ambient air (i.e. $\rho = \rho_0$). At approximately $x = 0$ m (i.e. centre of the source), the density of the flow suddenly decreases. This decrease is interpreted by the presence of the smoke flow. Hence, the longitudinal ventilation velocity that prevents the smoke from flowing upstream of the source corresponds to the critical velocity (i.e. $U_0 = U_{0,cr}$). Fig. 5.2b shows the mean density field in the region where the source is placed. From this figure, it is possible to see, just above the source, thick lines that define the front of the backlayering flow that forms behind impingement point, downstream of the source. The same method is used to determine the length of the smoke back-layering upstream of the source by measuring the distance along the centre of the tunnel ceiling between the source and the point where the profile of the flow density begins decreasing upstream of the source. In a similar way, the backflow length in the transverse ventilation is defined as the distance from the edge of the vent to the point at which the fluid density ρ reaches ρ_0 . Finally, the confinement velocity is defined as the minimum value of the induced longitudinal velocity that confines the smoke within the extraction zone.

5.3 Results

5.3.1 Behaviour of densimetric plumes in a longitudinally ventilated tunnel

The four cases of experimental configurations investigated by means of PIV (Chapter 2) are reproduced numerically (see Table 2.1). As in the experiments, the simulations are

conducted in two steps. First, the critical velocities are evaluated with a good grid resolution in the near-source region. Then, under critical conditions, the resolution is refined enough to obtain a high resolution on velocity field calculations. The results obtained are presented and compared with the experimental results.

5.3.1.1 Determination of the critical velocity

The tunnel domain is divided into three sub-domains: a central region, in which the mesh is more refined, and two lateral regions. For all cases considered, the central region is the same as the measurement region of the PIV experiments. The mesh size in the middle region is fixed according to McGrattan et al. [100]. According to Table 2.2 and using Eq. 5.2, the values of δx corresponding to the lowest heat release rate (i.e. $Q_c = 0.06$ KW) range from 1 mm to 5 mm and those corresponding to the highest HRR (i.e. $Q_c = 1.12$ KW) range from 4 mm to 16 mm. Therefore, $\delta x = 5$ mm is chosen to be the size of the cells in the region in which the source is placed (i.e. middle region). In the other domains the grid size is instead $0.01 \text{ m} \times 0.01 \text{ m} \times 0.01 \text{ m}$. As a result, the total number of cells reached for the simulation of forced and lazy plumes is 662256 cells and 748440 cells, respectively. To reduce the computational time, the parallel processing (i.e. distributed grid computing) using Message Passing Interface (MPI) libraries is used by assigning a multi-core processor (of 10 cores and 8 Gb RAM) to each sub-domain. For each case, the simulation time is set to 100 seconds, which is more than enough for the flow to reach a statistically steady state.

To estimate the value of the critical velocity of each simulated case, the longitudinal profile of the mean density was analysed (as previously shown in Fig. 5.2a). The results obtained are summarised in Table 5.1 and compared to those evaluated experimentally. Focusing on results for forced plumes (cases 1 and 2), a very good agreement can be observed between experimental and numerical results (the difference is below 2%). This concordance illustrates that, for momentum-driven forced plumes, the numerical model is able to properly take into account the effects of the density ratio ρ_i/ρ_0 (i.e. non-Boussinesq effects). Indeed, as shown by Jiang et al. [31] and by the experiments presented in Chapter 2, for a fixed Richardson number and a fixed source diameter, a reduced density ratio induces a reduced non-dimensional critical velocity. The experimental and numerical results for lazy plumes agree well also in case3 where $\rho_i/\rho_0 = 0.8$ (the difference is less than 3%). For case4 (where the density ratio is low $\rho_i/\rho_0 = 0.3$), the difference between numerical predictions and experimental results is instead larger, and attains 20%. This means that our numerical results exhibit a dependance on non-Boussinesq effects that has not been observed experimentally.

Table 5.1: Numerical results on the critical velocity and their comparison with the experimental results.

Case	Source conditions		Experimental results		Numerical results		$\frac{(U_{0,cr})_{num.} - (U_{0,cr})_{exp.}}{(U_{0,cr})_{num.}}$
	Γ_i	ρ_i/ρ_0	$U_{0,cr}$ (m/s)	$U_{0,cr}/W_i$ (-)	$U_{0,cr}$ (m/s)	$U_{0,cr}/W_i$ (-)	
1	0.0075	0.8	0.60	0.150	0.595	0.149	1%
2	0.0075	0.2	0.62	0.077	0.621	0.077	0%
3	1.45	0.8	0.15	0.365	0.155	0.378	3%
4	1.45	0.3	0.28	0.364	0.35	0.441	20%

5.3.1.2 Study of average and fluctuating flow components

To achieve a high spatial resolution of the velocity fields and capture the dominant flow features, the grid resolution must be fine enough to capture the kinetic energy containing eddy motions. Indeed, as in the numerical model, the fluid velocity is assumed to be uniform within each cell (changing only with time), the accuracy with which the flow dynamics is simulated depends on the number of cells considered into the simulation (i.e. the grid size relative to the domain size). For this purpose, the mesh should be further refined in the areas within which the source is placed (i.e. area of interest). Therefore, the size of the cells considered in these areas is equal to 1 mm. This means that, considering the largest eddy length scales equal to the tunnel height, the ratio between the largest and the smallest scales that can be computed numerically is of order 180, and this requires a large computational costs. In lazy plume simulations, this resolution induces numerical instabilities resulting from an abrupt change in grid sizes (see Fig. 5.3a). For this reason, in both cases (case3 and case4), the grid size in the near-source region is set to 2 mm and the simulations are performed without any appearance of the numerical instabilities (see Fig. 5.3b).

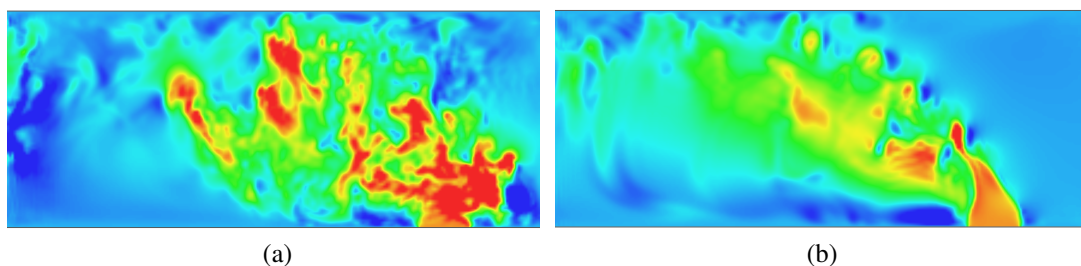


Figure 5.3: Instantaneous velocity fields of the vertical component taken from case3. a) With grid sizes of 1 mm (appearance of numerical instabilities). b) With grid sizes of 2 mm (no numerical instabilities).

The total number of cells in the current simulations of forced and lazy plumes is 17. 4 and 4.2 million grid cells, respectively. To save computing time, parallel computing is performed, dividing the computational domain into eight sub-domains and assigning a multi-core processor to each sub-domain. Despite this, the computation time for a simulation of 100 seconds was between two and three weeks for lazy plumes and between seven and eight weeks for forced plumes.

Fig. 5.4 shows an example on the effect of mesh size on the average velocity field of the vertical component. Fig. 5.4a illustrates the case with a cell size of 5 mm and Fig. 5.4b the case with a cell size of 1 mm: for the larger grid size (Fig. 5.4a), the vertical velocity within the buoyant plume decreases rapidly with z whereas for the finer grid, it remains almost constant in the lower half of the tunnel and then decreases gradually with z (Fig. 5.4b). The behaviour of the latter plume (Fig. 5.4b) is closer to that obtained experimentally (Fig. 5.5a). This shows that a 1 mm grid size is appropriate to reproduce numerically the behaviour of plumes. Note that this analysis, which is performed with one case (case1) of forced plumes, is also carried out with lazy plumes where the grid sizes are equal to 2 mm and the results obtained are similar (i.e. the results are better when the grid resolution is sufficiently refined near the source).

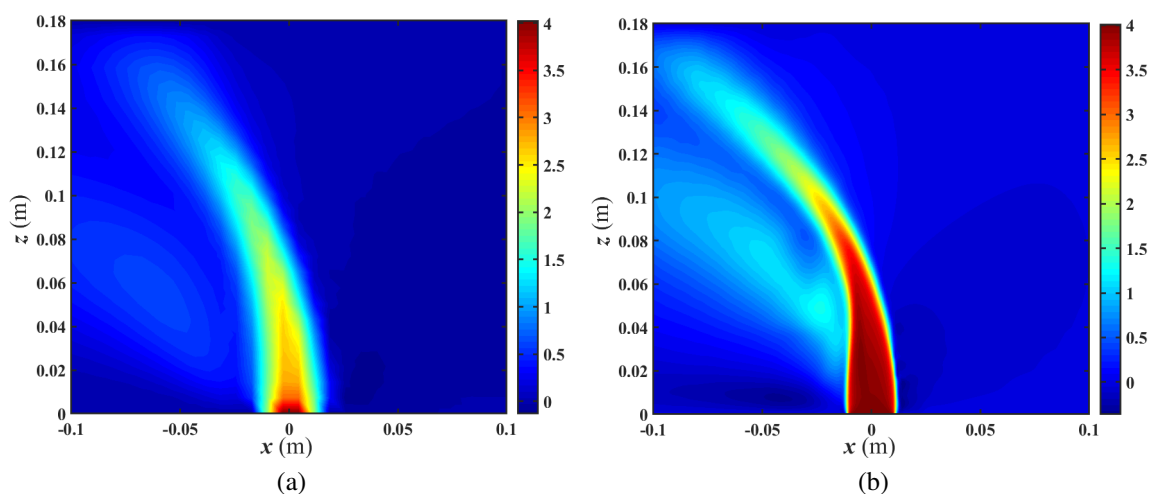


Figure 5.4: Numerical results on the average velocity fields of the vertical component (case1). a) With grid sizes of 5 mm. b) With grid sizes of 1 mm.

The average horizontal velocity (\bar{u}_x) and vertical velocity (\bar{u}_z), the standard deviations σ_x and σ_z as well as the Reynolds shear stress σ_{xz} are computed (in each grid cell) from instantaneous velocity fields obtained in steady-state conditions. All these quantities are normalised using the injection velocity (W_i) while the distances are normalised with the height of the tunnel (H). The results obtained are shown below. For each plume type (i.e.

forced or lazy), only one density ratio is analysed and compared to the experimental results.

5.3.1.2.1 Forced plumes

The numerical results for case1 ($\Gamma_i = 0.0075$ and $\rho_i/\rho_0 = 0.8$) are presented here and compared to the experimental results. The analysis of the results is first performed on mean velocities and then on second order statistics.

5.3.1.2.1.1 Average velocity

Fig. 5.5 shows the non-dimensional average velocity fields of the vertical component (\bar{u}_z/W_i) for case1. The experimental velocity field is shown in Fig. 5.5a while the numerical field is shown in Fig. 5.5b. In the bottom third of the tunnel (i.e. $z/H < 0.30$), the pattern of the two plumes is similar, both are axi-symmetric and their vertical velocity is high. Indeed, in this region, due to the top-hat profiles imposed at the source, the experimental velocities are generally higher than the numerical velocities. Above approximately $z/H = 0.30$, the plume in Fig. 5.5b begins to move progressively away from the source axis. This deflection becomes significant in the centre and in the upper part of the tunnel compared to that observed for the experimental plume. This behaviour can be due to the longitudinal ventilation flow which is characterised by high velocities at the centre of the tunnel (see Fig. 5.6a). The velocity profiles are different from those observed experimentally and the boundary layers are not well solved by the numerical model. In the vicinity of the source ($x/H = 0.10$), as shown in Fig. 5.6b, the longitudinal velocity in the experimental case decreases along the vertical axis due to the interaction between the ventilation flow and the

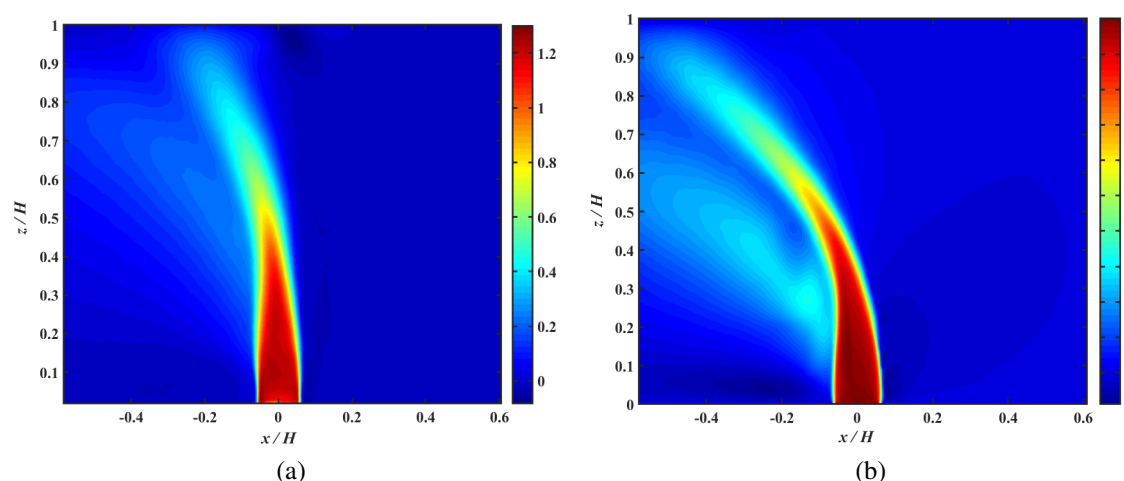


Figure 5.5: Non-dimensional average velocity fields of the vertical component \bar{u}_z/W_i for case1 ($\Gamma_i = 0.0075$ and $\rho_i/\rho_0 = 0.8$). a) An experimental result. b) A numerical result.

buoyant fluid, which causes a slowdown and a diversion of the longitudinal flow on either side of the plume. In the numerical case, approaching the source, the longitudinal velocity is reduced in the lower half of the tunnel but not in the upper part of the tunnel. Consequently, the plume impinges the ceiling in the region located far from the centre of the source (Fig. 5.5b). Despite the difference between the behaviour of the experimental plume and that of the numerical simulation, the critical conditions are reached at the same ventilation velocities. This indicates that, even though the impingement point of the numerical plume is located further downstream of the source (compared to that of the experimental plume), the front of the backlayering flow of the two plumes is set at the up-wind border of the source.

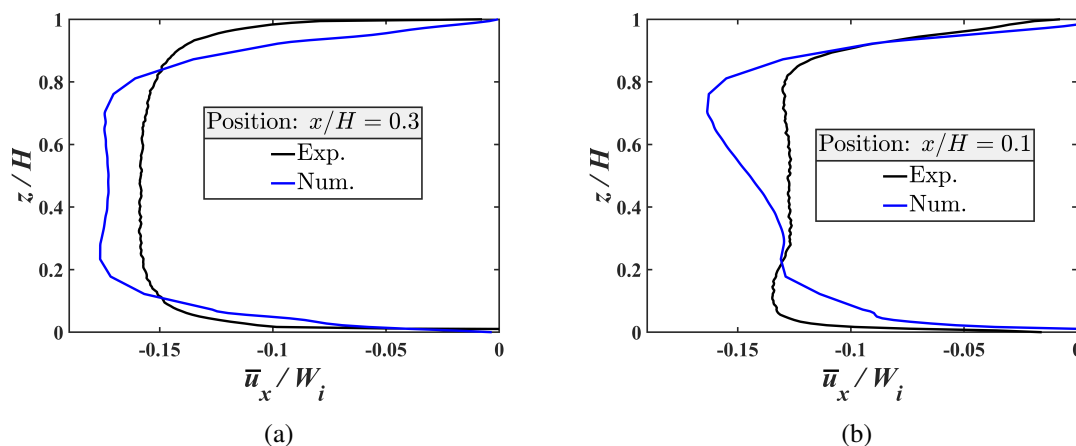


Figure 5.6: Experimental and numerical profiles of the non-dimensional longitudinal velocity component plotted at $x/H = 0.3$ (a) and $x/H = 0.1$ (b).

Fig. 5.7 shows experimental and numerical profiles of the non-dimensional vertical velocity (\bar{u}_z/W_i) for case1. The profiles are plotted at the position $z/H = 0.10$, $z/H = 0.40$ and $z/H = 0.70$ against the dimensionless longitudinal distance x/H . At $z/H = 0.10$, the experimental and numerical profiles reach their maximum of 1.22 and 1, respectively, on the central axis of the source. The numerical profile shows that a slight dispersion of the smoke, in the same direction as the ventilation flow, can be observed downstream of the source where the velocity profile remains above zero in the area from $x/H = -0.20$ to $x/H = -0.08$. Except for these differences, the two profiles are similar along the x/H -axis. At $z/H = 0.40$, the experimental profile also reaches its maximum value ($\bar{u}_z/W_i = 1.04$) at the central axis of the source, while the maximum of the numerical profile ($\bar{u}_z/W_i = 0.87$) is reached at $x/H = -0.05$. In the upper part of the tunnel (i.e. $z/H = 0.70$), the vertical velocity further decreases in both the experimental and numerical cases. At this height, the position of the maximum velocity profile is displaced downstream of the source in both cases, but more in

the numerical than in the experimental: at $x/H = -0.09$ in the experiments (where $\bar{u}_z/W_i = 0.49$) and at $x/H = -0.26$ in the simulations (where $\bar{u}_z/W_i = 0.42$).

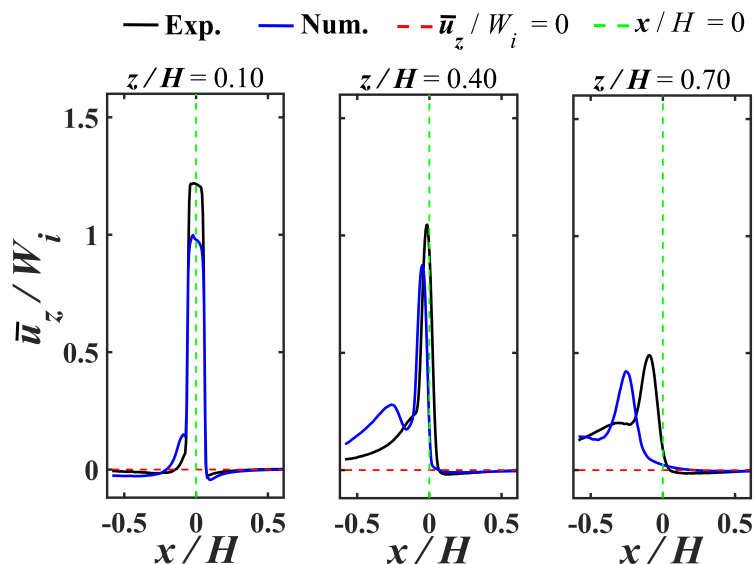


Figure 5.7: Profiles of the non-dimensional vertical velocity at $z/H = 0.10$, $z/H = 0.40$ and $z/H = 0.70$ against the non-dimensional longitudinal distance x/H (experimental profiles vs numerical profiles, case1: $\Gamma_i = 0.0075$ and $\rho_i/\rho_0 = 0.8$).

Fig. 5.8 shows the non-dimensional average velocity fields of the longitudinal component (\bar{u}_x/W_i), obtained experimentally (Fig. 5.8a) and numerically (Fig. 5.8b), for case1. The comparison between the two fields shows that the absolute longitudinal velocity is higher in the numerical case than in the experimental case in the right part of the plume (see dark blue area in Fig. 5.8b) and downstream of the source in the zone delimited by $-0.2 < x/H < -0.1$ and $z/H < 0.3$ (red area in Fig. 5.8b). Fig. 5.8b shows a rapid increase in longitudinal velocity in the right part of the plume, particularly in the zones where the rising column has undergone a strong deviation from the centre of the source (as previously shown in Fig. 5.5b). This acceleration of the smoke flow is observed along the zone ranging from approximately $z/H = 0.4$ to the tunnel ceiling. This obviously leads to an impingement region (of buoyant fluid release at the tunnel ceiling) situated further downstream of the source compared to that of the experimental case. Other comparison between numerical and experimental results are presented in Fig. 5.9, where we plot longitudinal velocity profiles at different positions of z/H against the dimensionless longitudinal distance x/H .

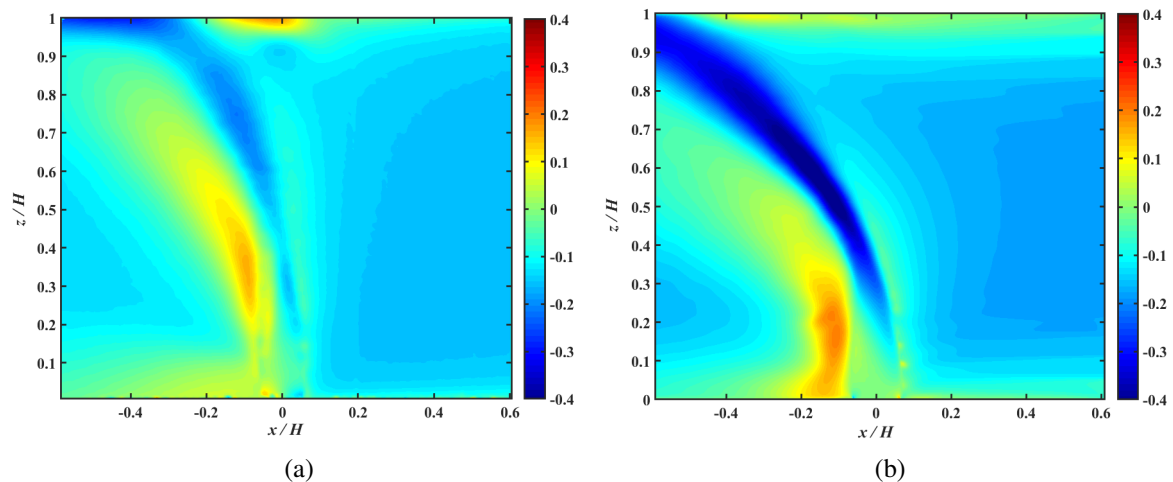


Figure 5.8: Non-dimensional average velocity fields of the longitudinal component \bar{u}_x/W_i for case1 ($\Gamma_i = 0.0075$ and $\rho_i/\rho_0 = 0.8$). a) An experimental result. b) A numerical result.

Fig. 5.9 shows experimental and numerical profiles of the longitudinal velocity plotted at $z/H = 0.04$, $z/H = 0.50$ and $z/H = 0.99$. Upstream of the source, the absolute value of the longitudinal velocity is higher near the tunnel floor and tunnel ceiling in the experimental case and at the centre of the tunnel in the numerical case, which is consistent with the results previously shown in Fig. 5.6. Near the ground level (i.e. $z/H = 0.04$), the maximum absolute value of \bar{u}_x/W_i is higher in the right part of the buoyant plume in the experimental simulation and in the left part in the numerical simulation. From right to left, the velocity peaks in each part of the plume are equal to -0.02 (peak directed downwards in the right part of the source because, in this part, the flow moves in the same direction as the ventilation flow and, therefore, the peak corresponds to the highest negative velocity) and 0.15 with the numerical case and to -0.08 and 0.06 with the experimental case. In the centre of the tunnel (i.e. $z/H = 0.5$), the amplitude of the negative peak (right part of the plume) is more significant in the numerical case, where it is equal to -0.42 against a value of -0.14 in the experimental case. Note that at this height, in the numerical case, the magnitude of the maximum longitudinal component \bar{u}_x/W_i is about half that of the maximum vertical component \bar{u}_z/W_i , which indicates a significant change in the direction of the buoyant plume in the same direction as the ventilation flow. This even causes a decrease in the longitudinal velocity of the smoke flow that moves against the ventilation in the other part of the plume (i.e. left part). As shown in Fig. 5.9, in this part, the peak of the velocity is equal to 0.04 against 0.11 in the experimental case. Close to the tunnel ceiling (i.e. $z/H = 0.99$), both profiles change sign (from negative velocities to positive velocities) at the same point upstream of

the source. This marks the front of smoke backlayering formed after the impingement of the release at the tunnel ceiling, which is set at $x/H = 0.08$ (i.e. the up-wind border of the source) for both the numerical and experimental cases. Downstream the source, the velocity profiles change also sign (from positive values to negative values). This occurs in the impingement region, from which the smoke backlayering develops in the opposite direction of the ventilation flow. According to Fig. 5.9, this appears at $x/H = -0.18$ and at $x/H = -0.40$ in the experimental and numerical cases, respectively.

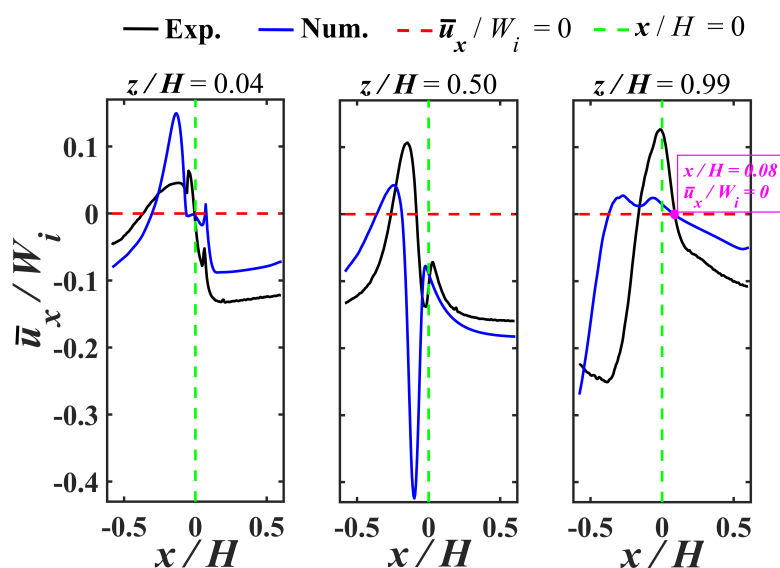


Figure 5.9: Profiles of the non-dimensional longitudinal velocity at $z/H = 0.04$, $z/H = 0.50$ and $z/H = 0.99$ against the non-dimensional longitudinal distance x/H (experimental profiles vs numerical profiles, case1: $\Gamma_i = 0.0075$ and $\rho_i/\rho_0 = 0.8$).

5.3.1.2.1.2 Velocity fluctuations

Fig. 5.10 shows the non-dimensional standard deviation of the vertical velocity component (σ_z/W_i) for case1, obtained experimentally (Fig. 5.10a) and numerically (Fig. 5.10b). Its magnitudes seem to be less significant in the numerical case than those observed in the experimental case. In order to compare the amplitude of the dimensionless standard deviation (σ_z/W_i) between the numerical and experimental results, we plotted profiles in three different positions of z/H against x/H (see Fig. 5.11).

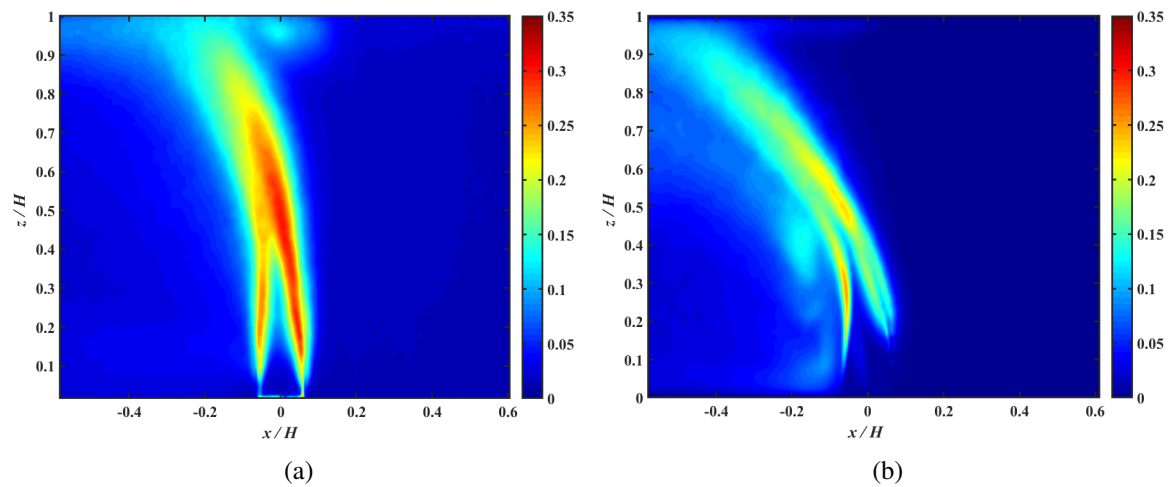


Figure 5.10: Non-dimensional standard deviation of the vertical velocity component σ_z/W_i for case1 ($\Gamma_i = 0.0075$ and $\rho_i/\rho_0 = 0.8$). a) An experimental result. b) A numerical result.

Fig. 5.11 shows that at $z/H = 0.3$, the magnitude of the dimensionless standard deviation in the right-hand part of the plume is more significant in the experimental case (where it reaches 0.28 against a value of 0.17 in the numerical case). In the left-hand part of the plume, the result for the numerical simulation is in close agreement with that obtained by the experiment, the values of σ_z/W_i are equal to 0.25 and 0.26, respectively. In the centre of the tunnel (i.e. $z/H = 0.5$), the vertical velocity fluctuations increase in the experimental case to reach a new maximum value of 0.3. In the numerical case, two peaks appear, one on each part of the plume, with a magnitude of 0.23 on the right side and 0.17 on the left side. In the upper part of the tunnel (i.e. $z/H = 0.80$), the amplitude of the peaks decreases in both cases and their location is situated further downstream of the source. For the experimental case, it is equal to 0.21 and located at $x/H = -0.1$, and for the numerical case, it is equal to 0.16 and located at $x/H = -0.31$. The maximum difference in the peak values of the standard deviation between the numerical and experimental results is equal to 23% and this is reached in the centre and in the upper part of the tunnel (without taking into account the bottom of the tunnel where in the numerical case σ_z/W_i is small).

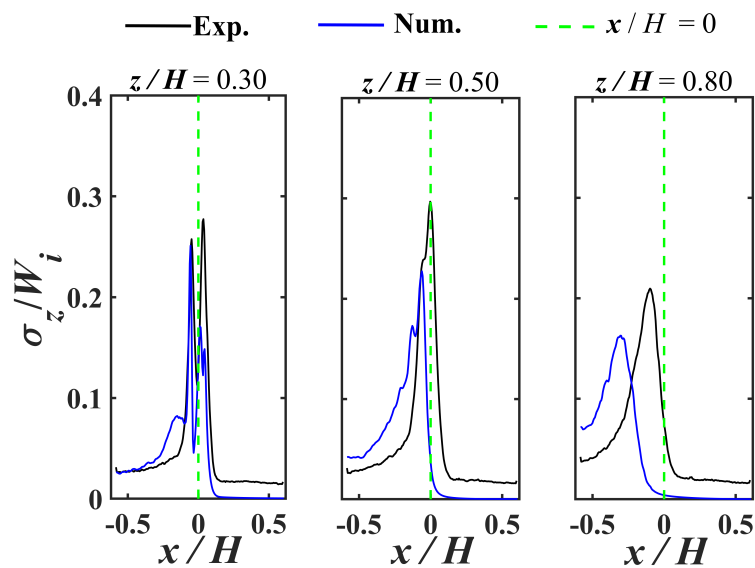


Figure 5.11: Standard deviation profiles of the vertical velocity component plotted at $z/H = 0.30$, $z/H = 0.50$ and $z/H = 0.80$ against the non-dimensional longitudinal distance x/H (experimental profiles vs numerical profiles, case1: $\Gamma_i = 0.0075$ and $\rho_i/\rho_0 = 0.8$).

Fig. 5.12a and Fig. 5.12b show the experimental and numerical results on the non-dimensional standard deviation of the longitudinal velocity component (σ_x/W_i) for case1. The magnitude of the standard deviation is relatively more pronounced in the experimental

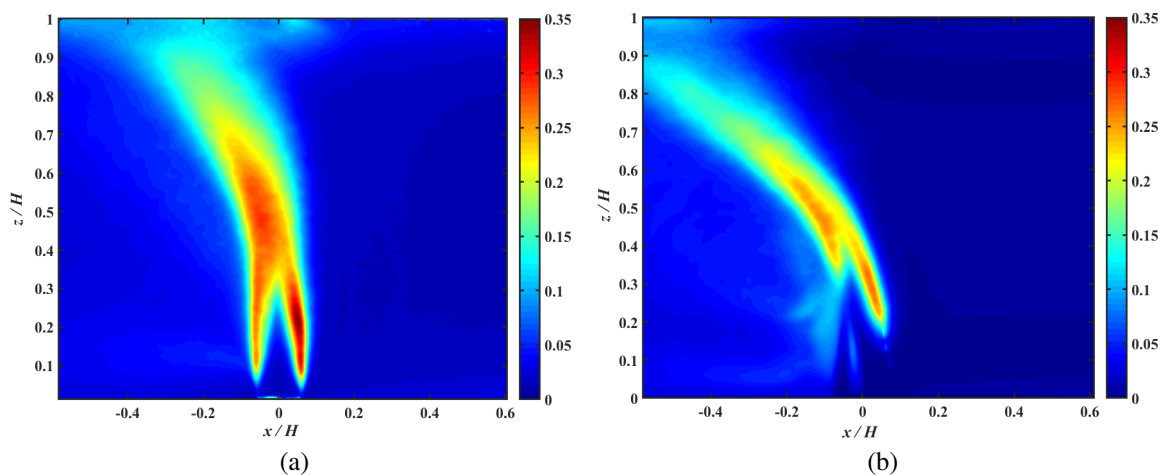


Figure 5.12: Non-dimensional standard deviation of the longitudinal velocity component σ_x/W_i for case1 ($\Gamma_i = 0.0075$ and $\rho_i/\rho_0 = 0.8$). a) An experimental result. b) A numerical result.

simulation than in the numerical simulation. To further analyse the magnitude of these fluctuations, three profiles are taken at three different heights: $z/H = 0.30$, $z/H = 0.50$ and $z/H = 0.80$ (see Fig. 5.13). At $z/H = 0.3$, the maximum values of the experimental and numerical standard deviation are very close on the right part of the plume and very different on the left part of the plume. From right to left, these values are equal to 0.28 and 0.27 for experimental case and 0.26 and 0.13 for numerical case. In the centre of the tunnel (i.e. $z/H = 0.50$), the peaks of the standard deviation for experimental and numerical cases are equal to 0.29 and 0.25 and their positions are located at $x/H = -0.05$ and $x/H = -0.12$, respectively. Near the tunnel ceiling (i.e. $z/H = 0.80$), the amplitude of these peaks is reduced and their location is moved further downstream the source. For the experimental and numerical cases, the maximum values of the standard deviation are equal to 0.18 and 0.14, respectively, and their positions are situated at $x/H = -0.18$ and $x/H = -0.44$. On the basis of these results, the difference between the experimental and the numerical standard deviations of the longitudinal velocity does not exceed 23% (without considering the bottom part of the tunnel where σ_x/W_i was inadequately computed by the numerical model). Note that the same difference between the experimental and numerical results was observed previously for the standard deviation of the vertical velocity.

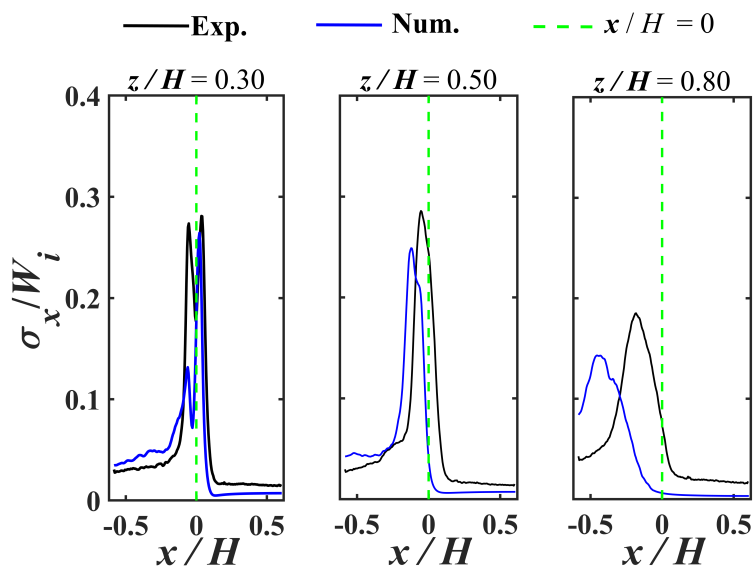


Figure 5.13: Standard deviation profiles of the longitudinal velocity component plotted at $z/H = 0.30$, $z/H = 0.50$ and $z/H = 0.80$ against the non-dimensional longitudinal distance x/H (experimental profiles vs numerical profiles, case1: $\Gamma_i = 0.0075$ and $\rho_i/\rho_0 = 0.8$).

Fig. 5.14 shows the non-dimensional Reynolds shear stress σ_{xz}/W_i^2 obtained experi-

mentally (Fig. 5.14a) and numerically (Fig. 5.14b) in case1. The difference between the two cases is that, in the numerical simulation, the size of the area with large values of σ_{xz}/W_i^2 is smaller compared to that in the experiments. In the numerical case, this extends from about $z/H = 0.2$ to $z/H = 0.55$ in the right part of the plume and from about $z/H = 0.22$ to $z/H = 0.42$ in the left part of the plume, against a furthermore range of about $z/H = 0.05$ to $z/H = 0.60$ for both parts in the experimental plume. The magnitude of σ_{xz}/W_i^2 seems to be relatively less important in the numerical case than in the experimental case.

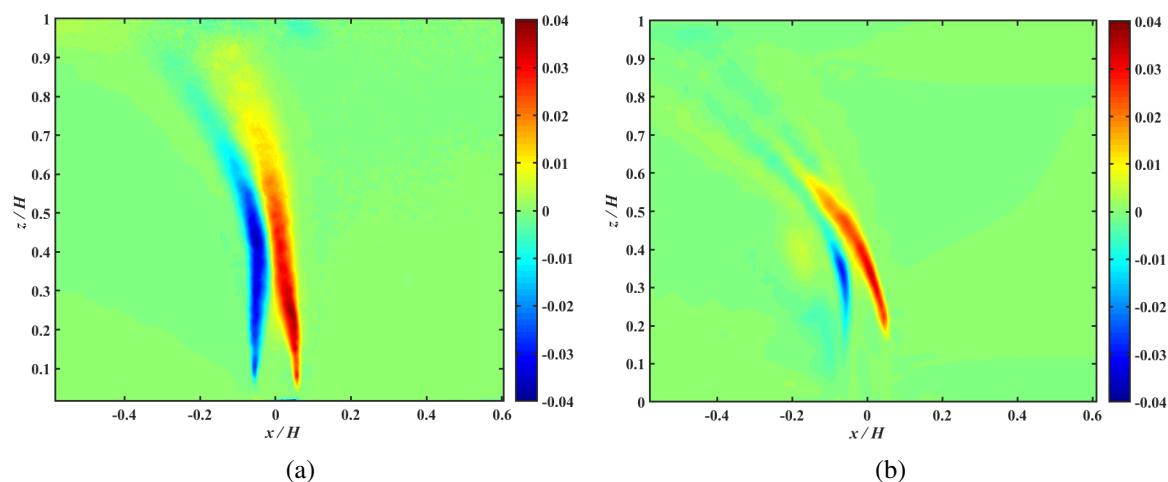


Figure 5.14: Non-dimensional Reynolds shear stress σ_{xz}/W_i^2 for case1 ($\Gamma_i = 0.0075$ and $\rho_i/\rho_0 = 0.8$). a) An experimental result. b) A numerical result.

Fig. 5.15 shows the evolution of the non-dimensional Reynolds shear stress against the dimensionless longitudinal distance at $z/H = 0.25$, $z/H = 0.40$ and $z/H = 0.55$. At $z/H = 0.25$, on each part of the plume, the maximum absolute value of the Reynolds shear stress is higher in the experimental case than in the numerical case. From right to left, they reach 0.039 and 0.030 in the experimental simulation and 0.026 and 0.016 in the numerical simulation. At $z/H = 0.40$, the magnitude of σ_{xz}/W_i^2 on the right part of the plume is equal to 0.029 in both experimental and numerical cases. On the left part, the absolute values of the peaks are 0.032 and 0.016 in the experimental case and the numerical case, respectively. At $z/H = 0.55$, the numerical results show only one peak of the Reynolds shear stress which appears on the right part of the plume (at $x/H = -0.12$) with a magnitude of 0.014. This is not the case in experimental results where two peaks appear, one on each part of the plume, with an absolute magnitude of 0.019 in the right part at $x/H = 0$ and 0.023 in the left part at $x/H = -0.07$.

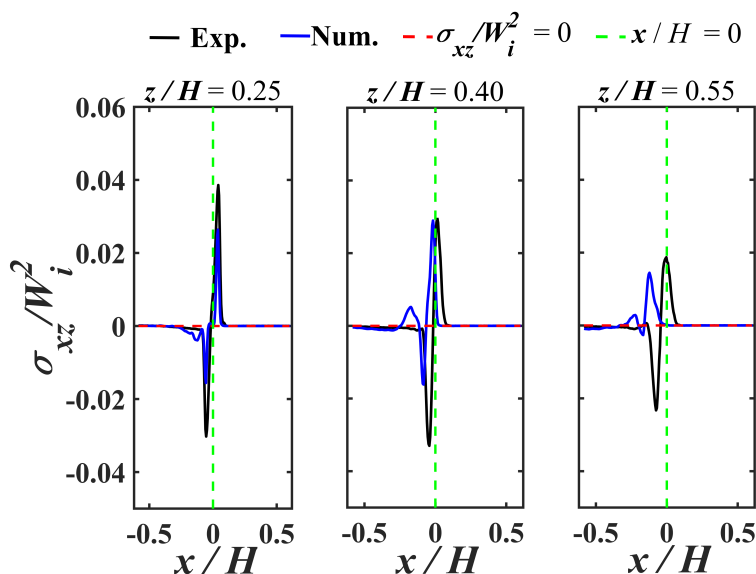


Figure 5.15: Profiles of the non-dimensional Reynolds shear stress at $z/H = 0.25$, $z/H = 0.40$ and $z/H = 0.55$ against the non-dimensional longitudinal distance x/H (experimental profiles vs numerical profiles, case1: $\Gamma_i = 0.0075$ and $\rho_i/\rho_0 = 0.8$).

5.3.1.2.2 Lazy plumes

The numerical results for case3 ($\Gamma_i = 1.45$ and $\rho_i/\rho_0 = 0.8$) are presented here and compared to the experimental results. The analysis of the results is first performed on mean velocities and then on second order statistics.

5.3.1.2.2.1 Average velocity

Fig. 5.16 shows the non-dimensional average velocity fields of the vertical component (\bar{u}_z/W_i) obtained experimentally (Fig. 5.16a) and numerically (Fig. 5.16b) for case3. As indicated previously in case1 (Fig. 5.5), at the bottom of the tunnel, the vertical velocity within the plume in the numerical case does not exceed the injection velocity (Fig. 5.16b), since a top-hat plume profile has been defined at the source. However, in the experimental case (as shown in Chapter 2), \bar{u}_z is greater than W_i in the lower part of the plume. Therefore, note that the ranges of the colour bar for the two fields shown in Fig. 5.16 are different. Thus, the comparison between the experimental and numerical results in terms of the velocity magnitude is not obvious, but it will be carried out by plotting some profiles at different heights above the source. Regarding the behaviour of the plume, Fig. 5.16 shows that the plume pattern obtained numerically is similar to that obtained experimentally. In both fields, we observe the appearance of a secondary plume that forms downstream of the main plume

and develops in the same direction as the ventilation flow (i.e. yellow column which is separated from the red column in Fig. 5.16a and Fig. 5.16b). In both cases, the vertical velocity is high in the core of the main plume, from source level to the centre of the tunnel. As the plume rises, the plume velocities decrease and its centre of mass moves progressively downstream of the source. However, its width seems to decrease rapidly in the experimental case, while its centre of mass seems to be slightly more displaced downstream of the source in the numerical case. On the other hand, the secondary plume is formed approximately at $z/H = 0.10$ and $z/H = 0.15$ above the source in the numerical and experimental cases, respectively. Its development in the numerical case similar to that in the experiments, and its high velocities are reached in its core. Experimental and numerical vertical velocity profiles, taken at three different positions of z/H , are presented in Fig. 5.17 as a function of the dimensionless longitudinal distance x/H .

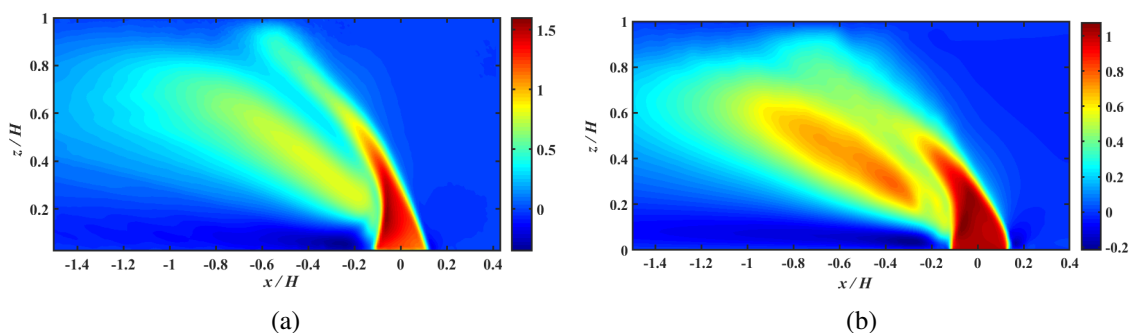


Figure 5.16: Non-dimensional average velocity fields of the vertical component \bar{u}_z/W_i for case3 ($\Gamma_i = 1.45$ and $\rho_i/\rho_0 = 0.8$). a) An experimental result. b) A numerical result.

As expected, near the source (i.e. $z/H = 0.10$), the peak of the vertical velocity is higher in the experimental case (where it is equal to 1.47 compared to 1.07 in the numerical case). Downstream the source, the dimensionless velocity in the experimental case decreases rapidly to reach its minimum value -0.19 at $x/H = -0.46$. In the numerical case, \bar{u}_z/W_i first decreases rapidly from 1.07 to 0.50 in the range $-0.15 < x/H < -0.06$, then gradually in the range $-0.85 < x/H < -0.15$ to finally reach a stable value of -0.09 at approximately $x/H = -0.85$. The change in vertical velocity evolution at $x/H = -0.15$ is due to the presence of the second plume. The negative values of the velocity are instead due to the presence of the recirculating flow regions. At $z/H = 0.40$, for each profile, two peaks appear, one in the main plume and the other in the secondary plume. These peaks are located slightly further downstream from the source in the numerical case and their magnitude is relatively higher in the experimental case. They reach 1.22 and 0.80 at $x/H = -0.10$ and $x/H = -0.39$ in the experimental case against 0.80 and 0.73 at $x/H = -0.16$ and $x/H = -0.49$ in the numerical

case. For the experiments, at $z/H = 0.70$, the two plumes remain separated from each other and a maximum value of 0.61 and 0.57 is reached in the main plume and in the secondary plume, respectively. However, in the numerical case, the two plumes are merged into one large column, whose maximum vertical velocity is 0.48.

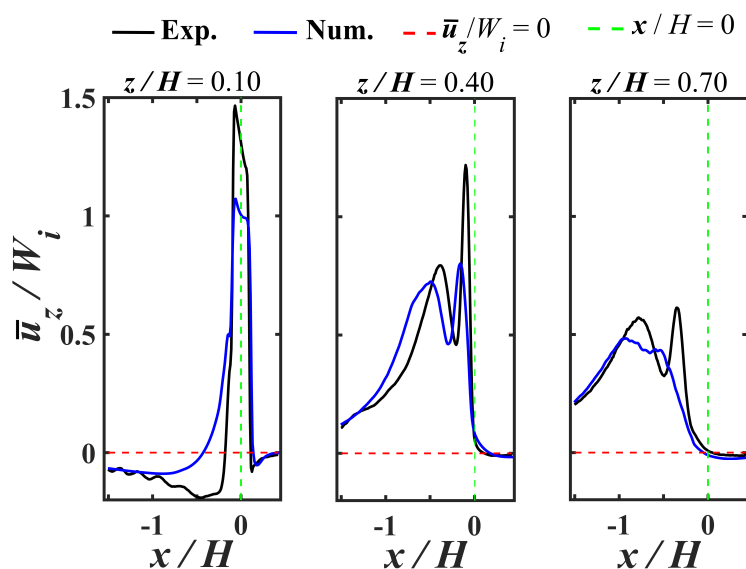


Figure 5.17: Profiles of the non-dimensional vertical velocity at $z/H = 0.10$, $z/H = 0.40$ and $z/H = 0.70$ against the non-dimensional longitudinal distance x/H (experimental profiles vs numerical profiles, case3: $\Gamma_i = 1.45$ and $\rho_i/\rho_0 = 0.8$).

Fig. 5.18 shows the experimental (Fig. 5.18a) and the numerical (Fig. 5.18b) results of the mean longitudinal velocity \bar{u}_x/W_i for case3. The results show that the experimental field of the longitudinal velocity is well reproduced numerically. In both numerical and experimental cases, we observe the appearance of the recirculating region in the lower part of the tunnel downstream the source (red zone in Fig. 5.18a and Fig. 5.18b). The dimensionless longitudinal velocity field is also similar in experiments and simulations. Two longitudinal velocity profiles, considered at two different positions of x/H , are presented in Fig. 5.19 as a function of the dimensionless height z/H . At $x/H = 0.30$, we observe the overlap of the experimental and numerical velocity profiles at the bottom and the top of the tunnel. A slight difference between the two profiles is instead observed in the range $0.1 < z/H < 0.9$: the numerical profile is perfectly symmetrical with respect to the tunnel axis whereas in the experimental case, the absolute velocities are higher in the upper part of the tunnel. Near the source (i.e. $z/H = 0.15$), the trend of the two superimposed curves is similar and their

maximum velocities are reached in the upper part of the tunnel (Fig. 5.19b), which results in a significant inclination of the plume (see Fig. 5.16 and Fig. 5.18).

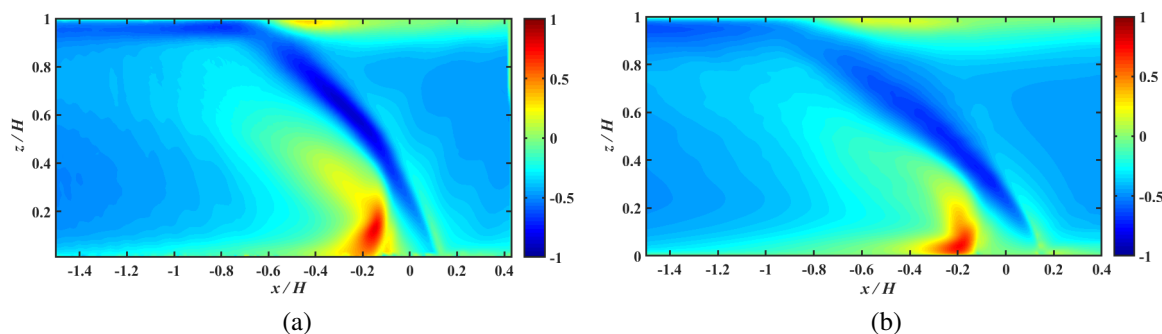


Figure 5.18: Non-dimensional average velocity fields of the longitudinal component \bar{u}_x/W_i for case3 ($\Gamma_i = 1.45$ and $\rho_i/\rho_0 = 0.8$). a) An experimental result. b) A numerical result.

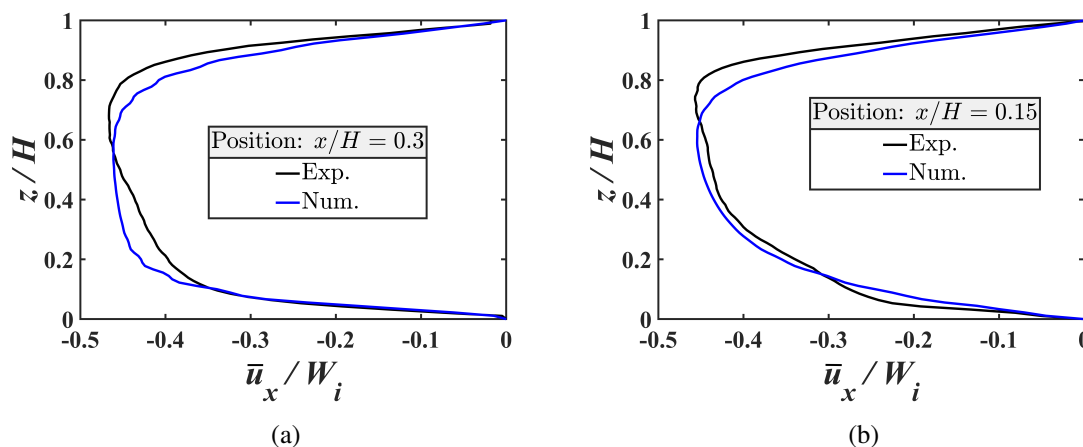


Figure 5.19: Experimental and numerical profiles of the non-dimensional longitudinal velocity component plotted at: a) $x/H = 0.30$, b) $x/H = 0.15$.

Fig. 5.20 shows experimental and numerical profiles of the longitudinal velocity plotted at $z/H = 0.05$, $z/H = 0.50$ and $z/H = 0.99$ as a function of the dimensionless longitudinal distance x/H . Close to ground level (i.e. $z/H = 0.05$), the two curves follow similar trends and reach their maximum in the recirculating region (at approximately $x/H = -0.18$), where the dimensionless longitudinal velocity is equal to 0.60 and 0.70 in the experiments and the simulations, respectively. In the centre of the tunnel ($z/H = 0.50$), the general trends of both curves are similar, with a numerical curve that has shifted further downstream from the source with respect to the numerical curve. In both cases, the longitudinal velocity is

negative, which means that all the smoke flow in the same direction as the ventilation flow. The maximum dimensionless velocities are reached in the plume core (with absolute values of 0.8 in the experimental case and 0.7 in the numerical case). Near the ceiling (i.e. $z/H = 0.99$), the front of the smoke back-layering is set at the same point for both the experimental and numerical cases. It is located at a distance $x = 0.07H$ upstream of the source. The point from which the smoke backlayer is formed is situated at $x/H = -0.56$ in the experimental case and at $x/H = -0.73$ in the numerical case.

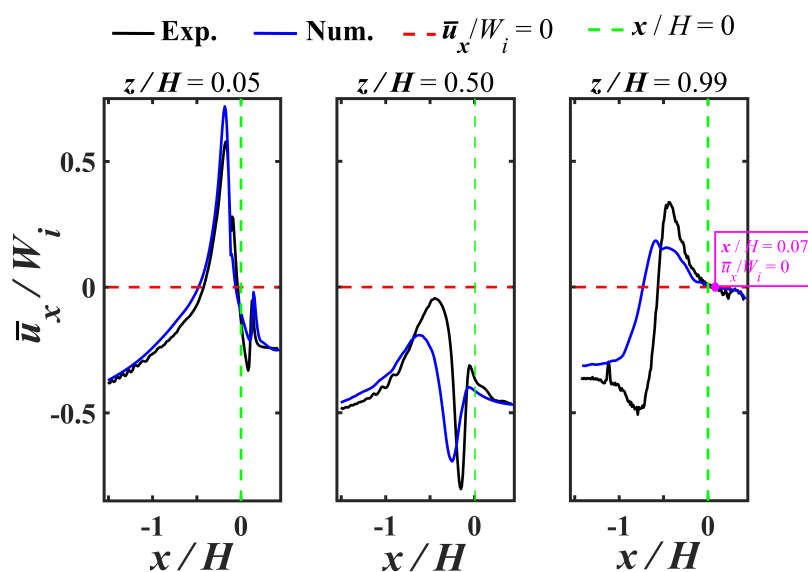


Figure 5.20: Profiles of the non-dimensional vertical velocity at $z/H = 0.05$, $z/H = 0.50$ and $z/H = 0.99$ against the non-dimensional longitudinal distance x/H (experimental profiles vs numerical profiles, case3: $\Gamma_i = 1.45$ and $\rho_i/\rho_0 = 0.8$).

5.3.1.2.2.2 Velocity fluctuations

Fig. 5.21 shows the non-dimensional standard deviation of the vertical velocity component (σ_z/W_i) for the experimental case (Fig. 5.21a) and the numerical case (Fig. 5.21b). As already observed in the experimental case (section 2.4.2.2), the numerical results (Fig. 5.21b) also show that the vertical fluctuations first develop only on the plume boundary up to about $z/H = 0.22$, then appear throughout the plume over the entire area that extends to the ceiling of the tunnel. In the numerical case, we observe the appearance of the vertical fluctuations in the recirculating region (i.e. near the ground level upstream of the source in Fig. 5.21b), which are not observed in the experiments. However, the magnitude of σ_z/W_i

is generally higher in the experimental case than in the numerical case, especially near the ceiling.

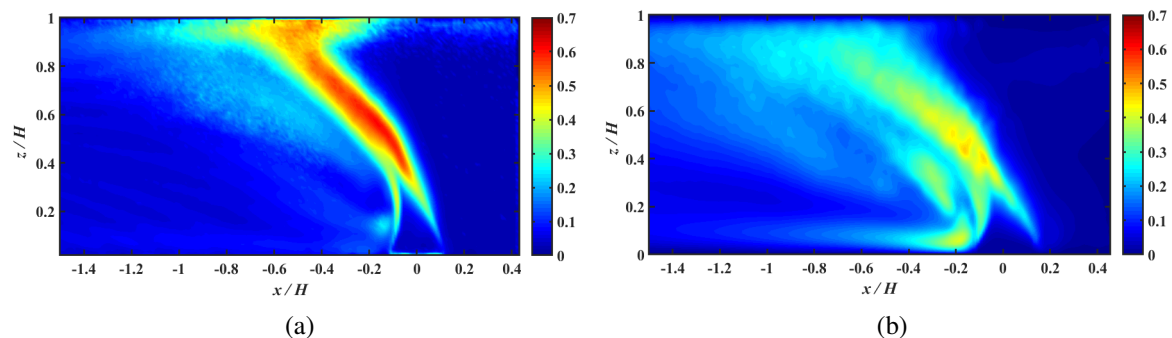


Figure 5.21: Non-dimensional standard deviation of the vertical velocity component σ_z/W_i for case3 ($\Gamma_i = 1.45$ and $\rho_i/\rho_0 = 0.8$). a) An experimental result. b) A numerical result.

Fig. 5.22 shows the experimental and numerical profiles of σ_z/W_i plotted at $z/H = 0.20$, $z/H = 0.40$ and $z/H = 0.60$ against the dimensionless longitudinal distance x/H . As expected, at $z/H = 0.20$, Fig. 5.22 shows two peaks in the experimental curve (one on each side of the plume boundary) and three peaks in the numerical curve (two in the plume boundary and one within the lower part of the secondary plume according to Fig. 5.21b). From right to left, their magnitudes are 0.31 and 0.38 in the experimental case and 0.27, 0.36 and 0.32 in the numerical case. At $z/H = 0.40$, in both cases, the amplitude of the peaks becomes more significant within the main plume, its value is 0.56 in the experimental case and 0.46 in the numerical case. Downstream these peaks, the curves decrease substantially in the experimental case and gradually in the numerical case where two peaks of magnitude 0.31 and 0.18 are observed within the secondary plume. At $z/H = 0.60$, σ_z/W_i reaches its maximum value of 0.59 in the experimental case and 0.40 in the numerical case. At this position, in both cases, the standard deviation in the secondary plume is not negligible, its maximum values reaching 23% of the injection velocity.

Fig. 5.23 shows the standard deviation of the longitudinal component of the velocity (σ_x/W_i) obtained experimentally (Fig. 5.23a) and numerically (Fig. 5.23b) in case3. The numerical result (Fig. 5.23b) shows that the longitudinal velocity fluctuations occur in the main plume and in the interface between the main plume and the secondary plume. These are more pronounced within the main plume region from about $z/H = 0.22$ to $z/H = 0.5$ (the red zone in Fig. 5.23b). However, unlike the experimental case (Fig. 5.23a), in the numerical case, the standard deviation σ_x is low near the tunnel ceiling. The same result has already been observed previously for σ_z (Fig. 5.21), which means that, in the numerical

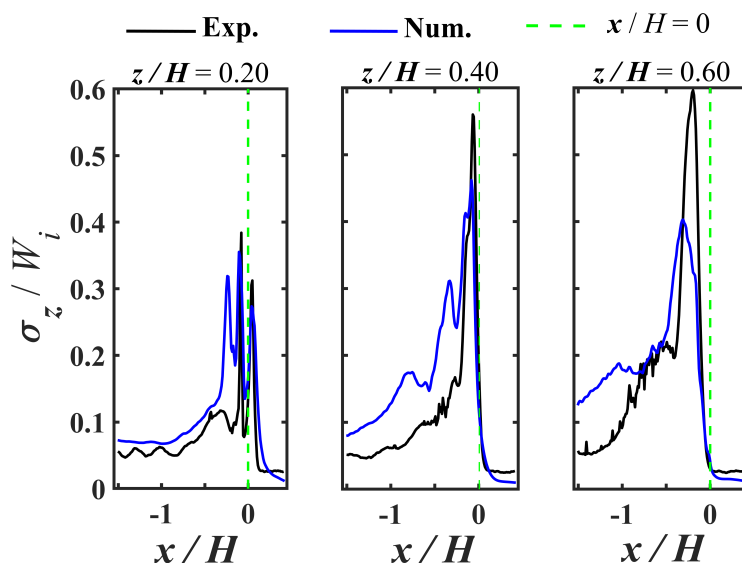


Figure 5.22: Standard deviation profiles of the vertical velocity component plotted at $z/H = 0.20$, $z/H = 0.40$ and $z/H = 0.60$ against the non-dimensional longitudinal distance x/H (experimental profiles vs numerical profiles, case3: $\Gamma_i = 1.45$ and $\rho_i/\rho_0 = 0.8$).

simulations, the fluctuations of the two velocity components near the tunnel ceiling are quite small.

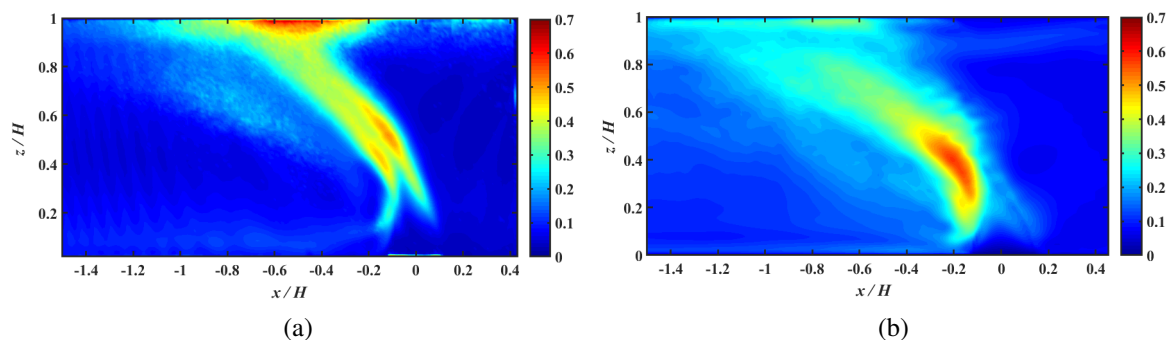


Figure 5.23: Non-dimensional standard deviation of the longitudinal velocity component σ_x/W_i for case3 ($\Gamma_i = 1.45$ and $\rho_i/\rho_0 = 0.8$). a) An experimental result. b) A numerical result.

Fig. 5.24 shows the experimental and numerical profiles of σ_x/W_i plotted at $z/H = 0.20$, $z/H = 0.40$ and $z/H = 0.60$ against the dimensionless longitudinal distance x/H . At $z/H = 0.20$, two peaks appear in the experimental case, one on each edge of the plume, with a magnitude of 0.20 on the right boundary and 0.29 on the left plume boundary. In the numer-

ical case, the curve shows only one peak of σ_x/W_i which appears on left boundary of the main plume (at $x/H = -0.16$) with a magnitude of 0.44. At $z/H = 0.40$, for the experimental case, the maximum values also appear on the plume boundary (with magnitudes of 0.41 and 0.46, from right to left). At the same position, a maximum value of 0.58 is reached in the main plume of the numerical simulation. In the experimental case, at $z/H = 0.60$, the two peaks are still located on the plume boundary and their amplitude is equal to 0.45 on the right edge and to 0.41 on the left edge. In the numerical case, only one peak is observed on the blue curve. It is located in the main plume at $x/H = -0.44$ and its magnitude is equal to 0.38. Downstream of these peaks, within the secondary plume, the dimensionless standard deviation reaches values of the order of 0.1–0.2 in the experimental case and of the order of 0.15–0.25 in the numerical case.

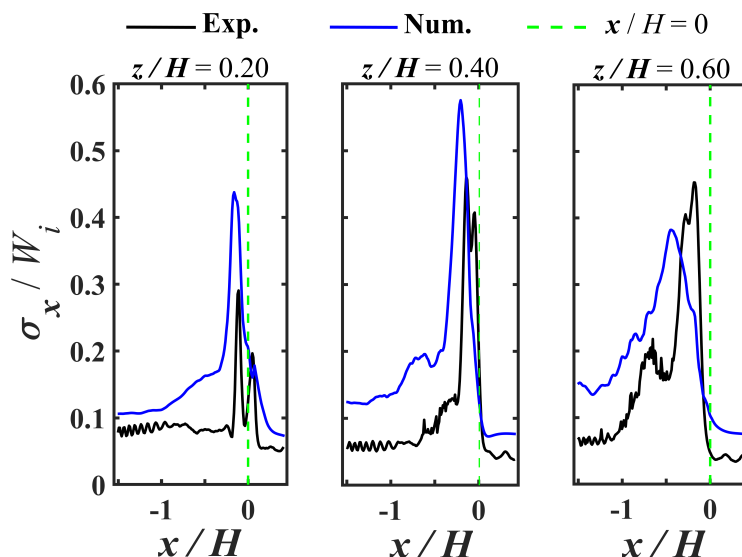


Figure 5.24: Standard deviation profiles of the longitudinal velocity component plotted at $z/H = 0.20$, $z/H = 0.40$ and $z/H = 0.60$ against the non-dimensional longitudinal distance x/H (experimental profiles vs numerical profiles, case3: $\Gamma_i = 1.45$ and $\rho_i/\rho_0 = 0.8$).

Fig. 5.25 shows the non-dimensional Reynolds shear stress σ_{xz}/W_i^2 obtained experimentally (Fig. 5.25a) and numerically (Fig. 5.25b) in case3. The comparison between the experimental and numerical results shows that, in the main plume, the extension of the area with positive value of σ_{xz}/W_i^2 is significant in the experimental case, whereas that of the area with negative values is greater in the numerical case. Fig. 5.26 shows the profiles of the dimensionless Reynolds shear stress measured at three different heights of z/H against the scaled longitudinal distance x/H .

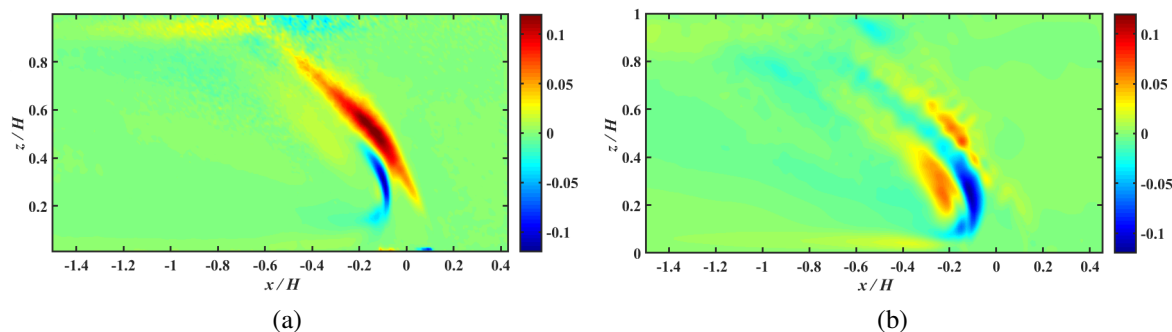


Figure 5.25: Non-dimensional Reynolds shear stress σ_{xz}/W_i^2 for case3 ($\Gamma_i = 1.45$ and $\rho_i/\rho_0 = 0.8$). a) An experimental result. b) A numerical result.

At $z/H = 0.20$, the maximum absolute values of σ_{xz}/W_i^2 in the experimental case are 0.019 and 0.056 at the right and left boundaries of the main plume, respectively. In the numerical case, σ_{xz}/W_i^2 reaches absolute values of 0.011, 0.104 and 0.053 on the right edge of the main plume, on the left edge of the main plume and at the interface between the main plume and the secondary plume, respectively. At $z/H = 0.40$, with the exception of the number of peaks observed previously, another peak appears in the experimental case at the interface between the main plume and secondary plume. From right to left, the absolute values of the peaks are 0.092, 0.059 and 0.012 in the experimental case and 0.041, 0.045

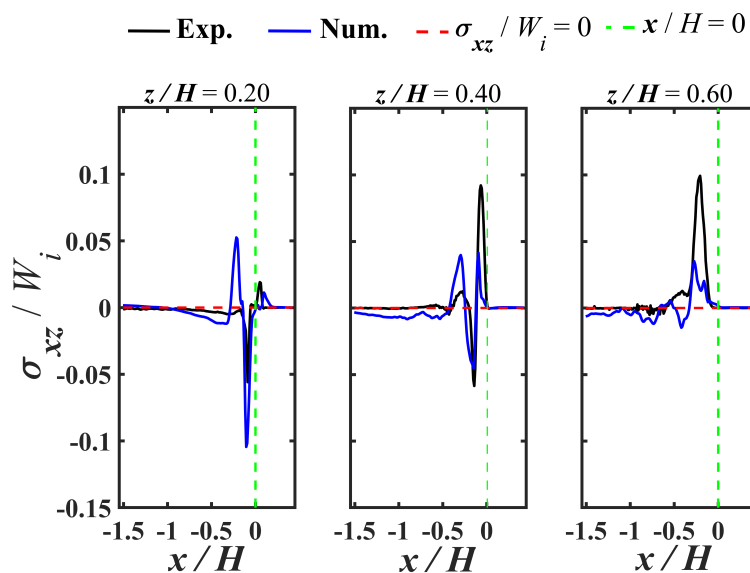


Figure 5.26: Profiles of the non-dimensional Reynolds shear stress at $z/H = 0.20$, $z/H = 0.40$ and $z/H = 0.60$ against the non-dimensional longitudinal distance x/H (experimental profiles vs numerical profiles, case3: $\Gamma_i = 1.45$ and $\rho_i/\rho_0 = 0.8$).

and 0.040 in the numerical case. At $z/H = 0.60$, for both case, the maximum absolute value is reached within the main plume. This is equal to 0.099 and located at $x/H = -0.21$ in the experimental case and equal to 0.035 and located at $x/H = -0.27$ in the numerical case.

5.3.2 Effect of solid barriers on the propagation of fire smoke within a longitudinally ventilated tunnel

5.3.2.1 Numerical simulations for studying the effects of barrier

In this section, a series of numerical simulations are conducted to investigate the effect of solid barriers on the spread of fire smoke within a longitudinally ventilated tunnel. We have simulated all the experimental cases that we have carried out in section 3.3.1.1, in which the effect of the barriers on the lengths of the smoke back-layering was evaluated in the tunnel without blocks. The plume Richardson number and the density ratio are kept constant: $\Gamma_i = 2$ and $\rho_i/\rho_0 = 0.7$. Both the small and large barriers are considered. The first case is that of multiple small barriers of height equal to one tenth of the total tunnel height, i.e. $h = H/10$. As in the experiments, two configurations are analysed: one with a spacing between two adjacent barriers equal to the tunnel height, i.e. $S = H$ (Fig. 3.1a) and one with $S = 2H$ (Fig. 3.1b). Secondly, the effects of a single large barrier, initially of height equal to one quarter of the total tunnel height, i.e. $h = H/4$, and then of height equal to one third of the total tunnel height, i.e. $h = H/3$, are evaluated. The barrier is placed in two different positions, one just downstream of the source, i.e. $d = 0$ (Fig. 3.1d) and the other at a distance equal to the tunnel height upstream of the source, i.e. $d = H$ (Fig. 3.1c).

The barriers consist entirely of rectangular steel sheets covering the entire width of the tunnel. They are assumed to be one layer of mesh cells thick. The mesh is uniform in both directions (y and z) and refined in the x -direction over the entire zone within which the source is placed. For $\Gamma_i = 2$ and $\rho_i/\rho_0 = 0.7$ and $D_i/H = 0.56$, the HRR is approximately 0.51 kW (using Eq. 2.1). Therefore, according to the criterion of McGrattan (Eq. 5.2), the grid size has to be in the range $0.003 < \delta x \text{ (m)} < 0.012$. Thus, a mesh size of 0.008 m is selected close to the source and a size of 0.01 m is chosen in the rest of the computational domain, resulting in a total of 864 000 cells in the entire domain. The simulation time is set to 100 seconds, allowing enough time for the flow to reach a steady state. It took about 50 s in the empty tunnel and slightly more time in the tunnel with barriers. To identify the presence of the back-layering flow inside the tunnel, the method used in section 5.2 (see Fig. 5.2a) was adopted. This is based on the estimate of the flow density just below the tunnel ceiling. Once steady state reached, the backlayer length is defined as the distance between the source position and the point at which the flow density at the tunnel ceiling

begins decreasing, this point indicates the edge of the backlayer.

5.3.2.2 Results and discussion

Numerical results on the fire simulations in the reduced-scale tunnel model with and without barriers are presented below and compared with the experimental results. As in the experimental part, the results are presented in the form of dimensionless quantities, i.e. the dimensionless backlayering length L/H against the dimensionless longitudinal ventilation velocity $U_0/U_{0,cr}$.

5.3.2.2.1 Small barriers

Fig. 5.27 shows the non-dimensional backlayer length as a function of the non-dimensional ventilation velocity for the two cases of small barriers. Experimental and numerical results for the case $S = H$ are presented in Fig. 5.27a and those for the case $S = 2H$ in Fig. 5.27b: the critical velocity $U_{0,cr}$ (i.e. the minimum value of U_0 imposing a zero value of L in the tunnel with no barriers) obtained numerically is equal to that obtained experimentally (i.e. the red square and the black circle are superimposed at $L/H = 0$ and $U_0/U_{0,cr} = 1$). By comparing the experimental and numerical data of the simulations in the tunnel without barriers (i.e. black and red graphs), it can be shown that the numerical simulations give similar smoke backlayer lengths to those obtained experimentally for $U_0/U_{0,cr} > 0.85$ and greater backlayer lengths for $U_0/U_{0,cr} < 0.85$. In the latter case (i.e. $U_0/U_{0,cr} < 0.85$), the numerical results are slightly shifted from the experimental results in the range $0.70 < U_0/U_{0,cr} < 0.85$ and significantly distant for $U_0/U_{0,cr} < 0.7$. This difference may be due to the limitations of the numerical code in characterising the behaviour of the boundary layer flow close to the wall.

In the tunnel with barriers (i.e. blue and green graphs), for each configuration, the values of the critical velocity reduction due to the presence of a small barrier just upstream of the source are similar in both the experimental and numerical cases. The reduction rate for the wider spacing of $2H$ is 17% (velocity ratio of $U_0/U_{0,cr}$ 0.83) and for the narrower spacing of H is 9% ($U_0/U_{0,cr}$ 0.91). At ventilation velocities below the critical value (i.e. $U_0 < 0.91U_{0,cr}$ for the configuration $S = H$ and $U_0 < 0.83U_{0,cr}$ for the configuration $S = 2H$), the small barriers located further upstream of the source are also effective in reducing the length of the backlayer. For each velocity ratio $U_0/U_{0,cr}$, the length of the back-layer is small in cases with barriers than in those without barriers. This is deduced for both configurations by comparing red and blue graphs for numerical simulations as well as black and green for experimental simulations. In the tunnel with barriers, for both configurations, the numerical results are in close agreement with the experimental results for all velocity ratios $U_0/U_{0,cr}$ greater than 0.75. For $U_0/U_{0,cr} < 0.75$, the numerical results progressively diverge from the

experimental results as the velocity ratio decreases, especially in the configuration with a spacing of H (see Fig. 5.27a) where the maximum difference between the numerical and experimental values of backlayer lengths reaches $5H$.

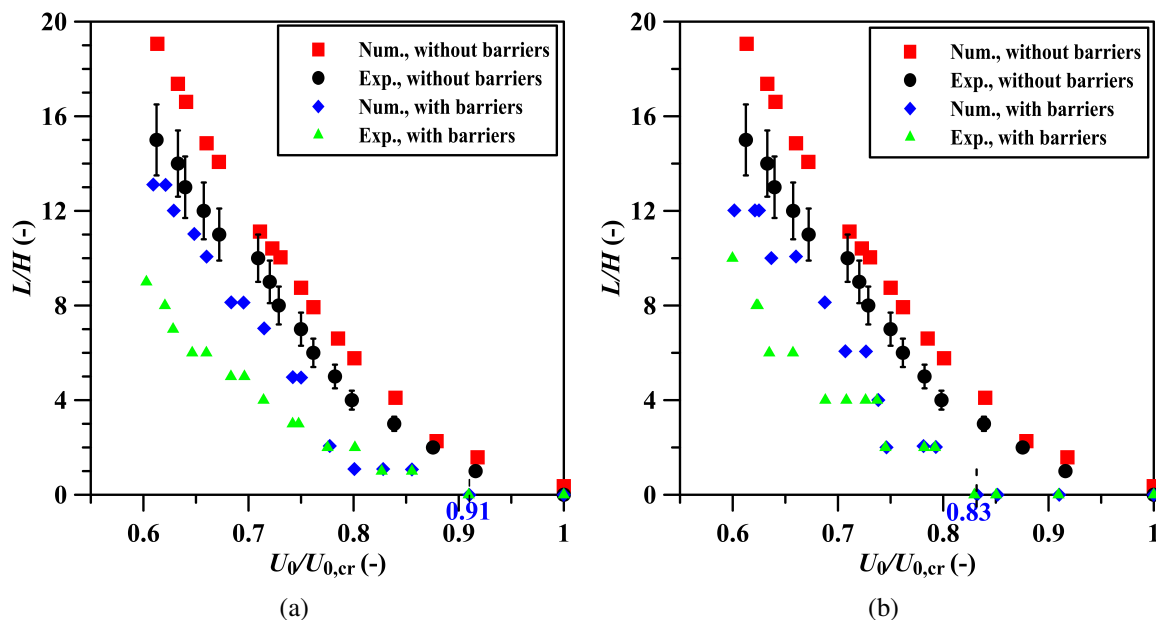


Figure 5.27: Smoke dimensionless back-layering length, L/H , against the ratio of longitudinal ventilation velocity to the critical velocity $U_0/U_{0,cr}$; $U_{0,cr}$ is the critical velocity measured experimentally in the tunnel without barriers. a) Tunnel without barriers vs. tunnel with small barriers ($h = H/10$ and $S = H$). b) Tunnel without barriers vs. tunnel with small barriers ($h = H/10$ and $S = 2H$).

Fig. 5.28 shows three examples of smoke visualisations for fire simulations in a longitudinally ventilated tunnel. They concern the case with no barriers (Fig. 5.28a), with small barriers for a spacing equal to H (Fig. 5.28b) and for a spacing equal to $2H$ (Fig. 5.28c). The tests are performed with same source conditions ($\Gamma_i = 2$, $\rho_i/\rho_0 = 0.7$ and $D_i/H = 0.56$) and at the same ventilation velocity ($U_0/U_{0,cr} = 0.83$). The purpose is to compare the length of the smoke back-layer reproduced in the empty tunnel with that observed in each configuration of the tunnel with small barriers. The black area shown in Fig. 5.28 indicates the domain filled by the smoke. Without barriers, a smoke back-layer flows upstream of the source in the opposite direction of the ventilation and its length at steady state is approximately four times the height of the tunnel ($L/H \approx 4$). With small barriers spacing by H , the barrier located just upstream of the source does not prevent the back-layering of smoke. But this is stopped by the second barrier placed upstream of the source and its length is

therefore equal to the tunnel height ($L/H = 1$). However, with a greater spacing ($2H$), the barrier situated just upstream of the source prevents the smoke from passing upstream the source (i.e. $L/H = 0$).

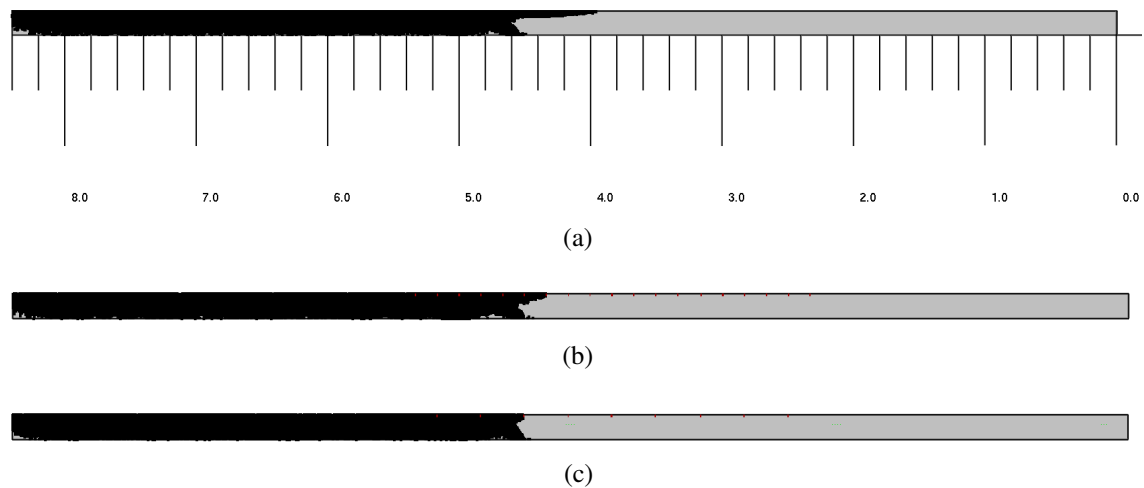


Figure 5.28: Simulations of smoke back-layering flow for $\Gamma_i = 2$, $\rho_i/\rho_0 = 0.7$, $D_i/H = 0.56$ and $U_0/U_{0,cr} = 0.83$. a) Tunnel without small barriers: appearance of a smoke back-layering flow, $L/H \approx 4$. b) Tunnel with small barriers ($S = H$): the barrier located upstream of the source at a distance equal to the tunnel height prevents the passage of smoke, $L/H = 1$. c) Tunnel with small barriers ($S = 2H$): the barrier located just upstream of the source prevents the passage of smoke, $L/H = 0$.

A small reduction in longitudinal velocity can change the lengths of the smoke back-layer of each of the three cases considered here. Fig. 5.29 shows another example of smoke visualisations for a velocity ratio $U_0/U_{0,cr} = 0.77$. In this case, the dimensionless length of the back-layer in the tunnel without barriers reaches approximately 6.5. However, in the tunnel with small barriers, for each configuration, the length of the back-layer is reduced to twice the height of the tunnel by the barrier located at $2H$ upstream of the source. In general, as the ventilation velocity decreases, the extension of the smoke back-layer increases both in the empty tunnel and in the tunnel with barriers, but less in the latter case because of the presence of multiple barriers that help prevent or reduce the smoke back-layering (see Fig. 5.27).

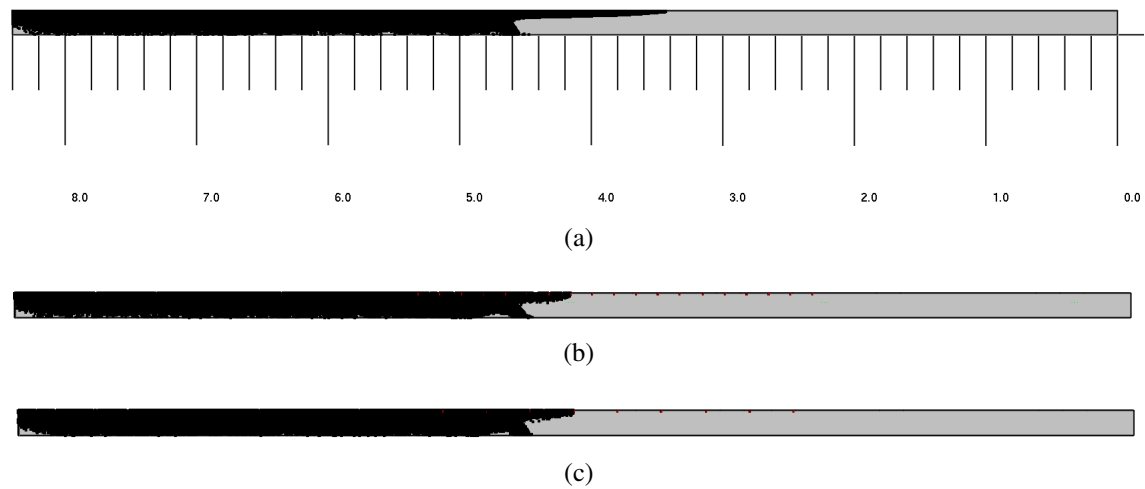


Figure 5.29: Simulations of smoke back-layering flow for $\Gamma_i = 2$, $\rho_i/\rho_0 = 0.7$, $D_i/H = 0.56$ and $U_0/U_{0,cr} = 0.77$. a) Tunnel without small barriers: appearance of a smoke back-layering flow, $L/H \approx 6.5$. b) Tunnel with small barriers ($S = H$): the barrier located upstream of the source at a distance equal to twice the tunnel height prevents the passage of smoke, $L/H = 2$. c) Tunnel with small barriers ($S = 2H$): the barrier located upstream of the source at a distance equal to twice the tunnel height prevents the passage of smoke, $L/H = 2$.

5.3.2.2.2 Large barriers

The numerical and experimental results for the tunnel with a large barrier of height $H/4$ are shown in Fig. 5.30 and compared to those obtained in the empty tunnel. The results for the configuration where the barrier is fixed just upstream of the source are presented in Fig. 5.30a and those for the configuration where the barrier is placed at a distance H upstream of the source are presented in Fig. 5.30b. The results for the tunnel without barriers are already discussed above in section 5.3.2.2.1. As already obtained in the experiments (section 3.3.1.1), the numerical results show that the large barrier $H/4$ can prevent the development of the back-layer for any ventilation velocity U_0 greater than $0.67U_{0,cr}$, regardless of the position of the barrier. Overall, we observe a good agreement between the numerical and experimental results. Both results give a same critical velocity, with a slight difference that can be seen when smoke passes below the barrier (i.e. $U_0/U_{0,cr} < 0.67$) where the numerical data gives slightly greater lengths of the smoke back-layering.

Fig. 5.31 plots the non-dimensional backlayer length as a function of the non-dimensional ventilation velocity for the largest barrier of size $H/3$. Fig. 5.31a shows the results for the barrier placed just upstream of the source and Fig. 5.31b shows the results for the barrier fixed at a distance H upstream of the source. As in the case above ($h = H/4$), the results show good agreement between the numerical and experimental results, except for small dif-

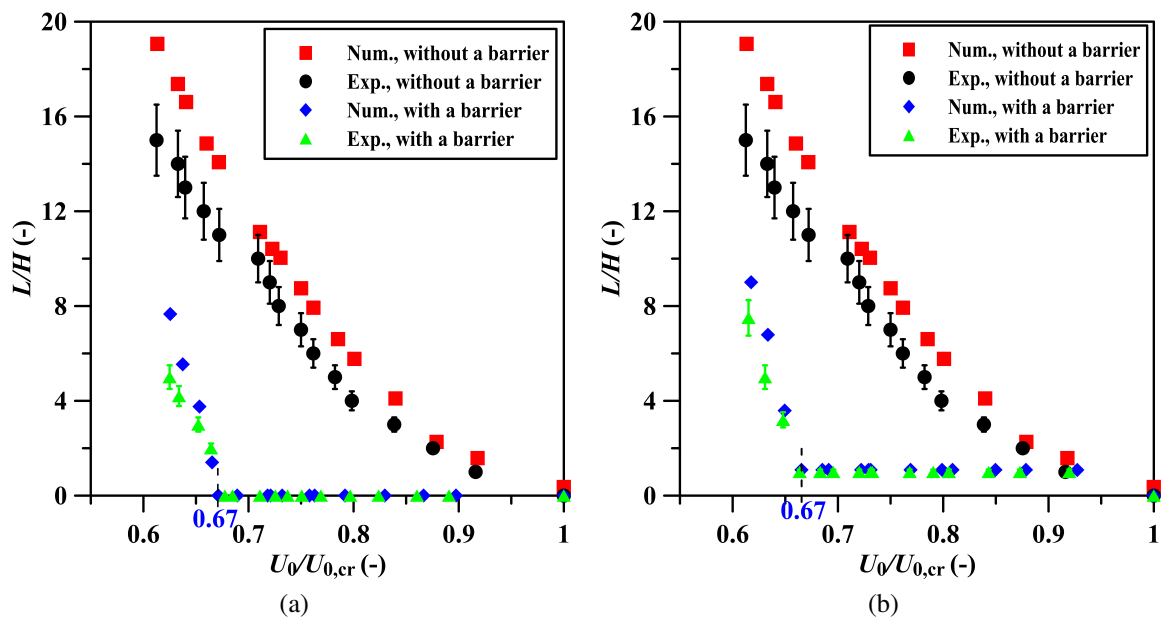


Figure 5.30: Smoke dimensionless back-layering length, L/H , against the ratio of longitudinal ventilation velocity to the critical velocity $U_0/U_{0,cr}$. a) Empty tunnel vs. tunnel with large barrier of height $H/4$ placed just upstream of the source. b) Empty tunnel vs. tunnel with large barrier of height $H/4$ placed at a distance H upstream of the source.

ferences in the lengths of the back-layer for the lowest ventilation velocities (see Fig. 5.31 for $U_0/U_{0,cr} < 0.55$). In both configurations, the barrier prevents the back-layering flow for each longitudinal ventilation velocity $U_0 > 0.56U_{0,cr}$. At ventilation velocities below this critical value, the smoke back-layer appears upstream of the barrier but its length remains lower than that estimated in the empty tunnel.

Fig. 5.32 shows a comparison between two smoke visualisations for numerical simulations performed with same source conditions $\Gamma_i = 2$, $\rho_i/\rho_0 = 0.7$, $D_i/H = 0.56$ and $U_0/U_{0,cr} = 0.67$. The first is carried out in a tunnel without a barrier (Fig. 5.32a) and the second in a tunnel with a barrier of height $H/4$ fixed to the tunnel ceiling just behind the source (Fig. 5.32b). The comparison between the results of the two cases clearly shows the importance of the barrier in controlling the spread of smoke in the event of a fire in longitudinally ventilated tunnels. Even at a very low velocity, the barrier provides a complete blockage of smoke (see Fig. 5.32b), which can extend over a length of $14.5H$ in the empty tunnel (see Fig. 5.32a).

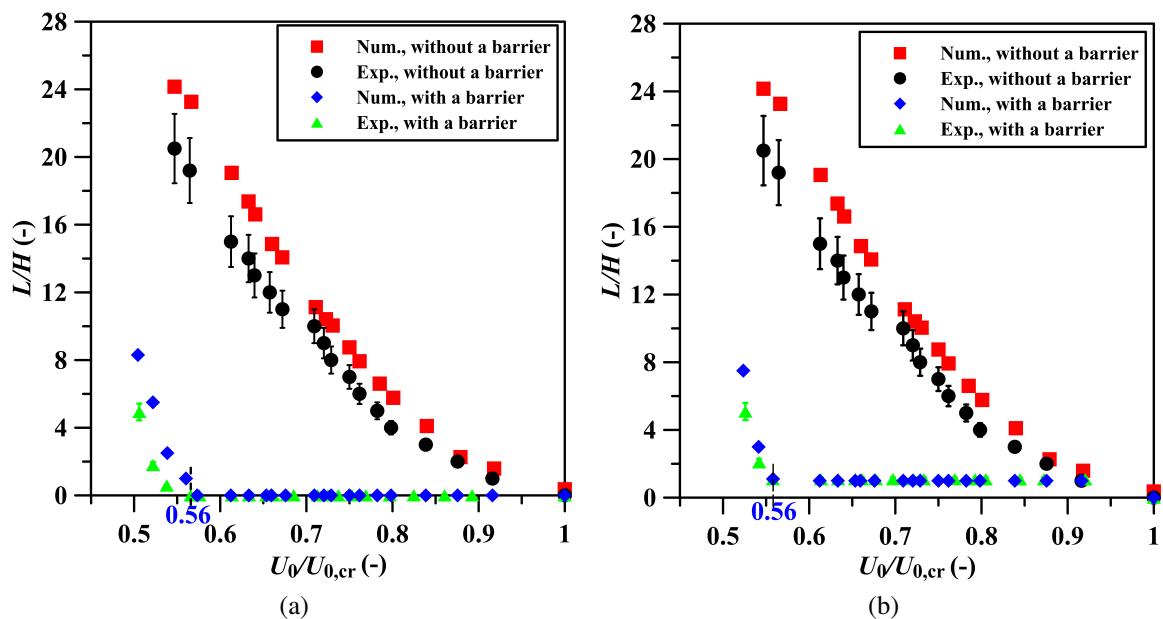


Figure 5.31: Smoke dimensionless back-layering length, L/H , against the ratio of longitudinal ventilation velocity to the critical velocity $U_0/U_{0,cr}$. a) Empty tunnel vs. tunnel with largest barrier of height $H/3$ placed just upstream of the source. b) Empty tunnel vs. tunnel with largest barrier of height $H/3$ placed at a distance H upstream of the source.

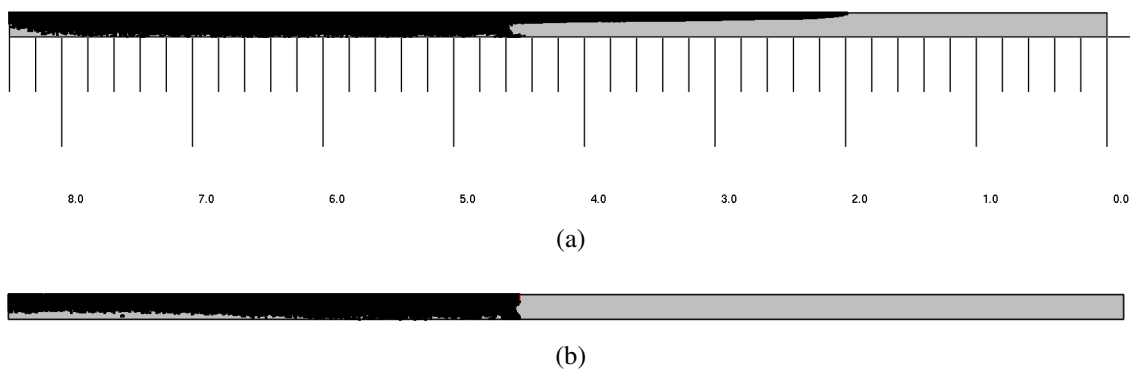


Figure 5.32: Simulation of smoke back-layering flow for $\Gamma_i = 2$, $\rho_i/\rho_0 = 0.7$, $D_i/H = 0.56$ and $U_0/U_{0,cr} = 0.67$. a) Tunnel without the barrier: appearance of the smoke back-layering flow, $L/H \approx 14.5$. b) Tunnel with a large barrier $H/4$ placed just upstream of the source: no smoke back-layering flow upstream of the source.

Fig. 5.33 shows the smoke visualisations in the tunnel with the largest barrier $H/3$ (Fig. 5.33a) and in the tunnel without barriers (Fig. 5.33b). The two simulations are performed imposing $\Gamma_i = 2$, $\rho_i/\rho_0 = 0.7$, $D_i/H = 0.56$ and $U_0/U_{0,cr} = 0.56$. The results show that the length of the back-layer in the empty tunnel is approximately 24 times the height of

the tunnel. Meanwhile, the largest barrier $H/3$ prevents the formation of the smoke back-layer. This indicates that the role of the barriers in road tunnels is extremely important for improving fire safety. These can reduce the spread of flames and smoke upstream of the fire source and, therefore, ensure the safe evacuation of occupants and allow the emergency services to take action.

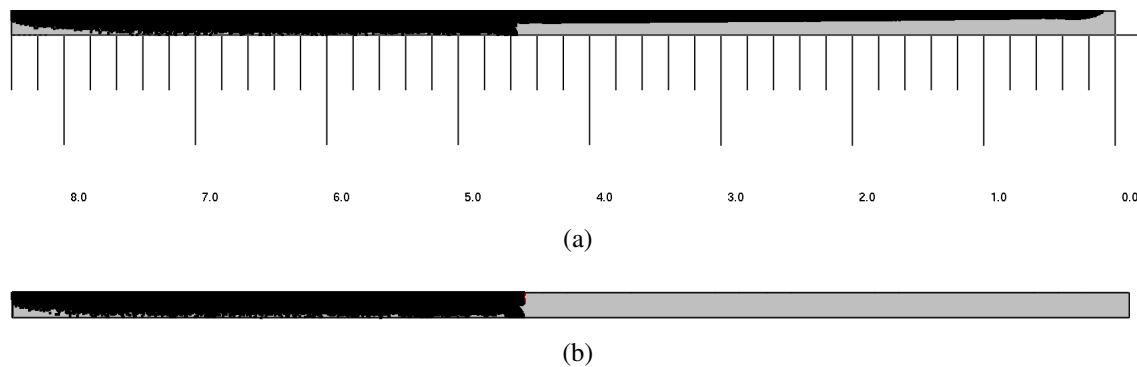


Figure 5.33: Simulation of smoke back-layering flow for $\Gamma_i = 2$, $\rho_i/\rho_0 = 0.7$, $D_i/H = 0.56$ and $U_0/U_{0,cr} = 0.56$. a) Tunnel without the barrier: appearance of the smoke back-layering flow, $L/H \approx 24$. b) Tunnel with a largest barrier $H/3$ placed just upstream of the source: no smoke back-layering flow upstream of the source.

5.3.3 Effects of the shape and position of vents on the confinement of fire smoke in a tunnel with a transverse ventilation system

5.3.3.1 Numerical simulations for studying the effects of the shape and position of dampers

Numerical simulations are performed to study the effects of the shape and position of the dampers on the confinement of fire smoke in a tunnel equipped with a transverse ventilation system. The tunnel dimensions are defined to be the same as the experimental apparatus shown in Fig. 4.1. The effect of the shape and position of the vent on the smoke confinement is evaluated by modelling the same vents tested experimentally, the dimensions of which are defined in section 4.2.1. The parameter of interest is the back-layer length which corresponds to the distance the smoke extends away from the source outside the extraction zone.

As in the experiments, the numerical simulations are carried out for $\Gamma_i = 8$, $\rho_i/\rho_0 = 0.7$ and $D_i/H = 0.56$. In these conditions, the corresponding HRR is approximately 0.25

kW and, therefore, the grid size δx must be between 0.002 m and 0.009 m in the region in which the source is located. As in section 5.3.2.1, in order to save computing time, a stretched mesh was used along the longitudinal direction to provide finer grids only near the source. In this region, the grid size is kept the same in the three directions 0.006 m \times 0.006 m \times 0.006 m, while in the other domains (outside the source region), the grid size is 0.08 m \times 0.006 m \times 0.006 m. As a result, the computational domain is divided into 1060 \times 60 \times 30 grids along the length, height and width direction, giving a total of 1 908 000 cells. The ventilation velocity through the tunnel is varied by changing the volume flow rate at the vents. For each simulation, the same extraction flow rate value is set in both vents. In transverse ventilation simulations, the flow requires a long time to reach a steady state, especially when the back-layer length is important. Therefore, the simulation time was set to 500 seconds for all simulated cases. For each simulation, 530 density receptors were set 0.01 m below the ceiling along the length of the tunnel centre. Once the simulation completed, the longitudinal profile of mean density is analysed to estimate the position of the front of the smoke back-layering. The length of the back-layer (L) is defined as the distance from the edge of the vent to the point at which the density of the flow reaches the density of the ambient air. For each of the three vent (Fig. 4.2), the volume flow rate at the vents is varied to simulate a range of ventilation velocities and the backlayer length is determined. The results obtained are presented below and compared with the experimental results.

5.3.3.2 Results and discussion

The numerical results on the smoke back-layering for the three vent configurations are presented in Fig. 5.34 and compared with the experimental results. Fig. 5.34a shows the results for rectangular vents, Fig. 5.34b shows the results for square centre vents and Fig. 5.34c shows the results for square side vents. The results are presented in the form of dimensionless quantities by plotting the non-dimensional backlayer length L/H against the extraction Froude number Fr_e . Ls and Rs refers to left side and right side, respectively. Note that in numerical simulations, the source was perfectly positioned at the centre of the tunnel (i.e. the source centre was located at $x = 8.4/2 = 4.2$ m). This resulted in a symmetrical propagation of the smoke flow within the tunnel and thus a similar extension of the backlayer beyond the two exhaust vents. Therefore, for numerical simulations, only the results obtained on one side are shown in Fig. 5.34.

For rectangular shaped dampers (RSD, i.e. Fig. 5.34a), the numerical data agree with the experimental data estimated on the left side of the source for all values of the extraction Froude number greater than approximately 1.2. Below this value, the difference between

experimental and numerical results becomes rapidly significant, so that the lengths of the back-layer remain higher in the experimental simulations. Nevertheless, for these vents, the confinement Froude number $Fr_{e,c}$ estimated numerically when the length of the back-layer is reduced to zero is close to that evaluated experimentally, its value is equal to 1.76 in the numerical case and to 1.72 in the experimental case.

For square shaped dampers placed in the centre of the tunnel ceiling (SSD-PC), at low values of the Froude number (less than 3.3), we observe a close agreement between the numerical data and the experimental data gathered on the right side of the source (Fig. 5.34b). At approximately $Fr_e = 3.6$, the backlayer in the experimental case decreases rapidly, until it reaches a length approximately equal to the height of the tunnel at $Fr_e = 4.03$. From this value, the variation of the back-layer length becomes insensitive to the variation of the extraction flow rate. In the numerical case, from $Fr_e = 3.6$ to approximately $Fr_e = 4.81$, the backlayer decreases less rapidly with the increase of the Froude number. At $L/H \approx 1$, the decrease in the back-layering length is very slow with the increase of the extraction flow rate. For these vents, the backlayer length is longer in the numerical simulations for all Froude number values greater than 3.6. As in the experiments, the confinement Froude number is defined as the minimum value from which the length of the back-layer is no longer affected by the extraction flow rate. This occurs (as shown in Fig. 5.34b) when the back-layer length is approximately equal to the tunnel height (i.e. at $L/H \approx 1$). Under these conditions, the corresponding values of the confinement Froude number in the experimental case and the numerical case are 4.03 and 4.81, respectively.

The results for the square shaped dampers placed at the side (SSD-PS) show a noticeable difference between the numerical and experimental data (see Fig. 5.34c). For all extraction velocities, the backlayer is estimated to be larger for the numerical case. In the experiments, the confinement conditions are reached for a Froude number equal to 6.37, where the back-layer becomes insensitive of the extraction flow rate when $L/H \approx 1$. However, in the numerical case, the smoke backlayer is insensitive to the variation of the extraction velocity when its length is approximately equal to 2.5 times the height of the tunnel. For this dimensionless length (i.e. $L/H \approx 2.5$), the confinement Froude number is equal to 5.76. It should be noted that in the experiments, the adoption of $L/H \approx 1$ as a reference condition for determining the confinement velocities is primarily intended to evaluate the effects of the position of the square vents on smoke control, since this condition was first considered for square centre vents then for square side vents. Otherwise, in the experiments, another condition can be chosen to define the confinement conditions for square vents placed to one side of the tunnel ceiling (for example, as it is obtained numerically, $L/H \approx 2.5$ may be taken in experiences).

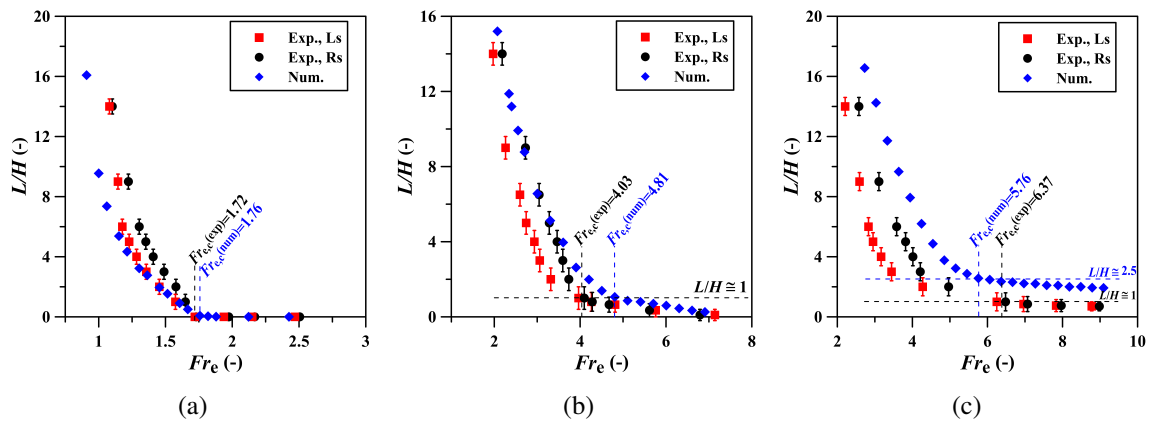


Figure 5.34: Numerical and experimental results on dimensionless back-layering length L/H versus the extraction Froude number Fr_e . a) Rectangular vents. b) Square centre vents. c) Square side vents.

Fig. 5.35 shows the numerical results on the behaviour of smoke in the confinement conditions for rectangular vents (Fig. 5.35a), square centre vents (Fig. 5.35b) and square side vents (Fig. 5.35c). Fig. 5.35a shows that the smoke is completely confined in the area between the two vents with a good preservation of the stratification. This is not the case with square vents, where a small back-layer appears beyond the vents and the stratification between the vents is destroyed, especially with the vents placed to one side of the tunnel ceiling (see Fig. 5.35c). In summary, as observed in the physical experiments, the rectangular vent is an effective configuration for smoke extraction as the wide width reduces the amount of smoke propagating in the tunnel. However, due to the reduced width of the square vent, a part of the smoke is extracted directly out the vent and the rest is propagated

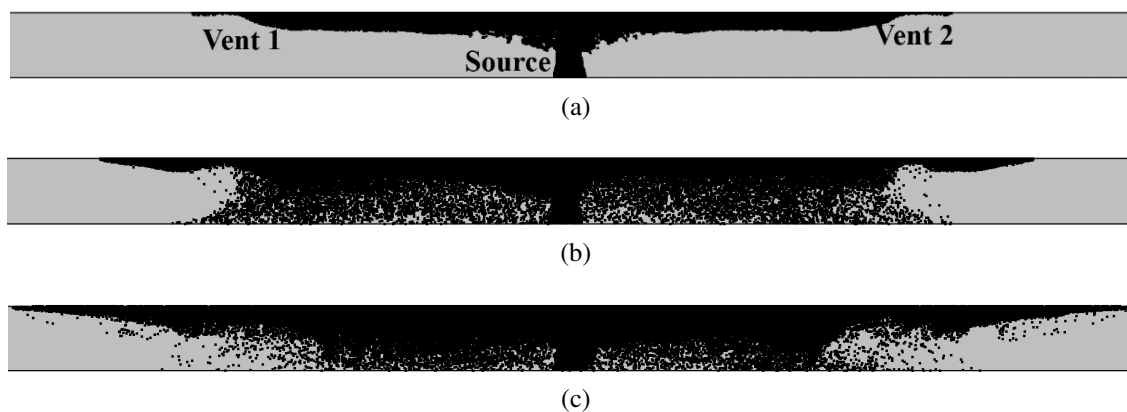


Figure 5.35: Behaviour of smoke in the confinement conditions. a) Rectangular vents ($Fr_{e,c} = 1.76$). b) Square centre vents ($Fr_{e,c} = 4.81$). c) Square side vents ($Fr_{e,c} = 5.76$).

down the tunnel between the edges of the vent and the wall. When the vent position is on one side of the tunnel, there is a larger gap between the edge of the vent and the tunnel wall, the smoke propagates down the length of the tunnel and the ventilation velocity must be increased further to reduce the backlayer length. This is illustrated in Fig. 5.36 by the three scenes of the time-averaged density ratio (ρ/ρ_0) taken near the tunnel ceiling. The colour bar legend shows that the red area indicates a density ρ equal to that of air ρ_0 (i.e. $\rho/\rho_0 = 1$), i.e. where no smoke is present. The backlayer distance is therefore the distance from the edge of the vent to the beginning of the red area. Fig. 5.36a shows the case of a low Froude number of value $Fr_e = 3.94$. The backlayer length is long and it is the same on both sides of the source ($L/H \approx 8$). In this case, the distance from the vent to the edge of the back layer is equal across the width of the tunnel. Fig. 5.36b shows the case of a Froude number value slightly lower than the confinement value, $Fr_e = 4.85$. On the left side of the source, the back-layer length appears to increase gradually across the width of the tunnel as the distance from the vent increases. Fig. 5.36c shows the case of a Froude number value greater than the confinement value, $Fr_e = 9.10$. In this case, the backlayer length at the centre of the vent is almost zero, while at the tunnel centre and in the opposite half to the ventilation shaft, the smoke is still spreading beyond the edge of the vents. In these areas, the length of the back layer is slightly reduced even though the Froude number is greatly increased (see Fig. 5.36b and Fig. 5.36c). However, the level of the smoke destratification for this Froude number

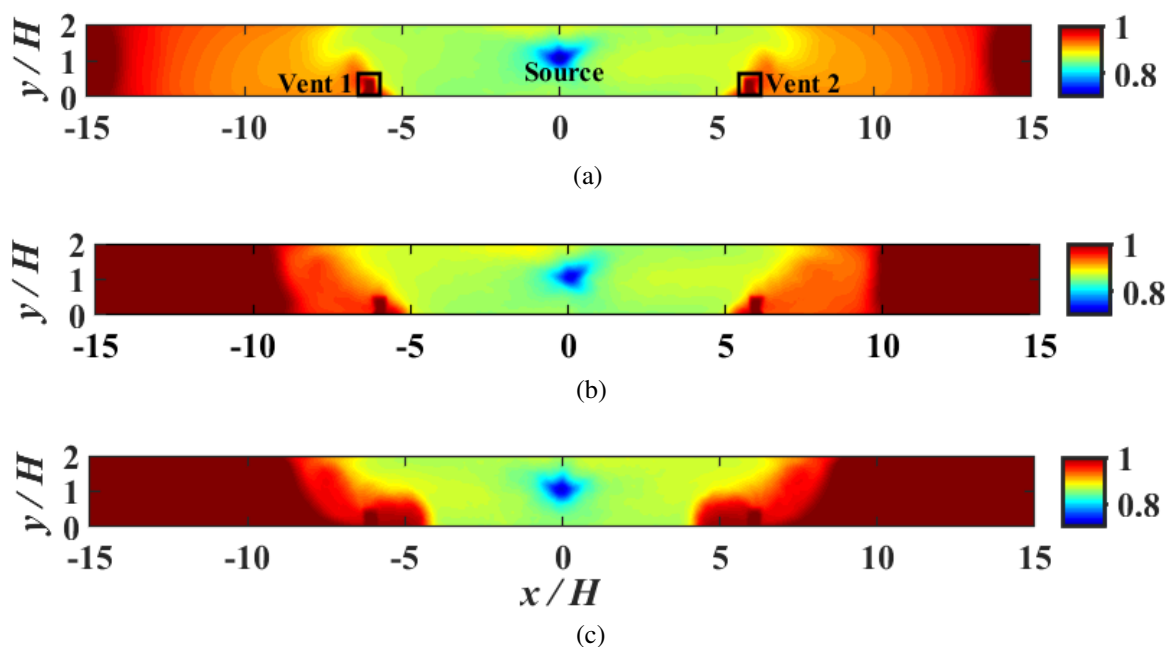


Figure 5.36: Time-averaged density ratio scenes near the tunnel ceiling for square vents placed on one side (top view). a) $Fr_e = 3.94$. b) $Fr_e = 4.85$. c) $Fr_e = 9.10$.

(i.e. $Fr_e = 9.10$) is too high (see Fig. 5.37).

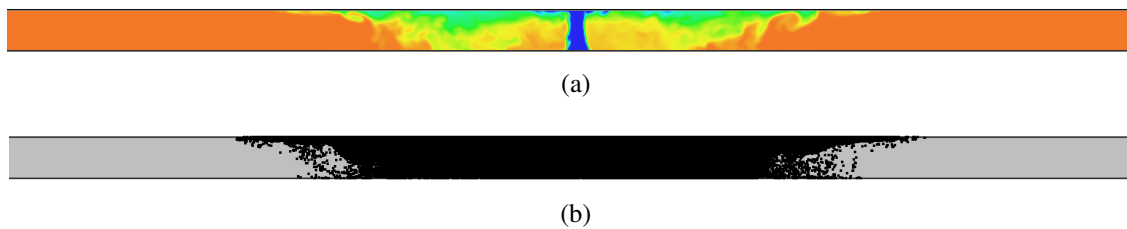


Figure 5.37: Numerical results in the steady state for a Froude number $Fr_e = 9.10$. a) Side view of the instantaneous density field. b) Side view on the behaviour of the smoke.

5.3.3.3 Effects of the solid barriers on the propagation of smoke

A further set of numerical simulations was conducted with transverse ventilation to assess the effects of solid barriers on the propagation of smoke. As in physical experiments, the barriers are added to the tunnel ceiling on the far edge of each vent. These barriers have the same dimensions as the large barriers defined in section 4.3.4, their numerical description was previously established in the numerical study of longitudinal ventilation (see section 5.3.2.1). These barriers aim to further reduce the confinement velocity and to improve the stratification of smoke, particularly for narrow-width vents. The simulations are performed imposing $\Gamma_i = 8$, $\rho_i/\rho_0 = 0.7$ and $D_i/H = 0.56$. The results below are presented in the confinement conditions, i.e. minimum extraction flow rate required to prevent smoke from passing the barriers.

Fig. 5.38 shows the effects of the barriers on smoke propagation for square dampers placed to one side of the tunnel ceiling. Fig. 5.38a shows the case with a barrier size $H/4$ and Fig. 5.38b the case with a barrier of size $H/3$. The confinement conditions are reached at a Froude number equal to 3.94 with a barrier $H/4$ and to 2.42 with a barrier $H/3$. The confinement velocity ratio, $Rc = \frac{U_{0,c \text{ with barrier}}}{U_{0,c \text{ without barrier}}}$, is therefore 0.68 with the barrier $H/4$ and 0.47 with the barrier $H/3$. This implies that the reduction rate of the confinement velocity ($1 - Rc$) due to the large barrier $H/4$ is equal to 32% and that due to the barrier $H/3$ is equal to 53%. These values are in good agreement with those obtained with the experiments (see section 4.3.4), i.e. 32% and 55% for barriers $H/4$ and $H/3$, respectively. As expected, the numerical results show that the barriers can improve the stratification of the smoke. This is well accomplished with the largest barrier $H/3$ where all smokes are maintained in the upper part of the tunnel. With a $H/4$ size barrier, the smoke appears even in the lower part of the tunnel, but with a density lower than that observed in the empty tunnel (see Fig. 5.35c

and Fig. 5.38a). This feature is consistent with the experimental visualisations illustrated in Fig. 4.15.

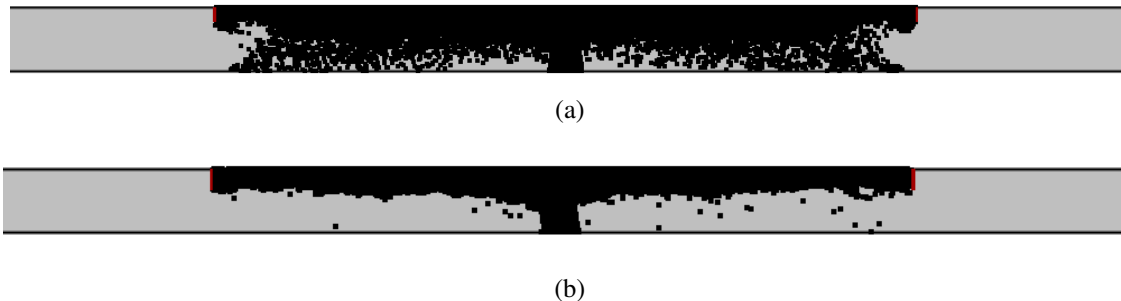


Figure 5.38: Effects of solid barriers on the spread of smoke for square side vents. a) Barrier with height $h = H/4$ ($Fr_{e,c} = 3.94$ and $Rc = 0.68$). b) Barrier with height $h = H/3$ ($Fr_{e,c} = 2.42$ and $Rc = 0.47$).

Fig. 5.39 shows the numerical results for square vents placed in the centre of the tunnel ceiling (with a barrier size $H/4$ and $H/3$). The $H/4$ size barrier and $H/3$ size barrier prevent the smoke back-layer for any Froude number greater than or equal to 2.84 and 1.78, respectively. In this case, the reduction rate of the confinement velocity ($1 - Rc$) is 41% with the barrier of size $H/4$ and 63% with the barrier of size $H/3$. These values indicate that the reduction of the confinement velocity is slightly better when the vent is placed in the centre for both barrier sizes, which is consistent with what observed in the experiments (see Fig. 4.14). The difference between the numerical and experimental results for the square centre vent is minimal. However, the reduction of the confinement velocity is slightly higher in the numerical case (as a reminder, in the experiments, the reduction rate is 38% with the barrier $H/4$ and 58% with the barrier $H/3$, see section 4.3.4). For this configuration, large barriers effectively contribute to the preservation of smoke stratification, even with an $H/4$ size.

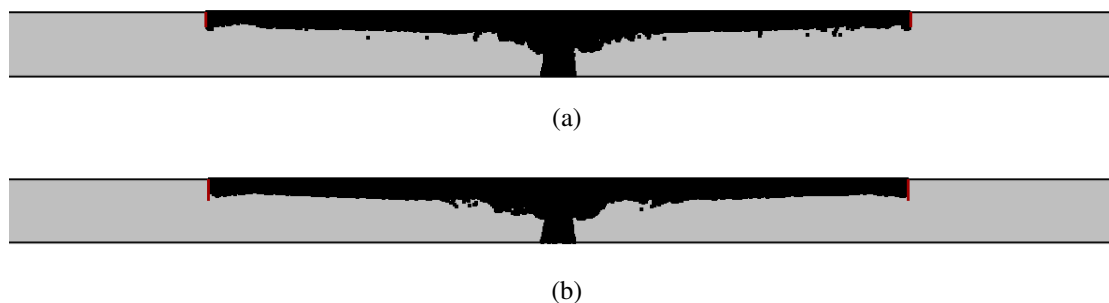


Figure 5.39: Effects of solid barriers on the spread of smoke for square centre vents. a) Barrier with height $h = H/4$ ($Fr_{e,c} = 2.84$ and $Rc = 0.59$). b) Barrier with height $h = H/3$ ($Fr_{e,c} = 1.78$ and $Rc = 0.37$).

In summary, in a tunnel where the vent does not span the entire width of the ceiling, the barriers significantly reduce the confinement ventilation velocity and improve the stratification of the smoke. The reduction rate in the confinement velocity is slightly dependent of the position of the vents but it is closely associated with the height of the barriers, the greater the barrier height, the greater the reduction in the confinement ventilation velocity. To ensure a good stratification of smoke in the tunnel equipped with square side vents, a large barrier of height $H/3$ must be added. However, in the tunnel equipped with square centre vents, deploying a barrier size $H/4$ is sufficient to confine the smoke in the area between the two vents and ensure a good level of smoke stratification.

5.4 Conclusions

In this study numerical simulations of longitudinal and transverse ventilation systems in road traffic tunnels have been analysed. The fire source was simulated with a buoyant source of helium and air, injected from square source (with the same area as the circular source of the experiment) into a small-scale tunnel of the same dimensions as the experimental apparatus. The aim was to reproduce numerically the experiments to get further insight on the flow dynamics, complete the interpretation of the experimental results and evaluate the ability of the numerical model to simulate the smoke propagation in ventilated tunnels.

PIV experiments were reproduced numerically by considering both the forced plumes (with $\Gamma_i = 0.0075$) and the lazy plumes (with $\Gamma_i = 1.45$) and varying the values of the density ratio ρ_i/ρ_0 . The main findings are the following:

- A slight disagreement between the experimental and numerical results is observed for the non-Boussinesq lazy plumes, where we observe an influence of the density ratio ρ_i/ρ_0 on the dimensionless critical velocity $U_{0,cr}/W_i$ that is not observed experimentally.
- The time-averaged fields of the two velocity components are well reproduced numerically, but the buoyant plumes are more inclined (in the direction of the flow) in the numerical case, particularly for forced releases.
- The magnitude dimensionless standard deviation of the two velocity components and the non-dimensional Reynolds shear stress is small in the numerical case than in the experiments.

Then, the effect of the blockage on the smoke propagation by fixing solid barriers to the tunnel ceiling was studied. Both the small fixed barriers and large mobile barriers were

evaluated. The comparison between the results of experimental simulations and numerical simulations showed that:

- The reduction rates of the critical ventilation velocity due to the presence of barriers of different sizes are similar.
- The lengths of the smoke back-layer are slightly greater with the numerical simulations.

In transverse ventilation conditions, the effect of different shapes and positions of vents in the tunnel ceiling was investigated. Square vent configurations coupled with the installation of large barriers to the tunnel ceiling were studied. The main conclusions are the following:

- Concerning the confinement velocity, the numerical data are in good agreement with the experiments for the rectangular vents and slightly different for the square vents.
- For square side vents, the back-layer is larger in the numerical simulations, while for the other two configurations of vents, the difference between the numerical and experimental data is generally not significant, especially when considering extraction velocities close to confinement velocity.
- Numerical results on the effects of solid barriers on smoke control are consistent with experimental results for both the reduction of confinement rate and the improvement of smoke stratification.

In conclusion, numerical simulations predict critical or confinement velocities that are not too different from the corresponding experimental velocities. In contrast, in most cases, numerical predictions of the back-layer lengths show non-negligible differences with experimental measurements, in particular when the imposed velocity is too low compared to the critical or confinement velocity. This difference between the experimental and numerical results may be due to the limitations of the numerical code in characterising the behaviour of the flow next to the wall. Therefore, efficient flow modeling near the walls is of utmost importance to numerically study the phenomenon of the smoke back-layering. This can be achieved by providing finer grids near the walls and using numerical model based on the Reynolds-Averaged Navier–Stokes equations (RANS equations) to save computing time.

GENERAL CONCLUSIONS

In this thesis, fires in road tunnels with longitudinal and transverse ventilation systems are investigated numerically and experimentally. The fire smoke is simulated as a buoyant plume obtained by injecting a mixture of air and helium into ambient air. With this simplified representation, the radiation and the heat losses at the walls are not taken into account, but the model can nevertheless provide relevant information on phenomenology and data fields that can be compared to real fires. In longitudinal ventilation, the parameters of interest were the critical ventilation velocity and the backlayer length. While in transverse ventilation, the backlayer length and confinement velocity as well as the smoke stratification are the parameters of interest. The study aimed to achieve various objectives, in particular increasing the efficiency of the mechanical ventilation systems and improving the safety of tunnels users in the event of fires.

The study included four distinct parts. First, experiments were conducted to measure, with a Particle Image Velocimetry (PIV) system, the velocity fields induced by turbulent buoyant plumes released within a longitudinally ventilated tunnel. The aim was to study, in the critical ventilation conditions, the non-Boussinesq effects (i.e. effects related to large density differences between the buoyant plume and the ambient air) on the dynamics of the momentum-driven releases and buoyancy-driven releases. The magnitude of both shear stresses and fluctuations (scaled by the injection velocity W_i) were much higher in buoyancy-dominated releases than in jets, suggesting that the buoyancy acts to enhance turbulent entrainment process and therefore to increase the turbulent mixing between the buoyant plume fluid and the ambient fluid. Upon reaching the ceiling, in this mixing process, the plume can therefore lose information about its source conditions, in particular its density, which leads to a negligible influence of the density ratio ρ_i/ρ_0 on the dimensionless critical velocity $U_{0,cr}/W_i$. Note that this is not the case with forced releases, for which the dimensionless critical velocity reduces for reducing density ratios.

The effect of solid barriers, placed at the tunnel ceiling, on the propagation of smoke in fire events within longitudinally ventilated tunnels was then studied. Two types of barrier: "small barriers" designed to be fixed in place and "large barriers" designed to be mobile

in real tunnels were considered. Experiments were carried out with and without vehicular blockage, modelled by blocks of different sizes and placed upstream of the source. It has been found that the presence of barriers and/or blocks prevents the smoke back-layering flow and reduces the critical velocity. The reduction rate of the latter depends on the blocking rate created by the obstacles (barriers, blocks or both) located just upstream of the source. Subsequently, the effect of blockages on pressure losses inside the tunnel was investigated. Large barriers have been shown to be more effective than small barriers because they prevent the smoke back-layering at very low critical velocities and they induce less pressure losses in congested tunnels.

The longitudinal ventilation system was then replaced by a transverse ventilation system and the confinement of smoke flow between two exhaust vents located on either side of a buoyant source was investigated. The effect of the shape and the position (with respect to the tunnel axis) of the dampers, including the specific case of full-width dampers, on the performance of the transverse ventilation system was evaluated. The extent of the back-flow length beyond the extraction dampers, the confinement velocity and the stability of the smoke stratification were studied. Results showed that the greater the proportion of the tunnel width the vent covers and the closer to the centre of the tunnel the vent is placed, the more efficient the ventilation system at confining the smoke to the extraction zone and ensuring the stability of the smoke stratification. The effect of solid barriers placed at the tunnel ceiling has also been assessed with transverse ventilation and it has been found that large barriers can improve the efficiency of vents that do not cover the full width of the tunnel, by reducing the confinement velocity and enhancing the stability of the smoke stratification.

Finally, numerical simulations of fires in a tunnel with longitudinal ventilation and transverse ventilation were carried out using Fire Dynamics Simulator (FDS) software and adopting Large Eddy Simulation (LES) approach. Several experimental tests were numerically reproduced to complete the interpretation of the experimental results. A good agreement has generally been reached between the experimental results and the numerical predictions. The large discrepancies between numerical and experimental results were observed when analysing the influence of non-Boussinesq effects on the flow dynamics for buoyancy dominated releases. Notably, our results show a dependence of the critical velocity on the density ratio that is not observed experimentally. The effects of solid barriers as well as those of the shape and position of the exhaust vents on smoke control were instead well reproduced numerically. The critical velocities and confinement velocities were in general similar to those obtained experimentally, but the lengths of the smoke back-layer were different in a great majority of the cases. A result that suggests that one of the limitations of FDS is the characterisation of the flow behaviour close to the walls.

PARTICLE IMAGE VELOCIMETRY TECHNIQUE: ACQUISITION, POST-PROCESSING AND QUALITY OF PIV DATA

A.1 Equipment and Apparatus

- The light sheets were obtained with a Quantel Brilliant Twins Double Pulse Nd:YAG laser, which is commonly used in PIV applications.
- The images were acquired with an Imager sCMOS camera, which incorporates a next-generation of Complementary Metal-Oxide Semiconductor (CMOS) sensors combined with the advantages of modern Charge Coupled Device (CCD) technology, providing high resolution image quality and unmatched performance.
- The plume fluid was seeded with nebulised oil while the ambient air was seeded using a theatre smoke generator (manufacturer: LOOK, model: Tiny FX). The Tiny FX is based on the vaporizer principle, i.e. a glycol fluid is evaporated and condenses into fog when leaving the fog nozzle. Over an operating period of 10 minutes, the released smoke extends to uniformly fill the enclosure and data acquisition begins once the motion induced by the buoyant plume is completely dissipated. The particle concentration must be chosen judiciously to achieve the desired spatial resolution, while maintaining adequate image quality. It should not be high enough to result in image saturation, nor so low that there are not enough particles in each interrogation area to carry out a reliable correlation and a well-marked correlation peak (A number of particles of 8 to 10 per interrogation area is generally desirable for computing the cross-correlation function). The size of particle images also plays a very important role on measurement quality, particle images should be in the 2–3 pixel diameter range [41]. For larger particle images, the achievable measurement uncertainty increases

while for smaller particle images, the bias errors commonly referred to as "Peak-locking effect" increase (section A.4.1).

- The images were finally processed with LaVision DaVis 8.4 software.

A.2 Camera calibration

The use of vision sensors for measurement purposes requires calibration of the intrinsic and extrinsic camera parameters. The process consists mainly in establishing a relationship between the physical space and the pixels of the camera field of view. This gives a conversion factor for changing the original scaling of the stored data from units of pixels to millimeters, as well as other information necessary for image correction, such as the possible existence of image distortion at the border.

LaVision[®] uses fully empirical calibration methods, based on perfectly defined geometric volume plates, to provide an extremely accurate and reliable calibration level. In the case of two-dimensional PIV measurements, as in this work, the calibration process is simple, the planar calibration target used is in-plane with the light sheet and only one camera is required. The camera is positioned in such a way that its viewing direction is square to both the object plane and the laser sheet. The calibration plate is equipped with circular markers with a diameter of 3.2 mm, placed on the horizontal and vertical lines with a spacing of 15 mm (Fig. A.1). The plate is dug so that a second plane of same marks is placed three millimeter from the foreground; this allows the system to be geometrically calibrated in the direction perpendicular to the lighting plane (fundamental for stereoscopic viewing). The plate is also equipped, on the left side at the top, with reference marks (a triangular mark on the first plane and a square mark on the second plane). The calibration plate is already known by the acquisition software and all the markers are automatically detected with image processing techniques in order to calculate the appropriate mappings between the object space and the image space.

In our experimental setup, one calibration is performed for lazy plumes and the other for forced plumes. This is because lazy plumes require a larger measuring field than forced plumes due to their inclination in the same direction as the longitudinal ventilation flow. Fig. A.1a and Fig. A.1b show the position of the calibration plate and the size of areas of interest for the forced and lazy plumes, respectively. The calibration process steps can be resumed as follows:

- Putting the calibration plate in the desired measurement plane (i.e. the plane passing through the centre of the source) while ensuring correct orientation, positioning and verticality, as it serves as a reference in the physical space.

A.2 Camera calibration

- Adjustment of the laser sheet by precisely aligning its light plane with the first plane of the calibration plate.
- Positioning of the camera in a way that the viewing direction is perpendicular to the object plane (i.e. a viewing angle of 90°), adjusting the objective focus to obtain a homogeneous view of the plate.
- Take a picture of the plate for the calibration numerical procedure and enter the correct scale values, measured by a ruler, in the acquisition software.
- Performing the calibration process (using a pinhole model) and setting the origin of the reference plane on the calibration map to use the real coordinates.

Once the calibration images are processed, the physical conversion factor is determined and the mapping function can henceforth link the physical space of the measured PIV fields to the pixel location of the images. The conversion factor values obtained for the configurations shown in Fig. A.1a and Fig. A.1b are $sc = 0.082$ mm/pixel and $sc = 0.082$ mm/pixel 0.159 (with same camera sensor, the conversion factor increases with the size of areas of interest).

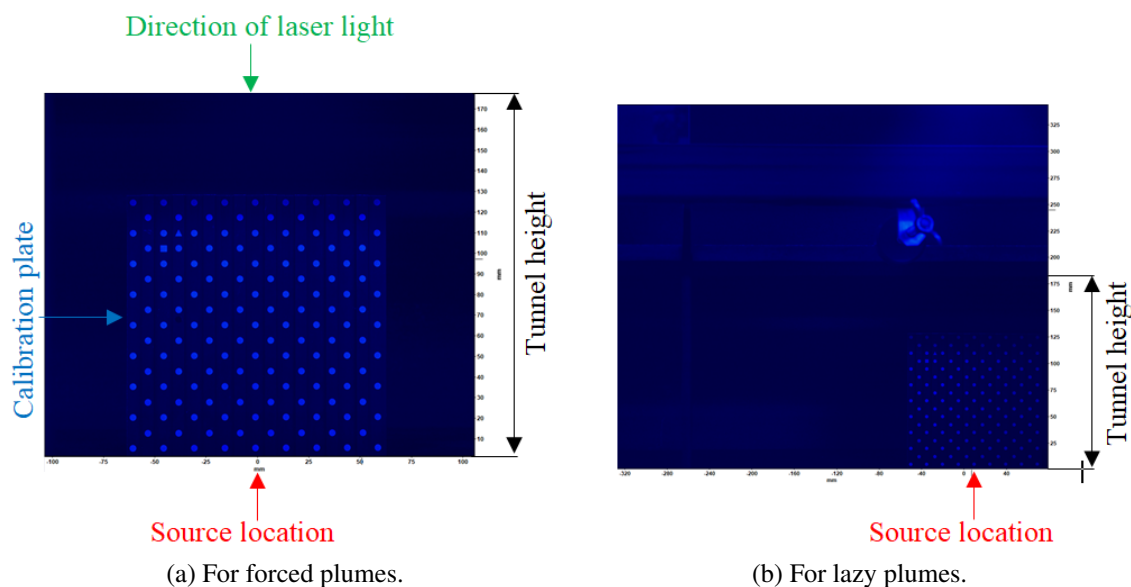


Figure A.1: Location of the calibration plate and the size of area of interest.

A.3 Recording and Processing of PIV Data

A.3.1 Preliminary Tests of PIV

PIV measurement tests are performed in order to check laser reflections in the areas of interest, to determine the optimal time separation Δt between laser shots and to control the seeding mass flow. The tests are carried out in the critical ventilation conditions of each case. For these tests, the camera is configured in live mode and no data is stored, it is just an on-line display of live camera images.

It should be noted that the presence of light reflections in the viewing area can introduce spurious vectors. For this purpose, during these tests (even for the following experiments), the laser power is kept as low as possible (without compromising PIV results) and the tunnel floor is made of matt-black painted wood in order to absorb and reduce the eventual presence of laser light reflections from the bounding surface. As a result, particle images obtained in these tests do not show the presence of light reflections, with the exception of a small number of points near the tunnel floor that do not affect the results of PIV. However, even if the intensity fluctuations in the background fields are significant, the PIV software provides several functions for pre-processing the particle images (e.g. the high-pass filter which is used to filter out large intensity and keep small intensity).

DaVis[®] performs inter-correlations between consecutive frames. Therefore, the time separation Δt between two frames (i.e. pulse separation) must be optimised to achieve a measurement uncertainty of less than 1%. It should be neither too high, resulting in a large number of uncorrelated points due to the out-of-plane motion of the fluid, nor too small so as not to lose the accuracy of the results [41]. With DaVis[®] software, a particle shift of 5 pixels is recommended to obtain the best accuracy. For this purpose, we tested several values of Δt and selected in each case the pulse delay which produces an appropriate particle displacement of about 5 pixels in the areas of highest velocity. The value of Δt achieved for each case is presented in Table A.1.

Ensuring an appropriate density of the tracer particles in the flow (i.e. the average number of particles per pixel "ppp") is one of the most difficult steps to accomplish in the PIV measurements. Ideally, the particle density value is close to 0.05 ppp, according to the information provided by DaVis[®]. Raffel et al. [41] recommended that at least 10 particles per interrogation area are suitable in order to achieve accurate data. To this end, several tests were carried out by fixing each time the seeding flow rate which is continuously released from the smoke generator and verifying that the number of particles is sufficient in most of the interrogation areas located in the zone of interest. The appropriate seeding rate associated with each case is then used in the PIV recording, expecting to obtain the correct

particle density values after the examination of the recorded images.

A.3.2 PIV Data Acquisition

The fundamental principle of PIV is to illuminate a seeded flow field with successive pulses of laser light and to record the particle images with a digital camera. The light scattered by the tracer particles can be recorded either on a single-frame or on a double-frames. We talk about a single-frame when the camera is unable to capture multiple frames at high speed and therefore two or more exposures of the same particles are captured on a single recording. In this case, a process called autocorrelation is used to analyse the flow field. However, the direction of the flow becomes unclear since there is no way to determine which image is due to the first pulse and which is due to the second pulse. Double-frame PIV recording is possible with digital cameras, such as sCMOS camera used here. In this case, each of the two subsequent exposures is recorded in two separated frames (F1 and F2) at two consecutive times " t " and " $t + \Delta t$ " (Fig. A.2). As is explained in section A.3.1, Δt is selected

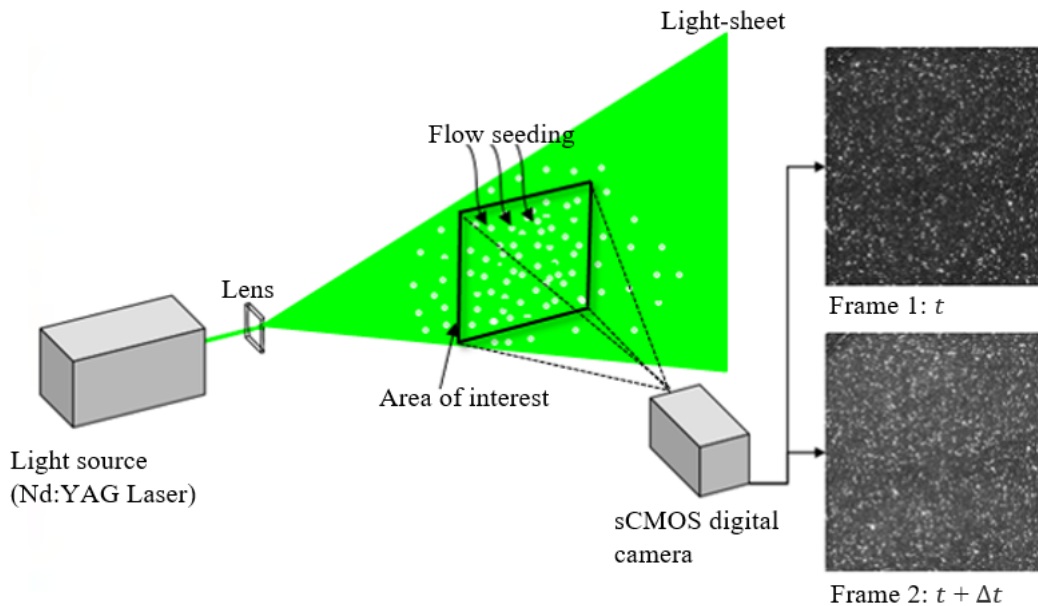


Figure A.2: Overall scheme of the PIV experimental device with double-frame recording method.

so that the image particle displacements are shifted by a few pixels. Setting the camera in recording mode and ensuring that the smoke flow and the flow seeding distribution are homogeneous over the observed domain, the process is repeated until the desired number of samples to be recorded is reached. For each case, 2000 samples were acquired over a period of approximately 5 minutes (per experiment). The recorded images can be manipulated after

they are transferred to the computer memory. DaVis[®] stores both frames of one "double-frame" recording in a single file. Each file has a size of approximately 20 MB, i.e. 40 GB per experiment for an acquisition of 2000 samples. These are stored in a folder and classified into consecutive buffers from B00001.im7 to B02000.im7. These images are then processed with PIV software, using cross-correlation method (section A.3.3).

A.3.3 PIV Data Processing

As already stated above, the image processing software used is DaVis 8.4 provided by LaVision. The software contains a large number of processing algorithms for performing each of the three stages of PIV data processing (pre-processing, processing, and post-processing).

The pre-processing stage consists of checking the images of tracer particles before performing vector calculations. This involves removing the excess noise and high intensities in PIV images in order to provide a good estimate of the particle displacement, thereby improving the quality of the results. In all cases, the average illumination of the particle images is homogeneous and no pre-processing of the images is therefore performed.

Data processing consists in estimating the actual displacement of particles to produce PIV velocity fields. To achieve that, the 2000 pairs of images acquired are divided in small regions called "interrogation areas". These are referenced on the array by their coordinates (i, j) . For each interrogation area, the local displacement vector for the particle images of the first and second illumination is determined by means of a statistical method called "FFT-based cross-correlation" (FFT refers to Fast Fourier Transformation). The cross-correlation algorithm is based on the principle that, between two illuminations, all tracer particles within each interrogation area are assumed to be homogeneously displaced. This algorithm examines the position of the tracer particles within each interrogation window of the first frame at time " t " and the second frame at time " $t + \Delta t$ ", and then compares these two interrogation windows by sweeping one over the other in both direction dx and dy . Once this sweeping process is completed, a correlation plane is provided (Fig. A.3). In this plane, a maximum correlation peak is obtained and it corresponds to the most probable average displacement (in pixel) of the tracer particles contained in the interrogation area. The location of the peak relative to the centre of the interrogation area describes the displacement and the direction of the tracer particles. The vector of the local flow velocity is then calculated taking into account the time delay between pulses, by a simple relation "velocity = displacement / Δt " and stored as a two-component velocity in units of "pixel/sec". The actual local flow velocity in units of "m/s" can then be calculated taking into account the magnification factor at imaging (previously determined in the section A.2).

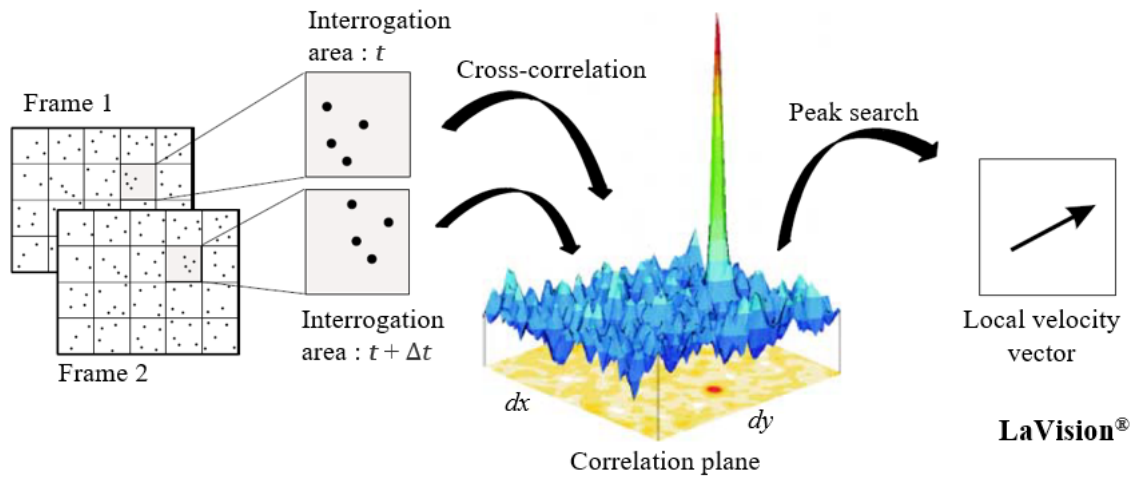


Figure A.3: Evaluation of PIV recordings using cross-correlation.

Note that only a single velocity vector is calculated in each interrogation area, and depending on its dimension, a number of vectors are computed in each field of view. In order to increase the accuracy of the displacement prediction, a multi-pass processing is used with decreasing size of the integration area from 64×64 pixels to a final window size of 24×24 pixels. The multi-pass method has the advantage of minimising the bias error due to FFT calculation, since it forces in each pass to focus the correlation peak on the correlation plane where the bias is the lowest, according to Raffel et al. [41]. Whereas, the successive reduction of the size of interrogation areas aims to increase the spatial resolution of the vector fields [115]. Furthermore, to better describe the fluid motion, more dense vector fields are created by specifying an overlap of 50% with interrogation areas of size 24×24 pixels. With this overlapping factor of the interrogation window, the spatial resolution increases and the size of each interrogation area becomes equal to 12×12 pixels.

Despite the precautions taken to ensure the best possible accuracy, the processing of PIV data can produce invalid computations or spurious vectors resulting from errors in determining the correlation peak. The spurious velocity vectors (frequently defined also as outliers) are characterised by anomalous magnitudes and directions compared to those of surrounding areas, red outlines in Fig. A.4a. These vectors, which were few in number, appeared at the boundaries of the data field (ceiling and floor tunnel). Therefore, it is necessary to filter out these errors and remove or replace the bad vectors to improve the quality of the data set. For this purpose, post-processing process is applied to calculate some statistical quantities in each velocity vector field obtained following the cross-correlation. The process relies on several methods to examine and treat each vector of each instantaneous flow

field. In this study, three criteria are applied. The first concerns the signal-to-noise ratio of the cross-correlation function. If the value of the ratio between the highest and the second highest peak of the correlation plane is less than 1.2 (recommended by LaVision[®]), the vector is deleted. The second concerns the application of a median filter method by choosing the option "remove & replace". The algorithm of this method computes the average vector (i.e. median vector) from a group of eight nearest neighbouring and compares it to the centre vector (i.e. middle vector). The centre vector is rejected if the absolute value of the difference between its magnitude and that of the average vector is three times greater than that of the deviation of the neighbouring vectors. This is then replaced by another vector that corresponds to the next highest correlation peak that meets the criterion. If it does not exist, the space point is then removed from the velocity vector map. The third method is introduced to delete the groups of wrong vectors that are not removed by the local median filter. These vectors are obtained when an error, induced for example by light reflections, is encountered at a position of the tracer particles image, which contributes considerably to the correlation signal. This leads to obtain a large number of wrong and isolated vectors, especially when a big overlap is used in the prediction of particle displacement (for more details, refer to DaVis[®] User Manual). Fig. A.4 shows an example of application of these methods. Fig. A.4a shows the vector field before the post-processing where the spurious

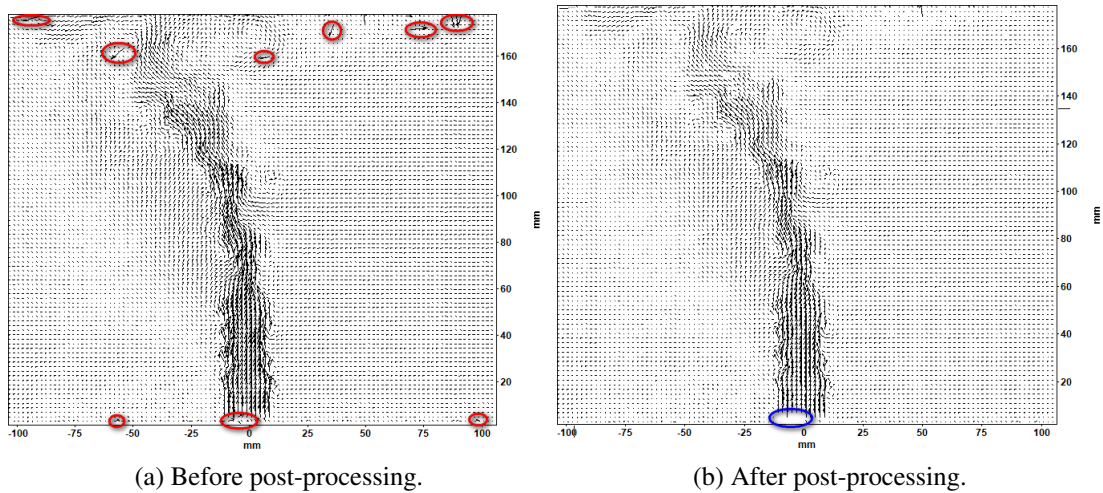


Figure A.4: Example of velocity vector map of instantaneous flow field (sample number 1013, case1).

vectors (due to noise and light reflection) appear at ground level and in the upper part of the tunnel. After post-processing, as shown in Fig. A.4b, the wrong vectors are deleted (blue outline) or replaced by means of the methods presented above. For each case, the percentage of rejected vectors is calculated and presented in Table A.1. Its value, as shown in this

table, is much less than 3%, which confirms the high quality of the data obtained from the PIV measurements.

A.4 Quality of PIV measurements

After the post processing of the PIV data, the quality of the measurements is checked. This consists of estimating the measurement uncertainty by calculating both systematic errors (i.e. bias errors) and statistical errors (i.e. residual errors).

A.4.1 Systematic errors

The systematic errors include all errors resulting from the inadequacy of the cross-correlation function in the evaluation of the PIV recording. This can be caused by several sources such as the low illumination within the studied field of view, seeding density (i.e. lack/excess of seed particles), out-of-plane motion, but mainly the use of an inappropriate sub-pixel peak estimator [41]. The latter can lead to significant bias errors known as "peak-locking", and its effect should first be verified.

Peak-locking phenomena

DaVis[®] uses PIV processing algorithms with sub-pixel methods that are able to output precise displacements to 1/10th of a pixel. This is necessary to measure the particle image shift by determining the correlation peak position with the best possible accuracy. In PIV measurements, a common source of systematic error is known as peak-locking. It is defined as the tendency for the measured displacement of a particle image to be slightly shifted towards integer values. This bias can limit the possible maximum accuracy of the vector computation and significantly affect the RMS (Root Mean Square) of velocity and Reynolds stress [116]. Peak-locking occurs when the size of captured particle images is too small, less than one pixel in diameter. This results in undersampled particle images, making it difficult to extrapolate particle displacements by a Gaussian. DaVis uses a method based on three-point estimator and a Gaussian function to fit the correlation peak. This method works best for rather narrow correlation peaks of 2-3 pixels width (LaVision[®]). However, if the particle images are too large, the magnitude of random error increases as the correlation value remains almost the same around the maximum correlation value [117]. The size of the particle images can be adjusted, either by a slight focusing or defocusing of the camera lens, or by moving the camera closer to or further from the measurement plane.

To quantify peak-locking effect, the method presented in LaVision DaVis software manual is used. This method uses the probability density function (PDF) to calculate the histogram

A.4 Quality of PIV measurements

of an instantaneous vector field where the u_x and u_z components are separated in certain velocity intervals for all values, from minimum to maximum (Fig. A.5a). From this histogram, the histogram of the decimal places of the displacement in pixel corresponding to the two components of the velocity is then calculated (i.e. " $u_x \cdot \Delta t / sc$ modulo 1" and " $u_z \cdot \Delta t / sc$ modulo 1"). If the peak-locking is low, the decimal places are distributed more or less uniformly over the entire pixel fraction range, as in histogram shown in Fig. A.5b. But if it is significant, the displacements will be concentrated only around the integer pixel values (i.e. around zero and one). The value of the peak-locking coefficient of each vector field is calculated from the centre of mass of the "particle displacement modulo 0.5" histogram (Fig. A.5c) as: Peak-lock = $(0.25 - \text{centre of mass}) \cdot 4$. If there is no peak locking (i.e. an equipartition of the decimal places), the center of mass should be about 0.25 and the peak locking coefficient is then equal to 0. The stronger the peak locking effect, the more the center of mass is shifted to zero, resulting in a peak lock close to 1. The commercial software provider LaVision suggests that the effect of peak locking is acceptable if this coefficient is less than 0.1. Keeping this in mind, the peak locking coefficient for the vector field chosen in Fig. A.5 has been evaluated and its value is equal to 0.001. This confirms that the particle displacements, for this instantaneous flow field, are accurate at the subpixel level.

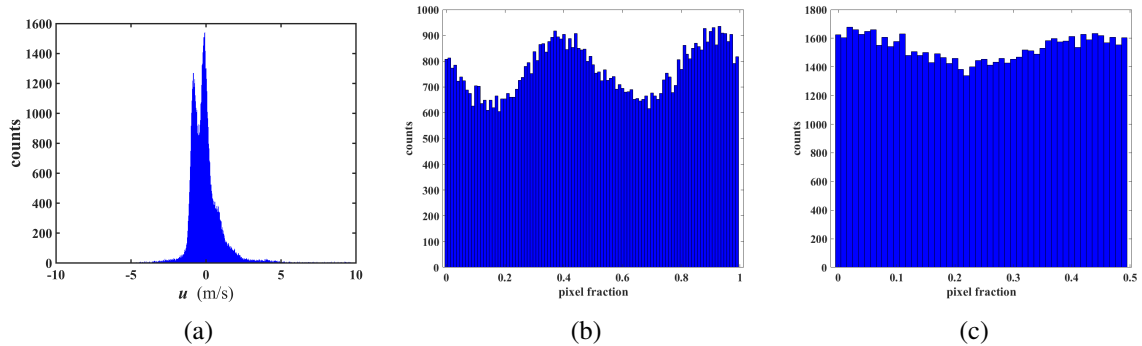


Figure A.5: Estimation of the peak locking coefficient of a vector field (sample number 70, case1). a) Histogram of velocity components, $u = (u_x, u_z)$. b) Histogram of particle displacement modulo 1. c) Histogram of particle displacement modulo 0.5 (i.e. histogram of particle displacement modulo 1 folded on itself with respect to 0.5).

Likewise, the peak locking coefficients are calculated for all acquisition samples of each case. The results, for example for the case1, are shown in Fig. A.6 where all the peak locking coefficients of the instantaneous vector fields are less than 0.1 and their average is equal to 0.036. The mean value of the peak-locking coefficient is also obtained low with the other three cases. This confirms that the quality of our PIV measurements is not affected by this type of systematic errors.

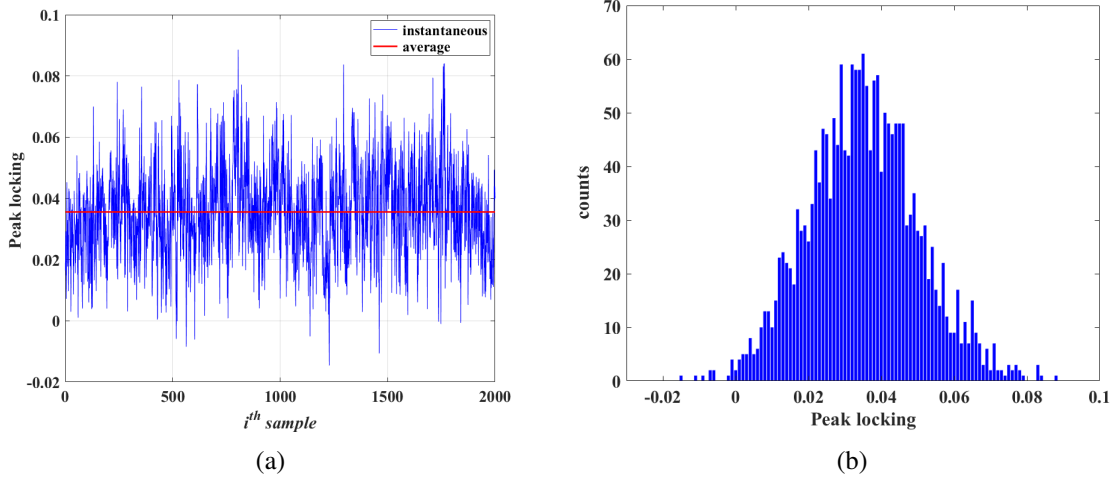


Figure A.6: a) Peak locking coefficient of each instantaneous vector field (case1). b) PDF of the peak locking coefficients.

The precision of the instantaneous velocity measurements is conditioned by the precision on the value of displacement calculated by cross-correlation function. In the absence of peak-locking, Stanislas et al. [118] reported that the uncertainty in the displacement measurements is generally comprised between 0.04 and 0.1 pixel. By adopting the maximum value (i.e. 0.1 pixel), the systematic error on the velocity measurement can be calculated as:

$$\varepsilon_{sys} = \frac{0.1 \cdot sc}{\Delta t} \quad (\text{A.1})$$

where "sc" is the image scale (i.e. conversion factor provided by the calibration in section A.2). The results of the maximum absolute velocity error due to the systematic error are summarised in Table A.1.

A.4.2 Statistical errors - steady flow

Assuming a Gaussian distribution for the 2000 instantaneous velocity values provided by PIV analysis in each interrogation area, the absolute statistical error $\varepsilon_{st,i}$ for the mean velocity value \bar{u}_i at a confidence level of 99.7% (i.e. $\bar{u}_i \pm \varepsilon_{st,i}$) can be calculated as follows:

$$\varepsilon_{st,i} = \frac{3 \cdot \sigma_i}{\sqrt{n-1}} \quad (\text{A.2})$$

where $n = 2000$ is the number of samples and $i = x, z$. In order to ensure that the number of samples is sufficient to reliably calculate the statistics (average velocity, standard deviation and statistical error), we conducted a study on the evolution of their convergence.

This is carried out with all cases and only the results obtained with the first case are shown here. The study is performed by choosing three crucial positions P1, P2 and P3, located in the line " $x = 0$ " at $z = 15$ mm, $z = 90$ mm and $z = 165$ mm. P1 is located in the centre of the plume near the injection source, P2 is located in the central axis of the tunnel while P3 is located near the tunnel ceiling (Fig. A.7).

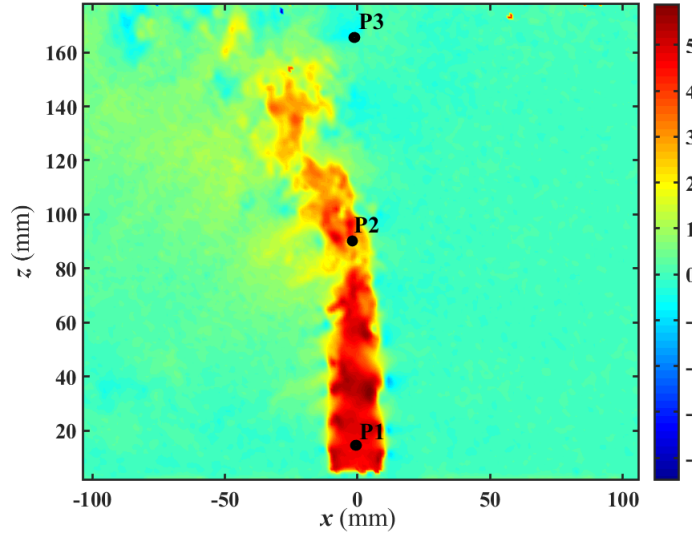


Figure A.7: Location of the chosen points in the plane of an instantaneous velocity field (instantaneous field of vertical velocity taken from the first case).

Fig. A.8 shows the evolution of the mean value of the two velocity components \bar{u}_x and \bar{u}_z (on the left side) and the uncertainty associated with the computation of the average velocities $\varepsilon_{st,x}$ and $\varepsilon_{st,z}$ (on the right side) against the number of samples, for each of the three points P1, P2 and P3. It can be seen that the average value of velocity components and uncertainty seems to be stabilised at about 700 samples for all points. This indicates that the data-set is sufficient to reliably calculate mean statistics and second statistical moments. Therefore, all the results presented, whether for the mean velocity fields or the standard deviation fields, will be calculated from 2000 instantaneous velocity fields.

It can also be noted that there is a rapid convergence of the mean velocity measured at the position P1 (blue curves in Fig. A.8a and Fig. A.8c), which is likely a consequence of the stationary nature of the flow in the region near the source. In this case, the estimated mean velocities of the two components after 2000 measurements are: $\bar{u}_x = -0.115 \mp 0.005$ m/s (a negative sign indicates that the direction of the longitudinal ventilation flow is in the opposite direction to the x-axis) and $\bar{u}_z = 4.862 \mp 0.008$ m/s. The ratio \bar{u}_x/\bar{u}_z is very low ($\bar{u}_x/\bar{u}_z = 0.023$), which means that the jet is essentially vertical.

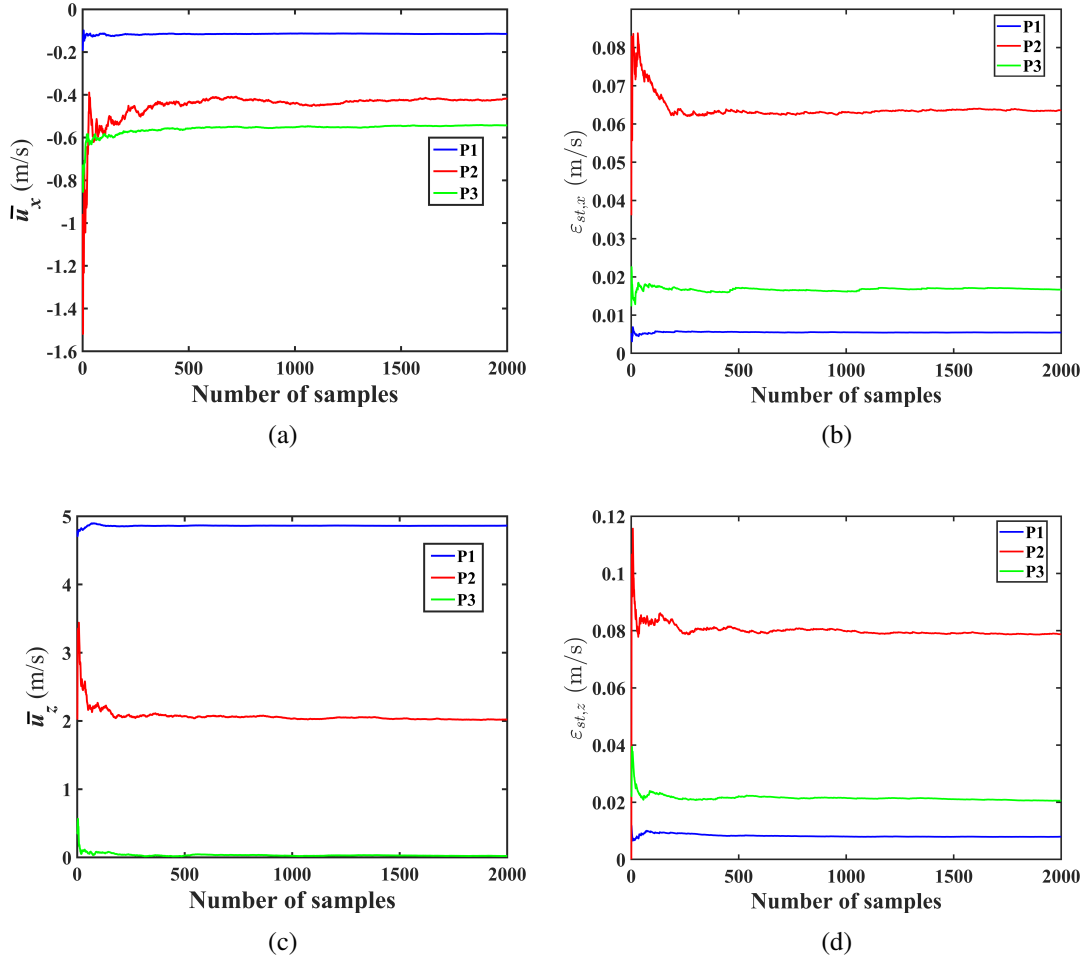


Figure A.8: Typical statistical convergence of the components of mean velocity and their associated uncertainty at three points P1 ($x = 0$ mm, $z = 15$ mm), P2 ($x = 0$ mm, $z = 90$ mm) and P3 ($x = 0$ mm, $z = 165$ mm) against the number of samples for the first case. a) Evolution of the mean value of \bar{u}_x . b) Convergence of the associated uncertainty $\epsilon_{st,x}$. c) Evolution of the mean value of \bar{u}_z . d) Convergence of the associated uncertainty $\epsilon_{st,z}$.

However, the statistical convergence of the mean velocity at the position P2 requires at least 700 instantaneous fields to be reached (red curves in Fig. A.8a and Fig. A.8c). This may be due to the strong interaction between the vertical flow arising from the source and the longitudinal ventilation flow. At this position, the longitudinal velocity (in absolute value) increased while the vertical velocity decreased (compared to those previously estimated at the position P1). Their values are: $\bar{u}_x = -0.419 \mp 0.064$ m/s and $\bar{u}_z = 2.019 \mp 0.079$ m/s; the ratio $\bar{u}_x/\bar{u}_z = 0.208$, which means that the vertical component of velocity is still predominant, except that the value of the longitudinal component in this case is not negligible. Furthermore, the high values of the statistical uncertainties $\epsilon_{st,x}$ and $\epsilon_{st,z}$ are reached

at this position, i.e. in the centre of the tunnel (red curves in Fig. A.8b and Fig. A.8d). Near the tunnel ceiling (P3), the longitudinal velocity becomes the predominant component. Its value $\bar{u}_x = -0.543 \mp 0.017$ m/s, while $\bar{u}_z = 0.021 \mp 0.021$ m/s. This results in a high velocity ratio \bar{u}_x/\bar{u}_z ($\bar{u}_x/\bar{u}_z = 26$), which means that the whole fluid flows in the longitudinal direction. The decrease in the vertical velocity of the injected flow is actually due to both the gravitational force and the longitudinal ventilation flow which forces the plume to tilt forward. It should be noted that in the areas where the mean vertical velocity is close to zero, the relative statistical error $\epsilon_{st,z}/\bar{u}_z$ is significant (at the P3 this ratio equal to 1).

However, the values of the total relative statistical error on the mean velocity, i.e. $e_{st} = \frac{\sqrt{\epsilon_{st}^2}}{\sqrt{\bar{u}_x^2 + \bar{u}_z^2}} = \frac{\sqrt{\epsilon_{st,x}^2 + \epsilon_{st,z}^2}}{\sqrt{\bar{u}_x^2 + \bar{u}_z^2}}$, at the positions P1, P2 and P3 are 0.2%, 4.9% and 5%, respectively. This ratio was calculated at each point of the mean velocity field and its value does not exceed 6%. By adding the maximum systematic error (Table A.1, case1) to the statistical error, the combining relative error on the mean velocity can be calculated as:

$e_{cm} = \frac{\sqrt{\epsilon_{sys}^2 + \epsilon_{st}^2}}{\sqrt{\bar{u}_x^2 + \bar{u}_z^2}}$. Hence, the maximum values of the relative combined error at the points P1, P2 and P3 are 1.9%, 6.6% and 17.4%.

It can be seen that the total relative error reaches its maximum in regions situated far from the plume, because of the low value of the mean velocity. In other words, the more the velocity tends towards zero, the higher the relative error. However, except these regions, the relative combined error in the regions of interest does not exceed 8% for the case1. A similar analysis was carried out for three other cases and the results showed that 2000 samples were largely sufficient to obtain the convergence of the components of mean velocity and mean statistical error. For each case, the maximum of both the statistical error and the combined relative error is summarised in Table A.1. The values of the combined relative error are given by excluding regions where the average velocity is low. These values, which range between 7% and 9% for the different cases, are rounded to 10% as presented in Table A.1.

A.4 Quality of PIV measurements

Table A.1: Quality parameters and errors for PIV measurement.

Case	sc (mm/pixel)	Δt (μs)	% of rejected vectors	$\max \varepsilon_{sys} $ (m/s)	$\max \varepsilon_{st} $ (m/s)	$\max e_{cm}$ (%)
1	0.082	90	0.91	0.091	0.101	10
2	0.082	60	1.21	0.137	0.153	10
3	0.159	1500	2.43	0.011	0.019	10
4	0.159	1000	2.63	0.016	0.032	10

MODELLING A PHYSICAL PROBLEM

To model fires in tunnels, many phenomena (that interact with one another in complicated ways) must be taken into account. First, the turbulence of the air flow in a tunnel exists even when fire is not present, since it is related to the significant parietal constraints. However, fires add a source of buoyancy, heat transfer, high temperature and velocity gradients, as well as high density variations that lead to the stratification of the flow inside the tunnel. Indeed, since the fire results in large density variations, the flow cannot be considered as an incompressible flow. But, the low longitudinal velocity leads to a very small number of Mach (much less than 0.3, which is generally known as the limit between compressible and incompressible flows). Therefore, the flow can be considered as compressible at low Mach, which requires a particular approximation of the equations. Here, the combustion and radiation problems are not detailed.

B.1 General form of the equations

In case of a compressible and viscous Newtonian fluid, the flow is described by the Navier-Stokes equations. These are obtained from mass, momentum and energy balances based on a volume of fluid. These equations as well as the equation of state for ideal gases are written as follows:

B.2 System of equations at a low Mach number

$$\frac{\partial \rho}{\partial t} + \frac{\partial \rho u_i}{\partial x_i} = 0 \quad (\text{B.1})$$

$$\frac{\partial \rho u_i}{\partial t} + \frac{\partial \rho u_i u_j}{\partial x_j} + \frac{\partial p}{\partial x_i} - \frac{\partial \tau_{ij}}{\partial x_j} - \rho g_i = 0 \quad (\text{B.2})$$

$$\frac{\partial \rho h}{\partial t} + \frac{\partial (\rho h u_i + q_i)}{\partial x_i} - \frac{dp}{dt} - \tau_{ij} S_{ij} - S = 0 \quad (\text{B.3})$$

$$p - \rho \frac{R}{m} T = 0 \quad (\text{B.4})$$

where x is the vector position, t is the time, $\vec{u}(x,t)$ is the velocity field of the three velocity components u_i (with $i = x, y, z$), $\rho(x,t)$ is the density field, $p(x,t)$ is the pressure field, g is the gravity acceleration, h is the internal enthalpy, S is the heat sources, $R \approx 8.314 \text{ J}/(\text{mol K})$ is the ideal gas constant, m is the molar mass of the gas, T is the absolute temperature, q_i is the diffusive heat flux, S_{ij} is the strain rate tensor and τ_{ij} is the viscous stress tensor. The last three terms are respectively expressed as follows:

$$q_i = -\lambda \frac{\partial T}{\partial x_i} \quad (\text{B.5})$$

$$S_{ij} = \frac{1}{2} \left(\frac{\partial u_i}{\partial x_j} + \frac{\partial u_j}{\partial x_i} \right) \quad (\text{B.6})$$

$$\tau_{ij} = \mu \left(2S_{ij} - \frac{2}{3} \frac{\partial u_k}{\partial x_k} \delta_{ij} \right) \quad (\text{B.7})$$

with $\lambda(T)$ the thermal conductivity, μ the dynamic viscosity and δ_{ij} the Kronecker symbol (its value equal to one if $i = j$ and to zero if $i \neq j$).

B.2 System of equations at a low Mach number

In road tunnels, the velocity of the air flow is generally low, it is less than 5 m/s. The corresponding Mach number defined by the ratio of the flow velocity to the speed of sound reaches values close to zero. Consequently, some terms in the previous equations (Eq. B.1 to Eq. B.4) can be neglected using the analysis of order of magnitude.

B.2.1 Equation of state

According to Viollet [119], in an infinitely thin stream tube, at any point, the velocity vector is collinear to the streamlines which form the contour of the tube. The balance of momentum

B.2 System of equations at a low Mach number

is written as:

$$dp = -\rho u du = -\rho d\left(\frac{u^2}{2}\right) \quad (\text{B.8})$$

For an ideal gas, the speed of sound, defined in a constant entropy as [120]:

$$c^2 = \left(\frac{\partial p}{\partial \rho}\right)_s \quad (\text{B.9})$$

is given by :

$$c = \sqrt{\frac{\gamma p}{\rho}} \iff \rho = \frac{\gamma p}{c^2} \quad (\text{B.10})$$

with γ the ratio of specific heats. By injecting Eq. B.10 into Eq. B.8, we get the relation below:

$$\frac{dp}{p} = \frac{\gamma d(u^2)}{2 c^2} \quad (\text{B.11})$$

In order of magnitude, $d(u^2) \simeq u^2$. Therefore, the pressure variation equation (Eq. B.11) can be expressed as follows:

$$\frac{dp}{p} \simeq \frac{\gamma u^2}{2 c^2} = \frac{\gamma}{2} M^2 \quad (\text{B.12})$$

where $M = \frac{u}{c}$ is the Mach number. In the tunnel, $M \ll 1$. Thus, in the logarithmic differentiation of the equation of state (Eq. B.4), which is written:

$$\frac{dp}{p} = \frac{d\rho}{\rho} + \frac{dT}{T} \quad (\text{B.13})$$

the term of pressure variations (i.e. $\frac{dp}{p}$) can be neglected and Eq. B.4 is then reduced to:

$$\rho T = \rho_0 T_0 \quad (\text{B.14})$$

where ρ_0 and T_0 are the reference temperature and the reference density, respectively.

The pressure can be decomposed into hydrostatic and hydrodynamic components, in the following form:

$$p = p_0 + p_h + p_d \quad (\text{B.15})$$

B.2 System of equations at a low Mach number

where p_0 is the reference pressure assumed constant, $\frac{\partial p_h}{\partial x_i} = \rho_0 g$ is the variation of the hydrostatic pressure and p_d is the hydrodynamic pressure, i.e. the flow-induced pressure.

B.2.2 Equation of enthalpy

In Eq. B.3, two terms can be neglected (see [43, 121, 122] for more details): the term of the pressure variation $\frac{dp}{dt}$ and the term of the heat production by mechanical energy dissipation $\tau_{ij}S_{ij}$.

Indeed, the first term, $\frac{dp}{dt}$, is negligible compared to the term $\frac{\rho dh}{dt}$. Note that the variation of the enthalpy is expressed as $dh = C_p(T)dT$, where C_p is the specific heat at constant pressure. In practice, despite the large temperature variations encountered during a fire, the value of C_p for air is considered to be independent of temperature and the enthalpy can be written as $h = C_p T$. Therefore:

$$\frac{\rho dh}{dt} \simeq \frac{\rho C_p dT}{dt} = \rho C_p T \frac{1}{T} \frac{dT}{dt} \quad (\text{B.16})$$

It was shown in Eq. B.13 that at very low Mach, the temperature differential is very large compared to that of the pressure. From where :

$$\frac{1}{T} \frac{dT}{dt} \gg \frac{1}{p} \frac{dp}{dt} \quad (\text{B.17})$$

Therefore:

$$\frac{\rho dh}{dt} \gg \rho C_p T \frac{1}{p} \frac{dp}{dt} \quad (\text{B.18})$$

Substituting Eq. B.4 into Eq. B.18, we obtain:

$$\frac{\rho dh}{dt} \gg \frac{m C_p}{R} \frac{dp}{dt} \quad (\text{B.19})$$

For air, the ratio between $m C_p$ and R is of the order of 100. Therefore:

$$\frac{\rho dh}{dt} \gg \frac{dp}{dt} \quad (\text{B.20})$$

From Eq. B.6 and Eq. B.7, the order of magnitude of the second term (i.e. $\tau_{ij}S_{ij}$) is $\rho_0 U^3 / ReL$, where U is the velocity of the flow in the tunnel, Re is the Reynolds number of the flow (its value is in the order of 10^6 in the tunnel) and L is the reference length scale. By comparison, the order of magnitude of the spatial variation of enthalpy is $\rho_0 C_p T_0 / L$. Given the low velocities in our case, $\rho_0 C_p T_0 / L$ is therefore predominant (since $(\rho_0 U^3 / ReL) / (\rho_0 C_p T_0 / L) = U^3 / \rho_0 C_p Re \ll 1$). Additional simplification is possible in Eq. B.3, because the quantity ρT is

constant and C_p is assumed to be independent of the temperature, and therefore the partial derivatives of $\rho h = \rho C_p T$ are zero. Therefore, the equation of enthalpy (Eq. B.3) reduces to:

$$\frac{\partial u_i}{\partial x_i} = \frac{1}{\rho_0 C_p T_0} \left(\frac{\partial}{\partial x_i} \left(\lambda \frac{\partial T}{\partial x_i} \right) + S \right) \quad (\text{B.21})$$

B.2.3 Poisson's equation

Poisson's equation is obtained from the momentum equation (given in Eq. B.2), which is simplified to take into account the low value of the Mach number. By dividing the momentum equation (Eq. B.2) by the density (ρ) and using the mass conservation equation (Eq. B.1), we obtain:

$$\frac{\partial u_i}{\partial t} + u_j \frac{\partial u_i}{\partial x_j} + \frac{1}{\rho} \frac{\partial p}{\partial x_i} - \frac{1}{\rho} \frac{\partial \tau_{ij}}{\partial x_j} - g_i = 0 \quad (\text{B.22})$$

According to Eq. B.15, $\frac{1}{\rho} \frac{\partial p}{\partial x_i}$ can be expressed as follows:

$$\frac{1}{\rho} \frac{\partial p}{\partial x_i} = \frac{1}{\rho} \frac{\partial p_0}{\partial x_i} + \frac{1}{\rho} \frac{\partial p_h}{\partial x_i} + \frac{1}{\rho} \frac{\partial p_d}{\partial x_i} \quad (\text{B.23})$$

where $\frac{1}{\rho} \frac{\partial p_0}{\partial x_i} = 0$ and $\frac{\partial p_h}{\partial x_i} = \rho_0 g$.

Substituting Eq. B.23 into Eq. B.22, we obtain:

$$\frac{\partial u_i}{\partial t} + u_j \frac{\partial u_i}{\partial x_j} + \frac{1}{\rho} \frac{\partial p_d}{\partial x_i} - \frac{1}{\rho} \frac{\partial \tau_{ij}}{\partial x_j} - \frac{\rho - \rho_0}{\rho} g_i = 0 \quad (\text{B.24})$$

Rearranging Eq. B.24 and taking its divergence, we obtain:

$$\frac{\partial^2 (p_d/\rho)}{\partial x_i \partial x_i} = -\frac{\partial}{\partial x_i} \left(p_d \frac{\partial (1/\rho)}{\partial x_i} \right) - \frac{\partial}{\partial t} \left(\frac{\partial u_i}{\partial x_i} \right) - \frac{\partial}{\partial x_i} \left(u_j \frac{\partial u_i}{\partial x_j} \right) + \frac{\partial}{\partial x_i} \left(\frac{1}{\rho} \frac{\partial \tau_{ij}}{\partial x_j} \right) + g_i \frac{\partial}{\partial x_i} \left(\frac{\rho - \rho_0}{\rho} \right) \quad (\text{B.25})$$

This last formulation constitutes the Poisson equation that allows p_d to be computed by the numerical methods.

B.3 Turbulence modeling

In road tunnel fires, most flows are turbulent. As already stated in the introduction of Chapter 5, the Navier–Stokes equations can be numerically solved using Direct Numerical Simulation (DNS). But this method is only possible when the mesh size is smaller

than the smallest turbulence scales, which requires high computation time and cost. Consequently, turbulence modeling is fundamental using one of the following two approaches : the Reynolds-Averaged Navier–Stokes method (RANS method) or the Large eddy simulation method (LES method).

B.3.1 Reynolds-Averaged Navier–Stokes method (RANS method)

The RANS method is based on the Reynolds decomposition, i.e. each flow variable is separated into mean (time-averaged) component and fluctuating component. For exemple for a variable f , we have:

$$f = F + f' \quad (\text{B.26})$$

where f can be the velocity u , the temperature T , the pressure p or the density ρ , $F = \bar{f}$, $\bar{F} = F$ and $\bar{f}' = 0$. The introduction of this decomposition and these definitions into the Navier-Stokes equation system leads to the following equations of the RANS model :

$$\frac{\partial \bar{\rho}}{\partial t} + \frac{\partial \bar{\rho} \bar{u}_i}{\partial x_i} + \frac{\partial \overline{\rho' u'_i}}{\partial x_i} = 0 \quad (\text{B.27})$$

$$\frac{\partial \bar{\rho} \bar{u}_i}{\partial t} + \frac{\partial \overline{\rho' u'_i}}{\partial t} + \frac{\partial \bar{\rho} \bar{u}_i \bar{u}_j}{\partial x_j} + \frac{\partial \overline{\rho' u'_i u'_j}}{\partial x_j} + \frac{\partial \bar{p}}{\partial x_i} - \frac{\partial \bar{\tau}_{ij}}{\partial x_j} - \bar{\rho} g_i = 0 \quad (\text{B.28})$$

$$\frac{\partial \bar{\rho} \bar{h}}{\partial t} + \frac{\partial \overline{\rho' h'}}{\partial t} + \frac{\partial (\bar{\rho} \bar{h} \bar{u}_i + \bar{q}_i)}{\partial x_i} + \frac{\partial \overline{\rho' h' u'_i}}{\partial x_i} - \frac{d\bar{p}}{dt} - \bar{\tau}_{ij} \bar{S}_{ij} - \bar{S} = 0 \quad (\text{B.29})$$

and for a low Mach number with C_p independent on temperature, Eq. B.29 is reduced according to Eq. B.21 to:

$$\frac{\partial \bar{u}_i}{\partial x_i} = \frac{1}{\rho_0 C_p T_0} \left(\frac{\partial}{\partial x_i} \left(\lambda \frac{\partial T}{\partial x_i} \right) + S \right) \quad (\text{B.30})$$

and Eq. B.28 is rewritten according to Eq. B.24 to:

$$\frac{\partial \bar{\rho} \bar{u}_i}{\partial t} + \frac{\partial \overline{\rho' u'_i}}{\partial t} + \frac{\partial \bar{\rho} \bar{u}_i \bar{u}_j}{\partial x_j} + \frac{\partial \overline{\rho' u'_i u'_j}}{\partial x_j} + \frac{\partial \bar{p}_d}{\partial x_i} - \frac{\partial \bar{\tau}_{ij}}{\partial x_j} - (\bar{\rho} - \rho_0) g_i = 0 \quad (\text{B.31})$$

This decomposition results in a nonlinear term $\overline{\rho' u'_i u'_j}$, generally referred to as the Reynolds stress, that introduces new unknowns. However, the number of total unknowns becomes

greater than the number of equations, which require additional modeling to close the system of the RANS equations. A model type closure for the Reynolds stresses, known as "Boussinesq eddy viscosity assumption" will be presented latter.

B.3.2 Large eddy simulation method (LES method)

The LES method consists in treating large and small scales separately. The principle is to use a low-pass filter on the Navier–Stokes equations for ignoring the smallest scales fluctuations. The large eddies of the flow which are responsible for transporting momentum and energy are directly simulated, while the effect of the small eddies on the flow field is modelled. Therefore, each flow variable present in the equations is separated into a "resolved" component and an "unresolved or residual" component. For a flow variable f , the filtered field is defined as:

$$\bar{f}(x) = \frac{1}{\Delta} \int f(r) \cdot \chi \left(\frac{x-r}{\Delta} \right) dr \quad (\text{B.32})$$

where Δ is the filter scale and χ is the filter convolution kernel, which can also be written as: $\bar{f} = \chi \star f$.

χ has an associated cutoff length scale Δ (and eventually cutoff time scale τ_c for temporal filtering operation). For spatial filtering operation, the scales larger than Δ are simulated while the scales smaller than Δ are eliminated from \bar{f} . Using this definition (Eq. B.32), any field f may be split up into a filtered quantity \bar{f} (that has to be explicitly resolved) and sub-filtered quantity f_{sgs} (that has to be modelled), as:

$$f = \bar{f} + f_{sgs} \quad (\text{B.33})$$

Applying the above low-pass filter (Eq. B.32) and the decomposition given by Eq. B.33, the set of equations B.1 to B.4 can be rewritten for a low Mach number as:

$$\frac{\partial \bar{\rho}}{\partial t} + \frac{\partial \bar{\rho} \bar{u}_i}{\partial x_i} = 0 \quad (\text{B.34})$$

$$\frac{\partial \bar{\rho} \bar{u}_i}{\partial t} + \frac{\partial \bar{\rho} \bar{u}_i \bar{u}_j}{\partial x_j} + \frac{\partial \bar{p}_d}{\partial x_i} - \frac{\partial}{\partial x_j} \left(\overline{\rho v \frac{\partial u_i}{\partial x_j}} \right) - (\bar{\rho} - \rho_0) g_i = 0 \quad (\text{B.35})$$

$$\frac{\partial \bar{u}_i}{\partial x_i} - \frac{1}{\rho_0 C_p T_0} \left(\frac{\partial}{\partial x_i} \left(\lambda \frac{\partial T}{\partial x_i} \right) + S \right) = 0 \quad (\text{B.36})$$

$$\bar{\rho} T - \rho_0 T_0 = 0 \quad (\text{B.37})$$

where Eq. B.36 is given by assuming that C_p is independent of the temperature and the viscous stress τ_{ij} is replaced by $\rho \nu \frac{\partial u_i}{\partial x_j}$ (for a Newtonian fluid) with $\nu(T) = \frac{\mu}{\rho}$ the kinematic viscosity.

For a variable density ρ , several cross terms appear in the above equations (i.e. Eq. B.34 to Eq. B.37) in the form of $\overline{\rho f}$ with $f = u_i$ or $f = u_i u_j$. To simplify the writing of these equations, Favre [123] proposed a density-weighted filtering operation, called Favre filtering, defined as:

$$\tilde{f} = \frac{\overline{\rho f}}{\bar{\rho}} \quad (\text{B.38})$$

with $\tilde{\rho} = \bar{\rho}$, $\tilde{T} = \frac{\overline{\rho T}}{\bar{\rho}} = \frac{\rho_0 T_0}{\bar{\rho}}$ therefore $\tilde{\rho} \tilde{T} = \bar{\rho} \tilde{T} = \rho_0 T_0$. The Favre filter of the velocity component is:

$$\tilde{u}_i = \frac{\overline{\rho u_i}}{\bar{\rho}} \quad (\text{B.39})$$

Applying the Favre filtering to the set of equations Eq. B.34 to Eq. B.37, we obtain:

$$\frac{\partial \tilde{\rho}}{\partial t} + \frac{\partial \tilde{\rho} \tilde{u}_i}{\partial x_i} = 0 \quad (\text{B.40})$$

$$\frac{\partial \tilde{\rho} \tilde{u}_i}{\partial t} + \frac{\partial \tilde{\rho} \tilde{u}_i \tilde{u}_j}{\partial x_j} + \frac{\partial \tilde{p}_d}{\partial x_i} - \frac{\partial}{\partial x_j} \left(\overline{\rho \nu \frac{\partial u_i}{\partial x_j}} \right) - \tilde{\rho} g_i = 0 \quad (\text{B.41})$$

$$\frac{\partial \tilde{u}_i}{\partial x_i} - \frac{1}{\rho_0 C_p T_0} \left(\frac{\partial}{\partial x_i} \left(\lambda \frac{\partial T}{\partial x_i} \right) + S \right) = 0 \quad (\text{B.42})$$

At a fixed point, we define ρ' the fluctuations of the density ρ as $\rho(t) = \bar{\rho}(t) + \rho'(t)$. According to Eq. B.39 we then obtain $\tilde{u} = \bar{u} + \frac{\rho' \bar{u}}{\bar{\rho}}$. In addition, by defining $u_i = \tilde{u}_i + u'_i$, and taking some simplifications into account, the set of equations (Eq. B.40 to Eq. B.42) can be rewritten in the following final form (for more details, the reader is referred to Pope [113]):

$$\frac{\partial \tilde{\rho}}{\partial t} + \frac{\partial \tilde{\rho} \tilde{u}_i}{\partial x_i} = 0 \quad (\text{B.43})$$

$$\frac{\partial \tilde{\rho} \tilde{u}_i}{\partial t} + \frac{\partial \tilde{\rho} \tilde{u}_i \tilde{u}_j}{\partial x_j} + \frac{\partial \bar{p}_d}{\partial x_i} - \frac{\partial}{\partial x_j} \left(\tilde{\rho} \mathbf{v}(\bar{T}) \frac{\partial \tilde{u}_i}{\partial x_j} - \tilde{\rho} R_{ij} \right) - \tilde{\rho} g_i = 0 \quad (\text{B.44})$$

$$\frac{\partial \tilde{u}_i}{\partial x_i} + \frac{\partial M_i}{\partial x_i} - \frac{1}{\rho_0 C_p T_0} \left(\frac{\partial}{\partial x_i} \left(\tilde{\rho} C_p \kappa(\bar{T}) \frac{\partial (\bar{T})}{\partial x_i} \right) + \bar{S} \right) = 0 \quad (\text{B.45})$$

with $\kappa(T) = \frac{\lambda}{\rho C_p}$ the thermal diffusivity, $R_{ij} = \widetilde{u'_i u'_j}$ and $M_i = \frac{\overline{\rho' u'_i}}{\tilde{\rho}}$ are the two unknown terms that require assumptions to close the system of equations. The most classic first-order models use a turbulent viscosity hypothesis, introduced by Boussinesq to express the tensor R_{ij} as a function of the gradients of mean velocity. The terms R_{ij} and M_i are modelled as follows:

$$R_{ij} = -\nu_t \left(\frac{\partial \bar{u}_i}{\partial x_j} + \frac{\partial \bar{u}_j}{\partial x_i} - \frac{2}{3} \frac{\partial \bar{u}_k}{\partial x_k} \delta_{ij} \right) \quad (\text{B.46})$$

$$M_i = -\kappa_t \frac{1}{T_0} \frac{\partial \bar{T}}{\partial x_i} \quad (\text{B.47})$$

where ν_t is the turbulent viscosity, $\kappa_t = \frac{\nu_t}{Pr_t}$ is the turbulent thermal diffusivity and Pr_t the turbulent Prandtl number.

The turbulent viscosity ν_t can be understood in two ways:

- In the physical space, it converts the momentum exchanges between molecules due to turbulence. It operates in an analogous manner to molecular viscosity ν , and generally $\nu_t > \nu$.
- In the spectral space, it accounts for the transfer of energy from large to small scales, and the dissipative effect of the latter.

Historically, the first turbulent viscosity model is that of Smagorinsky, developed in the sixties for the study of atmospheric flows. This is still used today and is the basis of many other models that were developed later. In this chapter, only the subgrid models implemented in Fire Dynamics Simulator (FDSv6) will be presented (see section B.4.2.1) which are: Smagorinsky constant, Smagorinsky dynamic, Deardorff and Vreman. Note that part of the following is an excerpt from the FDS Technical Reference Guide.

B.4 Fire Dynamics Simulator

As already mentioned in the report, FDS was chosen as the numerical model to simulate fires in ventilated tunnels (Chapter 5). The following is a general description of the software and its different physical models, that we can find in the FDS User Guide or the FDS Technical Reference Guide.

B.4.1 General presentation of FDS

FDS (Fire Dynamics Simulator) is a code developed by the National Institute for Standards and Technology (NIST) for the simulation of fires. It is currently in version 6.7.3, which offers, among others, the possibility of running calculations in parallel using Message Passing Interface (MPI) libraries. FDS is a numerical model suitable for low-speed flows with an emphasis on heat transport and smoke from fires. The code is supplied with Smokeview software which is a three-dimensional visualisation software. FDS solves, in DNS or LES, the Navier-Stokes equations (presented in previous sections for a low Mach number) written in discretized forms (a second-order central finite difference scheme). For the time discretization scheme, FDS uses an explicit predictor-corrector scheme with second-order accuracy. The Poisson equation is solved by the Fast Fourier Transformation (FFT) method.

B.4.2 Different physical models

To model turbulence and heat exchanges, FDS uses many models such as: subgrid models, combustion and radiation models.

B.4.2.1 Subgrid models

As already mentioned in section B.3, FDS offers four sub-grid models to close the system of equations (Eq. B.43 to Eq. B.45) and therefore to model the turbulent viscosity ν_t . These models are: Smagorinsky constant, Smagorinsky dynamic, Deardorff and Vreman. In FDS6, the Deardorff's turbulent viscosity model is the default. According to the FDS Technical Reference Guide, its selection as the default model was based on comparisons with a wide variety of full-scale experiments.

B.4.2.1.1 Constant coefficient Smagorinsky model

According to the analysis of Smagorinsky [109], the eddy viscosity ν_t can be modelled as follows:

$$v_t = (C_s \Delta)^2 |S| \quad ; \quad |S| = \left(2S_{ij}S_{ij} - \frac{2}{3} \left(\frac{\partial u_i}{\partial x_i} \right)^2 \right)^{1/2} \quad (\text{B.48})$$

with $S_{ij} = \frac{1}{2} \left(\frac{\partial \bar{u}_i}{\partial x_j} + \frac{\partial \bar{u}_j}{\partial x_i} \right)$, $C_s = 0.2$ the empirical Smagorinsky constant and $\Delta = (\delta x \delta y \delta z)^{1/3}$ the filter width.

B.4.2.1.2 Dynamic Smagorinsky model

For the dynamic Smagorinsky model [124], the coefficient C_s in Eq. B.48 is not assumed to be a constant. It is calculated at each time step based on the local flow conditions.

B.4.2.1.3 Deardorff's model

The Deardorff's model was already presented in the introduction of Chapter 5. Its principle is to model the turbulent viscosity v_t using the sub-grid kinetic energy k_{sgs} [112] as follows:

$$v_t = c_v \Delta \sqrt{k_{sgs}} \quad ; \quad k_{sgs} = \frac{1}{2} \left((\bar{u} - \hat{u})^2 + (\bar{v} - \hat{v})^2 + (\bar{w} - \hat{w})^2 \right) \quad (\text{B.49})$$

with C_D the model constant (generally $C_D = 0.1$ [113]) and (u, v, w) the three components of the velocity, where \bar{u} is the average value of u at the grid cell center and \hat{u} is a weighted average of u over the adjacent cells:

$$\bar{u}_{ijk} = \frac{u_{ijk} - u_{i-1,jk}}{2} \quad ; \quad \hat{u}_{ijk} = \frac{\bar{u}_{ijk}}{2} + \frac{\bar{u}_{i-1,jk} + \bar{u}_{i+1,jk}}{4}$$

The terms \bar{v} , \bar{w} , \hat{v} and \hat{w} are defined similarly.

B.4.2.1.4 Vreman's model

In Vreman's eddy viscosity model [125], the turbulent viscosity v_t is modelled by:

$$v_t = C_v \sqrt{\frac{B_\beta}{\Psi_{ij} \Psi_{ij}}} \quad (\text{B.50})$$

$$B_\beta = \beta_{11}\beta_{22} - \beta_{12}^2 + \beta_{11}\beta_{33} - \beta_{13}^2 + \beta_{22}\beta_{33} - \beta_{23}^2 \quad ; \quad \beta_{ij} = \Delta_m^2 \Psi_{mi} \Psi_{mj} \quad (\text{B.51})$$

$$\Psi_{ij} = \frac{\partial u_j}{\partial x_i} \quad (\text{B.52})$$

where the Vreman's model constant C_v is related to the empirical Smagorinsky constant C_s by $C_v = 2.5C_s^2$. This model is easy and inexpensive to compute in LES, since it does not need more than the first-order derivatives of the velocity field $\frac{\partial u_j}{\partial x_i}$ and the local filter width Δ . According to [125], the Vreman's model is much more accurate than the standard Smagorinsky model in LES of inhomogeneous turbulence. It shows an appropriate transitional and near wall-behaviour and remains robust in applications with a high Reynolds number. Note that, according to FDS developers, $C_s = 0.17$ gives accurate results for the highly resolved decaying isotropic turbulence and, therefore, the default Vreman constant is fixed to $C_v = 0.07$.

The turbulent thermal conductivity κ_t (already introduced previously in Eq. B.47) and turbulent mass diffusivity D_t are related to the turbulent viscosity ν_t by:

$$k_t = \frac{\nu_t}{Pr_t} \quad ; \quad D_t = \frac{\nu_t}{Sc_t} \quad (B.53)$$

For a given scenario, both the turbulent Prandtl number Pr_t and the turbulent Schmidt number Sc_t are assumed to be constant. The default value for these numbers is 0.5, but it can be changed by the user.

B.4.2.2 Combustion and Radiation models

Combustion and radiation models are also implemented in FDS. These models were not used in this thesis, where the fire source was modelled by injection of a light gas of air and helium. Some information are presented below, but for more details and relevant information, the reader is invited to refer to the FDS Technical Reference Guide.

B.4.2.2.1 Combustion model

The combustion model used in FDS is based on the mixing-limited, infinitely fast reaction of lumped species. The lumped species are reacting scalar quantities that represent a mixture of species. For an infinitely fast reaction, the reactant species in a given grid cell are converted to product species at a rate determined by a characteristic mixing time noted τ_{mix} (τ_{mix} depends on the following physical processes: advection, diffusion and buoyant acceleration). The heat release rate per unit volume \dot{q}''' is found by summing the lumped species mass production rates times their respective heats of formation:

$$\dot{q}''' = -\sum_{\xi} \dot{m}_{\xi}''' \Delta h_{f,\xi} \quad (\text{B.54})$$

where \dot{m}_{ξ}''' and $\Delta h_{f,\xi}$ are the mean chemical mass production rate and the heat of formation of species ξ , respectively.

B.4.2.2.2 Radiation model

Radiation is introduced into the energy equation and its net contribution \dot{q}_r''' is defined by:

$$\dot{q}_r''' = -\nabla \cdot \dot{q}_r''(x) = \zeta(x) [U(x) - 4\pi I_b(x)] \quad ; \quad U(x) = \int_{4\pi} I(x, s') ds' \quad (\text{B.55})$$

where $\zeta(x)$ is the coefficient of absorption, $I_b(x)$ is the source term and $I(x, s')$ is the solution of the radiation transport equation for non-scattering gases:

$$s \cdot \nabla I(x, s) = \zeta(x) [I_b(x) - I(x, s)]$$

Note that other models such as heat exchange models (conduction within solids, radiation heat transfer to solids, convective heat transfer to solids, etc.) are implemented in FDS and detailed in the Technical Reference Guide.

B.4.3 Solution Procedure

In a given grid cell and at the n th time step, the known variables are: the velocity u^n , the density ρ^n , the lumped species mass fractions Z_{ξ}^n , the fluctuating stagnation energy per unit of mass (or simply the perturbation pressure) H^n , the background pressure \bar{p}^n and the temperature T^n . As previously mentioned in section [B.4.1](#), these variables are advanced in time using an explicit second-order predictor-corrector scheme. The basic solution procedure is given as follows:

B.4.3.1 Predictor

1. First, ρ , Z_{ξ} and \bar{p} are estimated at the next time step with an explicit Euler step. For example, the density is estimated by:

$$\frac{\rho^* - \rho^n}{\delta t} + \nabla \cdot \rho^n u^n = 0 \quad (\text{B.56})$$

The asterisk indicates an accurate first-order estimate at the next time step.

2. The temperature T^* is computed from the equation of state.
3. The divergence of velocity field $(\nabla \cdot u)^*$ is estimated using the estimated thermodynamic quantities:

$$(\nabla \cdot u)^* = \frac{1}{\rho^n h_s} \left[\frac{\bar{p}^n - \rho^n h_s}{\delta t} + \nabla \cdot (\bar{p}^n - \rho^n h_s) u^n + (\dot{q}''')^n + (\dot{q}_r''')^n - (\dot{q}_b''')^n - \nabla \cdot (\dot{q}''')^n \right]$$

where h_s is the sensible enthalpy, \dot{q}_b''' is the energy transferred to subgrid-scale droplets and particles, and the term \dot{q}'' represents the conductive, diffusive, and radiative heat fluxes:

$$\dot{q}'' = -\lambda \nabla T - \sum_{\xi} h_{s,\xi} \rho D_{\xi} \nabla Z_{\xi} + \dot{q}_r'' \quad (\text{B.57})$$

4. The pressure term is computed by solving the Poisson equation (i.e. Eq. B.58 which is the simplified form of Eq. B.25) :

$$\nabla^2 H^n = -\frac{(\nabla \cdot u)^* - \nabla \cdot u^n}{\delta t} - \nabla \cdot F^n \quad (\text{B.58})$$

5. The velocity at the next time step is computed by Eq. B.59 (which is the simplified form of Eq. B.24):

$$\frac{u^* - u^n}{\delta t} + F^n + \nabla H^n = 0 \quad (\text{B.59})$$

Note that this procedure guarantees that the divergence of the updated velocity $\nabla \cdot u^*$ is

identically equal to the divergence that was computed solely from the thermodynamic variables $(\nabla \cdot u)^*$ in Step 3.

6. The time step δt is then checked that it satisfies the CFL and Von-Neumann stability conditions given respectively by:

$$\delta t \max \left(\frac{|u|}{\delta x}, \frac{|v|}{\delta x}, \frac{|w|}{\delta x} \right) < 1 \quad (\text{B.60})$$

$$\delta t \max [(\mu/\rho), D_\xi] \sum_i \frac{1}{\delta x_i^2} < \frac{1}{2} \quad (\text{B.61})$$

If the time step is too large, it will be reduced to satisfy the CFL and Von-Neumann stability conditions and the procedure returns to the beginning of the time step. Else (i.e. if the stability criteria are satisfied), the procedure continues to the corrector step.

B.4.3.2 Corrector

1. The density, lumped species mass fractions and background pressure are corrected at the next time step in a similar way. For example, the density is estimated by:

$$\frac{\rho^{**} - \frac{1}{2}(\rho^n + \rho^*)}{\delta t/2} + \nabla \cdot \rho^* u^* = 0 \quad (\text{B.62})$$

2. The temperature T^{**} is computed from the equation of state.
3. After the corrector step for the transport scheme, source terms are applied to the scalars (for both Lagrangian particles and chemical reactions). The source terms are then evaluated using the results from the corrected scalar transport scheme. For example:

$$\frac{(\rho Y_\xi)_{ijk}^{n+1} - (\rho Y_\xi)_{ijk}^{**}}{\delta t} = \dot{m}_{\xi,ijk}'''(Y^{**}, T^{**}) \quad (\text{B.63})$$

where Y_ξ is the primitive mass fraction of the species ξ and Y is the composition vector of the primitive species mass fractions.

4. With the updated density and composition, the final temperature T^{n+1} is computed from the equation of state.
5. The divergence $(\nabla \cdot u)^{n+1}$ is computed from the corrected thermodynamic quantities.
6. The pressure is computed using the estimated quantities:

$$\nabla^2 H^* = - \left[\frac{(\nabla \cdot u)^{n+1} - \frac{1}{2}(\nabla \cdot u^* + \nabla \cdot u^n)}{\delta t/2} \right] - \nabla \cdot F^* \quad (\text{B.64})$$

7. The velocity is then corrected at the next time step:

$$\frac{u^{n+1} - \frac{1}{2}(u^* + u^n)}{\delta t/2} + F^* + \nabla H^* = 0 \quad (\text{B.65})$$

Note that the divergence of the corrected velocity field $\nabla \cdot u^{n+1}$ is identically equal to the divergence that was computed from the thermodynamic quantities $(\nabla \cdot u)^{n+1}$ in Step 5.

REFERENCES

- [1] F. Saccomanno, P. Haastrup. Influence of Safety Measures on the Risks of Transporting Dangerous Goods through Road Tunnels. *Risk Anal.*, vol. 22, No. 6, 2002.
- [2] P. Casini, R. Hall, P. Pons. Transport of dangerous goods through road tunnels: Quantitative risk assessment model (version 3.20). User Guide, INERIS - WS Atkins - IRR, Report to OECD/PIARC/EU, December 1999.
- [3] HSC, Major hazard aspects of the transport of dangerous substances, Advisory Committee on Dangerous Substances, Health and Safety Commission, HMSO, London, 1991.
- [4] W. Hong. The progress and controlling Situation of Daegu Subway Fire Disaster, in 6th Asia-Oceania Symposium on Fire Science and Technology, 17-20 March, 2004, Daegu, Korea, pp. 28-46, 2004.
- [5] T. O. Naevestad and S. Meyer. A survey of vehicle fires in Norwegian road tunnels 2008-2011. *Tunn. Undergr. Space Technol.*, vol. 41, pp. 104-112, 2014.
- [6] J. Gehandler. Road tunnel fire safety and risk: a review. *Fire Sci. Rev.*, vol. 4, pp. 1-27, 2015.
- [7] H. K. Kim, A. Lonnermark and H. Ingason. Effective firefighting operations in road tunnels. Sweden, SP, Boras, 2010.
- [8] AIPCR, Maîtrise des incendies et des fumées dans les tunnels routiers, AIPCR, Tech. Rep., 1999.
- [9] CETU, Dossier pilote ventilation, Tech. Rep., 2003.
- [10] H. Ingason and A. Lonnermark. Heat Release Rates in Tunnel Fires: A Summary. In: Beard A, Carvel R (eds) *In The Handbook of Tunnel Fire Safety*, 2nd edn. ICE Publishing, London, pp 309-328, 2012.

- [11] DARTS, Durable and Reliable Tunnel Structures - The reports (CD Rom). CUR Gouda, Netherlands, 2004.
- [12] R. O. Carvel, A. N. Beard, P. W. Jowitt and D. D. Drysdale. Variation of heat release rate with forced longitudinal ventilation for vehicle fires in tunnels. *Fire Saf. J.*, vol. 36, pp. 569-596, 2001.
- [13] H. Ingason and Y.Z. Li. Model scale tunnel fire tests with longitudinal ventilation. *Fire Saf. J.*, vol. 45, pp. 371-384, 2010.
- [14] H. Ingason. Fire Development in Catastrophic Tunnel Fires (CTF). In: Ingason H (ed) International Symposium on Catastrophic Tunnel Fires (CTF). SP Swedish National Testing and Research Institute, Boras, Sweden, pp 31-47, 2003.
- [15] D. Purser. Hazards from toxicity and heat in fires, Hartford Environmental Research, Hatford, 2009.
- [16] P. Blomqvist. Emissions from Fires - Consequences for Human Safety and the Environment. Report 1030. Lund University, Lund, Sweden, 2005.
- [17] O. Vauquelin. Experimental simulations of fire-induced smoke control in tunnels using an air-helium reduced scale model: Principle, limitations, results and future. *Tunn. Undergr. Space Technol.*, vol. 23, pp. 171-78, 2008.
- [18] Memorial tunnel fire ventilation test program - test report, Massachussets Highway Department and federal Highway Administration, 1995.
- [19] Fires in Transport Tunnels: Report on Full-Scale Tests - EUREKA project EU 499 FIRETUN, editor: Studiengesellschaft Stahlanwendung e.V., Düsseldorf, 1995.
- [20] A. Lonnermark. On the characteristics of fires in tunnels. Ph.D. dissertation, Department of Fire Safety Engineering, Lund University, 2005.
- [21] Y. Oka, G.T. Atkinson. Control of smoke flow in tunnel fires. *Fire Saf. J.*, vol. 25, pp. 305-322, 1995.
- [22] Y. Wu, M. Bakar. Control of smoke flow in tunnel fires using longitudinal ventilation systems - a study of the critical velocity. *Fire Saf. J.*, vol. 35, pp. 363-390, 2000.
- [23] J. S. Roh, H. S. Ryou, D. H. Kim, W. S. Jung, Y. J. Jang. Critical velocity and burning rate in pool fire during longitudinal ventilation. *Tunn. Undergr. Space Technol.*, vol. 22, pp. 262-271, 2007.

- [24] G. Ko, S. Kim and H. Ryou. An experimental study on the effect of slope on the critical velocity in tunnel fires. *J. Fire. Sci.*, vol. 28, pp. 27-47, 2010.
- [25] J. Le Clanche, P. Salizzoni, M. Creyssels, R. Mehaddi, F. Candelier, O. Vauquelin. Aerodynamics of buoyant releases within a longitudinally ventilated tunnel. *Exp. Therm. Fluid Sci.*, vol. 57, pp. 121-127, 2014.
- [26] P. Salizzoni, M. Creyssels, L. Jiang, A. Mos, R. Mehaddi, O. Vauquelin. Influence of source conditions and heat losses on the upwind back-layering flow in a longitudinally ventilated tunnel. *Int. J. Heat Mass Tran.*, vol. 117, pp. 143-153, 2018.
- [27] L. Jiang, M. Creyssels, A. Mos, P. Salizzoni. Critical velocity in ventilated tunnels in the case of fire plumes and densimetric plumes. *Fire Saf. J.*, vol. 101, pp. 53-62, 2018.
- [28] D. Lacroix, P. Chasse, and T. Muller. Small scale study of smoke trap door systems, in 8th International Symposium on the Aerodynamics and Ventilation of Vehicle Tunnels, 1994.
- [29] J. G. Quintiere. Scaling applications in fire research, *Fire Saf. J.*, vol. 15, pp. 3-29, 1989.
- [30] G. G. Rooney and P. F. Linden. Similarity considerations for non-boussinesq plumes in an unstratified environment. *J. Fluid Mech.*, vol. 250, pp. 318-337, 1996.
- [31] L. Jiang, M. Creyssels, G. R. Hunt and P. Salizzoni. Control of light gas releases in ventilated tunnels. *J. Fluid Mech.*, vol. 872, pp. 515-531, 2019.
- [32] B.R. Morton. Forced plumes. *J. Fluid Mech.*, vol. 5, pp. 151-163, 1959.
- [33] G.R. Hunt, N.B. Kaye. Lazy plumes. *J. Fluid Mech.*, vol. 533, pp. 329-338, 2005.
- [34] Y. Oka and H. Oka. Velocity and temperature attenuation of a ceiling-jet along a horizontal tunnel with a flat ceiling and natural ventilation. *Tunn. Undergr. Space Technol.*, vol. 56, pp. 79-89, 2016.
- [35] A. Klein, W. Jessen, M. Oeser, W. Schroder and C. Sistenich. Investigations on smoke propagation with longitudinal ventilation by means of a model tunnel, 8th International Conference Tunnel Safety and Ventilation, Graz, 2016.

- [36] J. Lozano, W. Tachajapong, H. Pan, A. Swanson, C. Kelley, M. Princevac and S. Mahalingam. Experimental Investigation of the Velocity Field in a Controlled Wind-aided Propagating Fire Using Particle Image Velocimetry. *Fire Saf. Sci.*, pp. 255-266, 2009.
- [37] J. Y. Kim, S. W. Yoon, J. O. Yoo, T. B. Seo and D. H. Rie. A study on the smoke control characteristic of the longitudinally ventilated tunnel fire using PIV. *Tunn. Undergr. Space Technol.*, p. 302, 2006.
- [38] D. H. Rie, M. W. Hwang, S. J. Kim, S. W. Yoon, J. W. Ko and H. Y. Kim. A study of optimal vent mode for the smoke control of subway station fire, *Tunn. Undergr. Space Technol.*, pp. 300-301, 2006.
- [39] B.R. Morton, G.I. Taylor, J.S. Turner. Turbulent gravitational convection from maintained and instantaneous sources, *Proc. R. Soc. Lond. A* 234, pp. 1-23, 1956.
- [40] S. Saurabh, S. Maji, M. P. Bruchez. Evaluation of sCMOS cameras for detection and localization of single Cy5 molecules, *Opt. Express* 20, pp. 7338-7349, 2012.
- [41] M. Raffel, C. E. Willert, F. Scarano, C. J. kahler, S. T. Werely and J. Kompenhans. *Particle Image Velocimetry: A practical guide*, Third edn. Springer, 2018.
- [42] M. Marro, P. Salizzoni, F. X. Cierco, I. Korsakissok, E. Danzi and L. Soulhac. Plume rise and spread in buoyant releases from elevated sources in the lower atmosphere. *Environ. Fluid Mech.*, vol. 14, pp. 201-219, 2014.
- [43] L. Jiang. *Dynamics of Densimetric Plumes and Fire Plumes in Ventilated Tunnels*. Ph.D. dissertation Ecole Centrale de Lyon, 2017.
- [44] A.J.M Heselden. *Studies of fire and smoke behaviour relevant to tunnels*. Proceedings of the Second International Symposium of Aerodynamics and Ventilation of Vehicle Tunnels, Cambridge University Press, pp. 1-6, 1976.
- [45] G.T. Atkinson, Y. Wu. Smoke control in sloping tunnels. *Fire Saf. J.*, vol. 27, pp. 335-341, 1996.
- [46] O. Mégret, O. Vauquelin, P. Chassé and E. Casalé. A reduced scale tunnel for the study of fire-induced smoke control, 3rd International Conference on Safety in Road and Rail Tunnels, ITC, Nice, 1998.

- [47] L.H. Hu, R. Huo, H.B. Wang, Y.Z. Li, R.X. Yang. Experimental studies on fire-induced buoyant smoke temperature distribution along tunnel ceiling. *Build. Environ.*, vol. 42, pp. 3905-3915, 2007.
- [48] S. R. Lee, H. S. Ryou. A numerical study on smoke movement in longitudinal ventilation tunnel fires for different aspect ratio. *Build. Environ.*, vol. 41, pp. 719-725, 2006.
- [49] L.H. Hu, R. Huo, W.K. Chow. Studies on buoyancy-driven back-layering in tunnel fires. *Exp. Therm. Fluid Sci.*, vol. 32, pp. 1468-1483, 2008.
- [50] Y.Z. Li, B. Lei, H. Ingason. Study of critical velocity and backlayering length in longitudinally ventilated tunnel fires. *Fire Saf. J.*, vol. 45, pp. 361-370, 2010.
- [51] J.P. Kunsch. Critical velocity and range of a fire-gas plume in a ventilated tunnel. *Atmos. Environ.*, vol. 33, pp. 13-24, 1999.
- [52] S.R. Lee, H.S. Ryou. An experimental study of the effect of the aspect ratio on the critical velocity in longitudinal ventilation tunnel fires. *J. Fire Sci.*, vol. 23, pp. 119-138, 2005.
- [53] O. Vauquelin. Parametrical study of the back flow occurrence in case of a buoyant release into a rectangular channel. *Exp. Therm. Fluid Sci.*, vol 29, pp. 725-731, 2005.
- [54] C.C. Hwang , J.C. Edwards. The critical ventilation velocity in tunnel fires - a computer simulation. *Fire Saf. J.*, vol. 40, pp. 213-244, 2005.
- [55] K. C. Tsai, H. H. Chen, S. K. Lee. Critical ventilation velocity for multi-source tunnel fires. *J. Wind Eng. Ind. Aerodyn.*, vol. 98, pp. 650-660, 2010.
- [56] J. S. Roh, S. S. Yang, H. S. Ryou, M. O. Yoon, Y. T. Jeong. An experimental study on the effect of ventilation velocity on burning rate in tunnel fires - heptane pool fire case. *Build. Environ.*, vol. 43, pp. 1225-1231, 2008.
- [57] G.B. Grant, S.F. Jagger, C.J. Lea. Fires in tunnels. *Phil. Trans. R. Soc. B: Theme Issue on Fire Dynamics.* vol. 356, pp. 2873-2906, 1998.
- [58] G.B. Grant, D. Drysdale. Estimating heat release rates from large-scale tunnel fires, in: *Fire Saf. Sci. - Proceedings of the Fifth International Symposium, Melbourne*, pp. 1213-1224, 1995.

- [59] M. Janssens. Measuring Rate of Heat Release by Oxygen Consumption. *Fire Technol.*, pp.234-249, 1991.
- [60] C. Huggett. Estimation of the rate of heat release by means of oxygen consumption. *J. Fire Flammabl.*, vol. 12, pp. 61-65, 1980.
- [61] S. E. French. "EUREKA 499 - HGV Fire Test (Nov. 1992)-Summary Report" in: *Proceedings of the International Conference on Fires in Tunnels*, E. Ivarson (Ed.), SP Swedish National Testing and Research Institute, Boras, Sweden, pp. 63-85, 1994.
- [62] H. Ingason, A. Lonnermark. Heat release rates from heavy goods vehicle trailer fires in tunnels. *Fire Saf. J.*, vol. 40, pp. 646-668, 2005.
- [63] P.H. Thomas. The movement of buoyant fluid against a stream and venting of underground fire. Fire research station, Watford, London, 1958.
- [64] P. H. Thomas. The movement of smoke in horizontal passages against an air flow, *Fire Research Note*, No. 723, Fire Research Station, Watford, UK, 1968.
- [65] D. Ottl, P. Sturm, R. Almbauer, W. Ottl, A. Turner, G. Seitlinger. A new system to reduce the velocity of the air flow in the case of fire, *Proceedings of the Int. Conf. On Tunnel Safety and Ventilation*, Graz, 8.-10.4., pp. 279-286, 2002.
- [66] M. Bettelini, S. Rigert, N. Seifert. Flexible Devices for Smoke Control in Road Tunnels, *6th International Conference Tunnel Safety and Ventilation*, pp.265-272, Austria, 2012.
- [67] S. Rigert, M. Bettelini. New findings on the use of flexible curtains for smoke management in road tunnels, *15th International Symposium on Aerodynamics, Ventilation & Fire in Tunnels*, pp.147-159, Barcelona, Spain, 2013.
- [68] M. Seike, N. Kawabata, and M. Hasegawa. The Effect of Fixed Smoke Barriers on Evacuation Environment in Road Tunnel Fires with Natural Ventilation, *7th International Conference Tunnel Safety and Ventilation* , Graz, 2014.
- [69] Y.P. Lee and K. C. Tsai. Effect of vehicular blockage on critical ventilation velocity and tunnel fire behavior in longitudinally ventilated tunnels. *Fire Saf. J.*, vol. 53, pp. 35-42, 2012.
- [70] W. Tang, L. H. Hu and L. F. Chen. Effect of blockage-fire distance on buoyancy driven back-layering length and critical velocity in a tunnel: An experimental investigation and global correlations. *Appl. Therm. Eng.*, vol. 60, pp. 7-14, 2013.

- [71] W. U. Rojas Alva, G. Jomaas and A. S. Dederichs. The influence of vehicular obstacles on longitudinal ventilation control in tunnel fires. *Fire Saf. J.*, vol. 87, pp. 25-36, 2017.
- [72] S. Gannouni, R. B. Maad. Numerical study of the effect of blockage on critical velocity and backlayering length in longitudinally ventilated tunnel fires. *Tunn. Undergr. Space Technol.*, vol. 48, pp. 147-155, 2015.
- [73] S. Zhang, X. Cheng, Y. Yao, K. Zhu, K. Li, S. Lu, R. Zhang, H. Zhang. An experimental investigation on blockage effect of metro train on the smoke back-layering in subway tunnel fires. *Appl. Therm. Eng.*, vol. 99, pp. 214-223, 2016.
- [74] <http://www.bissistem.com/furness/files/FCO510-Laboratuvar-Tipi-Akis-Olcer.pdf>.
- [75] N. Danziger, W. Kennedy. Longitudinal ventilation analysis for the Glenwood canyon tunnels, 4th International Symposium Aerodynamics & Ventilation of Vehicle Tunnels, p. 169-186, 1982.
- [76] O. Vauquelin, O. Mégret. Smoke extraction experiments in case of fire in a tunnel. *Fire Saf. J.*, vol. 37, pp. 525-33, 2002.
- [77] O. Vauquelin, D. Telle. Definition and experimental evaluation of the smoke confinement velocity in tunnel fires. *Fire Saf. J.*, vol. 40, pp. 320-30, 2005.
- [78] Y. F. Wang, J. Jiang, D. Zhu. Full-scale experiment research and theoretical study for fires in tunnels with roof openings. *Fire Saf. J.*, vol. 44, pp. 339-348, 2009.
- [79] Y. F. Wang, T. Qin, X. F. Sun, S. Liu and J. C. Jiang. Full-scale fire experiments and simulation of tunnel with vertical shafts. *Appl. Therm. Eng.*, vol. 105, pp. 243-55, 2016.
- [80] H. Ingason and Y. Z. Li. Model Scale Tunnel Fire Tests with Point Extraction Ventilation. *J. Fire Prot. Eng.*, vol. 21, pp. 5-36, 2011.
- [81] C. G. Fan, J. Ji, Z. H. Gao, J. Y. Han and J. H. Sun. Experimental study of air entrainment mode with natural ventilation using shafts in road tunnel fires. *Int. J. Heat Mass Tran.*, vol. 56, pp. 750-57, 2013.
- [82] L.J. Li, Z. H. Gao, J. Ji, J.Y. Han and J.H. Sun. Research on the Phenomenon of Plug-holing under Mechanical Smoke Exhaust in Tunnel Fire, *Procedia Engineering*, 9th Asia-Oceania Symposium on Fire Science and Technology 62, pp. 1112-20, 2013.

- [83] D. Spratt and A. J. M. Heselden. Efficient extraction of smoke from a thin layer under a ceiling, Fire Research Note No. 1001. U.K. Joint Fire Research Organization, 1974.
- [84] H. P. Morgan and J. P. Gardiner. Design principles for smoke ventilation in enclosed shopping centers, BR186. Garston, U.K.: Building Research Establishment, 1990.
- [85] G. D. Lougheed, G. V. Hadjisophocleous, C. McCartney and B. C. Taber. Large-scale Physical Model Studies for an Atrium Smoke Exhaust System, ASHRAE Transactions, vol. 105, pp. 1-23, 1999.
- [86] J. Ji, Z. H. Gao, C. G. Fan, W. Zhong and J. H. Sun. A study of the effect of plugholing and boundary layer separation on natural ventilation with vertical shaft in urban road tunnel fires. *Int. J. Heat Mass Tran.*, vol. 55, pp. 6032-6041, 2012.
- [87] X. Jiang, X. Liao, S. Chen, J. Wang and S. Zhang. An experimental study on plugholing in tunnel fire with central smoke extraction. *Appl. Therm. Eng.*, vol. 138, pp. 840-848, 2018.
- [88] L. Yi, R. Wei, J. Peng, T. Ni, Z. Xu and D. Wu. Experimental study on heat exhaust coefficient of transversal smoke extraction system in tunnel under fire. *Tunn. Undergr. Space Technol.*, vol. 49, pp. 268-78, 2015.
- [89] T. Du, D. Yang, S. Peng, Y. Liu and Y. Xiao. Performance evaluation of longitudinal and transverse ventilation for thermal and smoke control in a looped urban traffic link tunnel. *Appl. Therm. Eng.*, vol. 96, pp. 490-500, 2016.
- [90] L. X. Yu, F. Liu, Y. Q. Liu, M.C. Weng and S. J. Liao. Experimental study on thermal and smoke control using transverse ventilation in a sloping urban traffic link tunnel fire. *Tunn. Undergr. Space Technol.*, vol. 71, pp. 81-93, 2018.
- [91] P. Zhao, Z. Yuan, Y. Yuan, N. Yu and T. Yu. A Study on Ceiling Temperature Distribution and Critical Exhaust Volumetric Flow Rate in a Long-Distance Subway Tunnel Fire with a Two-Point Extraction Ventilation System. *Energies*, vol. 12, p. 1411, 2019.
- [92] R. Harish, and K. Venkatasubbaiah. Effects of buoyancy induced roof ventilation systems for smoke removal in tunnel fires. *Tunn. Undergr. Space Technol.*, vol. 42, pp. 195-205, 2014.
- [93] H. H. Zhu, Y. Shen, Z. G. Yan, Q. C. Guo and Q. H. Guo. A numerical study on the feasibility and efficiency of point smoke extraction strategies in large cross-section

- shield tunnel fires using CFD modeling. *J. Loss Prev. Process Ind.*, vol. 44, pp. 158-170, 2016.
- [94] Q. Liang, Y. Li, J. Li, H. Xu and K. Li. Numerical studies on the smoke control by water mist screens with transverse ventilation in tunnel fires. *Tunn. Undergr. Space Technol.*, vol. 64, pp. 177-183, 2017.
- [95] E.J. Lee, C.B. Oh, K.C. Oh, Y.H. Yoo and H.J. Shin. Performance of the smoke extraction system for fires in the Busan-Geoje immersed tunnel, *Tunn. Undergr. Space Technol.*, vol. 25, pp. 600-606, 2010.
- [96] L.F. Chen, L.H. Hu, X.L. Zhang, X.Z. Zhang, X.C. Zhang, L.Z. Yang. Thermal buoyant smoke back-layering flow length in a longitudinal ventilated tunnel with ceiling extraction at difference distance from heat source. *Appl. Therm. Eng.* vol. 78, pp. 129-135, 2015.
- [97] Y. Yao, X. Cheng, S. Zhang, K. Zhu, L. Shi, H. Zhang. Smoke back-layering flow length in longitudinal ventilated tunnel fires with vertical shaft in the upstream. *Appl. Therm. Eng.*, vol. 107, pp. 738-746, 2016.
- [98] F. Tang, L.J. Li, M.S. Dong, Q. Wang, F.Z. Mei, L.H. Hu. Characterization of buoyant flow stratification behaviors by Richardson (Froude) number in a tunnel fire with complex combination of longitudinal ventilation and ceiling extraction. *Appl. Therm. Eng.*, vol. 110, pp. 1021-1028, 2017.
- [99] L. Jiang, M. Creyssels, P. Salizzoni, R. Perkins, A. Mos. Critical velocity in inclined tunnels, ISAVFT 17, 13-15 September 2017, Lyon, France.
- [100] K. McGrattan, S. Hostikka, R. McDermott, J. Floyd, C. Weinschenk, and K. Overholt. *Fire Dynamics Simulator, Technical Reference Guide*, National Institute of Standards and Technology, sixth edition, 2013.
- [101] K. B. McGrattan, R. G. Rehm, H. R. Baum. Large eddy simulations of smoke movement. *Fire Saf. J.* vol. 30, pp. 161-178, 1998.
- [102] E. Kim, J.P. Woycheese, N.A. Dembsey. Fire dynamics simulator (Version 4.0) simulation for tunnel fire scenarios with forced, transient, longitudinal ventilation flows. *Fire Technol.*, vol. 44, pp. 137-166, 2008.
- [103] H. Wang. Numerical and theoretical evaluations of the propagation of smoke and fire in a full-scale tunnel. *Fire Saf. J.*, vol. 49, pp. 10-21, 2012.

- [104] S. Gannouni, R. B. Maad. Numerical analysis of smoke dispersion against the wind in a tunnel fire. *J. Wind Eng. Ind. Aerodyn.*, vol. 158, pp. 61-68, 2016.
- [105] C.D. Ang, G. Rein, J. Peiro, R. Harrison. Simulating longitudinal ventilation flows in long tunnels: comparison of full CFD and multi-scale modelling approaches in FDS6. *Tunn. Undergr. Space Technol.*, vol. 52, pp. 119-126, 2016.
- [106] L. Hu, R. Huo, W. Peng, W. Chow, R. Yang. On the maximum smoke temperature under the ceiling in tunnel fires. *Tunn. Undergr. Space Technol.*, vol. 21, pp. 650-655, 2006.
- [107] L. Li, S. Li, X. Wang, H. Zhang. Fire-induced flow temperature along tunnels with longitudinal ventilation. *Tunn. Undergr. Space Technol.*, vol. 32, pp. 44-51, 2012.
- [108] Y. B. Huang, Y.F. Li, B.Y. Dong, J.M. Li, Q. Liang. Numerical investigation on the maximum ceiling temperature and longitudinal decay in a sealing tunnel fire. *Tunn. Undergr. Space Technol.*, vol. 72, pp. 120-130, 2018.
- [109] J. Smagorinsky. General circulation experiments with primitive equations-I, the basic experiment. *Mon. Weather Rev.*, vol. 91, pp. 99-105, 1963.
- [110] J. W. Deardorff. A Three-dimensional numerical study of turbulent channel flow at large Reynolds numbers. *J. Fluid Mech.*, vol. 41, pp. 453-480, 1970.
- [111] J. W. Deardorff. Stratocumulus-capped mixed layers derived from a three-dimensional model. *Bound-Lay. Meteorol.*, vol. 18, pp. 495-527, 1980.
- [112] J. W. Deardorff. Numerical Investigation of Neutral and Unstable Planetary Boundary Layers. *J. Atmos. Sci.*, vol. 29, pp. 91-115, 1972.
- [113] S. B. Pope. *Turbulent Flows*, Cambridge University Press, Cambridge, 2000.
- [114] H. Werner and H. Wengle. Large-eddy simulation of turbulent flow over and around a cube in a plate channel, In 8th Symposium on Turbulent Shear Flows, Munich, Germany, pp. 155-168, 1991.
- [115] F. Scarano, M. Riethmuller. Iterative multigrid approach in PIV image processing with discrete window offset. *Exp. Fluids.*, vol. 26, pp. 513-523, 1999.
- [116] K. Christensen. The influence of peak-locking errors on turbulence statistics computed from PIV ensembles., *Exp. Fluids.*, vol. 36, pp. 484-497, 2004.

- [117] R. J. Adrian and J. Westerweel. Particle image velocimetry, No. 30, Cambridge University Press, 2011.
- [118] M. Stanislas, K. Okamoto, C. J. Kahler, J. Westerweel and F. Scarano. Main results of the third international PIV challenge. *Exp. Fluids*, vol. 45, pp. 27-71, 2008.
- [119] P. L. Violette. Mécanique des fluides à masse volumique variable, Presse de l'Ecole Nationale des Ponts et Chaussées, 1997.
- [120] L. Landau and E. Lifchitz. Physique théorique - tome 6 - Mécanique des fluides, Editions Mir, 1989.
- [121] A. Rahmani. Simulation des grandes échelles pour les incendies en tunnels, Mécanique des fluides, Université Claude Bernard - Lyon I, 2006.
- [122] P. Carlotti. Eléments de mécanique des fluides pour la modélisation des incendies, Mécanique des fluides, Ecole Centrale de Lyon; Université Claude Bernard - Lyon I, 2013.
- [123] A. Favre. Turbulence: space-time statistical properties and behavior in supersonic flows. *Phys. Fluids*, vol. 23, pp. 2851-2863, 1983. .
- [124] M. Germano, U. Piomelli, P. Moin, and W.H. Cabot. A Dynamic Subgrid Scale Eddy Viscosity Model. *Phys. Fluids*, vol. 3, pp. 1760-1765, 1991.
- [125] B. Vreman. An eddy-viscosity subgrid-scale model for turbulent shear flow: Algebraic theory and applications. *Phys. Fluids*, vol. 16, pp. 3670-3681, 2004.

AUTORISATION DE SOUTENANCE

Vu les dispositions de l'arrêté du 25 mai 2016,

Vu la demande du directeur de thèse

Monsieur P. SALIZZONI

et les rapports de

M. P. BOULET

Professeur - LEMTA - 2 avenue de la Forêt de Haye - BP 90161 - 54505 Vandoeuvre cedex

et de

M. J. JAY

Professeur - Laboratoire CETHIL - Bâtiment Sadi Carnot - 7 rue de la physique
69621 Villeurbanne

Monsieur CHAABAT Fateh

est autorisé à soutenir une thèse pour l'obtention du grade de **DOCTEUR**

Ecole doctorale MECANIQUE, ENERGETIQUE, GENIE CIVIL ET ACOUSTIQUE

Fait à Ecully, le 4 février 2020

P/Le directeur de l'E.C.L.
Le directeur des Etudes



Grégory VIAL